Dissertation

submitted to the
Combined Faculties of the Natural Sciences and Mathematics
of the Ruperto-Carola-University of Heidelberg/Germany
for the degree of
Doctor of Natural Sciences

Put forward by

Sandra Isabelle Schmid

Born in: Ludwigsburg/Germany

Oral examination: 2011/11/30

Quantum optics with whispering gallery resonators coupled to atoms and fibers

Referees: **PD Dr. Jörg Evers**

Prof. Dr. Thomas Gasenzer

Zusammenfassung

In dieser Arbeit werden gekoppelte Systeme aus Flüstergallerieresonatoren, Atomen und Fasern untersucht. Es wird gezeigt, wie aus einer solchen Kavität und einem Mehrniveauatom ein kontrollierbares Photonendrehkreuz hergestellt werden kann, indem die Eigenschaften der Photonenstatistik ausgenutzt werden. Des weiteren wird eine Kette von gekoppelten Atom-Resonator-Systemen betrachtet, die über eine Faser miteinander verbunden sind. Durch den Energiefluss zwischen benachbarten Untersystemen in beide Richtungen bilden sich sogenannte Supermoden mit stark erhöhter Transmission verglichen mit einer Kette unabhängiger Systeme aus. Interferenzeffekte zwischen verschiedenen Wegen, die Licht durch ein solches System nehmen kann, bringen diese speziellen Moden hervor. Darüber hinaus werden in einer Anordnung von Mikroresonatoren solche Interferenzerscheinungen verschiedener Lichtwege untersucht. Es wird beobachtet, dass die Phasen der komplexen Kopplungskonstanten, mittels derer die Wechselwirkung zwischen benachbarten Resonatoren beschrieben wird, enormen Einfluss auf das Transmissions- und Reflexionsverhalten der Resonatoranordnung haben. Es wird gezeigt, dass dies zur Präzisionsmessung des Brechungsindexes einer dünnen Scheibe oder der Positions eines Teilchens ausgenutzt werden kann. Eine quantitative Analyse mittels FDTD Simulationen zur Sensitivität des Aufbaus wird durchgeführt. Die Lichtpropagation durch Scheibenresonatoren mit einem Loch als Lichtstreuer im Terahertz Regime wird studiert. Die Ergebnisse werden mit experimentellen Daten verglichen und stimmen mit diesen sehr gut überein.

Abstract

In this thesis, coupled systems of whispering gallery resonators, atoms and fibers are investigated. A setup for a controllable photon turnstile consisting of a multilevel atom and a cavity by exploiting the properties of the photon statistics is suggested. Furthermore, a chain of atom-cavity systems connected via a fiber is considered. Due to the energy flux between the subsystems in both directions so-called supermodes with vastly enhanced transmission compared to a chain of independent subsystems develop. Interference effects between pathways on which light can propagate through the system cause these special modes. Moreover, pathway interference effects in an array of microcavities are studied. It is observed that the phase angles of the complex coupling constants describing the interaction of neighboring cavities influence crucially the transmission and reflection behavior of the array. We show that this can be exploited for precision measurements of the refractive index of a thin slab or determining the position of a nearby particle on a sub-wavelength scale. A quantitative analysis of the sensitivity of the setup is performed via FDTD simulations. Light propagation through a disk resonator with a hole as light scatterer in the terahertz regime is studied. The results are compared to experimental data and a very good agreement is observed.

Within the framework of this Ph.D. thesis, the following articles were ...

... published in refereed journals:

- S. I. Schmid, K. Xia, and J. Evers,
  Pathway interference in a loop array of three coupled microresonators,
  Phys. Rev. A **84**, 013808 (2011).
- S. I. Schmid and J. Evers,
  Interplay of vacuum-mediated inter- and intraatomic couplings in a pair of atoms,
  Phys. Rev. A **81**, 063805 (2010).

... accepted for publication in refereed journals:

- S. I. Schmid and J. Evers,
  Microcavities coupled to multilevel atoms,
  Phys. Rev. A in print,
  arXiv:1108.1931 [quant-ph] (2011).

... submitted to refereed journals:

- S. I. Schmid and J. Evers,
  Formation of supermodes in a chain of atom-microcavity systems,
  submitted to Phys. Rev. Lett.,
  arXiv:1108.4525 [quant-ph] (2011).

Contents

Introduction

Whispering galleries form an intriguing feature of many famous works of architecture such as the dome of St. Peter's Basilica in Rome, the Echo Wall in the Temple of Heaven in Beijing, and the Alhambra in Granada. Due to reflections at the walls, such round shaped buildings can guide sound waves along their walls and thus the voice of a whispering person can be heard clearly by another person standing at distinct distant positions. This interesting behavior of sound waves has been fascinating people for several centuries. In 1892, The New York Times reported on this curious echo phenomenon in the Statuary Hall of the United States Capitol [1]. These special sound waves did not only find their way into famous works of literature such as Jules Verne's Journey to the Center of the Earth [2], but also played a central role during the scientific investigation of this wave dynamics. Probably the most famous realization of acoustic whispering gallery modes occurred in the dome of St. Paul's Cathedral in London [3]. It was in this church where the physics of acoustic whispering gallery modes was first studied by the later Nobel Prize Laureats Lord Rayleigh [4] and Raman [5] at the beginning of the last century.

Since the discovery of these special modes in acoustics, research on electromagnetic whispering gallery mode phenomena has been performed for many different wavelength regimes. In 1919, the propagation of electromagnetic waves around the earth was analyzed by the mathematician George N. Watson [6]. Resonant modes with extremely low frequencies (ELF) on the order of 1-300 Hz supported by the ionospheric whispering gallery were studied by the physicist W. O. Schumann and are referred to as Schumann Resonances [7–9]. In [10] it was shown, that the ionosphere forms a whispering gallery for radio waves with very low frequencies (VLF) of the order of 20-30 kHz. James R. Wait studied in detail the propagation of these radio waves around our planet in the 1960s [11, 12].

In recent decades, whispering galleries for light waves became very popular in optical sciences and photonics. With the evolution of modern fabrication techniques on smaller and smaller length scales, such as lithography, the field of whispering galleries for electromagnetic waves in the optical regime became accessible. These tiny so-called whispering gallery resonators with radii at the micrometer scale typically have very low loss rates and can trap light due to total reflections at the sidewalls of the resonators [13–15]. Typically,

these cavities have the form of rings, disks, toroids, or spheres. However, even tunable bottle shaped resonators have been developed [16, 17]. Since light can be stored in their very small volumes for many circulations which results in a long optical path, whispering gallery cavities became interesting for nonlinear optics where a crucial enhancement of nonlinear effects, occurring, e.g., in photorefractive materials such as lithium niobate, can already be achieved in small resonators [18, 19].

The outstanding properties of whispering gallery resonators promise numerous remarkable applications [20, 21]. The extremely long confinement times of light in these cavities cause very low threshold powers for nonlinear effects. Therefore, they are perfectly suited for microlasing applications [22–26]. Moreover, the sharp resonances of such microcavities make them interesting for selective wavelength filtering and ultrafast switching [27] needed for advanced telecommunication networks. In the simplest form, such an optical switch or filter consists of a ring or disk resonator sandwiched between two waveguides [28, 29].

Light in a whispering gallery cavity is not completely confined to the resonator's volume. Especially at the points of internal reflections the electromagnetic field leaks out of the cavity and exponentially decreases with the distance from the resonator. This so-called evanescent field allows the cavity to interact with external objects such as fibers, further resonators or particles in the surrounding environment. Additionally, this enables one to use microcavities as precision measurement devices for detecting slight changes, e.g., of the refractive index, in their environment. Due to the extremely low loss rates, which correspond to very high sensitivities, whispering gallery cavities are promising candidates for ultra sensitive biosensors [30–34]. Such sensors are of significant interest for life sciences and medical diagnostics where real-time label-free detection mechanisms for bacteria, molecules, viruses or proteins are necessary. How to accurately measure the size of a single nanoparticle down to 30 nm radius, which is located close to a whispering gallery cavity, by mode splitting is shown in [35]. Single molecule detection using microtoroid cavities has been demonstrated in [36]. For the purpose of biosensing, methods have been presented to detect single molecules, proteins or viruses coupling to the evanescent fields of a spherical whispering gallery cavity [37–42].

Furthermore, whispering gallery cavities are unique candidates for the development of a new generation of frequency combs for high precision frequency metrology. In contrast to conventional frequency combs [43], here, no external pump laser is required but the laser light is distributed to the comb peaks directly inside the microcavity due to nonlinearities, e.g., Kerr nonlinearities in the microtoroid's material [44]. Since light in high Q whispering gallery resonators is confined within a very small volume for many circulations, the threshold optical power for parametric oscillation is dramatically reduced [45]. Apart from the low initial power necessary for parametric frequency conversion, the advantages of these microcavity combs are their small size, very sharp resonance lines as well as the comparably large distance of the comb's spectral lines. Due to the high power per frequency line, they also promise various applications in modern highspeed telecommunications. Optical frequency combs have been experimentally realized using microcavities in the optical regime [46–48]. A fully stabilized frequency comb is presented in [49]. How to use a combination of an optical frequency comb with a tunable cavity diode laser for broadband spectroscopy is shown in [50].

Light forces which are caused by photons confined for long lifetimes in cavity modes of

high finesse resonators can be so high that they can measurably modify the motion of macroscopic objects such as microtoroids or mirrors. The long storage times of photons inside a whispering gallery cavity, which are comparable to a mechanical oscillation period, make these resonators to ideal tools for studying radiation force induced effects. The radiation pressure induced dynamical backaction between the resonator's small mass and the light field leads to a coupling of the system's optical and mechanical degrees of freedom and thus paves the way for a new research field called cavity optomechanics [51–58]. This coupling of optical and mechanical modes was theoretically proposed by V. B. Braginsky in 1977 [59]. More recently, optical control of mechanical motion of single nanocavities [60] or double-disk resonator structures [61, 62] has been studied. One goal is groundstate cooling of mechanical oscillators by using radiation pressure to damp the Brownian motion of whispering gallery cavities, similar to the routinely achieved atomic laser cooling. This is a prerequisite for investigations such as ultra sensitive measurements of forces or displacements as well as the observation of quantum phenomena of macroscopic objects. Here, the thermal oscillation modes of a cavity are damped due to the light forces which results in laser cooling of macroscopic whispering gallery cavities [63]. The mechanical motion modifies the optical path length and thus causes the excitation of sidebands. It was reported on sideband cooling of toroidal microcavities in theory [64] and experiment [65]. Moreover, exploiting this radiation pressure induced coupling of optical and mechanical modes, optomechanically induced transparency, analogous to electromagnetic induced transparency (EIT) in atoms or molecules, has been achieved [66].

Besides single cavity systems, arrays of coupled microcavities have received great attention. These coupled systems often allow for even sharper resonances and higher quality factors as compared to a single resonator. The arrangement of whispering gallery resonators to arrays thus allows to advance optical filtering and switching devices as compared to single cavity setups [67–80]. In these systems, ring or disk cavities are coupled to different constellations of waveguides, e.g., cross shaped setups, in order to optimize the array's properties. Additionally, loop arrangements have been considered [68, 69]. Photonic crystals can be used for the experimental design of such coupled cavity arrays [81, 82]. In optimized cavity arrays, switching times are of the order of picoseconds [83–87]. Furthermore, such cavity arrangements can be exploited for achieving slow light. A realization of ultraslow light pulse propagation with a group velocity below one hundredth of the vacuum light velocity was achieved in arrays of photonic crystal nanocavities [88].

Another similar approach to improve the functionality of microcavities as wavelength-selective filters and switches or as microlasers is combining them to photonic molecules by coupling several disk or ring cavities [89–92]. Similar to chemical molecules, these are clusters of closely located microcavities, the "photonic atoms", interacting via their evanescent fields. Here, in particular so-called supermodes are considered, which are collective multicavity modes describing the whole coupled system, similar to dressed states of an atom interacting with an external field or coupled atoms in a chemical molecule. Often very symmetric clusters of microcavities are investigated, where supermodes occur with strong enhanced quality factors as compared to modes of a single resonator. Since these supermodes can lead to directional radiation characteristics with narrow beams even in the far field, photonic molecules can serve as microlasers [93–96]. The narrow resonant linewidth and wide mode spacing additionally enhance their sensitivity to changes of, e.g., the refractive index in the cavity's environment. Hence, they are especially interesting

for label-free sensing applications [97, 98].

In recent years, coupled systems of cavities and atoms or quantum dots have drawn tremendous interest [99–102]. Couplings between cavities and atoms are achieved via the evanescent field surrounding the resonator. These coupled systems offer a variety of fascinating applications. For example, a photon transistor built of a microcavity coupled to a nearby three-level atom is suggested in [103, 104]. How a simple two-level atom coupled to a toroidal cavity can be used as a single photon turnstile is presented in [105]. Moreover, such systems are promising candidates for building quantum networks and quantum information devices [106–112].

Experimentally, such couplings are often realized using a falling cloud of cold atoms, since trapping an atom in the vicinity of the resonator can be difficult [99, 100, 105]. In order to achieve strong interaction between an atom and a microcavity, the atom has to be located within a distance smaller than the optical wavelength, where the evanescent field surrounding the cavity is not negligible. This is experimentally challenging, in particular since the trapping laser beams could heat and even melt the resonator, depending on its material. In order to avoid these problems, a typical experimental setup consists of a tapered fiber coupled to a toroid or ring resonator and an ensemble of atoms is cooled in a trap above the cavity. After cooling, the cloud of cold atoms is released and falls down close to the resonator's surface, such that a few atoms pass the evanescent field. Therefore, they interact via the evanescent field with the photonic cavity modes on their way falling down [99, 100, 105]. Another setup where atom-cavity coupling is achieved by an atomic fountain is presented in [113]. Here, a bottle whispering gallery resonator is mounted above a magneto-optical trap. The atomic cloud is launched upwards and passes the resonator's evanescent field at the turning point of the atomic fountain. However, in recent experiments a localization of single cesium atoms has been achieved as well [114, 115]. Here, the evanescent field itself is used to trap the atoms. This opens up a route to directly integrate cooled atomic ensembles into atom-microcavity networks.

In this Ph.D. thesis, different coupled systems of microcavities, nearby atoms of different inner structure, and fibers are studied. Especially, their applications as sensing and photon turnstile devices, optical switches and filters as well as microlasers are considered. Transmission and reflection spectra as well as higher order photon correlations and cross correlations between different photonic modes in a coupled multilevel-atom-cavity system are investigated. We show how to exploit the special properties of the resulting photon statistics as a controllable, bimodal photon turnstile. Furthermore, so-called supermodes occurring in a chain of atom-cavity systems and leading to a strong transmission enhancement are studied. Arrays of microcavities in special loop arrangements which lead to very sharp resonance lines in the transmission and reflection spectra are considered. Light pathway interference is analyzed in terms of a coupled mode theory. Precision measurement devices are suggested and their sensitivity is quantitatively analyzed via numerical FDTD (finite-difference time-domain) simulations. Moreover, a disk resonator with hole which functions as a finite light scatterer is found to exhibit anisotropic, directional radiation characteristics which could be exploited for microlasing as well as sensing purposes.

This thesis is divided into five parts. In part I, a mathematical model is presented for a very general form of a coupled chain of subsystems connected by a waveguide. Each of these subsystems consists of a multilevel atom as well as a coupled array of an arbitrary

number of whispering gallery mode cavities. Most of the setups considered in the later parts are reductions of the general model regarded in this introductory part. Since a theoretical description of such systems including all relevant coupling mechanisms is not part of standard literature yet, we here derive the Hamiltonian and the equations of motion describing the general system. We explain the different coupling mechanisms in detail and derive their contributions to the system's Hamiltonian. These coupling mechanisms as well as their energy contributions are relevant for the systems investigated in the later parts of this thesis. Additionally, the time evolution of the density operator and the equations of motion for the system operators are presented.

In part II, we consider a microcavity interacting with a nearby three-level atom in the Λ configuration, i.e., the atom has an internal structure with one upper and two lower states. The resonator is additionally coupled to a tapered fiber which allows to apply an input laser field. In many previous works, the atom coupling to the cavity modes has been modeled with two internal energy levels [99, 100, 102, 105]. To date, less research has been performed on multilevel atoms interacting with microresonators [103, 104]. Since coupling of several atomic transitions to the mode pairs within a resonator could enable more advanced control schemes, we here consider a whispering gallery resonator interacting with both transition dipoles of a nearby three-level atom in the Λ configuration. We assume two different pairs of whispering gallery modes to be supported by the cavity. Due to the choice of the polarization and the frequency, each pair can couple to one of the atomic transitions, respectively. Two fundamentally different parameter regimes are studied. Firstly, the strong coupling regime is considered, where the coupling of the cavity to the atom is much stronger than the coupling to the fiber and the scattering between different photon modes. Secondly, calculations are performed in the so-called bad cavity regime, where the coupling to the atom is assumed to be weak, which means that further coupling, scattering, and dissipative processes govern the system's dynamics. Different calculation methods for the two regimes are explained and discussed in detail. The first is based on a Fock mode truncation, where photonic Fock states up to a certain number of photons are taken into account and the respective equations of motion are solved numerically. For the bad-cavity regime additionally a method to adiabatically eliminate the cavity modes is explained. We study the impact of the atom on the transmission and reflection intensity of the different photon output modes for both the parameter regimes of interest. Furthermore, we consider higher order correlation functions and cross correlations between different photon modes. Exploiting the special properties of the photon statistics, a method to build a controllable photon turnstile for different output fluxes is found. Motivated by a previous publication [105], in which was reported on an experimental realization of a photon turnstile using a single mode pair and a nearby two-level atom, we further develop this model and propose a control method via the input fields. In addition, optical switching, single photon sources and the detection of particles close to the resonator surface are discussed as potential applications.

In part III, we investigate a chain of microcavities connected by a common waveguide to which weak input fields are applied for probing the system. Each microresonator additionally couples to a nearby two-level atom. Between the cavities, fluxes in both directions are possible. We are particularly interested in properties which differ from a chain of independent cavities. Here, independent means that backcoupling fluxes between the resonators are suppressed. The transmission and reflection behavior is studied in dependence on the chain length, the distance between neighboring subsystems as well as the different

coupling strengths. Two different calculation methods are applied. On the one hand, we numerically solve the equations of motion for this system in a semiclassical description. This calculation is very time consuming, especially for long chains. Therefore, on the other hand, a more efficient calculation method using a coupling matrix, which describes the system in the limit of weak input fields, is presented. The advantages and drawbacks of both these calculation methods are discussed. Light entering such a complex coupled system can take various different pathways before leaving the system and contributing to one of the output fluxes. Interference of such pathways plays an important role for the transmission and reflection behavior. The intercavity distances as well as the different coupling constants describing the various interaction mechanisms influence strongly the system's dynamics. Due to constructive interference of light pathways the formation of so-called supermodes becomes possible. These are collective modes of the whole coupled system, which can lead to crucially enhanced transmission. Configurations are studied in detail, where supermodes establish and therefore the transmission is considerably enhanced compared to the case of independent cavities. We find, that for long chains the influence on the system's dynamics increases with increasing chain length. The origin of these resonance supermodes is analyzed in terms of pathway interference. The transmission signal provides information about occurring supermodes, whereas the reflection signal could be used to detect which cavities of the chain couple to nearby atoms. This information cannot be obtained from the transmission signal, since the order of the chain elements has no influence on the transmission. Our setup could serve as a detector for measuring which of the subsystems possess a nearby coupling atom. This is relevant for experiments where it can be difficult to achieve simultaneous coupling of single atoms to all resonators of the chain, e.g., if a falling cloud of cold atoms is used to achieve atom-cavity coupling, see [99, 100, 105]. Furthermore, the position of single subsystems can be measured with high precision. We show that shifts of only one twentieth of the light wavelength already result in vastly different transmission intensities.

In part IV, we study an array of three cavities arranged in a loop configuration. In this arrangement, every resonator is coupled to both the other elements of the array. One of the resonators is additionally coupled to a waveguide. An input probe field is applied from one direction. The coupling between the cavities is described by complex coupling constants. There are cases, where the phases are not important and thus the coupling parameters can be taken as real numbers, neglecting the phase information [68, 69]. In our work, however, particular interest lies on the impact of these phase factors on the transmission and reflection behavior. A roundtrip process, where light moves on a pathway which leads through all three cavities is found to play a special role in the dynamics of this coupled array and gives rise to very sharp resonance lines in the transmission and reflection signal. The phases of the coupling constants and scattering rates can be manipulated by placing a small particle near one of the cavities or by changing the refractive index in the coupling region between the cavities, e.g., by placing a thin slab there or embedding the system into a liquid. This effect can be exploited for precisely measuring the refractive index of a thin slab, the concentration of a dissolved substance in a liquid, or for detecting the position of a nearby particle on a sub-wavelength scale.

In part V, the propagation of the electromagnetic field through different photonic systems is investigated by numerical FDTD simulations. Firstly, the array of three microcavities in a loop configuration as introduced in the preceding part is studied. A quantitative analysis of the suggested applications of the setup as precision measurement devices and

their sensitivity is performed. Secondly, a disk resonator with a hole which functions as a finite scatterer is simulated. We consider different sizes and positions of the disk and the hole. Our observables are the transmission spectrum as well as the radiation behavior in the near field. The results are compared to experimental data for the transmission spectra and the far field radiation measured at the Max Planck Institute for the Science of Light in Erlangen. We explain the main features of the radiation characteristics measured in the far field by simulations of the near field radiation and our results are found to be in very good agreement with the experimental findings.

Finally, our results are summarized and an outlook for future research is provided.

PART I

The Mathematical Model

I The Mathematical Model

In this part, a general mathematical model is introduced to describe coupled systems consisting of microcavities, atoms and fibers. Most of the systems investigated in the following parts are reductions of this general setup. The dynamics of such a system is governed by various coupling mechanisms. These different coupling mechanisms and their contributions to the Hamiltonian are discussed. A general master equation for such systems is derived. Eventually, we present the equations of motion for this general setup.

I.1. Introduction

Throughout this Ph.D. thesis, coupled systems consisting of microcavities, fibers and atoms are analyzed. During the last years, a lot of research was carried out in this field. However, in most works either coupled arrays of cavities without atoms [68, 69, 116] or single cavities coupled to a nearby atom [55, 99, 101–103, 105, 117, 118] are studied. We take both these different coupling mechanisms into account and consider coupled arrays containing both microcavities and atoms. In this section we derive a general master equation taking into account contributions from both inter-cavity coupling terms and cavity-atom coupling terms.

Since we consider systems consisting of whispering gallery modes (WGM), we first explain the physics of these special modes. As shown in Fig. I.1.(a), light can be totally reflected on a boundary of two media with different refractive indices. In the language of ray optics, due to the different light velocities, light propagating from a medium with refractive index n_1 towards a medium with refractive index n_2 changes its propagation direction by an angle $\Delta\alpha = \alpha - \beta$. For the refracted light, the refractive angle β can be calculated via Snell's law

$$\frac{\sin\alpha}{\sin\beta} = \frac{n_2}{n_1}\,. \tag{I.1.1}$$

However, if the upper medium in Fig. I.1.(a) is of lower optical density than the lower medium, i.e., $n_2 < n_1$, also total reflection can take place if the incident angle α exceeds a certain maximum angle α_{max}, which leads to an output angle of $\beta = 90°$. For the output angle $\beta = 90°$, the incident angle is

$$\alpha_{max} = \arcsin\left(\frac{n_2}{n_1}\right)\,. \tag{I.1.2}$$

Further increasing the angle α leads to total reflection of the incident light as shown in Fig. I.1.(a). This effect which can take place at a boundary between a medium of

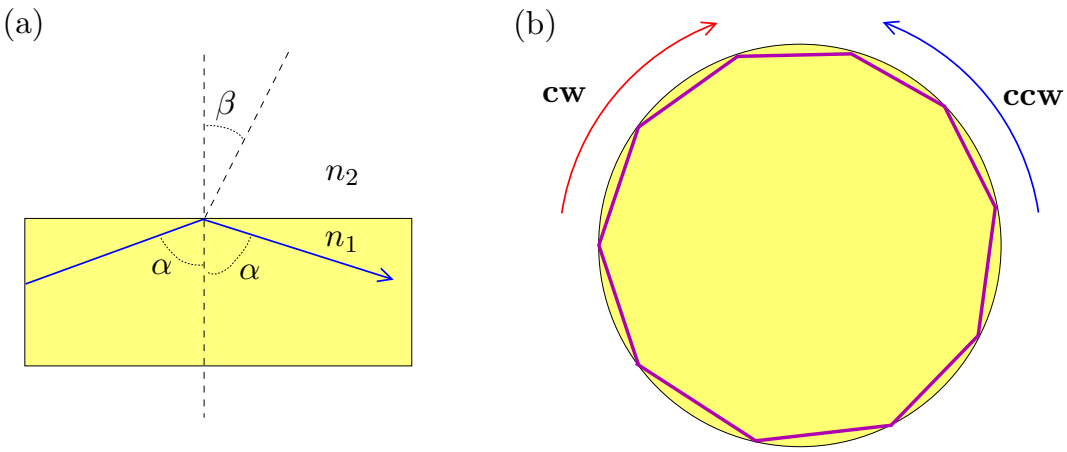

Figure I.1.: (a) Snell's law and (b) propagation of whispering gallery modes.

higher refractive index to another medium of smaller refractive index, is exploited for WGM resonators. Usually, these cavities have the shape of a disk, ring or toroid. Due to total reflection at the resonator's boundaries, entering light can propagate on a polygonal pathway in the cavity. For modes concentrated at the circumference of such a resonator, the number of edges of these polygons is very high and thus these light pathways can be approximated as circles.

At the points of the resonator boundary, where the total reflection occurs, light can leak out of the resonator. This so-called evanescent light field surrounds the cavity and exponentially decays with the radial distance from the cavity. Other objects can couple to the cavity modes and influence the system's dynamics if they are located within this short distance, where the evanescent field is not negligible. On the one hand, if another cavity is placed close to such a resonator and additionally their resonance frequencies are similar, photonic coupling between these two neighboring resonators can occur. On the other hand, atoms or molecules whose transition frequencies match the cavity modes can couple to the WGM resonator. In the next section, we study these different types of coupling mechanisms in detail and derive their contributions to the Hamiltonian $\mathcal{H}$ of our system and to the time evolution of the density operator ρ.

I.2. Theoretical description of the system

In this section we introduce a general form of the coupled systems studied in this thesis. Our general model system consists of a chain of subsystems connected by a common fiber. Each subsystem is composed of several microcavities and a nearby quantum system, e.g., a quantum dot or an atom. For simplicity, we write "atom" in stead of "quantum system" in the following. We describe the possible coupling mechanisms and their contribution to the master equation of the density operator as well as to the equations of motion for the quantum mechanical operators relevant for our system. An example of such a general system is shown in Fig. I.2. We consider a chain of N coupled subsystems, each of which consists of a number of D_n coupled cavities and one nearby atom, which is coupled to the first cavity of the respective subsystem n, here $n \in \{1, .., N\}$. In our mathematical theory, each cavity can be coupled to every other cavity of the respective subsystem but

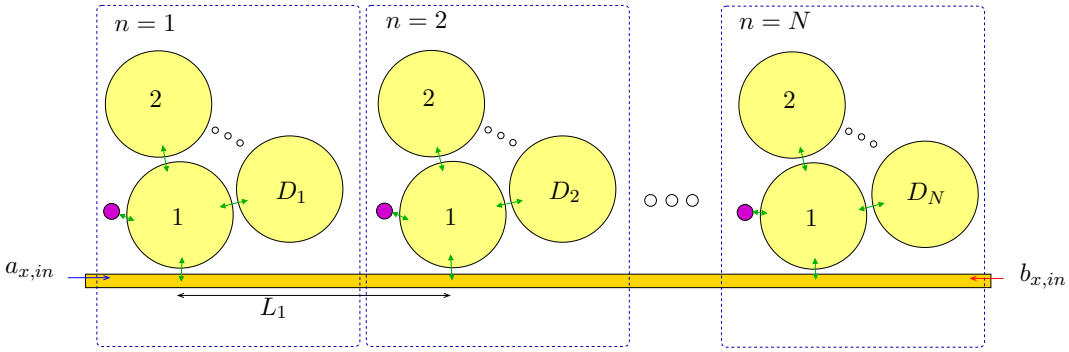

Figure I.2.: Our general coupled system consisting of N subsystems arranged in a chain. Each subsystem n consists of D_n coupled cavities and a nearby atom. In each cavity X different whispering gallery mode pairs $\{a^{(d)}_{x,n}, b^{(d)}_{x,n}\}$ can propagate.

only cavity 1 of each subsystem couples to the fiber. However, in an experiment, many of these inter-cavity couplings vanish just due to geometrical reasons. For the atom we assume an inner structure as shown in Fig. I.3.(d) with one upper state $|e_n\rangle$ and X lower states $|g_{x,n}\rangle$ and X possible transitions, $x \in \{1, .., X\}$. The frequency differences of the lower levels $\omega_{g_{x,n}} - \omega_{g_{y,n}}$ are assumed to be much smaller than each of the transition frequencies $\omega_{x,n} = \omega_{e,n} - \omega_{g_{x,n}}$ with $x, y \in \{1, .., X\}$. The atom couples only to cavity 1 of each subsystem which is also coupled to the fiber. We consider so-called whispering gallery mode (WGM) resonators. Whispering gallery modes always occur in pairs and two modes belonging to the same pair only differ by their propagation direction but have the same frequency. One of them propagates clockwise whereas the other one on a counter-clockwise circle. We assume that X possible mode pairs can propagate in our cavities and the pair with index x can couple to the transition $|g_{x,n}\rangle \leftrightarrow |e_n\rangle$ of the atom close to cavity 1 of the respective subsystem. Such a selective coupling can be achieved by choosing different atomic transition frequencies or orthogonal transition dipole moments. The photonic operators describing these whispering gallery mode pairs are denoted by $\{a^{(d)}_{x,n}, b^{(d)}_{x,n}\}$ with $d \in \{1, .., D_n\}$. We assume weak input probe fields applied from both directions with photonic operators $a_{x,in}$ and $b_{x,in}$, respectively, and laser frequencies ω_{L_x}. The different detunings are defined as

$$\begin{aligned} \Delta_{x,n} &= \omega_{x,n} - \omega_{L_x} \,, \\ \delta^{(d)}_{x,n} &= \omega^{(d)}_{cav,x,n} - \omega_{L_x} \,, \\ \epsilon^{(\mu\nu)}_{xy,n} &= \omega^{(\mu)}_{cav,x,n} - \omega^{(\nu)}_{cav,y,n} \,, \end{aligned} \tag{I.2.3}$$

where $\Delta_{x,n}$ is the detuning between the transition frequency of transitions x of the atom at subsystem n and the field probe fields. The detunings between the input probe fields and the cavities' resonance modes of frequency $\omega^{(d)}_{cav,x,n}$ are described by $\delta^{(d)}_{x,n}$ and $\epsilon^{(\mu\nu)}_{xy,n}$ is the frequency difference between two cavity resonance mode pairs $\{a^{(\mu)}_{x,n}, b^{(\mu)}_{x,n}\}$ and $\{a^{(\nu)}_{y,n}, b^{(\nu)}_{y,n}\}$ where $x, y \in \{1, .., X\}$ and $\mu, \nu \in \{1, .., D_n\}$.

In principle, four fundamentally different coupling mechanisms are of importance for our system. Firstly, the coupling of the waveguide to the first cavity of each subsystem as depicted in Fig. I.3.(a) governs the input flux of the subsystem. By varying the distance between this cavity and the fiber the coupling strength can be controlled. Of course, by

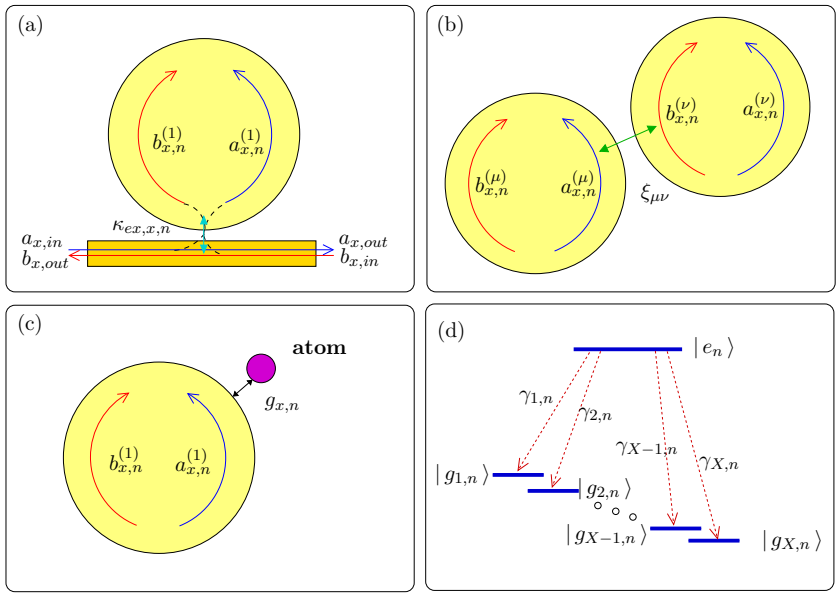

Figure I.3.: The different coupling mechanisms. (a) coupling between a microresonator and a fiber, (b) coupling between two nearby cavities, (c) coupling between a nearby atom and a resonator, and (d) internal structure of the atoms.

increasing this distance $l_{wg,n}$ such that the evanescent field of the fiber does no longer overlap with the cavity, the coupling strength is zero. Secondly, scattering between counterpropagating modes within one resonator can take place, e.g., due to material imperfections or the cavity's surface roughness. Thirdly, two neighboring cavities can exchange photons, if their mutual distance is such small that their evanescent fields overlap, see Fig. I.3.(b). Finally, the atom-cavity coupling shown in Fig. I.3.(c) is important for our system, if the atom is close enough to cavity 1.

These interaction mechanisms as well as their respective contributions to the Hamiltonian and the master equation are discussed in more detail in the next section.

I.3. The Hamiltonian

In this section, we derive the Hamiltonian describing our general coupled system. We start by considering the energy contributions of the atoms to the Hamiltonian. We define the atomic transition operators $\mathcal{S}^{+}_{x,n} = |e_n\rangle\langle g_{x,n}|$ and $\mathcal{S}^{-}_{x,n} = |g_{x,n}\rangle\langle e_n|$. Here, n is the index for the subsystem and x the index for the internal transition of atom n and $n \in \{1, .., N\}$ whereas $x \in \{1, .., X\}$. In our description, all energies are considered relative to the upper atomic level, whose energy is set to zero. Then, the part of the Hamiltonian which governs the free time evolution of the atoms of the N subsystems reads [119]

$$\mathcal{H}_{at} = \sum_{n=1}^{N} \sum_{x=1}^{X} -\hbar\omega_{x,n}\, \mathcal{S}^{-}_{x,n}\mathcal{S}^{+}_{x,n} \,. \tag{I.3.4}$$

Similarly, we obtain the contribution for each photon mode, which can propagate in our system. The Hamiltonian of the free photon field including all pairs of WGMs $\{a^{(d)}_{x,n}, b^{(d)}_{x,n}\}$

reads

$$\mathcal{H}_{phot} = \sum_{n=1}^{N} \sum_{x=1}^{X} \sum_{d=1}^{D_n} \hbar\omega_{cav,x,n}^{(d)} \, a_{x,n}^{(d)\dagger} a_{x,n}^{(d)} + \hbar\omega_{cav,x,n}^{(d)} \, b_{x,n}^{(d)\dagger} b_{x,n}^{(d)} \, . \tag{I.3.5}$$

Here, $d \in \{1, .., D_n\}$ is the index for the cavity number within subsystem n.

The Hamiltonian of the free input laser field reads

$$\mathcal{H}_{laser} = \sum_{x=1}^{X} \hbar\omega_{L_x} \left(a_{x,in}^{\dagger} a_{x,in} + b_{x,in}^{\dagger} b_{x,in} \right) . \tag{I.3.6}$$

After introducing the terms of the Hamiltonian that govern the free time evolution of the atoms and the light field, we now turn to the contributions which describe interaction processes and the different coupling mechanisms. We start with the coupling of cavity 1 to the fiber, see Fig. I.3.(a). If this cavity is close enough to the fiber, light can couple via the evanescent field of the fiber into the nearby cavity. For a pair of input modes with annihilation operators $\{a_{x,n,in}, b_{x,n,in}\}$ this coupling mechanism is described by the pair of coupling constants $\{\kappa_{ex,a_x,n}, \kappa_{ex,b_x,n}\}$ for cavity 1 belonging to subsystem n. However, since modes a and b of the same WGM pair have the same frequency, we assume their coupling strengths from the fiber into the cavity to be identical. This allows us to define the external coupling parameter $\kappa_{ex,x,n} = \kappa_{ex,a_x,n} = \kappa_{ex,b_x,n}$. Including all N subsystems and each of the X different input mode pairs the term of the Hamiltonian originating from the coupling between the fiber and the N subsystems reads [120]

$$\mathcal{H}_{ext} = \sum_{n=1}^{N} \sum_{x=1}^{X} \hbar\sqrt{2\kappa_{ex,x,n}} \cdot a_{x,n,in}^{\dagger} \, a_{x,n}^{(1)} + \sqrt{2\kappa_{ex,x,n}} \cdot b_{x,n,in}^{\dagger} \, b_{x,n}^{(1)} + \text{H.c.} \, . \tag{I.3.7}$$

Another possible coupling mechanism is photonic coupling between two neighboring cavities with very small inter-cavity distance, see Fig. I.3.(b). If the inter-cavity distance is such small that the evanescent fields of the neighboring cavities are overlapping, a photon exchange is possible. This photonic coupling between two nearby cavities is described by the constants $\xi_{\mu\nu,n}$ where $\mu, \nu \in \{1, .., D_n\}$ are the indices for the cavity numbers in subsystem n. At the position where the distance of two nearby cavities μ and ν is smallest, the tangential vectors of the propagation direction of $a_{x,n}^{(\mu)}$ and $b_{x,n}^{(\nu)}$ point in the same direction. For the reason of momentum conservation, we only take into account interaction processes, where a b_x photon of cavity ν is annihilated and an a_x photon of cavity μ is created or the other way around rather than couplings of a_x photons of the two cavities which are considered as second order processes. A coupling, where a b_x photon of cavity ν is annihilated and an a_x photon of cavity μ is created can be described by terms as [121]

$$\hbar\xi_{\mu\nu,n} \cdot a_{\mu,n}^{\dagger} b_{\nu,n} \, . \tag{I.3.8}$$

However, such interaction processes take place not only between modes of neighboring cavities but also within the same cavity. For example, an a_x photon can be scattered into mode b_x of the same WGM pair in the same cavity. These scattering processes within one cavity can be caused, e.g., by the surface roughness or imperfections of the resonator's material or by nearby particles.

Until now, we considered interactions between mode pairs of the same number x. In principle, also scattering processes between different mode pairs are possible. However,

for the reason of energy conservation couplings of modes of different frequencies are less probable in the experiment. Since the frequencies of different mode pairs typically are not the same, in a suitable interaction picture, the contribution describing this type of scattering is time dependent and oscillates with the frequency difference $\epsilon_{xy,n}^{(\mu\nu)} = \omega_{cav,x,n}^{(\mu)} - \omega_{cav,y,n}^{(\nu)}$ defined in Eq. (I.2.3). Since this oscillation becomes faster with increasing $\epsilon_{xy,n}^{(\mu\nu)}$, the coupling of mode pairs with large frequency differences can be neglected.

The total contribution to the Hamiltonian describing the different kinds of couplings among the photon modes reads

$$\mathcal{H}_{cs} = \sum_{n=1}^{N} \sum_{x,y=1}^{X} \sum_{\mu,\nu=1}^{D_n} \hbar \xi_{xy,n}^{(\mu\nu)} a_{x,n}^{\dagger(\mu)} b_{y,n}^{(\nu)} + \text{H.c.} \,. \tag{I.3.9}$$

This term includes scattering between modes of neighboring cavities as well as scattering between modes within a WGM pair in the same cavity or between different pairs. Note that the frequency difference, which determines whether the contribution in the appropriate interaction picture is time dependent or not $\epsilon_{xy,n}^{(\mu\nu)}$ is zero for $x = y$, i.e., for interactions within one mode pair or for pairs of equal frequency but, e.g., different polarization. Only for the process of scattering into another WGM pair this dependence on time arises in case of different frequencies of the respective mode pairs.

Next, we consider the coupling of an atom to a microcavity depicted in Fig. I.3.(c). If the atom is located within the evanescent field of the cavity, it can interact with the cavity modes. In case of cavity modes with polarizations matching the orientations of the atomic transition dipoles and frequencies similar to the atomic transition frequencies, the atom can be excited by absorbing a cavity photon or de-excited by emitting a photon into the cavity. Such interaction processes in subsystem n are described by the coherent coupling strength $g_{a_x,n}$ and $g_{b_x,n}$ where x is the index for the mode pair as well as for the respective coupling atomic transition. Since the atom always couples to cavity 1 of the respective subsystem, we do not need an index d for this coupling constant. For modes within the same WGM pair, for the atomic coupling constants the relation $g_{a_x,n} = g_{b_x,n}^{*} = g_{x,n}$ holds. The coupling strength crucially depends on the position of the nearby atom and, particularly for modes whose intensity is centered on the cavity's circumference, can be written as $g_{x,n} = g_{x,n}^{0} \cdot f(r,z)\, e^{ik_{x,n}l}$ where $k_{x,n}$ denotes the wavenumber, l the position along the resonator circumference, r the radial position relative to the cavity's center, and z is the vertical coordinate. The corresponding contribution to the Hamiltonian reads

$$\mathcal{H}_{ac} = \sum_{n=1}^{N} \sum_{x=1}^{X} g_{x,n} \mathcal{S}_{x,n}^{+} a_{x,n}^{(1)} + g_{x,n}^{*} \mathcal{S}_{x,n}^{+} b_{x,n}^{(1)} + \text{H.c.} \,. \tag{I.3.10}$$

Here, we assume that each atomic transition can couple to only one WGM pair. This selective coupling also occurs in many real systems. For example, if $X = 2$ and the atomic transition dipoles are orthogonal or the frequency spacing is sufficiently large. Such a system could be realized by tuning the Zeeman splitting of two atomic magnetic sublevels to the frequency spacing of the two WGM pairs in the resonator.

Using the above contributions, the total Hamiltonian of our general coupled system reads

$$\mathcal{H} = \mathcal{H}_{at} + \mathcal{H}_{phot} + \mathcal{H}_{laser} + \mathcal{H}_{ac} + \mathcal{H}_{cs} + \mathcal{H}_{ext} \,. \tag{I.3.11}$$

In the next step, we derive a master equation for the density operator ρ of our coupled system. The basis for the coherent part is the Hamiltonian $\mathcal{H}$. Yet, in order to describe our system adequately, we additionally take the incoherent contributions into account.

I.4. The master equation

In this section, a master equation is derived for the density operator ρ of our general coupled system shown in Fig. I.2. For the coherent part we use the Hamiltonian $\mathcal{H}$ derived in the previous section I.3., see Eq. (I.3.11). With the help of this Hamiltonian, the coherent part of the time evolution of the quantum state ρ of the chain of N coupled cavity-atom subsystems can be calculated from the Liouville superoperator obtained from the Von-Neumann Equation [122]

$$\mathcal{L}_{coh}\rho = -\frac{i}{\hbar}\left[\mathcal{H},\rho\right] . \tag{I.4.12}$$

Next, we consider the different incoherent decay channels. On the one hand, the atom can spontaneously emit a photon into the surrounding vacuum by decaying from the excited state $|e_n\rangle$ into one of the ground states $|g_{x,n}\rangle$. For subsystem n this decay is described by the decay rate $\gamma_{x,n}$. The contribution to the time evolution of the density operator ρ can be written in terms of a Liouville superoperator $\mathcal{L}_{atom}$ in the so-called Lindblad form [123] which is defined as

$$\mathcal{L}_{at,x,n}\rho = \frac{\gamma_{x,n}}{2}\left(2\mathcal{S}^-_{x,n}\rho\mathcal{S}^+_{x,n} - \mathcal{S}^+_{x,n}\mathcal{S}^-_{x,n}\rho - \rho\mathcal{S}^+_{x,n}\mathcal{S}^-_{x,n}\right) . \tag{I.4.13}$$

On the other hand, the cavity modes can decay spontaneously. For two modes $\{a^{(d)}_{x,n}, b^{(d)}_{x,n}\}$ this spontaneous decay is described by the decay rate $\kappa^{(d)}_{int,a_x,n} = \kappa^{(d)}_{int,b_x,n}$, respectively. Since modes forming a WGM pair have the same frequency but only differ by their propagation direction, we assume their loss rates to be equal. Therefore, we define $\kappa^{(d)}_{int,x,n} = \kappa^{(d)}_{int,a_x,n} = \kappa^{(d)}_{int,b_x,n}$. The total decay is given by the cavities' total loss rates $\kappa^{(d)}_{x,n} = \kappa^{(d)}_{ex,x,n} + \kappa^{(d)}_{int,x,n}$. This total loss rates include both the decay originating from the coupling $\kappa^{(d)}_{ex,x,n}$ and the internal loss rate $\kappa^{(d)}_{int,x,n}$, which is the loss occurring due to decay into the surrounding vacuum. The Liouville superoperators which describe this incoherent loss can be written in the Lindblad form as

$$\begin{aligned}
\mathcal{L}^{(d)}_{a_{x,n}}\rho &= \kappa^{(d)}_{x,n}\left(2a^{(d)}_{x,n}\rho a^{(d)\dagger}_{x,n} - a^{(d)\dagger}_{x,n}a^{(d)}_{x,n}\rho - \rho a^{(d)\dagger}_{x,n}a^{(d)}_{x,n}\right) , \\
\mathcal{L}^{(d)}_{b_{x,n}}\rho &= \kappa^{(d)}_{x,n}\left(2b^{(d)}_{x,n}\rho b^{(d)\dagger}_{x,n} - b^{(d)\dagger}_{x,n}b^{(d)}_{x,n}\rho - \rho b^{(d)\dagger}_{x,n}b^{(d)}_{x,n}\right) .
\end{aligned} \tag{I.4.14}$$

Using these Liouville superoperators we can write the master equation describing the complete system as

$$\partial_t\rho = -\frac{i}{\hbar}\left[\mathcal{H},\rho\right] + \sum_{x=1}^{X}\sum_{n=1}^{N}\left(\mathcal{L}_{at,x,n}\rho + \sum_{d=1}^{D_n}\left(\mathcal{L}^{(d)}_{a_{x,n}} + \mathcal{L}^{(d)}_{b_{x,n}}\right)\rho\right) . \tag{I.4.15}$$

I.5. The equations of motion

For the calculations, it is often useful to consider the respective system operators in an appropriate interaction picture. If, e.g., classical input laser fields $E_x(t) = \mathcal{E}_x\, e^{i\omega_{L_x} t}$ with field amplitudes $\mathcal{E}_x$ are considered, transforming to a frame rotating with one of the input laser frequencies ω_{L_x} can be useful. Here, we derive the equations of motion for our general system's operators in an interaction picture. We denote the transformed operators by $\tilde{\mathcal{O}}$ where $\mathcal{O} \in \{a^{(d)}_{x,n}, b^{(d)}_{x,n}, \mathcal{S}^{-}_{x,n}\}$. Then, the coherent part of the time evolution of a system operator $\tilde{\mathcal{O}}$ is given by the Heisenberg equation [119, 124]

$$\left(\partial_t \tilde{\mathcal{O}}\right)_{coh} = -\frac{i}{\hbar}\left[\tilde{\mathcal{O}}, \tilde{\mathcal{H}}\right] , \tag{I.5.16}$$

if $\tilde{\mathcal{H}}$ is the Hamiltonian in the respective interaction picture.

We obtain the incoherent part of the time evolution by applying the trace on the respective Liouville operators of Eqs. (I.4.13) and (I.4.14) contributing to the density operator ρ and changing from the Schrödinger to the interaction picture. These incoherent contributions to the time evolution of the respective operator can be written as

$$\mathscr{D}_{\tilde{\mathcal{O}}} = -\gamma_{\tilde{\mathcal{O}}} \tilde{\mathcal{O}} , \tag{I.5.17}$$

where the decay rates are given by

$$\begin{aligned} \gamma_{\tilde{a}^{(d)}_{x,n}} &= \gamma_{\tilde{b}^{(d)}_{x,n}} = \kappa_{\tilde{a}^{(d)}_{x,n}} = \kappa_{\tilde{b}^{(d)}_{x,n}} = \kappa^{(d)}_{x,n} \\ \gamma_{\tilde{\mathcal{S}}^{-}_{x,n}} &= \frac{\gamma_{x,n}}{2} . \end{aligned} \tag{I.5.18}$$

Adding these incoherent terms, the time evolution of the operator $\tilde{\mathcal{O}}$ reads

$$\partial_t \tilde{\mathcal{O}} = -\frac{i}{\hbar}\left[\tilde{\mathcal{O}}, \tilde{\mathcal{H}}\right] - \gamma_{\tilde{\mathcal{O}}} \tilde{\mathcal{O}} . \tag{I.5.19}$$

PART II

A microcavity coupled to a Λ atom

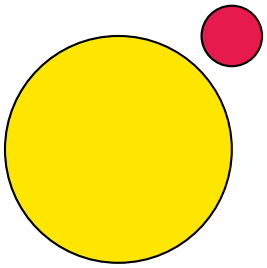

A microcavity coupled to a Λ atom

In this part, a three-level atom in the Λ-configuration coupled to a microcavity is studied. The two transitions of the atom are assumed to couple to different counterpropagating mode pairs in the cavity. We analyze the dynamics both in the strong-coupling and in the bad cavity limit. We find that compared to a two-level setup, the third atomic state and the additional control field modes crucially modify the system dynamics and enable more advanced control schemes. All results are explained using appropriate dressed state and eigenmode representations. As potential applications, we discuss optical switching and turnstile operations as well as the detection of particles close to the resonator surface.

II.1. Introduction

Whispering gallery microcavities are an attractive implementation for quantum optical setups, often motivated by the very low loss rate that can be achieved. This has led to a multitude of applications [20, 21], such as switches [68, 78, 84, 116, 125], transistors [103, 104], quantum networks [106, 108], photonic entanglement [126], or optomechanics [66, 127–130].

The light is confined to the resonator by total internal reflection, which leads to an exponentially damped evanescent field around the cavity. On the one hand this allows to couple the cavity, e.g., to an external fiber. But on the other hand, the evanescent field also allows the resonator field to interact with nearby particles. Since the cavity volume and the resonator linewidth can be small, even the near-resonant coupling of a single atom can have a substantial effect on the resonator dynamics [131] and modify the photon statistics of transmitted photons [132]. In [105], a photon turnstile was created by coupling a two level atom to the cavity. The sensitivity of the resonator to nearby atoms can also be used to measure the presence of nearby particles, their optical properties, or their concentration [33, 35–39]. The evanescent field can also be used to trap atoms, as has been demonstrated for atoms coupled to a tapered fiber [114, 115, 133].

In most cases, the particle interacting with the resonator is treated as a two-level atom, but there is some related previous work on more complex level schemes. For example, in [104] a three level atom in Λ configuration coupled to a nearby microcavity was considered. There, however, the atom only couples to the cavity with one of its transitions, while the other one is coupled to an external laser field in order to control the atom-

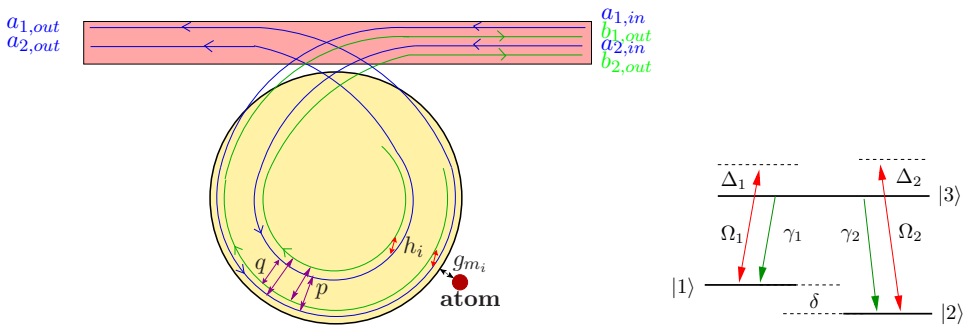

Figure II.1.: In the upper subfigure our setup with the glass fiber, the microcavity and the atom is shown. The lower subfigure shows the internal structure of the Λ-atom.

resonator interaction. In [134], a three level V system inside a cavity was considered to create entangled photon pairs. In [135], a three-level atom in V configuration coupled to a resonator was studied, focusing on the effect of the scattering between the different cavity modes on the optical spectra. Transmission and reflection amplitudes for single photon wave packets interacting with a resonator coupled to a three-level atom were considered in [136]. Finally, in a related work [137], photon scattering from a three-level atom coupled to a 1D wave guide was studied. These works are not least motivated by the fact that a setup in which several transitions of the particle are coupled to respective modes of a single resonator, potentially could be more flexible and thus enable more advanced control schemes.

To demonstrate this, here, we study a three-level atom in the Λ configuration coupled to a microcavity, see Fig. II.1. We consider the case in which each atomic transition couples to a pair of counterpropagating cavity modes, respectively. In addition, the resonator is coupled to a fiber which allows to probe the atom-cavity setup. We analyze the dynamics and the optical properties of the system in dependence on the fields applied via the fiber using two different approximations with complementary validity ranges. First, we assume weak input fields, and restrict the Hilbert space to low excitations. Second, we adiabatically eliminate the cavity and derive an effective master equation for the atomic degrees of freedom alone. We find that the existence of two coupling mode pairs and two atomic ground states crucially changes the system's dynamics as compared to the two-level case and opens up new possibilities to control the coupled system. For this, we typically treat one of the fields as probe field, and the other as control field. As potential applications, we discuss controllable optical switching and photon turnstile operations, as well as the measurement of the position of particles close to the resonator. All results are interpreted based on the system's dressed states or eigenmodes.

Our system could be realized, for example, by tuning the Zeeman splitting of two atomic magnetic sublevels to the frequency spacing of two mode pairs in the resonator. Alternatively, different polarizations could be used to selectively couple the transitions to different modes, but the leakage pattern of evanescent fields with different polarizations around the resonator surface is not uniform. Finally, also a setup with two nearby resonators as shown in Fig. II.2 could be considered in which the resonators do not interact in the absence of the atom as they are not in resonance with each other. The atom could then act as a quantum link between the resonators, with each transition coupling to one

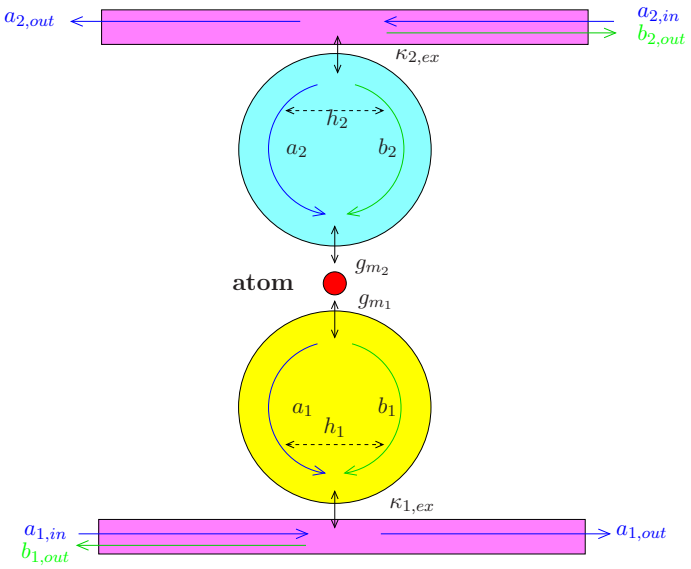

Figure II.2.: Model setup for cavity mode pairs of different frequencies.

of the resonators, respectively.

This part is organized as follows. In Sec. II.2.1., we introduce our model system and derive the equations of motion. In Sec. II.2.2., we describe the two calculation methods used throughout the analysis in detail. The first is based on a truncation of the Hilbert space (II.2.2.2) whereas the second relies on an adiabatic elimination of the resonator (II.2.2.3). Our observables, the transmission and reflection intensities as well as second order correlations are introduced in Sec. II.3. The following Sec. II.4. discusses our results. We present our findings for the strong coupling regime in Sec. II.4.1. and explain them via a dressed state atomic level scheme. Afterwards we show how our setup in this parameter regime could be used as a precision measurement device for the position of a nearby atom. In Sec. II.4.2. we show our results for the bad cavity regime. We present transmission and reflection intensities as well as our studies on the photon statistics. Finally, in Sec. II.4.2.3. we show how our coupled system can be used as a tunable bimodal photon turnstile in the bad cavity regime.

II.2. Theoretical considerations

II.2.1. Model system

The system we investigate is shown in Fig. II.1. It consists of a toroidal microresonator, which is driven by a fiber, and coupled to an atom placed within the evanescent field surrounding the resonator. The atom is modeled with three states in Λ configuration with a energy difference δ of the two ground states. The resonator is modeled with two pairs of counterpropagating whispering gallery modes, with one pair coupling to each transition in the atom, respectively. This selective coupling could be achieved either via different mode frequencies, or via different polarizations. This means, in this part we consider a reduction of the general system introduced in part I by choosing $N = 1$, $D_1 = 1$ and $X = 2$. An alternative possible realization is shown in Fig. II.2., and will be discussed

in more detail in Sec. II.5. In our system a number of different coupling mechanisms are of importance. First, within the resonator, each pair of counterpropagating modes with photon destruction operators a_i, b_i is coupled via the scattering rate h_i ($i \in \{1,2\}$). In principle, also photons from one mode pair could be scattered into the other pair of modes. This coupling is described by the parameters p and q. But in particular if the two mode pairs have different frequencies or polarizations, p and q will be negligible. Next, the fiber couples via the evanescent field to the cavity such that photons of the two probe fields with coupling strength $\mathcal{E}_1$ and $\mathcal{E}_2$ can enter the cavity. This coupling is described by the constants $\kappa_{m_i,ex}$, where $m \in \{a,b\}$ and $i \in \{1,2\}$. The incoherent decay of the cavity modes into the vacuum we include by the internal decay rate $\kappa_{m_i,in}$. Then, the overall loss rate for the cavity modes is

$$\kappa_{m_i} = \kappa_{m_i,in} + \kappa_{m_i,ex}\,. \tag{II.2.1}$$

Finally, the coupling of the atom to the resonator is described by the constants g_{m_i}. The respective coupling strength depends on the position of the atom characterized by the radial position r and the azimuthal position x along the resonator circumference, and is of the form

$$g_{a_i} = g_0^i f(r,z) e^{ik_i x}\,, \tag{II.2.2a}$$
$$g_{b_i} = g_{a_i}^*\,. \tag{II.2.2b}$$

Here, k_i is the wave number of the mode pair i and z is the vertical coordinate. The first mode pair $i=1$ couples to the first atomic transition $|1\rangle \leftrightarrow |3\rangle$, whereas the second pair $i=2$ couples to the second transition $|2\rangle \leftrightarrow |3\rangle$. We further define the atomic transition operators

$$\mathcal{S}_i^+ = |3\rangle\langle i|\,, \tag{II.2.3a}$$
$$\mathcal{S}_i^- = |i\rangle\langle 3|\,. \tag{II.2.3b}$$

Since in general the frequencies of the driving fields, the resonator modes, and the atomic transition frequencies may be different, we introduce the detunings

$$\epsilon = \omega_c^1 - \omega_c^2\,, \tag{II.2.4a}$$
$$\delta_i = \omega_c^i - \omega_p^i\,, \tag{II.2.4b}$$
$$\Delta_i = (\omega_3 - \omega_i) - \omega_p^i\,, \tag{II.2.4c}$$

where ω_c^i are the two cavity mode pair resonance frequencies, ω_p^i the laser frequencies of the probe fields in the fiber, and $\omega_3 - \omega_i = \omega_a^i$ the atomic transition frequencies. The index a stands for $atom$ whereas c labels $cavity$ quantities.

With these definitions, the Hamiltonian $\mathcal{H}_{ab}$ for our system can be written as

$$\mathcal{H}_{ab} = \mathcal{H}_{ab}^0 + \mathcal{H}_{ab}^s + \mathcal{H}_{ab}^c\,, \tag{II.2.5a}$$
$$\mathcal{H}_{ab}^0 = -\hbar \sum_{i=1}^{2} \Delta_i\, \mathcal{S}_i^- \mathcal{S}_i^+ + \hbar \sum_{i=1}^{2} \sum_{m\in a,b} \delta_i m_i^\dagger m_i\,, \tag{II.2.5b}$$
$$\mathcal{H}_{ab}^s = \hbar p(a_1^\dagger a_2 + b_1^\dagger b_2)e^{i\epsilon t} + \hbar q(a_1^\dagger b_2 + b_1^\dagger a_2)e^{i\epsilon t} + \hbar \sum_{i=1}^{2} h_i a_i^\dagger b_i + \text{H.c.}\,, \tag{II.2.5c}$$
$$\mathcal{H}_{ab}^c = \hbar \sum_{i=1}^{2} \mathcal{E}_i^* a_i + \hbar \sum_{i=1}^{2} \sum_{m\in a,b} g_{m_i}^* m_i^\dagger \mathcal{S}_i^- + \text{H.c.}\,, \tag{II.2.5d}$$

where $\mathcal{H}^0_{ab}$ contains the free energies of the atom and the cavity, $\mathcal{H}^s_{ab}$ the scattering between the different modes within the resonator, and $\mathcal{H}^c_{ab}$ the coupling between fiber and resonator as well as from resonator to the atom. The subindex ab indicates that the Hamiltonian is written in terms of the resonator modes a_i and b_i. Including the incoherent processes leads to the master equation

$$\partial_t \rho = -\frac{i}{\hbar}\left[\mathcal{H}_{ab}, \rho\right] + \mathcal{L}_\kappa \rho + \mathcal{L}_\gamma \rho\,, \tag{II.2.6}$$

$$\mathcal{L}_\kappa \rho = \sum_{i=1}^{2} \sum_{m\in\{a,b\}} \kappa_{m_i} \left(2 m_i \rho m_i^\dagger - m_i^\dagger m_i \rho - \rho m_i^\dagger m_i\right)\,, \tag{II.2.7}$$

$$\mathcal{L}_\gamma \rho = \sum_{i=1}^{2} \frac{\gamma_i}{2} \left(2\mathcal{S}_i^- \rho \mathcal{S}_i^+ - \mathcal{S}_i^+ \mathcal{S}_i^- \rho - \rho \mathcal{S}_i^+ \mathcal{S}_i^-\right)\,, \tag{II.2.8}$$

where $\mathcal{L}_\kappa \rho$ describes cavity decay, and $\mathcal{L}_\gamma \rho$ the atomic spontaneous emission.

We next introduce the normal modes [99, 105]

$$\mathcal{A}_i = \frac{a_i + b_i}{\sqrt{2}}\,, \tag{II.2.9a}$$

$$\mathcal{B}_i = \frac{a_i - b_i}{\sqrt{2}}\,, \tag{II.2.9b}$$

which leads to a partial diagonalization of the Hamiltonian Eqs. (II.2.5) and we obtain

$$\mathcal{H}_{\mathcal{AB}} = \mathcal{H}^0_{\mathcal{AB}} + \mathcal{H}^c_{\mathcal{AB}} + \mathcal{H}^a_{\mathcal{AB}} + \mathcal{H}^s_{\mathcal{AB}}\,, \tag{II.2.10a}$$

$$\mathcal{H}^0_{\mathcal{AB}} = -\hbar \sum_{i=1}^{2} \Delta_i \mathcal{S}_i^- \mathcal{S}_i^+ + \hbar \sum_{i=1}^{2} (\delta_i + h_i) \mathcal{A}_i^\dagger \mathcal{A}_i + \hbar \sum_{i=1}^{2} (\delta_i - h_i) \mathcal{B}_i^\dagger \mathcal{B}_i\,, \tag{II.2.10b}$$

$$\mathcal{H}^c_{\mathcal{AB}} = \frac{\hbar}{\sqrt{2}} \sum_{i=1}^{2} (\mathcal{E}_i^* \mathcal{A}_i + \mathcal{E}_i^* \mathcal{B}_i) + \text{H.c.}\,, \tag{II.2.10c}$$

$$\mathcal{H}^a_{\mathcal{AB}} = \hbar \sum_{i=1}^{2} \left(g_{\mathcal{A}_i}\, \mathcal{A}_i^\dagger\, \mathcal{S}_i^- - i g_{\mathcal{B}_i}\, \mathcal{B}_i^\dagger\, \mathcal{S}_i^-\right) + \text{H.c.}\,, \tag{II.2.10d}$$

$$\mathcal{H}^s_{\mathcal{AB}} = \hbar(p-q) e^{i\epsilon t} \mathcal{B}_1^\dagger \mathcal{B}_2 + \hbar(q+p) e^{i\epsilon t} \mathcal{A}_1^\dagger \mathcal{A}_2 + \text{H.c.}\,, \tag{II.2.10e}$$

where $g_{\mathcal{A}_i} = g_0^{(i)} \cos(k_i x)$ and $g_{\mathcal{B}_i} = g_0^{(i)} \sin(k_i x)$.

Transforming also the incoherent parts to the new basis, we obtain the equations of motion for the normal modes as

$$\begin{aligned}\partial_t \mathcal{A}_i(t) &= -\frac{i}{\hbar}[\mathcal{A}_i(t), \mathcal{H}_{\mathcal{AB}}] - \kappa_{\mathcal{A}_i} \mathcal{A}_i \\ &= -i(\delta_i + h_i)\mathcal{A}_i - i\frac{\mathcal{E}_i}{\sqrt{2}} - i g_{\mathcal{A}_i} \mathcal{S}_i^- - i(q+p) e^{i\epsilon t} \mathcal{A}_{\neg i} - \kappa_{\mathcal{A}_i} \mathcal{A}_i\,,\end{aligned} \tag{II.2.11a}$$

$$\begin{aligned}\partial_t \mathcal{B}_i(t) &= -\frac{i}{\hbar}[\mathcal{B}_i(t), \mathcal{H}_{\mathcal{AB}}] - \kappa_{\mathcal{B}_i} \mathcal{B}_i \\ &= -i(\delta_i - h_i)\mathcal{B}_i - i\frac{\mathcal{E}_i}{\sqrt{2}} - g_{\mathcal{B}_i} \mathcal{S}_i^- - i(p-q) e^{i\epsilon t} \mathcal{B}_{\neg i} - \kappa_{\mathcal{B}_i} \mathcal{B}_i\,,\end{aligned} \tag{II.2.11b}$$

where the two mode pairs are labeled by $i \in \{1, 2\}$, and $\neg i$ is 1 for $i = 2$ and vice versa. Since modes of one pair $\{a_i, b_i\}$ are of the same frequency, it is reasonable to

assume $\kappa_{a_i} = \kappa_{b_i} = \kappa_i$ holds. The incoherent part remains diagonal also after the basis transformation, and we can write $\kappa_{\mathcal{A}_i} = \kappa_{\mathcal{B}_i} = \kappa_i$ and analogously for the internal and external decay rates $\kappa_{\mathcal{A}_i,ex} = \kappa_{\mathcal{B}_i,ex} = \kappa_{i,ex}$ and $\kappa_{\mathcal{A}_i,in} = \kappa_{\mathcal{B}_i,in} = \kappa_{i,in}$, respectively. As expected, it can be seen from Eqs. (II.2.11) that for $p = 0 = q$, the different normal modes $\mathcal{A}_i$ and $\mathcal{B}_i$ become independent apart from the coupling via the atom.

II.2.2. Two calculation methods

In this section, we outline the approaches used in the following to solve the given system. We start by characterizing the two parameter regimes studied throughout the later analysis. Then, we describe two different methods to obtain the steady state solution for our model system. In the first method, we assume weak input fields. This allows us to approximate the infinite series of Fock states of each photon mode by the lowest few photon number states. This truncation of the Hilbert space renders the system finite, and thus allows us to numerically calculate a steady state density matrix. We call this method the truncated Hilbert space (TH) method, and discuss it in Sec. II.2.2.2. In the second model, we assume the bad cavity regime for the resonator, such that the loss and photon scattering channels of the resonator dominate the system dynamics. Then, the cavity modes can be adiabatically eliminated. This method will be termed adiabatic elimination (AE) method, and is analyzed in Sec. II.2.2.3. Finally, in Sec. II.2.2.4. we compare the two methods and discuss their respective validity ranges.

II.2.2.1. Parameter regimes of interest

We consider two fundamentally different parameter regimes [138]. On the one hand, we study the strong coupling case, in which the coupling between the atom and the cavity dominates the dynamics compared to the loss dynamics of the cavity modes. Thus, the conditions $\kappa_i \ll g_{m_i}$ are fulfilled. For the resonator-fiber part of the system, we assume critical coupling characterized by

$$\kappa_{i,ex} = \sqrt{h_i^2 + \kappa_{i,in}^2}\,. \tag{II.2.12}$$

As the rates κ_i contain the coherent scattering rates h_i via $\kappa_{i,ex}$ as well as the incoherent photon decay rates $\kappa_{i,in}$, in the strong coupling regime, we also have $h_i < \kappa_i \ll g_{m_i}$. On the other hand, we consider the bad cavity regime. Here, the incoherent dynamics of the cavity modes dominates the dynamics, and the condition $g_{m_i} \ll \kappa_i$ holds. As before, then also $g_{m_i} \ll h_i$ is fulfilled.

II.2.2.2. Fock mode truncation - TH method

The general state of our system is determined by the state of the atom, as well as the state of the four different cavity modes. The dynamics can thus be described using basis states of the form

$$|\text{atom}, n(\mathcal{A}_1), n(\mathcal{B}_1), n(\mathcal{A}_2), n(\mathcal{B}_2)\rangle\,, \tag{II.2.13}$$

where $n(\mathcal{M})$ denotes the number of photons in mode $\mathcal{M}$. If the parameter are chosen such that the mean occupation number of a cavity mode remains low, then it is possible to restrict the corresponding state space to low Fock number states. Taking into account

states with at most l photons in each mode would lead to a state space reduced to dimension $3 \times (l+1)^4$, since also the state without photons has to be considered for each mode. In the following, we assume the case in which at most one photon can be in each of the cavity modes. The number of basis states then reduces to $3 \times 2^4 = 48$, and the corresponding reduced density matrix ρ_{Fock} has $48^2 = 2304$ elements. Note that taking into account up to two excitations per mode would already lead to 59049 density matrix elements, which is impractically large even though the number can be considerably reduced due to symmetries of the density matrix.

We arrange all elements of ρ_{Fock} in a vector and eliminate the last element using the trace condition $Tr(\rho_{Fock}) = 1$. The resulting vector $\vec{\rho}_{Fock}$ has $48^2 - 1$ elements, and we can rewrite the equations of motion for the density matrix elements as

$$\partial_t \vec{\rho}_{Fock} = \mathcal{G} \cdot \vec{\rho}_{Fock} + \vec{K} \,. \tag{II.2.14}$$

The steady state $\vec{\rho}_{Fock,stst}$ can then be obtained by solving the system of linear equations to give

$$\vec{\rho}_{Fock,stst} = -\mathcal{G}^{-1} \cdot \vec{K} \,. \tag{II.2.15}$$

II.2.2.3. Adiabatic elimination of the cavity modes - AE method

In this approach, we assume that the dissipative dynamics of the cavity dominates the system dynamics, such that the degrees of freedom of the cavity can be adiabatically eliminated from the system [139]. In particular, we assume the bad cavity condition $g_{m_i} \ll \kappa_i$ to be fulfilled. After the elimination, we obtain an effective master equation for the atomic degrees of freedom only. This significantly reduces the system dimension and thus simplifies the solution.

We apply standard techniques to eliminate the resonator modes [139]. Details on the calculation can be found in Appendix II.A. After the basis transformation Eqs. (II.2.9), we can treat the two normal mode pairs $\mathcal{A}_i$ and $\mathcal{B}_i$ separately. For each mode pair, first, we assume low occupation of the resonator modes due to the large dissipative dynamics, and expand the total density matrix in the photon occupation number. In the resulting density matrix equations, we assume

$$\frac{|\mathcal{L}_{\text{atom}}|}{\kappa_i} \ll 1 \,, \tag{II.2.16}$$

where $|\mathcal{L}_{atom}|$ represents the magnitude of terms corresponding to the coherent dynamics of the system, with $|\cdot|$ a suitable norm. Setting furthermore the time derivatives of off-diagonal elements in the expanded density matrix to zero, and inserting the thereby obtained expressions for the off-diagonal elements into the diagonal elements, we finally obtain an effective master equation for the atomic dynamics alone given by

$$\partial_t \varrho_{\text{atom}} = -\frac{i}{\hbar}[\mathcal{H}_{\text{atom}}, \varrho_{\text{atom}}] + \mathcal{L}_\Gamma \varrho_{\text{atom}} \,, \tag{II.2.17a}$$

$$\mathcal{L}_\Gamma \rho = \sum_{i,j=1}^{2} \frac{\Gamma_{ij}}{2} \left(2\mathcal{S}_j^- \rho \mathcal{S}_i^+ - \mathcal{S}_i^+ \mathcal{S}_j^- \rho - \rho \mathcal{S}_i^+ \mathcal{S}_j^- \right) \,, \tag{II.2.17b}$$

$$\mathcal{H}_{\text{atom}} = \hbar \sum_{i,j=1}^{2} \Delta_{ij} \mathcal{S}_i^+ \mathcal{S}_j^- - \hbar \sum_{i=1}^{2} \Delta_i \mathcal{S}_i^- \mathcal{S}_i^+ + \hbar \Omega_i \mathcal{S}_i^+ + \hbar \Omega_i^* \mathcal{S}_i^- \,. \tag{II.2.17c}$$

The constants Δ_{ij} and Ω_i are effective detunings and Rabi frequencies arising from the cavity elimination, respectively. Their values depend on the various coupling constants governing our system's dynamics. Explicit expressions can be found in Appendix II.B. Note that related results were obtained for a two-level atom coupled to a resonator with only one mode pair in [105].

II.2.2.4. Comparison of the two calculation methods

The adiabatic elimination method leads to an effective master equation, which can easily be solved and thus considerably reduces the computational effort. This comes at the price that the method only applies to the bad cavity limit, in which the dissipative dynamics dominates the system. In contrast, the Fock state truncation method does not a priori exclude either the bad cavity or the strong coupling regime, but rather puts a constraint on the mean occupation number of the cavity modes alone. While potential resonant enhancement of the cavity occupation for low cavity loss rates must be taken into account, a weak input field generally suffices to remain within the validity range, such that this method also allows to access the strong coupling regime. Drawbacks of this method are the higher computational effort compared to the AE method, and the fact that by construction higher order correlation functions involving two photons are not accessible from the results. We further analyzed this point for a two-level atom coupled to the resonator, for which higher Fock modes can be included while keeping the total number of equations reasonably low. We found that it is not sufficient to take Fock states with two photonic excitations in total into account in order to reliably calculate the second order correlation function. Rather, one has to include two excitations per mode. As already mentioned, in the three-level atom case, including up to two photons per mode would increase the state space substantially, effectively rendering the calculations unfeasible.

Thus in summary, in the bad cavity regime, both methods can be used, and we verified that the two methods give the same results. Due to the reduced computational effort, here, the AE method will be used. In contrast, in the strong coupling regime, only the TH method can be applied.

II.2.3. Input-output relations

In this section, we relate the fields inside the resonator to the fields in the fiber. First, we derive an expression for the driving terms proportional to $\mathcal{E}_i$ in the equations of motion for the modes (II.2.11). For this, we take the expectation value of Eqs. (II.2.11), and obtain

$$\langle \partial_t \mathcal{A}_i \rangle = \langle \partial_t \mathcal{A}_i \rangle_{sys} - \frac{i\mathcal{E}_i}{\sqrt{2}} , \tag{II.2.18}$$

and equivalently for modes $\mathcal{B}_i$. The index sys indicates all internal terms of the atom-cavity system not related to the external driving. Note that we neglect the fluctuations of the input field in the driving terms entering the equations of motion for the modes by equating $\langle \mathcal{E}_i \rangle = \mathcal{E}_i$. On the other hand, written in terms of an external input field operator $\mathcal{A}_{i,in}$, the corresponding equation for $\langle \partial_t \mathcal{A}_i \rangle$ can be expressed as

$$\langle \partial_t \mathcal{A}_i \rangle = \langle \partial_t \mathcal{A}_i \rangle_{sys} + \sqrt{\kappa_{i,ex}} \cdot \langle \mathcal{A}_{i,in} \rangle . \tag{II.2.19}$$

From Eq. (II.2.18) and (II.2.19), we can thus conclude

$$\langle \mathcal{A}_{i,in} \rangle = -\frac{i\mathcal{E}_i}{\sqrt{2\kappa_{i,ex}}} \,. \tag{II.2.20}$$

Note that if no input field is applied to the modes b_i, then $\langle \mathcal{A}_{i,in} \rangle = \frac{\langle a_{i,in} \rangle}{\sqrt{2}}$.

Next, we consider the output from the resonator to the fiber. Using the input-output formalism [140, 141], we find

$$\begin{aligned} a_{i,out} &= -\, a_{i,in}(t) + \sqrt{2\kappa_{i,ex}} a_i(t) \\ &= -\, \langle a_{i,in} \rangle - a'_{i,in}(t) + \sqrt{\kappa_{i,ex}} \left[\mathcal{A}_i(t) + \mathcal{B}_i(t) \right] \,, \qquad \text{(II.2.21a)} \\ b_{i,out} &= -\, b_{i,in}(t) + \sqrt{2\kappa_{i,ex}} b_i(t) \\ &= -\, b'_{i,in}(t) + \sqrt{\kappa_{i,ex}} \left[\mathcal{A}_i(t) - \mathcal{B}_i(t) \right] \,, \qquad \text{(II.2.21b)} \end{aligned}$$

where $a'_{i,in}(t)$ and $b'_{i,in}(t)$ are fluctuations, such that for example $a_{i,in} = \langle a_{i,in} \rangle + a'_{i,in}(t)$. As long as we consider normal ordered output fields we can substitute the output operators according to [105]

$$\begin{aligned} a_{i,out} &= \alpha_{i0} + \alpha_{i1} \mathcal{S}_1^- + \alpha_{i2} \mathcal{S}_2^- \,, \qquad \text{(II.2.22a)} \\ b_{i,out} &= \beta_{i0} + \beta_{i1} \mathcal{S}_1^- + \beta_{i2} \mathcal{S}_2^- \,. \qquad \text{(II.2.22b)} \end{aligned}$$

Here, the complex coefficients α_{i0} and α_{i1} and α_{i2} are calculated as follows. We solve the equations of motion Eq. (II.2.11b) for the normal cavity modes $\mathcal{A}_i$ and $\mathcal{B}_i$ in the steady state. For the modes $\mathcal{A}_i$ the terms without an atomic operator we call α_{i0}, the coefficient of $\mathcal{S}_1^-$ in the equation for $\mathcal{A}_i$ we call α_{i1} and the terms in front of operator $\mathcal{S}_2^-$ are α_{i2}. Analogously for the modes $\mathcal{B}_i$ we define the coefficients as β_{i0}, β_{i1} and β_{i2}.

II.3. Observables

II.3.1. Transmission and reflection spectra

The transmission spectra can be calculated from the normalized first order correlation functions as [142]

$$\mathcal{T}_{F_{m_i}} = \frac{\langle m^\dagger_{i,\,out} m_{i,\,out} \rangle}{\langle a^\dagger_{i,\,out} a_{i,\,out} \rangle_{\Delta_i \gg \kappa}} = \frac{\langle m^\dagger_{i,\,out} m_{i,\,out} \rangle}{\langle a_{i,\,in} \rangle^2} \tag{II.3.23}$$

for modes characterized by $m \in \{a,\, b\}$ and $i \in \{1,\, 2\}$. The output photon operators can be related via Eqs. (II.2.22) to the solution of equations describing the cavity-atom system. $\mathcal{T}_{F_{a_i}}$ can be interpreted as the transmission in dependence of the input field frequencies, whereas $\mathcal{T}_{F_{b_i}}$ is the corresponding reflection. The transmission and reflection can be calculated by both the AE and the TH methods introduced in Sec. II.2.2., and are thus accessible in both the strong coupling and the bad cavity regime.

II.3.2. Photon statistics

In order to investigate the photon statistics of the output photons we have to consider the normalized second order correlation functions at equal times. They can be calculated as [142]

$$\boldsymbol{g}^{(2)}_{F_{m_i,m_j}} = \frac{\langle m^{\dagger}_{i,\,out} m^{\dagger}_{j,out} m_{j,\,out} m_{i,\,out}\rangle}{\langle m^{\dagger}_{i,\,out} m_{i,\,out}\rangle \langle m^{\dagger}_{j,\,out} m_{j,\,out}\rangle} \,. \tag{II.3.24}$$

If $i = j$, the function $\boldsymbol{g}^{(2)}_{F_{m_i,m_i}}$ gives the photon statistics of a single mode. If the correlation function is one, then the photons obey Poissonian statistics. Higher or lower values indicate super- or sub-Poissonian statistics, respectively. In case $i \neq j$, the function $\boldsymbol{g}^{(2)}_{F_{m_i,m_j}}$ is a cross correlation function for photons arriving at the detectors at the same time but in different modes m_i and m_j. As it was found in [105] for a two-level atom coupled to a resonator, and as we also find in our analysis, the obtained photon statistics in the critical coupling regime is predominantly determined by the atom because the resonator contribution is suppressed by destructive interference in the critical coupling case. This suggests that sub-Poissonian statistics can be associated with anti-bunching, whereas super-Poissonian statistics can be connected to bunching. The second order correlation functions $\boldsymbol{g}^{(2)}_{F_{m_i,m_j}}$ can only have positive values ≥ 0. The slope of $\boldsymbol{g}^{(2)}_{F_{m_i,m_j}}$ at time delay $\tau = 0$ determines whether the photons exhibit bunching or anti-bunching. Bunching is indicated by a negative slope of $\boldsymbol{g}^{(2)}_{F_{m_i,m_j}}$ whereas anti-bunching occurs for positive slopes. For $\boldsymbol{g}^{(2)}_{F_{m_i,m_j}} = 0$ the slope can only be non-negative and therefore in case of $\boldsymbol{g}^{(2)}_{F_{m_i,m_j}} = 0$ we can conclude that we have anti-bunching.

Since for these second order correlation functions two photon processes are crucial, we can calculate them only by using the AE method introduced in Sec. II.2.2.3., but not via the TH method including only up to one-photon Fock states. Thus we only present results in the photon statistics in the bad cavity regime.

II.4. Results

In this section, we present the results obtained numerically for our observables. As the system has many degrees of freedom, we have to make a number of parameter choices. Throughout the analysis, we assume that the coupling between different pairs of modes is weak and set $q = p = 0$. Furthermore, we consider the natural case that the two modes belonging to one WGM pair have similar properties, which leads to a number of parameter choices. First, we set $\kappa_{\mathcal{A}_1} = \kappa_{\mathcal{B}_1} = \kappa_1$ and $\kappa_{\mathcal{A}_2} = \kappa_{\mathcal{B}_2} = \kappa_2$ where $\kappa_i = \kappa_{i,ex} + \kappa_{i,in}$ and $\kappa_{i,ex} = \sqrt{\kappa^2_{i,in} + h^2_i}$. Similarly, for our calculations we assume similar properties of the two pairs of modes. We assume the prefactors in the atom-cavity coupling strengths Eqs. (II.2.2) to be equal, i.e. $g^{(1)}_0 = g^{(2)}_0 \equiv g_0$. Note, however, that the different position-dependence still in general leads to different couplings of mode $\mathcal{A}_i$ and $\mathcal{B}_i$ to the two atomic transitions. For the coupling between resonator and fiber we set $\kappa_{ex,1} = \kappa_{ex,2} \equiv \kappa_{ex}$, for the atomic decay rate $\gamma_1 = \gamma_2 \equiv \gamma$ and for the scattering inside the cavity $h_1 = h_2 \equiv h$. The internal decay rate of the cavity modes are set to $\kappa_{i,in} = \gamma$, from which follows $\kappa_1 = \kappa_2 \equiv \kappa$. Furthermore, if not noted otherwise,

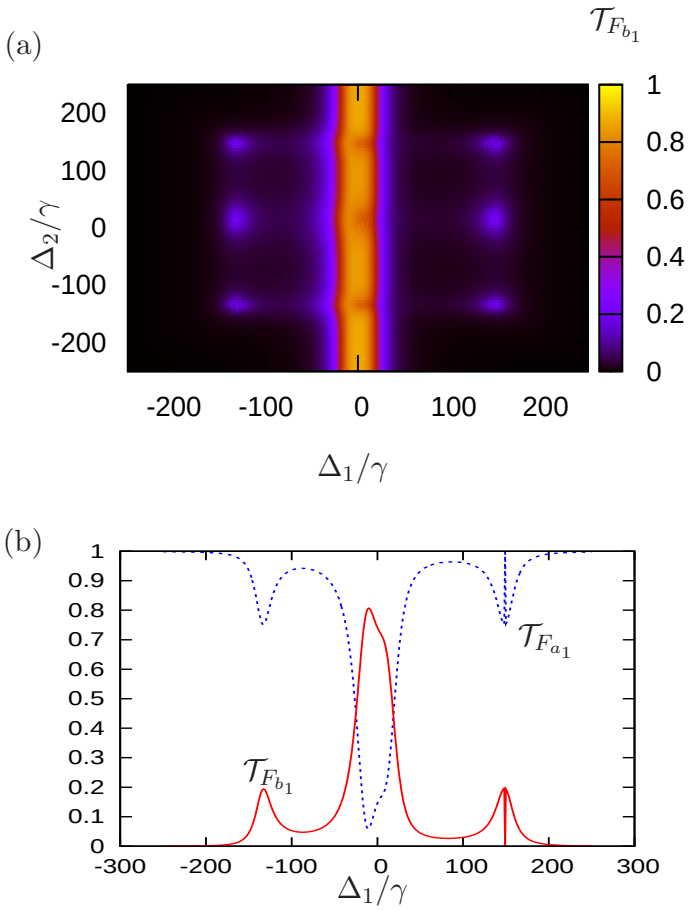

Figure II.3.: In (a) the normalized output flux $\mathcal{T}_{F_{b_1}}$ of mode $b_{1,out}$ in dependence of Δ_1 and Δ_2 is shown. (b) shows a cut of $\mathcal{T}_{F_{a_1}}$ and $\mathcal{T}_{F_{b_1}}$ at $\Delta_2 = 149\gamma$, which is very close to one of the eigenvalues of our system. The parameters are $(g_0, h, \kappa_{i,in})/\gamma = (100, 15, 1)$

we choose $k_i x = \pi/2$ which results in $g_{\mathcal{A}_i} = 0$ and $g_{\mathcal{B}_i} = g_0$. Also, we assume that both the cavity mode pairs are on resonance with the atomic transition they couple to, respectively. Then, for the detuning $\delta_i = \Delta_i$ holds. The energy separation between the two ground states is set to $\delta = 0$.

II.4.1. Strong coupling regime

In this section, we show our results for the transmission and reflection in the strong coupling regime. For the calculation we use the TH method described in Sec. II.2.2.2. As parameters we choose $g_0 = 100\gamma$ and $h = 15\gamma$. First, we present our results for the output flux of the different modes. Afterwards, we explain them using a dressed state model of the coupled atom.

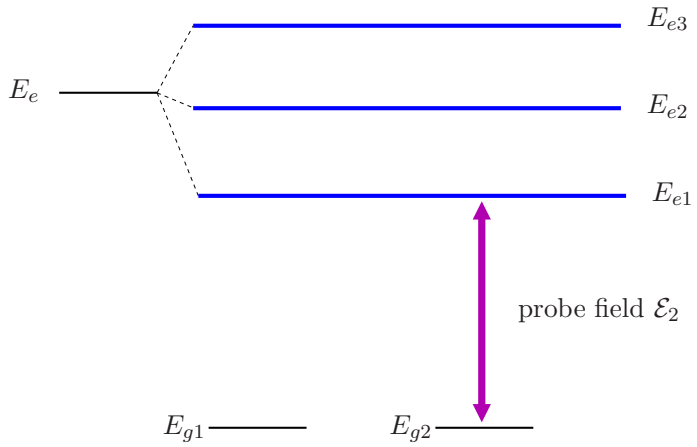

Figure II.4.: Dressed state atomic level splitting for excitation with up to one cavity mode photon.

II.4.1.1. Transmission and reflection

Fig. II.3. shows the transmission $\mathcal{T}_{F_{a_1}}$ and reflection $\mathcal{T}_{F_{b_1}}$ in dependence on the two probe field detunings Δ_1 and Δ_2 In the following, we analyze different regions in this figure and interpret the results with the help of the eigenstates of the system and the populations in the different atomic states. For this, the relevant state space determined below is shown in Fig. II.4., and the populations of the atomic states in Fig. II.5.

If the absolute value of one of the detunings $|\Delta_i|$ is large, then the corresponding atomic transition $|i\rangle \rightarrow |3\rangle$ essentially decouples from the cavity. This leads to optical pumping into the atomic state $|i\rangle$, such that the corresponding population approaches one. For example, at $\Delta_1 = -250\gamma$ and $|\Delta_2| < |\Delta_1|$ the atom is more likely excited from state $|2\rangle$ to state $|3\rangle$ than it is from $|1\rangle$ to $|3\rangle$. Therefore, in the longtime limit the atom moves into state $|1\rangle$. Eventually, the atom can be neglected, and the two mode pairs decouple. As for large detuning the light passes the resonator unperturbed, the reflection $\mathcal{T}_{F_{b_1}}$ is negligible.

A special situation arises if $\Delta_1 = \Delta_2$. Then, both transitions of the atom are driven in the same way, and the atom evolves into a dark state [119] with both ground states equally populated, and no population in the upper level $\mathcal{P}_3$, as shown in Fig. II.5. This suppresses the interaction of the atom with the resonator, and thus the results on the main diagonal line $\Delta_1 = \Delta_2$ of Fig. II.3. are equal to the case without atom.

The further structures of the atomic populations $\mathcal{P}_i$ and the reflection $\mathcal{T}_{F_{b_1}}$ can be understood from an eigenstate analysis of the matrix governing the equations of motion of our system. For this, we diagonalize the system's internal Hamiltonian without external input field and thus calculate the eigenenergies and the dressed eigenstates of the coupled cavity-atom system. We note that our parameter choice $\kappa_i x = \pi/2$ leads to $g_{\mathcal{A}_i} = 0$ and thus only the modes $\mathcal{B}_i$ can couple to the atom. Then, the relevant basis states reduce to $|\text{atom}, n(\mathcal{B}_1), n(\mathcal{B}_2)\rangle$. Including up to one photon per cavity mode, five different eigenvalues and eleven eigenstates are obtained. The eigenvalues for the parameters

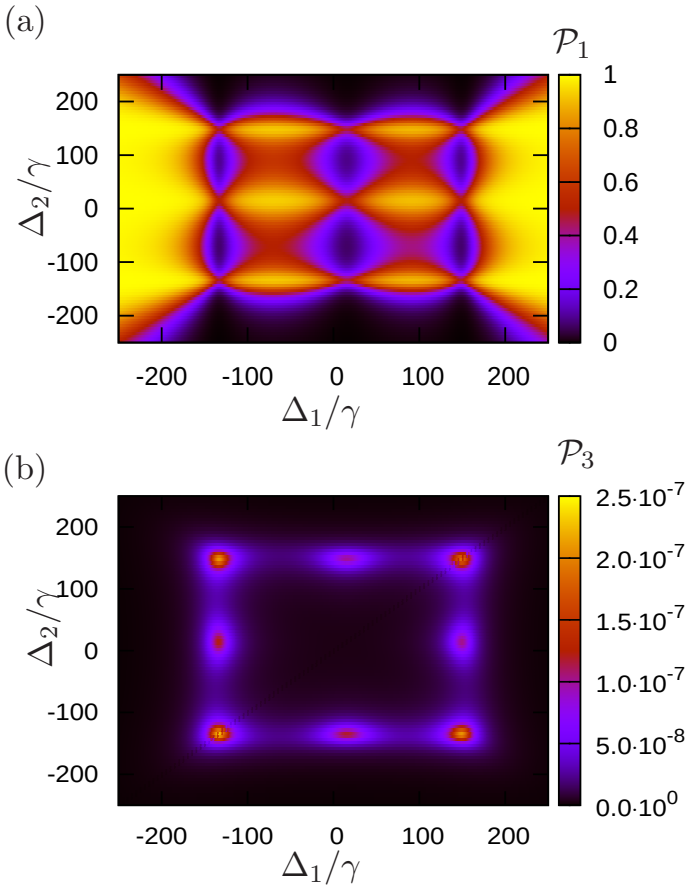

Figure II.5.: In (a) the population of the atomic state $|1\rangle$ is shown in dependence of both the detunings. The parameters are $(g_0, h, \kappa_{i,in})/\gamma = (100, 15, 1)$. In (b) the population of state $|3\rangle$ is shown.

used in Figs. II.3. and II.5. are

$$E_{g1} = E_{g2} = 0\,, \tag{II.4.25a}$$

$$E_{e1} = \frac{1}{2}\left(-h - \sqrt{8g_{\mathcal{B}_i}^2 + h^2}\right) = -149\gamma\,, \tag{II.4.25b}$$

$$E_{e2} = -h = -15\gamma\,, \tag{II.4.25c}$$

$$E_{e3} = \frac{1}{2}\left(-h + \sqrt{8g_{\mathcal{B}_i}^2 + h^2}\right) = 134\gamma\,, \tag{II.4.25d}$$

$$E_{e4} = \frac{1}{2}\left(-3h + \sqrt{4g_{\mathcal{B}_i}^2 + h^2}\right) = 77\gamma\,, \tag{II.4.25e}$$

$$E_{e5} = \frac{1}{2}\left(-3h - \sqrt{4g_{\mathcal{B}_i}^2 + h^2}\right) = -122\gamma\,, \tag{II.4.25f}$$

and the corresponding eigenstates read

$$|V_{g,1}\rangle = |1,0,0\rangle\,, \qquad |V_{g,2}\rangle = |2,0,0\rangle\,, \tag{II.4.26a}$$

$$|V_{e1}\rangle = |1,1,0\rangle + |2,0,1\rangle - \frac{iE_{e5}}{g_{\mathcal{B}_i}}|3,0,0\rangle\,, \tag{II.4.26b}$$

$$|V_{e2,1}\rangle = |2,1,0\rangle\,, \qquad |V_{e2,2}\rangle = |1,0,1\rangle\,, \tag{II.4.26c}$$

$$|V_{e2,3}\rangle = -|1,1,0\rangle + |2,0,1\rangle$$

$$|V_{e3}\rangle = |1,1,0\rangle + |2,0,1\rangle - \frac{E_{e1}}{g_{\mathcal{B}_i}}|3,0,0\rangle\,, \tag{II.4.26d}$$

$$|V_{e4,1}\rangle = \frac{i(E_{e2}+2h)}{g_{\mathcal{B}_i}}|1,1,1\rangle + |3,0,1\rangle\,, \tag{II.4.26e}$$

$$|V_{e4,2}\rangle = \frac{i(E_{e2}+2h)}{g_{\mathcal{B}_i}}|2,1,1\rangle + |3,1,0\rangle\,, \tag{II.4.26f}$$

$$|V_{e5,1}\rangle = \frac{i(E_{e4}+2h)}{g_{\mathcal{B}_i}}|1,1,1\rangle + |3,0,1\rangle\rangle\,, \tag{II.4.26g}$$

$$|V_{e5,2}\rangle = \frac{i(E_{e4}+2h)}{g_{\mathcal{B}_i}}|2,1,1\rangle + |3,1,0\rangle\rangle\,, \tag{II.4.26h}$$

We can identify three different kinds of eigenstates. The first group contains the ground states $|V_{g,1}\rangle$ and $|V_{g,2}\rangle$, with the atom in one of its two ground states and no photon in the cavity. Since we typically apply weak probe fields, our coupled system is mostly in one of these two states. The second group contains all states containing a single excitation of the system. The eigenstates belonging to this group are $|V_{e1}\rangle$, $|V_{e2,1-3}\rangle$ and $|V_{e3}\rangle$. These three states $|V_{e2}\rangle$ are the states in which the atom is in one of the ground states but the cavity is populated by one photon. The states $|V_{e1}\rangle$ and $|V_{e3}\rangle$ are superpositions including also the state with excited atom and no photon in the cavity modes. The third group contains states in which the system contains two excitations, one of mode $\mathcal{B}_1$ and one of mode $\mathcal{B}_2$. It should be noted that these states cover only a small part of the doubly excited eigenstate space due to our initial choice of considering at most one photon per mode. But due to the low excitation considered, the doubly excited states have only negligible weak influence on the system dynamics and therefore can be neglected for the interpretation. The states including up to one excitation are shown in Fig. II.4.

To interpret the system, it is important to note that due to our definition of the detunings, the probe fields are resonant to an atomic dressed state transition if the detuning has the opposite sign of the respective eigenenergy shift. First, we focus on the line defined by $\Delta_2 = 149\gamma$, for which the probe field $\mathcal{E}_2$ is resonant with the transition $|V_{g,2}\rangle \rightarrow |V_{e1}\rangle$. Fig. II.3.(b) shows the transmission $\mathcal{T}_{F_{a_1}}$ and the reflection $\mathcal{T}_{F_{b_1}}$ at this detuning. For $\Delta_1 = -250\gamma$, the condition $|\Delta_2| \ll |\Delta_1|$ holds and thus $\mathcal{T}_{F_{b_1}} \approx 0$ and the atom is almost completely in state $|1\rangle$, see Fig. II.5. Scanning Δ_1 towards zero detuning, a resonance structure with increased reflection can be seen at around $\Delta_1 = -134\gamma$. At this point, the field $\mathcal{E}_1$ is near-resonant with the transition $|V_{g,1}\rangle \rightarrow |V_{e3}\rangle$, which leads to a scattering of photons in the reflection channel via the atom. This can also be seen by the increase in the excited state population of the atom, see Fig. II.5. Further increasing Δ_1, the reflection becomes minimal at $\Delta_1 \approx -80\gamma$. In this region, field $\mathcal{E}_1$ is relatively far detuned from the eigenstates of the system, as can be seen from the high population of the atomic state $|1\rangle$. As $\mathcal{P}_3$ is relatively small, also the reflection remains low. At

$\Delta_1 = -15\gamma = -h$, a strong resonance is observe in the reflection spectrum. This peak can be attributed to the non-coupling cavity mode $\mathcal{A}_1$. A closer analysis shows that the structure around $\Delta_1 = -15\gamma = -h$ in fact contains two separate peaks, which leads to the apparent asymmetry. The second peak is located at $\Delta_1 = 15\gamma = h = -E_{e2}$ and is due to the coupling to the eigenstates $|V_{e2}\rangle$. At positive detunings Δ_1, we first encounter a region with low reflection, which can be interpreted in the same way as the region around $\Delta_1 = -80\gamma$. At detunings around $\Delta_1 = 149\gamma$, both probe fields couple to the eigenstate on the transition $|V_{g,1}\rangle \rightarrow |V_{e1}\rangle$. At exact two-photon resonance $\Delta_1 = \Delta_2$, a narrow dip in the reflection can be seen, which is due to the above-mentioned dark state. In this case the system behaves as if the atom was not present. In the vicinity of the dark state, the population of the excited state is relatively high due to the near-resonant coupling to the eigenstate $|V_{e1}\rangle$, which leads to the increase in reflection.

Next, we analyze the region around $\Delta_1 \approx 0$ in Fig. II.3.(a), where high reflectivities occur. It can be seen that this structure has a small residual dependence on Δ_2. At detunings Δ_2 for which the second field is in resonance with one of the system's eigenstates, the reflection resonance is centered around $\Delta_1 = -h = -15\gamma$. For all other values of Δ_2, the structure is centered approximately around $\Delta_1 = 0$. The reason for this is as follows. If the second field is detuned from all resonances, then the atom is optically pumped into state $|V_{g2}\rangle$ by the first field, and the system again acts as if no atom was present. Without atom, the two cavity mode pairs are symmetrically split due to their coupling h such that they have resonances at $\pm h = \pm 15\gamma$. As these two resonances are close to each other compared to the line width, they overlap and appear as a single resonance centered around $\Delta_1 = 0$. In contrast, if Δ_2 is tuned to resonance with one of the system's eigenstates, then the atom contributes to the system's dynamics. Then, in the reflection spectrum the non-coupling mode at $\Delta_2 = -15\gamma$ dominates, as already explained for the central resonance of Fig. II.3.(b). Considering the atomic population of the excited state $\mathcal{P}_3$ in Fig. II.5. we observe peaks for $\Delta_1 = 0$ at $\Delta_2 = 134\gamma$ and $\Delta_2 = -149\gamma$ whereas for the third eigenvalue $\Delta_2 = 15\gamma$ the population $\mathcal{P}_3 \approx 0$. This is because the eigenstates $V_{e2,1-3}$ do not include any state in which the atom is excited.

II.4.1.2. Dependence on the atom position

In this section, we analyze the dependence of the results on the position of the atom. In general, the position of the atom determines the coupling constants $g_{\mathcal{A}_i}$ and $g_{\mathcal{B}_i}$, which in turn influence the spectral properties of the total system. A potential realization for the following analysis could be an atom trapped in a potential created by the evanescent field of the resonator. This would lead to a trapping in radial direction, but could still allow for movements of the particle along the azimuthal direction.

In Fig. II.6., we show our results for $\Delta_2 = 0$ for different positions of the Λ atom. Here, the distance to the cavity is constant but the azimuthal position along the resonator circumference and thus the phase $k_i x$ is varied. If $k_i x = \pi/2$, the atom couples to modes $\mathcal{B}_i$ only as assumed for the previously shown results. In case of $k_i x = 0$, the atom couples to the $\mathcal{A}_i$ modes only. Intermediate values lead to coupling to both modes. Changing $k_i x$ from 0 to $\pi/2$ corresponds to moving the atom over a distance of $\lambda/4$ along the circumference. It can be seen in Fig. II.6. that while the general structure of the spectrum remains constant, the positions of both sidebands oscillate around their mean position. Also the height of the sideband peaks changes, with maxima for the two

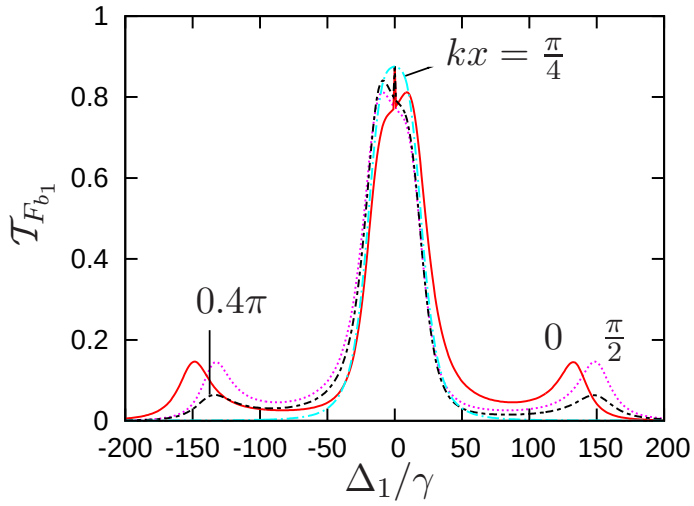

Figure II.6.: Reflection $\mathcal{T}_{F_{b_1}}$ for different azimuthal positions x of the atom and fixed $\Delta_2 = 0$. We chose $kx = 0$, $\frac{\pi}{4}$, 0.4π, and $\frac{\pi}{2}$.

cases in which a single mode pair couples to the atom. At $k_i x = \pi/4$, the sideband peaks vanish. Additionally, the slight asymmetry in the central resonance around $\Delta_1 = 0$ changes. For example, in moving from $k_i x = 0$ to $k_i x = \pi/2$, the structure becomes mirrored at the $\Delta_1 = 0$ axis. This is because the modes $\mathcal{A}_i$ and $\mathcal{B}_i$ exchange their roles as coupled and uncoupled modes. For $k_i x = 0.4\pi$, both mode pairs $\mathcal{A}_i$ and $\mathcal{B}_i$ couple to the atom, but with different coupling strengths. For $k_i x = \pi/4$ the atom couples with equal strength to the $\mathcal{A}_i$ and $\mathcal{B}_i$ modes. Therefore, the middle peak structure is symmetric around $\Delta_1 = 0$.

The radial dependence is directly governed by the absolute value of the coupling constants $g_{\mathcal{A}_i}$ and $g_{\mathcal{B}_i}$. The peaks in the spectrum lie at the eigenenergies given in Eq. (II.4.25). For fixed Δ_2 they move to higher values of $|\Delta_1|$ when increasing the strength of the coupling between the atom and the cavity.

This dependence of the spectral properties on the particle position can also be used to detect the presence of the particle, or to measure its position.

II.4.2. Bad cavity regime

In this Section we analyze the bad cavity regime, and choose $g_0 = 70\gamma$ and $h = 250\gamma$, and all other parameters are chosen as in Sec. II.4.1. Our observables are the output fluxes and the second order correlation functions. For the calculations we use the AE method as described in Sec. II.2.2.3.

II.4.2.1. Transmission and reflection

We start by analyzing the transmission into mode $a_{1,out}$ shown in Fig. II.7. As in the strong coupling case, the transmission approaches one if the first probe field is far detuned, i.e., for large $|\Delta_1|$. Negligibly weak interactions with the first laser field lead to a trapping of the atom in state $|1\rangle$ if the second field is less detuned. Decreasing the absolute value

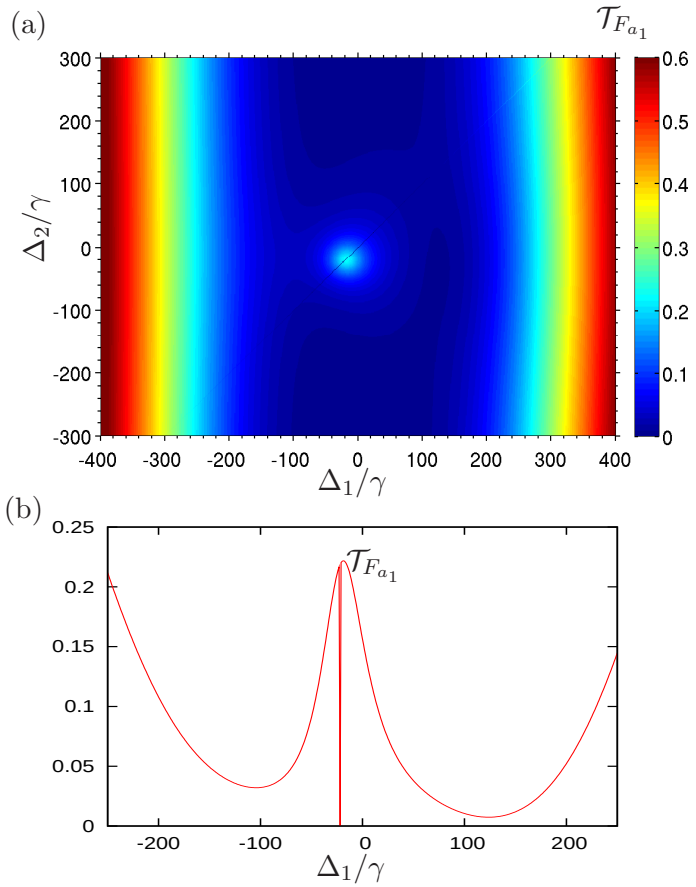

Figure II.7.: (a) $\mathcal{T}_{F_{a_1}}$ for the bad cavity regime with $g_0 = 70\gamma$ and $h = 250\gamma$. (b) Cut at $\Delta_2 = -22\gamma$ for the same parameters.

of Δ_1, the transmission reduces and approaches zero almost independently from the second detuning Δ_2. There is a single resonance structure around $\Delta_1 = -19\gamma$ and $\Delta_2 = -19\gamma$ with increased transmission $\mathcal{T}_{F_{a_1}}$. A cut through Fig. II.7.(a) at $\Delta_2 = -22\gamma$ is shown in Fig. II.7.(b). A closer analysis revealed that both the position and the amplitude of this peak depend on the atom position via the phase $k_i x$. In Fig. II.7., $k_i x = \pi/2$ which means that modes $\mathcal{B}_i$ couple to the atom whereas modes $\mathcal{A}_i$ do not couple. On the other hand, choosing $k_i x = 0$ such that $\mathcal{A}_i$ couples and $\mathcal{B}_i$ not, the resonance structure moves to $\Delta_1 = 19\gamma$, $\Delta_2 = 19\gamma$, and has the same intensity as for $k_i x = \pi/2$. For values of $k_i x$ between 0 and $\pi/2$ the resonance moves along the diagonal line and has reduced amplitude. For equal coupling of the two modes, $g_{\mathcal{A}} = g_{\mathcal{B}}$, the resonance vanishes. We can thus directly trace the resonance back to the coupled atom. A similar resonance was also found for a two level atom coupled to a resonator in the strong coupling regime [105]. Interestingly, however, the resonance is not located at one of the eigenstates of the system obtained by diagonalizing the coherent part of the initial interaction Hamiltonian. Rather, the resonance coincides with maximum population in the atom's upper state. This can be explained by diagonalizing the effective Hamiltonian obtained after the adiabatic elimination in Eq. (II.2.17c). The only nonvanishing eigenvalue of the system after the adiabatic elimination is equal to the sum of the corrected effective detunings $\Delta_{11} + \Delta_{22}$. For our parameters $\Delta_{11} =$

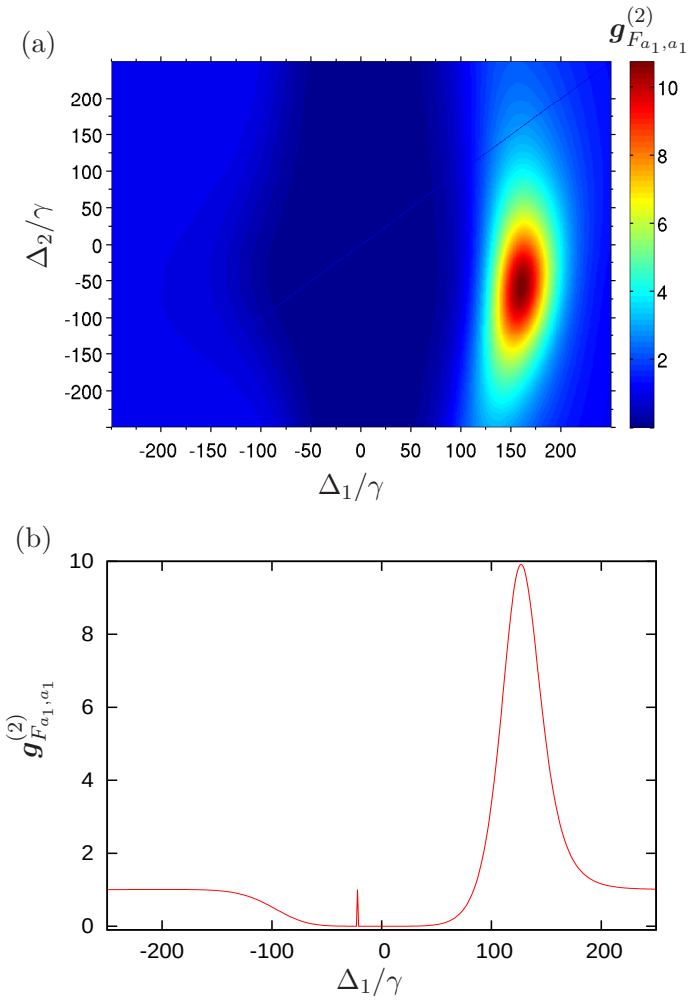

Figure II.8.: (a) Second order correlation function $g^{(2)}_{F_{a_1,a_1}}$ for the bad cavity regime with $g_0 = 70\gamma$ and $h = 250\gamma$. (b) Cut at $\Delta_2 = -22\gamma$ for the same parameters.

$\Delta_{22} = \frac{g_0^2 h}{h^2+\kappa^2}$. Inserting the parameters yields an expected position of the resonance of $\Delta_1 = \Delta_2 = -19.5\gamma$. Finally, on the diagonal line $\Delta_1 = \Delta_2$, the atom is in a dark state such that it decouples from the resonator. Thus the transmission is as in the case without atom for these parameter values. In the lower subfigure, the dark state leads to the sharp dip around $\Delta_1 = -22\gamma$.

II.4.2.2. Second order correlation functions

In this section, we analyze the second order correlation functions $g^{(2)}_{F_{m_i,m_j}}$. First, we consider the case $i = j$. In Fig. II.8., we show the second order correlation function for mode $a_{1,out}$. In the lower subfigure, a cut at $\Delta_2 = -22\gamma$ is shown. The dominant feature is a peak around $\Delta_1 = 130\gamma$ and $\Delta_2 = -30\gamma$. Around this position, $g^{(2)}_{F_{a_1,a_1}}$ reaches high values up to 10. Thus, for these detunings the photons obey a super-Poissonian statistics. This structure is due to small values of $\mathcal{T}_{F_{a_i}}$ for these detunings. Since the correlation function $g^{(2)}_{F_{a_1,a_1}}$ is normalized to the output flux, see Eq. (II.3.24), small

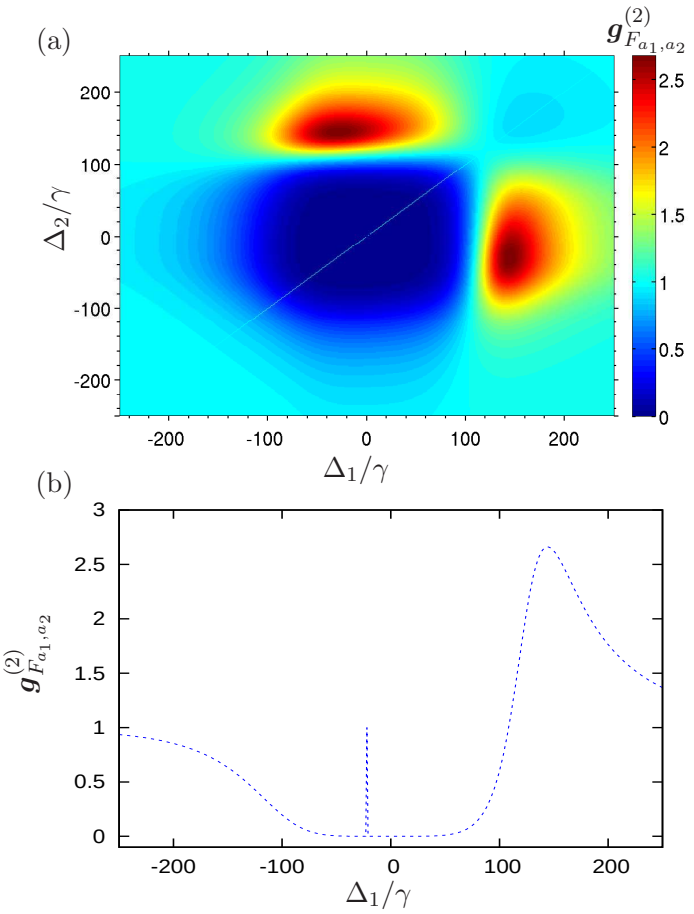

Figure II.9.: (a) Cross correlation $\boldsymbol{g}^{(2)}_{F_{a_1,a_2}}$ for the bad cavity regime, $g_0 = 70\gamma$ and $h = 250\gamma$. (b) Cut at $\Delta_2 = -22\gamma$ for the same parameters.

intensities lead to an enhancement of $\boldsymbol{g}^{(2)}_{F_{a_1,a_1}}$. Another important feature is the large area around zero detunings in which the system exhibits sub-Poissonian statistics. This area coincides with the resonance in the transmission around $\Delta_1 = -19\gamma$, $\Delta_2 = -19\gamma$ found in Fig. II.7. In this parameter regime, non-classical light with sub-Poissonian photon statistics is generated. Since this second order correlation function has values around zero, we can conclude from this information that we have anti-bunching. The non-classical light arises from the interaction with the atom, similar to the turnstile operation reported in [105]. Without atom, the transmission is negligible due to destructive interference in forward direction downstream of the resonator. But excess excitations emitted from the atom can be transmitted in forward directions, and these exhibit sub-Poissonian statistics and anti-bunching due to the fact that the atom requires a finite time to be excited. Finally, in the dark state case $\Delta_1 = \Delta_2$, the photon statistics is Poissonian, $\boldsymbol{g}^{(2)}_{F_{a_1,a_1}} = 1$.

Next, we considered the cross correlation functions. In Fig. II.9., the cross correlation of mode $a_{1,out}$ and $a_{2,out}$ is presented. This figure shows that also this cross correlation function is close to zero in the region around $\Delta_1 = -19\gamma$, $\Delta_2 = -19\gamma$ which is the position of the transmission resonance in $\mathcal{T}_{F_{a_1}}$. This extends the turnstile operation to two distinct modes $a_{1,out}$ and $a_{2,out}$. Thus a detector placed in the transmission direction

only detects individual photons in either of the two modes. We also observe two regions with high second order correlation $\boldsymbol{g}^{(2)}_{F_{a_1,a_2}}$ in Fig. II.9.(a). Analogously as for $\boldsymbol{g}^{(2)}_{F_{a_1,a_1}}$, this can be explained by minima in either of the two output intensities to which the correlation function is normalized. In the region around $(\Delta_1, \Delta_2) = (130, -30)\gamma$ the first order correlation $\mathcal{T}_{F_{a_1}} \approx 0$. In the second peak region around $(\Delta_1, \Delta_2) = (-30, 130)\gamma$ the transmission of mode a_2 almost vanishes.

II.4.2.3. Applications

In this section, we outline possible applications of our setup in the bad cavity regime. First, we show that the coupled cavity atom system can be used as a single photon source. Next, we show that it acts as a bi-modal photon turnstile. Finally, we show that our bimodal photon turnstile is tunable by the input fields and their detunings. This could be exploited as an optical switch.

Considering Fig. II.8.(a), we see that in a region of the resonance in $\mathcal{T}_{F_{a_1}}$ close to $(\Delta_1, \Delta_2) = (-19, -19)\gamma$ (c.f. Fig. II.7.) the second order correlation $\boldsymbol{g}^{(2)}_{F_{a_1,a_1}}$ vanishes. This means that photons of mode $a_{1,out}$ leave the system individually, such that it is impossible to detect two photons of this mode at the same time. Moreover, the cross correlation $\boldsymbol{g}^{(2)}_{F_{a_1,a_2}}$ also vanishes, see Fig. II.9.(a). This means, the photons of each mode come out individually and additionally, if an a_1 photons is detected no a_2 photon can be detected at the same time. Consequently, whenever an $a_{1,out}$ photon is detected, it is impossible that an $a_{2,out}$ photons arrives at the detector at the same time. Therefore we know, that in a direction only individual photons leave the systems. The output intensity of both transmission modes $a_{i,out}$ is different from zero $\mathcal{T}_{F_{a_1}} \neq 0$ and $\mathcal{T}_{F_{a_2}} \neq 0$, see Fig. II.7. Thus our coupled system can be used as bi-modal single photon source in a_i direction.

This can also be used as a photon turnstile, in a direction. Photons come out individually and turn their propagation direction in case of non vanishing atom cavity interaction, which means that the atom is not in a kind of dark state. The turnstile can be controlled by changing the detunings and therewith driving the atom into a dark state. Controllable here means that we can turn the output flux on or off simply by changing the detuning of one of the input probe fields. For example, if we choose $\Delta_2 = -19\gamma$ and $\Delta_1 \approx -19\gamma$ but $\neq -19\gamma$. Then the transmission intensities $\mathcal{T}_{F_{a_1}}$ and $\mathcal{T}_{F_{a_2}}$ are almost maximum and thus $\neq 0$. However, when slightly tuning the input laser field $\mathcal{E}_1$ to $\Delta_1 = \Delta_2 = -19\gamma$, the atom is in the dark state and thus does not interact with the cavity any more. Then the system behaves as if no atom was there and the transmission of both the modes is almost zero. Thus, whether we have a nonvanishing transmission intensity or not can be controlled by slightly changing either of the input detunings.

Furthermore, an optical switch for the modes $a_{i,out}$ can be realized by our system in the bad cavity regime. If the parameters are such that the atom is effectively decoupled from the resonator, due to the critical coupling condition no incoming $a_{i,in}$ photon can be transmitted. Thus all incoming photons are reflected back from the cavity. But enabling the atom-cavity coupling, some photons are transmitted and thus the flux in a direction becomes non-zero. As an example, we found that for $\Delta_1 \approx -19\gamma$ but $\Delta_1 \neq -19\gamma$ and $\Delta_2 = -22\gamma$ the transmission $\mathcal{T}_{F_{a_1}}$ is maximum, see Fig. II.7.(b). But if the input field $\mathcal{E}_2$ is switched off, the atomic population is completely transferred to ground state $|2\rangle$

such that the atom decouples from the resonator. Then, the transmission $\mathcal{T}_{F_{a_1}} \approx 0$, and all light is reflected.

II.5. Summary and discussion

We presented a system consisting of a tapered glass fiber and a whispering gallery microcavity coupling to a three-level atom in the Λ configuration. Each transition is coupled to one whispering gallery mode pair, respectively. We considered two different parameter regimes, the strong coupling regime and the bad cavity regime. For both these regimes we presented adequate calculation methods in order to solve the equations of motion for the system's operators, namely, one based on a truncation of the Hilbert space, and one based on an adiabatic elimination of the resonator. We compared the respective validity ranges, and their advantages and drawbacks. Our observables were the transmission and reflection output fluxes, the atomic populations as well as second order correlation functions and cross correlations between different photonic output modes. In both, the strong and weak coupling regime, we explained the structures of the transmission and reflection using respective dressed states or eigenmodes of the system. As potential application, we found that our system can work as a tunable bimodal photon turnstile which can be controlled by the detunings of the two input fields or as a photonic switch. Additionally, we analyzed the dependence of our observables on the position of the nearby atom and found that our setup could be used for detecting the position of a nearby particle on a sub-wavelength scale.

In our calculations, we neglected direct interactions between different mode pairs in the resonator, and assumed selective coupling of the two atomic transitions to one mode pair, respectively. This could be realized by using the similar frequency, but different polarizations for the two mode pairs which, however, is technically challenging. Alternatively, different frequencies and similar polarizations could be used, and the atom could be tuned in resonance with both modes by adjusting a Zeeman shift using an external magnetic field. Finally, our system can also be realized by two cavities coupling to the same Λ atom. This alternative implementation for the considered setup is shown in Fig. II.2. In this setup, the atom couples to two resonators, and each mode pair is restricted to one of the resonators. As the modes in the two resonators have different polarization or different frequencies, direct coupling between the resonators could be avoided. This setup at the same time could provide a connection to studies on quantum transport of electrons through single molecules [143].

II.A. Details on the adiabatic elimination

We start with the Hamiltonian given in Eq. (II.2.10e) and the complete master equation including all cavity modes and the atomic states

$$\partial_t \rho = -\frac{i}{\hbar}[\mathcal{H}_{\mathcal{AB}}, \rho] + \mathcal{L}_\kappa \rho + \mathcal{L}_\gamma \rho \tag{II.A.1}$$

with the Liouville superoperators

$$\mathcal{L}_\kappa \rho = \sum_{\mathcal{M}\in\{\mathcal{A}_i,\mathcal{B}_i\}} \kappa_{\mathcal{M}} (2\mathcal{M}\rho\mathcal{M}^\dagger - \mathcal{M}^\dagger\mathcal{M}\rho - \rho\mathcal{M}^\dagger\mathcal{M}) \tag{II.A.2}$$

and

$$\mathcal{L}_\gamma \rho = \sum_{i=1}^{2} \frac{\gamma_i}{2} (2\mathcal{S}_i^- \rho \mathcal{S}_i^+ - \mathcal{S}_i^+ \mathcal{S}_i^- \rho - \rho \mathcal{S}_i^+ \mathcal{S}_i^-) \,. \tag{II.A.3}$$

Due to the weak input field and the fast decay of the cavity population, we can assume that the average occupation number is low. Furthermore, after the basis transformation Eq. (II.2.9), we can treat the two normal mode pairs $\mathcal{A}_i$ and $\mathcal{B}_i$ separately. We show the elimination formalism with modes $\mathcal{A}_i$ in the following. We start by expanding the density matrix in the photon number occupation, keeping terms including up to one photon per mode. The expanded density operator reads [139]

$$\begin{aligned}\rho_{exp} =& \rho_{00} \otimes |00\rangle\langle 00| + \rho_{10} \otimes |10\rangle\langle 00| + \rho_{20} \otimes |01\rangle\langle 00| + \rho_{01} \otimes |00\rangle\langle 10| \\ &+ \rho_{02} \otimes |00\rangle\langle 01| + \rho_{03} \otimes |00\rangle\langle 11| + \rho_{11} \otimes |10\rangle\langle 10| + \rho_{12} \otimes |10\rangle\langle 01| \\ &+ \rho_{21} \otimes |01\rangle\langle 10| + \rho_{22} \otimes |01\rangle\langle 01| + \rho_{03} \otimes |00\rangle\langle 11| + \rho_{30} \otimes |11\rangle\langle 00| \\ &+ \rho_{31} \otimes |11\rangle\langle 10| + \rho_{32} \otimes |11\rangle\langle 01| + \rho_{33} \otimes |11\rangle\langle 11| + \rho_{23} \otimes |01\rangle\langle 11| \\ &+ \rho_{13} \otimes |10\rangle\langle 11| \,,\end{aligned} \tag{II.A.4}$$

where the photon states for the two modes of the $\mathcal{A}_i$ pair are defined as $|n(\mathcal{A}_1), n(\mathcal{A}_2)\rangle$. The ρ_{ij} are the residual part of the density matrix.

Substituting the expanded density matrix Eq. (II.A.4) into the master equation II.A.1, we obtain equations of motion for the elements ρ_{ij}. The equations corresponding to the lowest photon number occupation evaluate to

$$\begin{aligned}\partial_t \rho_{00} =& \mathcal{L}_{\text{atom}} \rho_{00} + 2\kappa_1 \rho_{11} + 2\kappa_2 \rho_{22} - i \left(\left(\frac{1}{\sqrt{2}} \mathcal{E}_1^* + g_{\mathcal{A}_1} \mathcal{S}_1^+ \right) \rho_{10} \right. \\ &+ \left(\frac{1}{\sqrt{2}} \mathcal{E}_2^* + g_{\mathcal{A}_2} \mathcal{S}_2^+ \right) \rho_{20} - \rho_{01} \left(\frac{1}{\sqrt{2}} \mathcal{E}_1 + g_{\mathcal{A}_1} \mathcal{S}_1^- \right) \\ &\left. - \rho_{02} \left(\frac{1}{\sqrt{2}} \mathcal{E}_2 + g_{\mathcal{A}_2} \mathcal{S}_2^- \right) \right) \,,\end{aligned} \tag{II.A.5a}$$

$$\begin{aligned}\partial_t \rho_{10} =& \mathcal{L}_{\text{atom}} \rho_{00} - \kappa_1 \rho_{10} - i \Big((\delta_1 + h_1) \rho_{10} \\ &+ \left(\frac{1}{\sqrt{2}} \mathcal{E}_1 + g_{\mathcal{A}_1} \mathcal{S}_1^- \right) \rho_{00} - \rho_{11} \left(\frac{1}{\sqrt{2}} \mathcal{E}_1 + g_{\mathcal{A}_1} \mathcal{S}_1^- \right) \\ &- \rho_{12} \left(\frac{1}{\sqrt{2}} \mathcal{E}_2 + g_{\mathcal{A}_2} \mathcal{S}_2^- \right) + \left(g_{\mathcal{A}_2} \mathcal{S}_2^+ + \frac{1}{\sqrt{2}} \mathcal{E}_2^* \right) \rho_{30} + (m+p) e^{i\epsilon t} \rho_{20} \Big) \,,\end{aligned} \tag{II.A.5b}$$

$$\begin{aligned}\partial_t \rho_{11} =& \mathcal{L}_{\text{atom}} \rho_{11} - 2\kappa_1 \rho_{11} - i \left(\left(\frac{1}{\sqrt{2}} \mathcal{E}_1 + g_{\mathcal{A}_1} \mathcal{S}_1^- \right) \rho_{01} \right. \\ &\left. - \rho_{10} \left(\frac{1}{\sqrt{2}} \mathcal{E}_1^* + g_{\mathcal{A}_1} \mathcal{S}_1^+ \right) \right) \,.\end{aligned} \tag{II.A.5c}$$

Here, $\mathcal{L}_{\text{atom}} \rho$ is defined as

$$\mathcal{L}_{\text{atom}} \rho = -\frac{i}{\hbar} [\mathcal{H}_0, \rho] + \mathcal{L}_\gamma \rho \,, \tag{II.A.6}$$

$$\mathcal{H}_0 = -\hbar \sum_{i=1}^{2} \Delta_i \mathcal{S}_i^- \mathcal{S}_i^+ \,. \tag{II.A.7}$$

In the bad cavity regime, the cavity loss dynamics dominates over the coherent dynamics, such that

$$\frac{|\mathcal{L}_{\text{atom}}|}{\kappa_i} \ll 1\,, \tag{II.A.8}$$

and thus the terms $\mathcal{L}_{\text{atom}}$ can be neglected in Eqs. (II.A.5). Setting further the time derivative of the diagonal elements in Eqs. (II.A.5) to zero, we arrive at

$$\begin{aligned}\rho_{10} =& \frac{-i}{\kappa_1 + i(\delta_1 + h_1)} \cdot \Big((\frac{1}{\sqrt{2}}\mathcal{E}_1 + g_{\mathcal{A}_1}\mathcal{S}_1^-)\rho_{00} \\ & - \rho_{11}(\frac{1}{\sqrt{2}}\mathcal{E}_1 + g_{\mathcal{A}_1}\mathcal{S}_1^-) - \rho_{12}(\frac{1}{\sqrt{2}}\mathcal{E}_2 + g_{\mathcal{A}_2}\mathcal{S}_2^-) \\ & + (g_{\mathcal{A}_2}\mathcal{S}_2^+ + \frac{1}{\sqrt{2}}\mathcal{E}_2^*)\rho_{30} + (m+p)e^{i\epsilon t}\rho_{20}\Big)\,. \end{aligned} \tag{II.A.9}$$

Now we calculate the time evolution of the atomic density matrix using the diagonal elements of $\partial_t \rho_{exp}$

$$\partial_t \varrho_{\text{atom}} = \partial_t \rho_{00} + \partial_t \rho_{11} + \partial_t \rho_{22}\,. \tag{II.A.10}$$

Since our cavity is almost always empty, we substitute the terms obtained for the off diagonal elements ρ_{ij} only up to ρ_{00} order.

Therewith we finally arrive at an atomic master equation of the form as shown in Eq. (II.2.17c).

II.B. Constants for the atomic master equation

The constants used in order to calculate the atomic master equation Eq. (II.2.17c) are defined as follows:

$$\begin{aligned}
\Delta_{11} &= g_{\mathcal{A}_1}^2 \Re(\lambda_{\mathcal{A}}) + g_{\mathcal{B}_1}^2 \Re(\lambda_{\mathcal{B}}) \\
\Delta_{22} &= g_{\mathcal{A}_2}^2 \Re(\xi_{\mathcal{A}}) + g_{\mathcal{B}_2}^2 \Re(\xi_{\mathcal{B}}) \\
\Delta_{12} &= \Delta_{21} = 0 \\
\Omega_1 &= \Omega_{\mathcal{A}_1} + \Omega_{\mathcal{B}_1} \\
\Omega_2 &= \Omega_{\mathcal{A}_2} + \Omega_{\mathcal{B}_2}
\end{aligned}$$

with

$$\begin{aligned}
\Omega_{\mathcal{A}_1} &= \lambda_{\mathcal{A}}^* g_{\mathcal{A}_1} \frac{\mathcal{E}_1}{\sqrt{2}} + \mathcal{F}_{\mathcal{A}}^* \mu g_{\mathcal{A}_1} \frac{\mathcal{E}_2}{\sqrt{2}} \\
\Omega_{\mathcal{A}_2} &= \xi_{\mathcal{A}}^* g_{\mathcal{A}_2} \frac{\mathcal{E}_2}{\sqrt{2}} + \mathcal{F}_{\mathcal{A}}^* \mu^* g_{\mathcal{A}_2} \frac{\mathcal{E}_1}{\sqrt{2}} \\
\Omega_{\mathcal{B}_1} &= i\lambda_{\mathcal{B}}^* g_{\mathcal{B}_1} \frac{\mathcal{E}_1}{\sqrt{2}} + i\mathcal{F}_{\mathcal{B}}^* \nu g_{\mathcal{B}_1} \frac{\mathcal{E}_2}{\sqrt{2}} \\
\Omega_{\mathcal{B}_2} &= i\xi_{\mathcal{B}}^* g_{\mathcal{B}_2} \frac{\mathcal{E}_2}{\sqrt{2}} + i\mathcal{F}_{\mathcal{B}}^* \nu^* g_{\mathcal{B}_2} \frac{\mathcal{E}_1}{\sqrt{2}} \\
\Gamma_{11} &= 2 \cdot (g_{\mathcal{A}_1}^2 \Im(\lambda_{\mathcal{A}}) + g_{\mathcal{B}_1}^2 \Im(\lambda_{\mathcal{B}})) + \gamma_1 \\
\Gamma_{22} &= 2 \cdot (g_{\mathcal{A}_2}^2 \Im(\xi_{\mathcal{A}}) + g_{\mathcal{B}_2}^2 \Im(\xi_{\mathcal{B}})) + \gamma_2 \\
\Gamma_{12} &= 2 \cdot (g_{\mathcal{A}_1} g_{\mathcal{A}_2} \mu \Im(\mathcal{F}_{\mathcal{A}}) + g_{\mathcal{B}_1} g_{\mathcal{B}_2} \nu \Im(\mathcal{F}_{\mathcal{B}})) \\
\Gamma_{21} &= \Gamma_{12}^*
\end{aligned}$$

$$
\begin{aligned}
\mu &= (q+p)e^{i\epsilon t} \\
\nu &= (p-q)e^{i\epsilon t} \\
\lambda_{\mathcal{A}} &= \frac{f_{\mathcal{A}_1}}{1 - f_{\mathcal{A}_1} f_{\mathcal{A}_2} \mu\mu^*} \\
\lambda_{\mathcal{B}} &= \frac{f_{\mathcal{B}_1}}{1 - f_{\mathcal{B}_1} f_{\mathcal{B}_2} \nu\nu^*} \\
\xi_{\mathcal{A}} &= \frac{f_{\mathcal{A}_2}}{1 - f_{\mathcal{A}_1} f_{\mathcal{A}_2} \mu\mu^*} \\
\xi_{\mathcal{B}} &= \frac{f_{\mathcal{B}_2}}{1 - f_{\mathcal{B}_1} f_{\mathcal{B}_2} \nu\nu^*} \\
\mathcal{F}_{\mathcal{A}} &= \frac{f_{\mathcal{A}_1} f_{\mathcal{A}_2}}{1 - f_{\mathcal{A}_1} f_{\mathcal{A}_2} \mu\mu^*} \\
\mathcal{F}_{\mathcal{B}} &= \frac{f_{\mathcal{B}_1} f_{\mathcal{B}_2}}{1 - f_{\mathcal{B}_1} f_{\mathcal{B}_2} \nu\nu^*} \\
f_{\mathcal{A}_1} &= \frac{i}{\kappa_{\mathcal{A}_1} - i(\delta_1 + h_1)} \\
f_{\mathcal{B}_1} &= \frac{i}{\kappa_{\mathcal{B}_1} - i(\delta_1 - h_1)} \\
f_{\mathcal{A}_2} &= \frac{i}{\kappa_{\mathcal{A}_2} - i(\delta_2 + h_2)} \\
f_{\mathcal{B}_2} &= \frac{i}{\kappa_{\mathcal{B}_2} - i(\delta_2 - h_2)}
\end{aligned}
\tag{II.B.1}
$$

PART III

Formation of supermodes in a chain of coupled atom-cavity systems

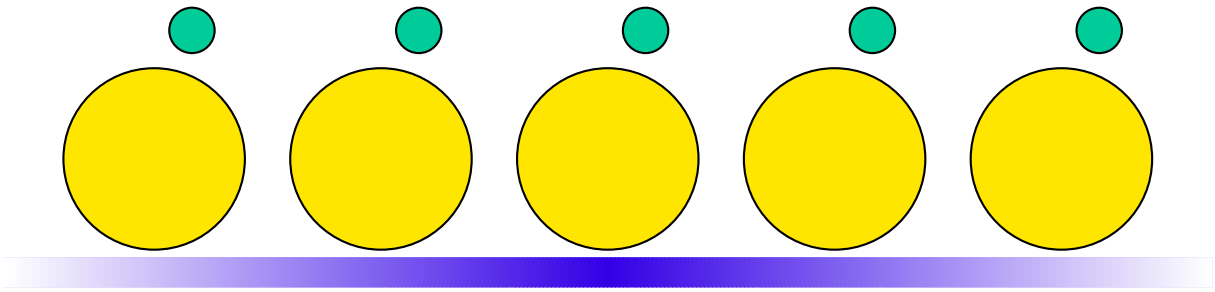

III Formation of supermodes in a chain of coupled atom-cavity systems

In this part, a chain of atom-microcavity systems is considered which are coupled by a common fiber. We study the transmission and reflection behavior of this coupled system probed by a weak input field. We are particularly interested in effects originating from the energy exchange of neighboring cavities via the connecting waveguide. We analyze the formation of supermodes that lead to strong enhancement of the transmission, focusing on the influence of the chain geometry and the number of atom-cavity subsystems on our observables. We show that the significance of supermodes for the transmission increases with the number of atom-cavity subsystems. Additionally, we identify spectral ranges in which the chain geometry decides whether supermodes are formed and ranges which are insensitive to the geometry. Furthermore, we show that the reflection signal allows to identify which cavities couple to atoms, which is a crucial information in experimental realizations of longer atom-cavity chain systems.

III.1. Introduction

Already the simplest case of a single particle coupled to a single microcavity has led to a number of fascinating proposals and experiments. For example, strong coupling of a microcavity was demonstrated to atoms [99] and quantum dots [101], a single photon turnstile was realized in [105], and the complex interplay of counterpropagating resonator modes already due to a classical particle was observed in [144]. Small chains of atom-cavity systems have been analyzed as well. For example, in [145], two coupled atom-cavity systems are considered for applications in quantum networks, see also [108]. But in that study, light can propagate only in one direction through the system, and backward couplings and thus supermodes between the subsystems are neglected. This restriction was lifted in [146], where two atom-cavity systems coupled to a fiber are considered including the scattering between the cavities. However, only a single cavity mode instead of a pair of modes was considered in each resonator. The non-coupling eigenmode of the resonator, found, e.g., in [99], which can have strong influence on the system's optical properties, is not considered. Furthermore, only the transmission was analyzed, and cases with more than two atom-cavity systems, the reflection, and the

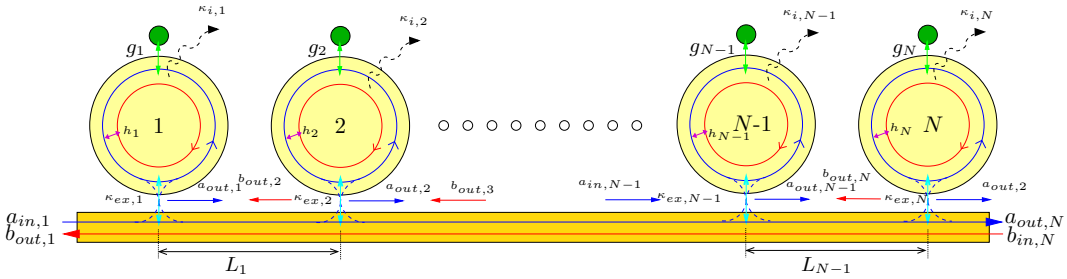

Figure III.1.: Chain of N coupled atom-microcavity systems connected by a common waveguide.

formation of supermodes were not studied. Meanwhile, recent experiments indicate that a realization of chains of coupled atom-cavity systems is within reach. For example, next to the single atom-cavity systems [99, 105], it was also shown that atoms can be trapped by the evanescent field of a tapered fiber [114, 115]. Furthermore, real-time detection and feedback to monitor single atoms near a microresonator was recently demonstrated, which is an important step towards larger networks of atom-cavity systems [100].

Motivated by this, in this project, we investigate a chain of N coupled cavity-atom subsystems connected via a waveguide and probed by a weak input field as shown in Fig. III.1. We mainly study the formation of supermodes, which can arise due to the scattering of light between the different subsystems. To identify and quantify these modes, we define a "superness" measure, which is given by the difference in transmission for the complete system relative to the transmission of a corresponding system of independent cavities without backward coupling. We find that the formation of supermodes crucially depends on the length of the chain and the relative distances between the subsystems. We also show that while the overall transmission decreases with increasing number of atom-cavity subsystems in the chain, the relative contribution of the supermodes increases. Since it can be difficult to achieve simultaneous coupling of all resonators to individual atoms in experiments, we also show that the atom-cavity coupling configuration of the chain can be determined from the reflected light, whereas the transmitted light does not contain this information. In this sense, the reflection and transmission contain complementary information.

As described in detail in part I, many different interaction processes can take place in such coupled systems. If a cavity is located close to a fiber, light propagating in the fiber can couple into the cavity. Similarly, if a particle is placed within the evanescent field of the resonator, the atom's transitions can be driven by the cavity modes, as long as the frequencies are comparable. All these coupling mechanisms crucially influence the dynamics of our system. In our research we study their respective influence on the transmission and reflection behavior. We consider a chain of N coupled cavity-atom subsystems connected via a waveguide. The system is assumed to be probed by weak input fluxes. Since the atomic transition frequencies are assumed to be similar to the cavities' resonance frequencies, the cavity modes can coupled to a nearby atom as long as the atom is located within the evanescent field. Additionally, the N cavity-atom subsystems are coupled via the connecting fiber. For this reason, output fluxes of each cavity contribute to the input fluxes of the neighboring subsystems. We assume this energy transfer to be possible in both the directions. Two fundamentally different calculation methods of solving the

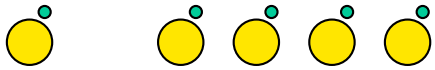

equations of motion in the steady state are presented. Firstly, we numerically solve the equation system for the complete coupled chain. Secondly, we calculate our observables using a coupling matrix. We found, that the presence of backward couplings crucially influences the dynamics of our system and gives rise to interference effects which lead to supermodes where a strong enhancement of the transmission is achieved.

This part is organized as follows. In Sec. III.2. we describe the model system with the equations of motion and introduce the observables. We proceed in Sec. III.3. by introducing two fundamentally different calculation methods for solving the equations of motion and discuss their respective advantages and drawbacks. In Sec. III.4. we show our results. We start by analyzing the dependence of the transmission and reflection behavior on the length of the chain N for equidistant subsystems. Next, we consider asymmetric chains. Finally, we suggest how to use our setup to measure which of the subsystems possess a nearby atom. In Sec. III.4.2.1. we present results for parameters where a supermode of the coupled system is excited and explain how interference effects cause a large transmission enhancement of the coupled system.

III.2. Description of the model system

We consider a chain of N subsystems as shown in Fig. III.1. A tapered fiber connects the N cavities and each resonator is additionally coupled to an atom whose internal structure has two energy levels, an excited state $|2\rangle$ and a ground state $|1\rangle$. This means, we consider a reduction of the general system introduced in part I with N subsystems, $D_n = 1$ for $n \in \{1, .., N\}$ and $X = 1$. A pair of whispering gallery modes (WGMs) can propagate inside every cavity. The clockwise mode is denoted by a and the counterclockwise mode by b. The vacuum coupling between two neighboring cavities is neglected which means that their distances are assumed to be large enough. Probe fields can be applied from both sides, a_{in} or b_{in} respectively. The interaction between a coupling photonic mode of microcavity number n and the respective nearby atom is described by the coupling constant g_n. Modes belonging to one pair $\{a_n, b_n\}$ are coupled via scattering with rate h_n. The coupling of resonator n to the fiber is $\kappa_{ex,n}$. L_n is the distance between cavity n and $n+1$. The transition frequency of the nearby atom at subsystem n is $\omega_{at,n}$ and the respective cavity resonance frequency is called $\omega_{cav,n}$. The detunings are defined as

$$\begin{aligned} \Delta_n &= \omega_{at,n} - \omega_L \,, \\ \delta_n &= \omega_{cav,n} - \omega_L \,, \end{aligned} \tag{III.2.1}$$

where ω_L denotes the input laser frequency.

III.2.1. Hamiltonian and equations of motion

In order to partly diagonalize our Hamiltonian we use normal modes [99, 105] for our calculations. These normal modes read

$$\begin{aligned} \mathcal{A}_n &= \frac{a_n + b_n}{\sqrt{2}} \\ \mathcal{B}_n &= \frac{a_n - b_n}{\sqrt{2}} \,. \end{aligned} \tag{III.2.2}$$

We start with the Hamiltonian using the normal modes $\mathcal{A}_n$ and $\mathcal{B}_n$ for one two-level atom cavity system n

$$\begin{aligned}\mathcal{H}_{\mathcal{AB}}(n) = &- \hbar\Delta_n \mathcal{S}_n^- \mathcal{S}_n^+ \\ &+ \hbar(\delta_n + |h_n|)\mathcal{A}_n^\dagger \mathcal{A}_n + \hbar(\delta_n - |h_n|)\mathcal{B}_n^\dagger \mathcal{B}_n \\ &+ i\hbar\sqrt{2\kappa_{ex,n}}\left(\mathcal{A}_{in,n}\mathcal{A}_n^\dagger + \mathcal{B}_{in,n}\mathcal{B}_n^\dagger + \text{H. c.}\right) \\ &+ \hbar\left(g_{\mathcal{A}_n}\mathcal{A}_n^\dagger \mathcal{S}_n^- - ig_{\mathcal{B}_n}\mathcal{B}_n^\dagger \mathcal{S}_n^- + \text{H. c.}\right) . \end{aligned} \tag{III.2.3}$$

$\mathcal{S}_n^\pm$ are the excitation and annihilation operators of the atom close to cavity number n and $\mathcal{A}_{in,n}$ and $\mathcal{B}_{in,n}$ the respective input field amplitudes. The coupling of the atom to the normal modes of the respective cavity is described by the parameters $g_{\mathcal{A}_n}$ and $g_{\mathcal{B}_n}$, respectively. For modes concentrated on the resonator's circumference, coupling constants can be written as $g_{\mathcal{A}_n} = g_n \cdot f(r,z)\cos k_n x$ and $g_{\mathcal{B}_n} = g_n \cdot f(r,z)\sin k_n x$ where k_n is the wavenumber, x the position along the resonator's circumference, r the radial position to the cavity's center and z the vertical coordinate. Later, for our numerical calculations, we assume the atoms to couple to mode $\mathcal{B}_n$ only and thus set $g_{\mathcal{A}_n} = 0$ and $g_{\mathcal{B}_n} = g_n$. For our N cavity system, the Hamiltonian reads

$$\mathcal{H}_N = \sum_{n=1}^{N} \mathcal{H}_{\mathcal{AB}}(n) . \tag{III.2.4}$$

where N is the number of resonators.

The decay of the cavity modes of resonator n is denoted by $\kappa_n = \kappa_{i,n} + \kappa_{ex,n}$. The spontaneous emission rate of the respective nearby atom is $\gamma_{\parallel,n}$ and $\gamma_{p,n}$ describes the dephasing. We can write the incoherent part of the system's dynamics by the Liouville operator

$$\mathcal{L}_N \rho = \sum_{n=1}^{N} (\mathcal{L}_{\mathcal{A}_n} + \mathcal{L}_{\mathcal{B}_n} + \mathcal{L}_{\parallel n} + \mathcal{L}_{p,n})\rho . \tag{III.2.5}$$

Here,

$$\begin{aligned}\mathcal{L}_{\mathcal{A}_n}\rho &= \kappa_{\mathcal{A}_n}(2\mathcal{A}_n\rho\mathcal{A}_n^\dagger - \mathcal{A}_n^\dagger\mathcal{A}_n\rho - \rho\mathcal{A}_n^\dagger\mathcal{A}_n) , \\ \mathcal{L}_{\mathcal{B}_n}\rho &= \kappa_{\mathcal{B}_n}(2\mathcal{B}_n\rho\mathcal{B}_n^\dagger - \mathcal{B}_n^\dagger\mathcal{B}_n\rho - \rho\mathcal{B}_n^\dagger\mathcal{B}_n) , \\ \mathcal{L}_{\parallel n}\rho &= \frac{\gamma_{\parallel n}}{2}(2\mathcal{S}_n^-\rho\mathcal{S}_n^+ - \mathcal{S}_n^+\mathcal{S}_n^-\rho - \rho\mathcal{S}_n^+\mathcal{S}_n^-) , \\ \mathcal{L}_{p,n}\rho &= \frac{\gamma_{p,n}}{2}(\mathcal{S}_n^z\rho\mathcal{S}_n^z - \rho) , \end{aligned} \tag{III.2.6}$$

where we used $\mathcal{S}_n^z = [\mathcal{S}_n^+, \mathcal{S}_n^-]$.

Using these definitions, we obtain the following equations of motion for our operators

$$\begin{aligned}\partial_t\mathcal{A}_n &= -i(\Delta_n + |h_n|)\mathcal{A}_n - ig_{\mathcal{A}_n}\mathcal{S}_n^- - \kappa_{\mathcal{A}_n}\mathcal{A}_n + \sqrt{2\kappa_{ex,n}}\mathcal{A}_{in,n} , \\ \partial_t\mathcal{B}_n &= -i(\Delta_n - |h_n|)\mathcal{B}_n - g_{\mathcal{B}_n}\mathcal{S}_n^- - \kappa_{\mathcal{B}_n}\mathcal{B}_n + \sqrt{2\kappa_{ex,n}}\mathcal{B}_{in,n} , \\ \partial_t\mathcal{S}_n^- &= -i\Delta_n\mathcal{S}_n^- + ig_{\mathcal{A}_n}^*\mathcal{S}_n^z\mathcal{A}_n - g_{\mathcal{B}_n}^*\mathcal{S}_n^z\mathcal{B}_n - \left(\gamma_{p,n} + \frac{\gamma_{\parallel,n}}{2}\right)\mathcal{S}_n^- , \\ \partial_t\mathcal{S}_n^z &= 2ig_{\mathcal{A}_n}\mathcal{A}_n^\dagger\mathcal{S}_n^- - 2ig_{\mathcal{A}_n}^*\mathcal{A}_n\mathcal{S}_n^+ + 2g_{\mathcal{B}_n}\mathcal{B}_n^\dagger\mathcal{S}_n^- + 2g_{\mathcal{B}_n}^*\mathcal{B}_n\mathcal{S}_n^+ - \gamma_{\parallel,n}(1 + \mathcal{S}_n^z) . \end{aligned} \tag{III.2.7}$$

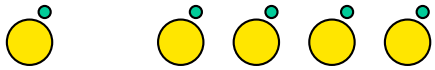

We use a semiclassical treatment for our calculations and neglect fluctuations by assuming that the expectation values of a product of operators are equal to the product of the respective expectation values, i.e., replace operators with their respective expectation values [101].

III.2.2. Recursive calculation of the input field amplitudes

In order to solve the above derived equations of motion of Eq. (III.2.7), we need to know the input field amplitudes for each of the N cavity-atom systems. Usually only the inputs of the outer cavities, i.e., cavity 1 and cavity N are known. In this section, we therefore explain how to recursively calculate the input field amplitudes of the cavities in between.

For a single cavity the input and output modes are connected via the input-output relation [141]

$$\begin{aligned} \langle a_{out,n} \rangle &= -a_{in,n} + \sqrt{2\kappa_{ex,n}} \langle a_n \rangle \\ \langle b_{out,n} \rangle &= -b_{in,n} + \sqrt{2\kappa_{ex,n}} \langle b_n \rangle \,. \end{aligned} \tag{III.2.8}$$

The input field amplitudes of cavity n can then be calculated from the outputs of the neighboring cavities via

$$\begin{aligned} a_{in,n} &= \langle a_{out,n-1} \rangle \, e^{ikL_{n-1}} \\ b_{in,n} &= \langle b_{out,n+1} \rangle \, e^{ikL_n} \,. \end{aligned} \tag{III.2.9}$$

Finally, the input field amplitudes of the normal modes are given by

$$\begin{aligned} \mathcal{A}_{in,n} &= \frac{a_{in,n} + b_{in,n}}{\sqrt{2}} \\ \mathcal{B}_{in,n} &= \frac{a_{in,n} - b_{in,n}}{\sqrt{2}} \,. \end{aligned} \tag{III.2.10}$$

For an arbitrary n, the terms for the input field amplitudes are very complicated, in particular if the chain is long, i.e., large N. Therefore, when plugging Eq. (III.2.10) into our equations of motion Eq. (III.2.7), especially for long chains with large N the equation system we have to solve becomes very complicated.

III.2.3. Observables

III.2.3.1. Transmission and reflection

As observables we particularly consider the transmission and reflection properties of our system. Using the input-output relation of Eq. (III.2.8) we can calculate the output flux of each cavity within our coupled chain. If $b_{in,N} = 0$ the transmission T and reflection R can be calculated according to

$$\begin{aligned} T &= \frac{|\langle a_{out,N} \rangle|^2}{|a_{in,1}|^2} \\ R &= \frac{|\langle b_{out,1} \rangle|^2}{|a_{in,1}|^2} \,. \end{aligned} \tag{III.2.11}$$

III.2.3.2. "Superness" of modes ΔT

For our chain of microresonators coupled to atoms we are particularly interested in constellations where the output intensities strongly differ from a chain of uncoupled, i.e., independent cavity-atom systems. For a chain of independent cavities the backward fluxes between cavity n and $n+1$ are zero, which means that the total transmission $T_{ind,N}$ can be calculated as

$$T_{ind,N} = T_1 \cdot T_2 \cdots T_N \,. \tag{III.2.12}$$

Here, T_n denotes the transmission of the single subsystem n. As indicator to quantify the importance of backward fluxes and thus to identify occurring supermodes in our system, we define a "superness" measure, which is given by the difference in transmission for the complete system relative to the transmission of a corresponding system of independent cavities without backward coupling

$$\Delta T = T - T_{ind,N} \,. \tag{III.2.13}$$

III.2.3.3. Atomic populations

The populations of the atomic states $|1\rangle$ and $|2\rangle$ can be calculated from the operators $\mathcal{S}_n^z$. Using the trace condition and the definitions of $\mathcal{S}_n^z$ for the populations we arrive at

$$\begin{aligned} \mathscr{P}_{1,n} &= \frac{1}{2}(1 - \langle \mathcal{S}_n^z \rangle) \,, \\ \mathscr{P}_{2,n} &= \frac{1}{2}(1 + \langle \mathcal{S}_n^z \rangle) \,. \end{aligned} \tag{III.2.14}$$

Here, $\mathscr{P}_{1,n}$ is the population of the ground state $|1\rangle$ of the atom close to cavity n whereas $\mathscr{P}_{2,n}$ is the population of the excited state $|2\rangle$.

III.3. Two different calculation methods

In the following, we present two different methods for solving the equations of motion Eq. III.2.7 while using a semiclassical treatment, i.e., replacing the operators by their expectation values. We calculate a steady state solution of the variables which is independent of the initial conditions. In the following, we set the resonance frequencies of the atoms equal to the resonance frequencies of the cavities, i.e., $\omega_{cav,n} = \omega_{at,n}$ which results in $\Delta_n = \delta_n$.

III.3.1. Numerical solution of the complete system (NC)

We solve the equations of motion Eq. (III.2.7) for a chain of N subsystems numerically, where we use the semiclassical approximation and solve these equations by numerical integration for the expectation values [101]. Since we have to split each operator equation into its real and imaginary part, our differential equation system consists of $2{*}4{*}N = 8N$ equations. This seems not too much, however, since the equations are nonlinear and include the complicated terms for the input fluxes resulting from Eq. (III.2.9), their

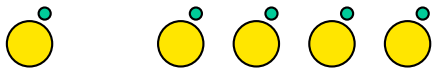

solution is not trivial. As solution we obtain the expectation values both for the atomic operators $\mathcal{S}_n^{\pm}$ and the photon mode operators $\mathcal{A}_n$ and $\mathcal{B}_n$. With their help we can then calculate our observables as defined in Sec. III.2.3.

Since the number of equations of motion increases linearly with N, this method is no longer efficient for long chains. In order to investigate longer chains with more than three or four cavities, we describe a more efficient way of calculation in the following section. In Sec. III.3.3. we compare the two methods and discuss their advantages and drawbacks.

III.3.2. Reduction to the solution of N single-cavity problems - Matrix method (MM)

If we numerically solve the differential system of our equations of motion, the calculation times quickly become very long when increasing N. Therefore, at least for longer chains with more than two or three cavities, we need a more efficient way to calculate our observables. In this section we describe a method which allows us to obtain the observables by solving the equations of motion only for a single cavity and via matrix multiplication.

In [147] an analytical derivation of such a coupling matrix is given for two coupled cavities without nearby atom. However, the presence of the atom makes the system much more complex and therefore such an analytical calculation is no longer performable. Yet, we found a method to numerically determine such a coupling matrix via solving the equations of motion for each single subsystem separately. This allows us a much faster calculation of T and R as compared to the NC method. Even for calculating specific quantities of one cavity within the chain as, e.g., the atomic population, we can still break our N cavity problem down to N single cavity problems.

This matrix method (MM), however, has some restrictions on the parameters. We have to ensure that either no nearby atom is present or the atom is very low excited, i.e., the population of the upper state is almost zero. This situation is given if the absolute values of the input field amplitudes of the modes which can couple to the atoms are much smaller than h_n, κ_n and the coupling to the atom of the coupling mode(s) g_{B_n} or/and g_{A_n}. This restriction is discussed in more detail in Sec. III.3.3.

III.3.2.1. Calculations of transmittivity t and reflectivity r of a single cavity-atom system

For employing the MM, we first have to calculate the transmittivity t and reflectivity r of each single cavity-atom system. These parameters are complex numbers which specify such a subsystem. $|t|$ and $|r|$ are the absolute values and ϕ_r and ϕ_t the phase angles of the transmittivity and reflectivity. The parameters t and r depend on the laser detuning Δ_n of the probe field but not on the values of the single cavity input field amplitudes $a_{in,sc}$ and $b_{in,sc}$ as long as they are small enough such that the atom is far from saturation where $\mathscr{P}_{1,n} = \mathscr{P}_{2,n} = \frac{1}{2}$. A more detailed discussion of the validity range is provided in Sec. III.3.3.

By assuming weak input fields, we ensure low excited atoms which allows us to apply the MM. Firstly, we solve the equations of motion of Eq. (III.2.7) for a single cavity system ($N = 1$), for different values of the laser detuning $\Delta_1 = \Delta$. Using the input output relation, see Eq. (III.2.8), we obtain $\langle a_{out,sc} \rangle$ and $\langle b_{out,sc} \rangle$. In order to calculate

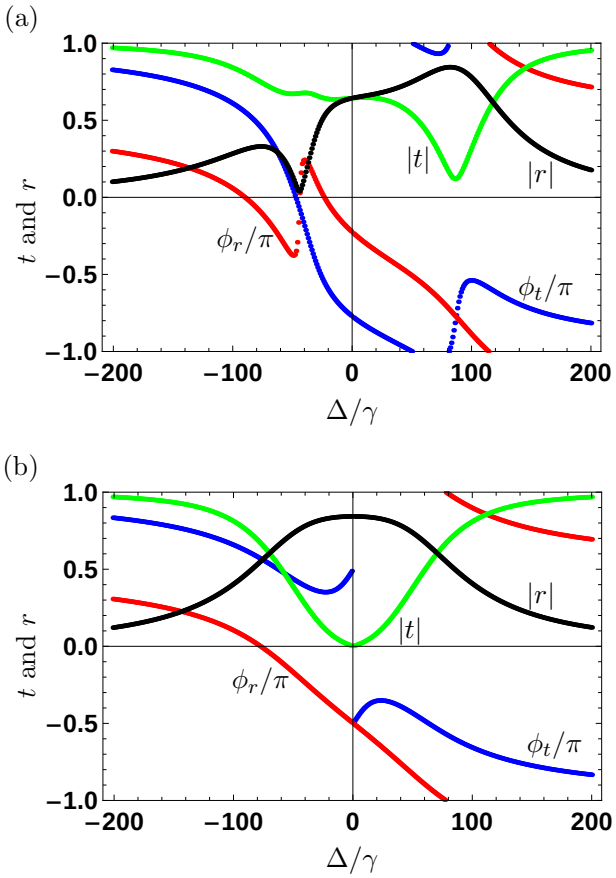

Figure III.2.: Absolute values $|t|$ and $|r|$ and phases ϕ_t and ϕ_r of the complex transmittivity $t(\Delta)$ and reflectivity $r(\Delta)$ for a single subsystem with $h = 50\gamma$ and $g_{\mathcal{A}} = 0$. (a) $g_{\mathcal{B}} = 70\gamma$ and atom far from saturation. (b) no nearby atom, i.e., $g_{\mathcal{B}} = 0$.

the parameters t and r, we solve the following equation system

$$\begin{aligned} \langle a_{out,sc} \rangle &= t \cdot a_{in,sc} + r \cdot b_{in,sc} \\ \langle b_{out,sc} \rangle &= r \cdot a_{in,sc} + t \cdot b_{in,sc} \end{aligned} \tag{III.3.15}$$

for weak input field amplitudes $a_{in,sc} \neq b_{in,sc}$.

Then, t and r read

$$\begin{aligned} t &= \frac{a_{in,sc}\langle a_{out,sc} \rangle - b_{in,sc}\langle b_{out,sc} \rangle}{a_{in,sc}^2 - b_{in,sc}^2} \\ r &= \frac{a_{in,sc}\langle b_{out,sc} \rangle - \langle a_{out,sc} \rangle b_{in,sc}}{a_{in,sc}^2 - b_{in,sc}^2} \,. \end{aligned} \tag{III.3.16}$$

From these equations we can see, that the denominator becomes zero if $a_{in,sc}^2 = b_{in,sc}^2$ and thus in such a case the system has no well-defined solution. For the special case of $b_{in,sc} = 0$ the transmission of a single cavity-atom system is given by

$$T_{sc} = |t|^2 \,. \tag{III.3.17}$$

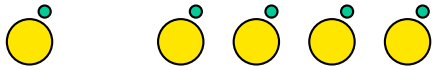

The coefficients t and r strongly depend on the probe laser detuning. Consequently, we have to calculate these parameters for each detuning Δ_n separately by solving the single cavity problem as described above. Using the result of Eq. (III.3.16), we can describe each cavity-atom system in the chain by two parameters t_n and r_n with $n \in \{1, .., N\}$. Fig. III.2. shows two examples for $t(\Delta)$ and $r(\Delta)$ where we choose $h = 50\gamma$ and $g_{\mathcal{B}} = 70\gamma$. For the data of the upper subfigure the atom is only low excited whereas the lower graph shows the coefficients for the case without atom ($g_{\mathcal{B}} = 0$).

In the following, we are especially interested in the regime, where the atom is far from saturation and thus the matrix method is applicable. In this parameter regime, we additionally calculated our results for short chains, e.g., $N = 2$, using the NC method and we obtained the same results as for the MM method, see Sec. III.3.3.

III.3.2.2. Coupling matrix $\mathcal{M}_{total}$ for the coupled chain of N cavity-atom systems

We proceed by calculating the transmission T and reflection R for a chain of N cavity-atom systems using the parameters t and r for each single cavity of the chain.

Therefore, we describe each contributing system by a coupling matrix $\mathcal{M}_n$ which connects the input and output fluxes of a single cavity-atom subsystem. This means, if we know the input field amplitudes $a_{in,n}$ and $b_{in,n}$ as well as the coupling matrix $\mathcal{M}_n$, we can calculate the output field amplitudes $\langle a_{out,n}\rangle$ and $\langle b_{out,n}\rangle$.

Next, we calculate the matrix $\mathcal{M}_n$ and afterwards show how to couple the single systems to a chain and calculate the transmission and reflection of the whole chain. Using Eq. (III.3.15), we obtain $\mathcal{M}_n$ as follows

$$\mathcal{M}_n = \begin{pmatrix} \frac{t_n^2 - r_n^2}{t_n} & \frac{r_n}{t_n} \\ -\frac{r_n}{t_n} & \frac{1}{t_n} \end{pmatrix} . \tag{III.3.18}$$

With the matrix $\mathcal{M}_n$ the dependence of the output modes on the input fields for each cavity can be written as

$$\begin{pmatrix} \langle a_{out,n}\rangle \\ b_{in,n} \end{pmatrix} = \mathcal{M}_n \cdot \begin{pmatrix} a_{in,n} \\ \langle b_{out,n}\rangle \end{pmatrix} = \begin{pmatrix} \frac{t_n^2 - r_n^2}{t_n} & \frac{r_n}{t_n} \\ -\frac{r_n}{t_n} & \frac{1}{t_n} \end{pmatrix} \begin{pmatrix} a_{in,n} \\ \langle b_{out,n}\rangle \end{pmatrix} . \tag{III.3.19}$$

In order to take the optical path between neighboring cavities into account, we use the matrix

$$\mathcal{M}_{\phi,n} = \begin{pmatrix} e^{i\phi_n} & 0 \\ 0 & e^{-i\phi_n} \end{pmatrix} , \tag{III.3.20}$$

which connects the input and output field amplitudes according to

$$\begin{pmatrix} a_{in,n} \\ \langle b_{out,n}\rangle \end{pmatrix} = \mathcal{M}_{\phi,n} \cdot \begin{pmatrix} \langle a_{out,n-1}\rangle \\ b_{in,n-1} \end{pmatrix} . \tag{III.3.21}$$

Here, the phase angles ϕ_n are defined by the intercavity distances L_n as $\phi_n = kL_n = 2\pi\frac{L_n}{\lambda}$ where λ is the light wavelength.

The matrix $\mathcal{M}_{total}$, which describes our whole system and connects the input field amplitudes $a_{in,1}$ and $b_{in,N}$ with the output field amplitudes $\langle a_{out,N}\rangle$ and $\langle b_{out,1}\rangle$, can then be calculated according to

$$\mathcal{M}_{total} = \mathcal{M}_N \cdot \mathcal{M}_{\phi_{N-1}} \cdot \mathcal{M}_{N-1} \cdots \mathcal{M}_2 \cdot \mathcal{M}_{\phi_1} \cdot \mathcal{M}_1 \,. \tag{III.3.22}$$

Using this matrix the inputs and outputs of our system can be calculated according to

$$\begin{pmatrix} \langle a_{out,N}\rangle \\ b_{in,N} \end{pmatrix} = \mathcal{M}_{total} \cdot \begin{pmatrix} a_{in,1} \\ \langle b_{out,1}\rangle \end{pmatrix} \,. \tag{III.3.23}$$

III.3.2.3. Calculation of atomic and photonic populations of subsystem n

So far, we can calculate the transmission T and reflection R of a chain of cavity-atom systems via the coupling matrix $\mathcal{M}_{total}$. However, we are also interested in the mean values of mode and atomic operators as well as atomic and cavity mode populations of each single atom-cavity system belonging to our coupled chain. Using the equations derived in the preceding section, we explain a step by step calculation of these observables for every element of the chain. We have to solve the equations of motion for each single cavity n in order to obtain the expectation values of the mode operators $\{\mathcal{A}_n, \mathcal{B}_n\}$ as well as the atomic operators $\mathcal{S}_n^{\pm}$. In order to solve this equation system for subsystem n, we need to know the input field amplitudes $a_{in,n}$ and $b_{in,n}$. We can calculate these input fields step by step beginning at one end of the chain, e.g., with $n = 1$. Then, $a_{in,1}$ is given since it is the input field amplitude of the whole chain. Since also $\langle b_{out,1}\rangle$ is given from Eq. (III.3.23), $\langle a_{out,1}\rangle$ and $b_{in,1}$ can be determined using Eq. (III.3.19). We can solve the equations of motion Eq. (III.2.7) for the single cavity-atom system $n = 1$ with the help of these input field amplitudes. Via $\mathcal{M}_{\phi,1}$ the field amplitudes $a_{in,2}$ and $\langle b_{out,2}\rangle$ can be calculated and therewith the equations of motion for subsystem 2 can be solved. We obtain the observables for all subsystems of the chain by iterating this procedure up to subsystem N.

III.3.3. Comparison of the two methods

In this section, we compare the two calculation methods introduced in the two preceding sections and discuss their advantages and drawbacks. If we directly solve the equations of motion numerically, as done for the NC method, we solve the equation system of Eq. (III.2.7) and determine the steady state solution by numerical integration. If the input field is too weak the calculation becomes longer and longer since the system takes more time to reach the steady state. Additionally, in case of very long chains (large N), the equation system to be solved includes a large number of equations, namely $8N$ equations if we consider real and imaginary part separately. In particular the recursively calculated complicated terms for the input field amplitudes (see Eq. (III.2.9)) cause long calculation times. Therefore, for $N > 3$ or 4 the NC method is not efficient. For this reason, we use the MM for larger N to calculate T and R. However, this method requires some restrictions on the input field amplitudes. We found that the transmittivity and reflectivity of a single atom-cavity system are only constant for a fixed detuning if the atom is either very low excited or no atom is present, i.e., $g_{\mathcal{A}_n} = g_{\mathcal{B}_n} = 0$. In general, an atomic state between saturation $\mathscr{P}_{2,n} = 0.5$ and low excitation $\mathscr{P}_{2,n} \approx 0$ is reached in

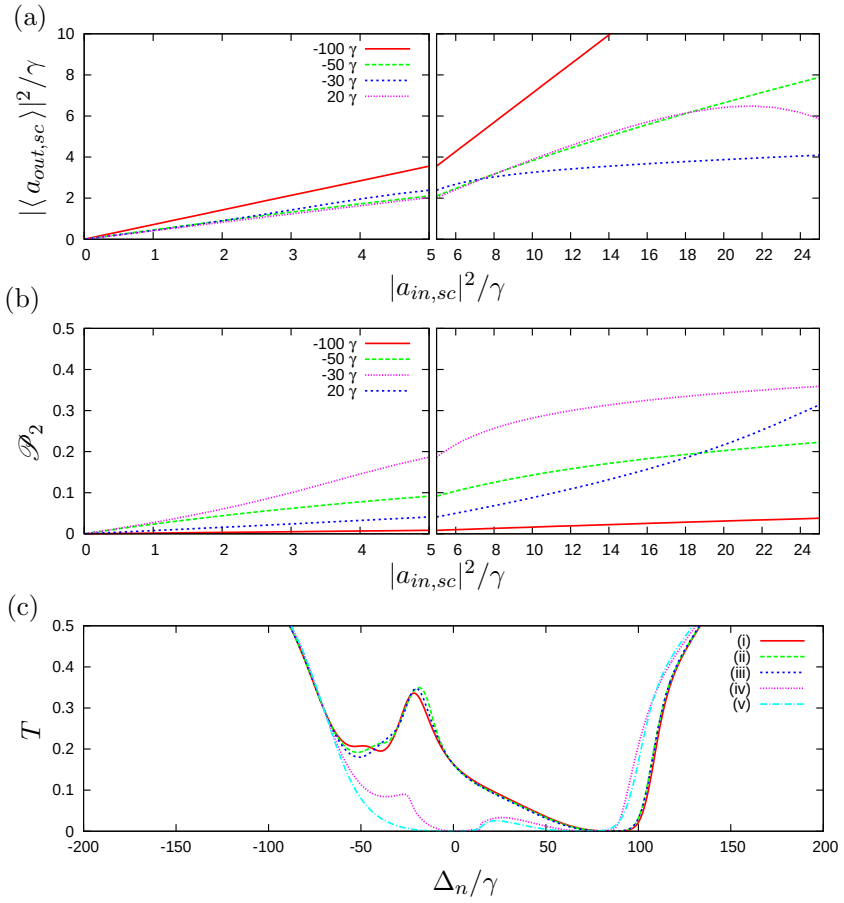

Figure III.3.: Comparison and validity range of the two calculation methods NC and MM. Subfigure (a) shows the output flux in transmission direction of a single atom-cavity system dependent on the input flux for fixed detunings $\Delta_n = -100\gamma$, $\Delta_n = -50\gamma$, $\Delta_n = -30\gamma$, and $\Delta_n = 20\gamma$. In (b) the population of the atom's upper state in a single atom-cavity system is depicted for the same detunings. Subfigure (c) shows results for the transmission T for both the calculation methods in case of $N = 2$. (i) weak input field $|a_{in,sc}|^2/\gamma < 1$ where T is identical for the two calculation methods, (ii) NC method and $|a_{in,sc}|^2/\gamma = 3$, (iii) MM and $|a_{in,sc}|^2/\gamma = 3$, (iv) NC and $|a_{in,sc}|^2/\gamma = 25$, and (v) MM and $|a_{in,sc}|^2/\gamma = 25$.

the steady state and thus the coefficients t and r strongly depend on the respective input fluxes of each system n. However, for weak input fields, the steady state population of the upper state is very low. For our calculations, the values for the input fields are chosen such that all atoms are far from saturation where t and r are independent of the input field amplitudes. Since for our numerical results we assume the atoms couple to mode $\mathcal{B}_n$ only and $g_{\mathcal{A}_n} = 0$, the value $|a_{in,n} - b_{in,n}|^2/2$ has to be much smaller than $g_{\mathcal{B}_n}$,k_n and h_n in order to ensure that the atom near cavity n is only low excited.

Applying the NC method, we obtain not only the transmission T and the reflection R as solution but also the quantities describing each subsystem, e.g., the populations of the N atoms and the photonic mode populations of all cavities. These quantities can also be calculated via the MM method by solving N times the equations for a single cavity

as described in Sec. III.3.2. For long chains this is also a time consuming calculation, yet still faster than the NC method. For parameter regimes where both the methods are valid, i.e., for short chains where all atoms are far from saturation or no atoms are present, we verified that the respective results are indistinguishable. In Fig. III.3. this linear response for weak input fields and the nonlinear behavior for stronger input fields is depicted. Fig. III.3.(a) shows the output flux of a single cavity for fixed laser detunings $\Delta_n = -100\gamma$, $\Delta_n = -50\gamma$, $\Delta_n = -30\gamma$, and $\Delta_n = 20\gamma$ dependent on the only input flux $|a_{in,sc}|^2$, $b_{in,sc}$ is set to zero. We observe that the output flux $|\langle a_{out,sc}\rangle|^2$ increases linearly with the input flux for small $|a_{in,sc}|^2/\gamma < 3$. The slope of these straight lines is equal to the transmission of a single atom-cavity system T_{sc}. For stronger input fields, however, the functions become nonlinear, as shown in the right subfigure. In order to understand this, in Fig. III.3.(b) we plotted the atomic upper state population $\mathscr{P}_2$ which increases linearly for small input fluxes. In the parameter region, where the atomic excitation increases linearly with the input field amplitude, the matrix description models our system very well and therefore both the methods lead to the same results for our observables. Fig. III.3.(c) shows results for the transmission T obtained from both the calculation methods, NC and MM: curve (i) shows the transmission for a weak input field ($|a_{in,sc}|^2/\gamma < 1$) where both the methods are applicable. Comparing the curves obtained from the NC method (ii) and the MM (iii) for $|a_{in,sc}|^2/\gamma = 3$, slight differences for some detunings are already visible. For larger inputs $|a_{in,sc}|^2/\gamma = 25$ as chosen for the calculation of curve (iv) and (v), as expected, the results obtained from the two methods differ considerably.

The two calculation methods presented here allow the calculations of the transmission and reflection as well as the photonic and atomic populations. In an experiment, however, higher order photon correlations can also be of relevance, e.g., for building non-classical light sources or photon turnstile devices. The complexity of our system increases very fast with the number of subsystems. If we, e.g., consider Fock states with up to one photon per mode in each subsystem, we obtain 8^N states and $(8^N)^2$ density matrix elements. In order to calculate second order correlations or cross correlations we would have to take at least two photons per mode in each cavity into account. We checked for a single cavity coupled to a nearby two-level atom that two excitations in the whole system are not enough to calculate second order correlations but two photons per mode are necessary. This would lead to 18^N states and $(18^N)^2$ density matrix elements. For example, already for $N = 2$ this would require to solve a system of more than 100 000 equations.

III.3.4. General considerations

III.3.4.1. Mirror interpretation approach

In this section, we do a little gedankenexperiment. Since each of our cavity-atom subsystems is described by its properties t_n and r_n, it can also be pictured as a mirror with reflectivity r_n and transmittivity t_n with $\{r_n, t_n\} \in \mathbb{C}^2$. This simple picture is shown in Fig. III.4. In the following, we use this picture in order to consider certain pathways and their interference behavior in detail. Conditions for constructive interference for leading order pathways are derived. Here, we focus on pathways possible for $a_{in,1}$ light, since in our numerical calculations we set $b_{in,N} = 0$.

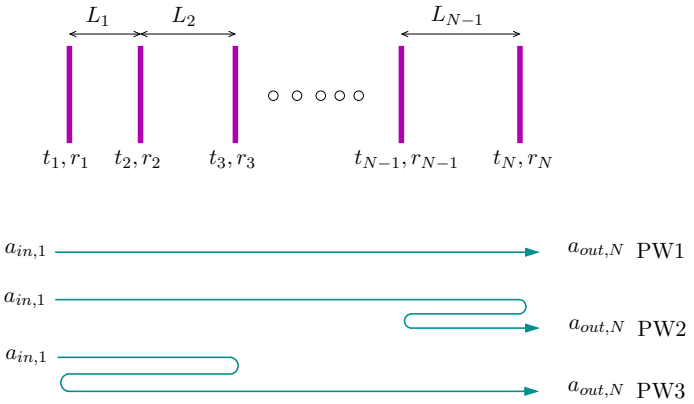

Figure III.4.: Mirror interpretation of the coupled atom-cavity chain and possible pathways for $a_{in,1}$ light.

III.3.4.2. Pathways and interference considerations

We now look at intensity contributions and their phases originating from different pathways contributing to the output fluxes. As shown in Fig. III.4. light can take various different pathways before leaving the system and contributing to either the transmission or reflection signal. First, we consider pathways contributing to the transmission T and thus to the output flux $|\langle a_{N,out}\rangle|^2$. To obtain a high transmission intensity, constructive interference of contributions originating from different pathways is favorable. In this section, we analyze the importance and the interplay of these pathways and their interference behavior. We focus on the pathways contributing to the output flux in transmission direction, in particular since they are of relevance for the superness ΔT defined in Sec. III.2.3.2.

As the simplest possible pathway, light can be transmitted by all N cavities and leave the system as $a_{out,N}$ light. This contribution can be calculated from the input flux $a_{in,1}$ as

$$a_{N,PW1} = a_{in,1} \cdot t_1 \cdot t_2 \cdots t_N \cdot e^{i(\phi_1+\phi_2+\cdots+\phi_N)} = a_{in,1} \prod_{n=1}^{N} t_n \, e^{i\phi_n} \, . \qquad \text{(III.3.24)}$$

However, since backward fluxes in b direction between the cavities are possible in our chain, light can also propagate on more complex pathways. For example, marked in Fig. III.4. as PW2, light can be transmitted by all cavities except the last cavity N where it is reflected back to cavity $N-1$, reflected at cavity $N-1$, then transmitted by cavity N and finally contributes to the output flux $|\langle a_{out,N}\rangle|^2$. The contribution to the transmission arising from this pathway reads

$$a_{N,PW2} = a_{N,PW1} \cdot r_N \cdot r_{N-1} \cdot e^{2i\phi_{N-1}} \, . \qquad \text{(III.3.25)}$$

In order to obtain a high output transmission, it is favorable that contributions arising from different pathways interfere constructively. By definition, constructive interference occurs if the phases of the different terms are equal. For example, contributions from PW1 (III.3.24) and PW2 (III.3.25) interfere constructively if the condition

$$\phi_{r_N} + \phi_{r_{N-1}} + 2\phi_{N-1} = m \cdot 2\pi \, , \qquad \text{(III.3.26)}$$

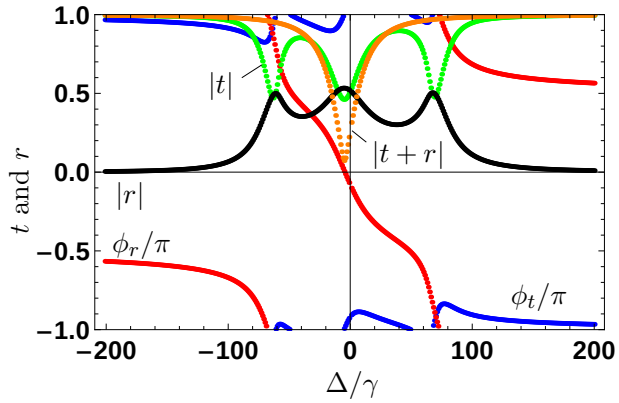

Figure III.5.: Absolute values $|t|$ and $|r|$ and phases ϕ_t and ϕ_r of the complex transmittivity t and reflectivity r for a single subsystem with $h = 5\gamma$ and $g_{\mathcal{B}} = 70\gamma$.

where $m \in \mathbb{Z}$, is fulfilled. Furthermore, especially for longer chains, light can propagate on a variety of other pathways. One more example is shown in Fig. III.4. denoted by PW3. Here, light moves back and forth not only between direct neighbors but between second neighbors. For a $N = 3$ chain, the respective contribution to the transmission signal is

$$a_{N,PW3} = a_{N,PW1} \cdot r_3 \cdot t_2 \cdot r_1 \cdot t_2 \cdot e^{2i(\phi_1+\phi_2)} \,. \tag{III.3.27}$$

PW3 interferes constructively with PW1 if the phase angles satisfy the condition

$$\phi_{r_3} + 2\phi_{t_2} + \phi_{r_1} + 2\phi_1 + 2\phi_2 = m \cdot 2\pi \,. \tag{III.3.28}$$

Note that m is an arbitrary integer which is not fixed but can have different values for the different interference conditions. Regarding Eqs. (III.3.24), (III.3.25), and (III.3.27) we can also see, that for all contributions to T the order of the cavities in the chain has no influence as long as the input flux $b_{in,N} = 0$. This is caused by the commutative law and can also be proven by the definition of the coupling matrix $\mathcal{M}_{total}$ of Eqs. (III.3.22) and (III.3.23). As we will see later in our results, this is particularly interesting for asymmetric systems. For example, for an $N = 2$ chain, whether an atom is only at cavity 1 and cavity 2 has no nearby atom or only at cavity 2 and cavity 1 is without atom results in equal transmissions, however, different reflections, see Sec. III.4.2.2. The reason why the reflection crucially depends on the arrangement of the cavities in the chain is, that not all cavities have an influence on all light pathways that contribute to the reflection. For example, in a system of two cavities, light of mode $a_{in,1}$ can be reflected at cavity 1 and thus never reaches cavity 2. Since pathways where the input light does not reach all cavities of the chain strongly contribute to the reflected output flux, exchanging the positions of the cavities within the chain in general leads to completely different reflections.

III.4. Results

For the numerical results presented here, we assume the resonance frequencies of the resonators to be equal to the transition frequencies of their nearby atom which results in $\Delta_n = \delta_n$ and additionally set the detunings for all cavities identical $\Delta_n = \Delta$. We assume

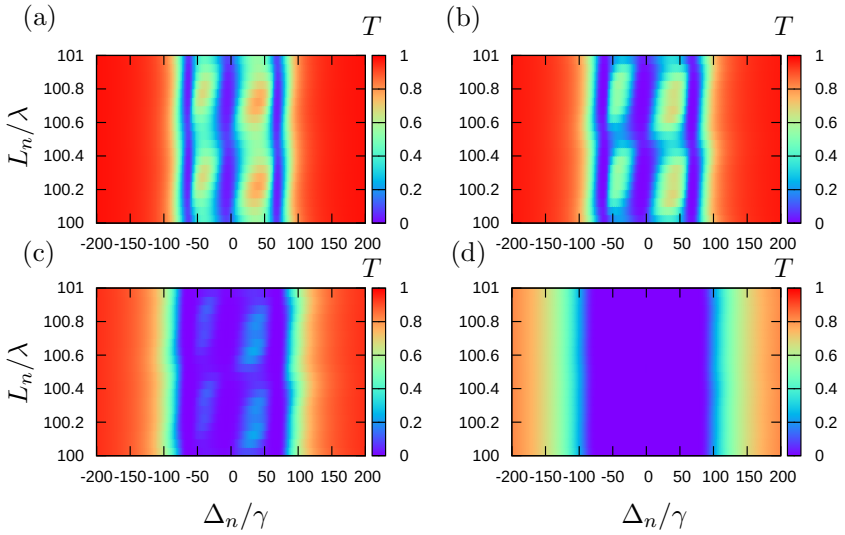

Figure III.6.: Transmission T for different N for $h = 5\gamma$ and $g_{\mathcal{B}} = 70\gamma$ dependent on the distance L_n. In (a) $N = 2$, (b) $N = 3$, (c) $N = 6$ and (d) $N = 20$. The resolution in L_n direction is 0.05λ.

equal decay rates for the atoms $\gamma_{\parallel,n} = \gamma$ and neglect dephasing $\gamma_{p,n} = 0$. We apply input fields in transmission direction $a_{in,1}$ and set $b_{in,N} = 0$. The decay rates for both the normal modes inside one cavity are assumed to be identical, i.e., $\kappa_{\mathcal{A}_n} = \kappa_{\mathcal{B}_n} = \kappa_n$ and we choose the internal decay rates $\kappa_{i,n} = \gamma$. For the coupling of the fiber we assume the critical coupling condition $\kappa_{ex,n} = \sqrt{\kappa_{i,n}^2 + h_n^2}$ to be fulfilled. Furthermore, we assume the atoms to couple to mode $\mathcal{B}_n$ and thus set $g_{\mathcal{A}_n} = 0$.

In Sec. III.4.1. we start with symmetric systems, i.e., all N subsystems are identical and arranged equidistantly, separated by intercavity distances $L_n = L$. For a better comparability of the values of the phase angles ϕ_n, introduced in Sec. III.3.2. to take into account the optical path between the subsystems, we generally write the respective numbers modulo 2π since this has no influence on the results. We study the transmission and reflection behavior in dependence on the chain length and show that the presence of supermodes becomes more important with increasing chain lengths. We proceed in Sec. III.4.2. by considering asymmetric chains of cavity-atom subsystems. First, we analyze the occurrence of supermodes for different intercavity distances L_n in Sec. III.4.2.1. in terms of pathway interference. Second, in Sec. III.4.2.2. we investigate chains of subsystems with different atomic coupling strengths $g_{\mathcal{B}_n}$. We show that the reflection signal can be exploited to detect which of the cavities couple to nearby atoms. Third, we consider chains consisting of subsystems with different intracavity scattering rates h_n in Sec. III.4.2.3. This is of relevance for experiments, since the fabrication of exactly identical cavities with radii in the size of μm in the optical regime is challenging.

III.4.1. Symmetric chains: dependence on the chain length N

We start with our results for the transmission T, the reflection R as well as the superness ΔT for chains of different lengths N, assuming equal intercavity distances $L_n = L$ leading to phase angles $\phi_n = \phi_L$. Furthermore, the N subsystems are identical, i.e.,

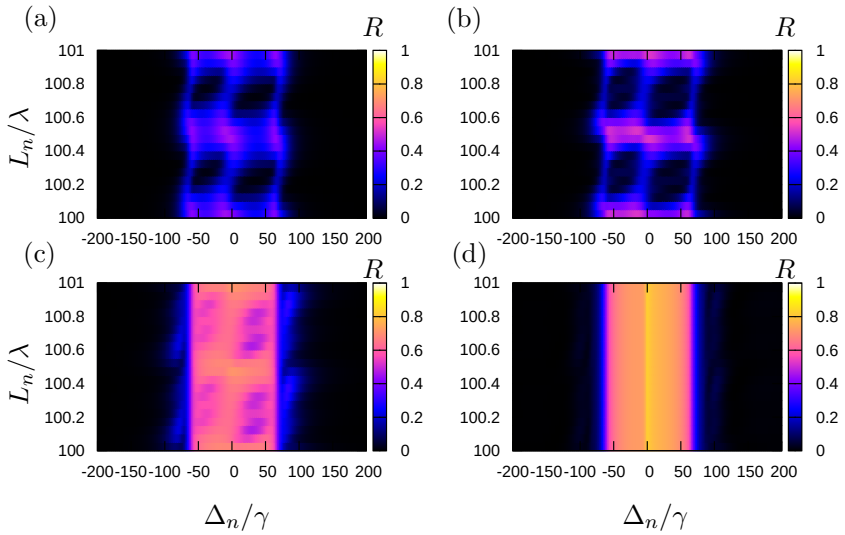

Figure III.7.: Reflection R for different N for $h = 5\gamma$ and $g_{\mathcal{B}} = 70\gamma$ in dependence on the distance L_n. In (a) $N = 2$, (b) $N = 3$, (c) $N = 6$ and (d) $N = 20$.

$\kappa_{ex,n} = \kappa_{ex}$, $g_{\mathcal{B}_n} = g_{\mathcal{B}}$ and $h_n = h$. Throughout this section we set $g_{\mathcal{B}_n} = 70\gamma$ which is a realistic value also found in experiments [99, 105].

III.4.1.1. Transmission T, reflection R, and superness ΔT for scattering rate $h = 5\gamma$

We consider a chain of N cavities coupled to nearby atoms with an intracavity scattering rate of $h = 5\gamma$. This corresponds to the strong coupling regime, where the atomic coupling is much stronger than the intermodal coupling inside one cavity, see also Sec. II.4.1. Here, we choose the strong coupling case, since in this regime the structures of our observables can be explained straightforward by an eigenvalue analysis. The absolute values as well as the phases of t and r are plotted in Fig. III.5. We first explain the structure of $|t|$ which (via $T_{sc} = |t|^2$) defines the transmission of a single subsystem of the chain. $|t|$ has three dips with positions at $\Delta_n = -5\gamma$, $\Delta_n = -67\gamma$ and $\Delta_n = 72\gamma$. The central dip at -5γ is the position of the non-coupling mode $\mathcal{A}_n$ as also identified in Sec. II.4.1. The two sideband peaks are at the eigenvalues of the coupled system $\frac{1}{2}(h + \sqrt{4g_{\mathcal{B}}^2 + h^2})$ and $-\frac{1}{2}(-h + \sqrt{4g_{\mathcal{B}}^2 + h^2})$, see also [99, 105].

Fig. III.6. shows the transmission T for $N = 2$, 3, 6 and 20 cavity-atom systems. As expected, the transmission is nearly one for far detuned probe fields in all four plots, since almost no light enters the cavity-atom subsystems. In Fig. III.7. we show the results for the reflection for the same parameters. In general, for parameters where the transmission is high, the reflection is minimum. In the following, we start by analyzing the results for $N = 2$, then consider $N = 3$, and finally discuss the findings for longer chains with $N = 6$ and $N = 20$.

Regarding Fig. III.6.(a) for $N = 2$ at $L_n = 100.0\lambda$, we can clearly see the three dips analogous to the transmittivity t plotted in Fig. III.5. However, these dips change their positions for different distances L_n. This effect is caused by interference, explained in

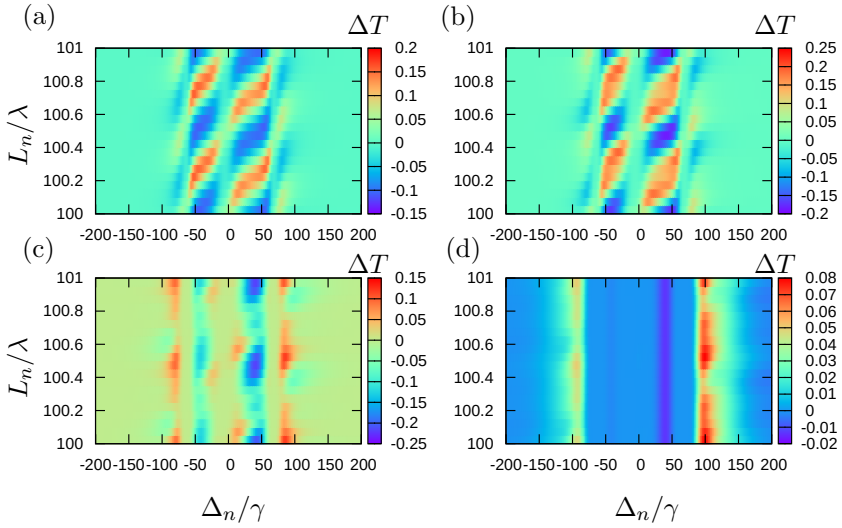

Figure III.8.: Superness ΔT for different N for $h = 5\gamma$ in dependence on the distance $L_n = L$ (same parameters as in Fig. III.6. and III.7.). In (a) $N = 2$, (b) $N = 3$, (c) $N = 6$ and (d) $N = 20$. Note that the color range is chosen differently for each subfigure and appropriate to the respective values of ΔT.

the following. For a chain of two cavity-atom systems, entering light can take the simple pathway, where it is transmitted by both the cavities. On the other hand, it can take loop pathways such as PW2 shown in Fig. III.4. and explained in Sec. III.3.4. The pathways PW1 and PW2 interfere constructively if the condition given in Eq. (III.3.26) is fulfilled. Since we assume equidistant and identical cavity-atom systems, this condition simplifies to

$$\phi_r + \phi_L = m \cdot \pi \,. \tag{III.4.29}$$

For example, for $L_n = 100.0\lambda$, which leads to a multiple of 2π for the phases $\phi_n = \phi_L$ and thus can be considered as $\phi_n = 0$, the condition (III.4.29) is satisfied for $\phi_r = m \cdot \pi$. We see from Fig. III.5. that this is approximately fulfilled at $\Delta_n = -68\gamma$, $\Delta_n = -5\gamma$, and $\Delta_n = 72\gamma$ which are the eigenvalues of a single atom-cavity system and thus the detunings where we obtain minima in the transmission of a single coupled system. Even though the different contributions interfere constructively, since their intensities are low, the result is a minimum output flux in transmission direction. Here, minima in the transmission for a single subsystem cause minima in the transmission for the coupled chain of two systems. However, although we obtain minima in the transmission of the coupled chain, Fig. III.8. shows, that the superness ΔT is not zero but shows minor maxima for these probe field detunings. The reason for these minor maxima is the constructive interference of the two pathways PW1 and PW2. Besides these two first order pathways, incoming light can also take more than one loop between the two subsystems. The intensities of these higher order pathways are not negligible but they are lower than the intensities of PW1 and PW2 and thus most features of the transmission and the superness are dominated by contributions arising from PW1 and PW2. For the same detunings we observe maxima in the reflection shown in Fig. III.7. as expected.

Since the phases ϕ_t and ϕ_r depend strongly on the laser detuning, the condition for constructive interference is fulfilled for different detunings when increasing L. For $L_n =$

100.25λ ($\phi_L = \frac{\pi}{2}$) the condition for constructive interference Eq. (III.4.29) is fulfilled around $\Delta_n = \pm 45\gamma$ where $\phi_r = \pm\frac{\pi}{2}$, see Fig. III.5. Due to this constructive interference, the peaks in the transmission shown in Fig. III.6(a) are slightly moved to larger detunings as compared to the $L_n = 100.0\lambda$ case. Here, the interference condition Eq. (III.4.29) is fulfilled for probe field detunings where $|t|$ is maximum and therefore the transmission of the coupled chain as well as ΔT has particularly high values in the region around $\Delta_n = \pm 45\gamma$. However, the impact of this interference effect is much more important for ΔT. As shown in Fig. III.8.(a), for $\Delta_n = \pm 45\gamma$ the difference between a chain of independent cavities and coupled cavities is maximum. For large detunings $\Delta_n > 100\gamma$, the interference condition Eq. (III.4.29) of PW1 and PW2 is also fulfilled, however, here the transmission of a single system $T_{sc} \approx 1$ and therefore $\Delta T \approx 0$.

Now, we turn to a chain of three coupled cavity-atom systems. We consider the transmission T and the superness ΔT shown in Fig. III.6.(b) and III.8.(b), respectively. For $L_n = 100.0\lambda$ we observe minima in T and minor maxima in ΔT close to the positions of the eigenvalues of a single cavity-atom system. The explanations provided for the $N = 2$ case hold here, too. The peaks and dips of our observables remain approximately at the same position as for $N = 2$ and are only very slightly shifted. However, for certain distances $L_n \neq 100.0\lambda$ some structures in the transmission, the reflection and the superness are more strongly affected by the coupling of a third cavity to the chain. Regarding the superness ΔT in Fig. III.8.(b), we can see, that, e.g., for $L_n = 100.15\lambda$ and $L_n = 100.3\lambda$ the major peak is shifted to larger detunings. The reason for this shift is that one more pathway and thus one more interference condition becomes important. For a chain of three coupled systems, also pathways as shown in Fig. III.4. as PW3 are possible. Here, incoming light propagates on a loop not between direct neighbor cavities but second neighbors. Since we assume three identical subsystems as well as equal distances, the condition for constructive interference of pathway PW2 and PW3 can be derived from Eq. (III.3.28) and Eq. (III.4.29) as

$$\phi_t + \phi_L = m \cdot \pi \,. \tag{III.4.30}$$

Hence, if the conditions of Eq. (III.3.28) and Eq. (III.4.29) are fulfilled, then all three pathways PW1, PW2 and PW3 interfere constructively if additionally the condition of Eq. (III.4.30) is satisfied. Eq. (III.3.28) and Eq. (III.4.29) can only be satisfied at the same time if $\phi_r - \phi_t = m \cdot \pi$. This holds for the detunings $\Delta_n = -68\gamma$, $\Delta_n = -5\gamma$, and $\Delta_n = 72\gamma$ which are again the detunings corresponding to the eigenvalues of a single subsystem. For constructive interference between all three described pathways, the condition given in Eq. (III.4.30) has to be fulfilled at the same time. For example, if the detuning is $\Delta_n = -68\gamma$ the phases of the t and r are $\phi_t = \phi_r \approx 0.9\pi$. This means, condition Eq. (III.4.30) is fulfilled for $\phi_L = 0.1\pi \mathrel{\widehat{=}} L_n = 100.2\lambda$. At these detunings $|t|$ is minimum and even though constructive interference is achieved, we observe minimum transmissions at these points in Fig. III.6.(b). This is the same effect observed for the $N = 2$ chain in Fig. III.6.(a). However, as it can be seen from Fig. III.8.(b), partly constructive interference of pathway PW3 with PW1 and PW2 shifts the peak in ΔT to higher detunings for the respective distances, where Eq. (III.3.25), Eq. (III.3.28) and/or Eq. (III.4.30) are satisfied, as compared to the $L_n = 100.0\lambda$ case. For example, considering the detuning $\Delta_n = 50\gamma$, $L_n = 100.0\lambda$ leads to a minimum in ΔT whereas $L_n = 100.3\lambda$ leads to a global maximum in the superness for this intercavity distance, see Fig. III.8.(b). Regarding Fig. III.5., for this detuning $\phi_t - \phi_r \approx \frac{\pi}{2}$ leads to constructive

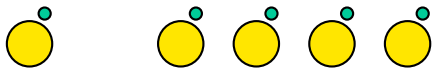

interference of PW2 and PW3, however, destructive interference of PW1 with both PW2 and PW3. This results in a minimum in ΔT for $L_n = 100.0\lambda$. By contrast, for $L_n = 100.3\lambda$ ($\phi_L = 0.6\pi$) all three considered leading order pathways interfere partly constructively which finally results in maximum superness. Even though, increasing N generally leads to decreasing absolute ΔT for longer chains ($N > 5$), for the three cavity chain we obtain even higher ΔT values than for the $N = 2$ case for $L_n = 100.3\lambda$.

Now, we consider a long chain with many coupled cavity-atom systems, i.e., up to $N = 20$. For such a long chain a large variety of different pathways can be taken by light entering the system. In this limit of many coupled subsystems, the transmission almost vanishes in a large range of detunings around the resonance frequency whereas the reflection is almost one, see Fig. III.6.(c) and (d) and III.7.(c) and (d). For $N = 6$ the interference structure depending on the distance L is still visible. Yet, for an even longer chain such as $N = 20$ this structure almost vanishes. Since the reflectivity r has relatively low values for most of the detunings, namely $|r| < 0.5$, not only pathways where light is reflected at the front end of our chain contribute to the output mode $b_{out,1}$ in reflection direction but also pathways where light is reflected for the first time at a cavity with larger n cannot be neglected. That is why the reflection of $N = 6$ and $N = 20$ exhibit different structures. As depicted in Fig. III.8.(d) ΔT almost vanishes for a chain of $N = 20$ coupled elements. If the transmission T_{sc} of a single cavity-atom system is < 1, the transmission of a chain of N independent cavities is T_{sc}^N and hence approaches zero for large N. Also for a chain where backward fluxes are allowed, the transmission of the coupled system becomes very low for large N. This is the reason why also the transmission difference ΔT approaches zero for long chains. However, we found that the relative contribution of supermodes to the transmission $\frac{\Delta T}{T}$ increases with N and approaches 100% for long chains of $N = 20$ in the respective spectral range, where constructive interference of pathways occurs.

A detailed analysis of occurring supermodes for optimized parameters is presented in the next Sec. III.4.1.2. The formation of supermodes as well as their importance for the transmission in dependence on the geometry and the chain length are analyzed. Furthermore, in Sec. III.4.2.1. a distinct supermode in a system of three atom-cavity elements is explained in terms of pathway interference.

III.4.1.2. Transmission T, reflection R, and superness ΔT for scattering rate $h = 50\gamma$

In this section we consider a chain of cavity-atom systems with higher scattering rate inside the cavities, namely $h = 50\gamma$. This means, we are no longer in the strong coupling regime. Instead, the atomic coupling $g_{\mathcal{B}}$ and the coupling between photon modes within one WGM pair $\{a_n, b_n\}$ are of comparable magnitude. We choose this parameter regime since we found that they lead to very high superness ΔT. In Fig. III.9.(a) and (b) we show our results for T and ΔT for $N = 2$ coupled subsystems in dependence on the detuning Δ_n and the intercavity distance $L_n = L_1$. For T we observe a large region at $\Delta_n \in [0, 50\gamma]$ with mostly minimum transmission, yet for some values of L_1 maxima arise. These maxima can be explained by pathway interference similar to the $h = 5\gamma$ case. For the values of Δ_n and L_1, where we have maxima in T, also ΔT is maximum. For these specific parameters we obtain transmission differences as compared to a chain of independent atom-cavity systems up to $\Delta T > 0.4$. The reflection for $h = 50\gamma$ is

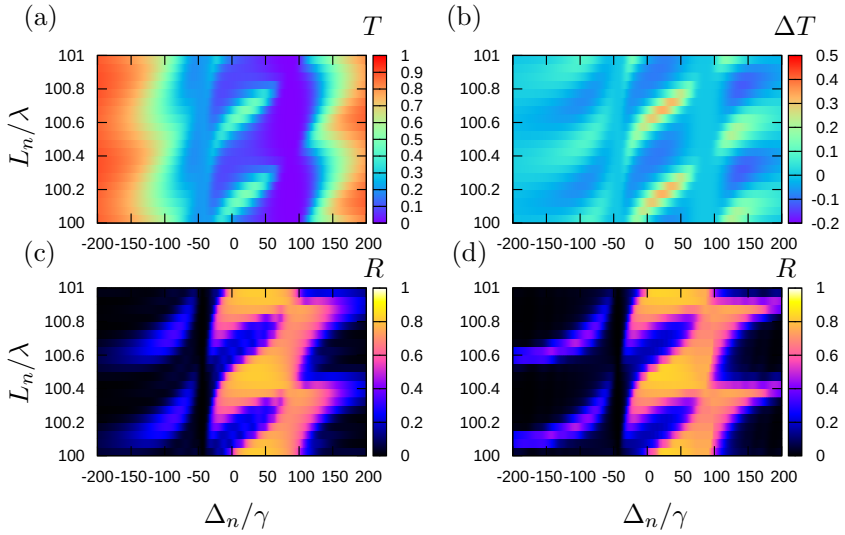

Figure III.9.: Transmission T, ΔT and R for different N for $h = 50\gamma$ and in dependence on the distance L_n. All further parameters are chosen as in Figs. III.6., III.7., and III.8. In (a) $N = 2$, (b) $N = 2$, (c) $N = 3$ and (d) $N = 20$. Different color scales are chosen for a better visibility of the significant features of the respective observables.

shown in the lower subfigures of Fig. III.9.(c) and (d). Here, we see that for $N = 3$ (c) and $N = 20$ (d) the structure of the reflection hardly changes. The reason is that only the first few cavities of the chain have a considerable impact on the reflection. This means that $b_{out,1}$ flux is dominated by light pathways where entering light is reflected at one of the first subsystems of the chain.

Next, we investigate the formation of supermodes and their influence on the system's dynamics in dependence on the intercavity distance L_n and the chain length N for optimized parameters with $h = 50\gamma$. We start with the $N = 2$ case. Fig. III.10. shows the superness ΔT for $N = 2$ and $L_n = 100.0\lambda$, 100.15λ, 100.2λ, 100.25λ, and 100.35λ. These curves are cuts at the respective intercavity distances of Fig. III.9.(b). We observe that for specific detunings the transmission behavior depends crucially on the intercavity distance whereas for other detunings the system behaves almost as a chain of independent cavity-atom systems ($\Delta T \approx 0$). In particular, at $\Delta_n \approx 95\gamma$ and $\Delta_n \approx -50\gamma$, the transmission of the full system is equal to the combination of the individual systems for all distances. This can be explained by noting that for these detunings, either $|t_n|$ (for $\Delta_n \approx 95\gamma$) or $|r_n|$ (for $\Delta_n \approx -50\gamma$) is small, see Fig. III.2.(a). In case of small $|r_n|$, the backcoupling between the cavities almost vanishes such that the system is similar to the uncoupled case. For $\Delta_n \approx -50\gamma$ we found that the population of the upper level of both the atoms is relatively high. Comparing Fig. III.2.(a) and (b), we observe that the presence of the atom suppresses the reflection which results in $|r_n| \approx 0$. For the small $|t_n|$ at $\Delta_n \approx 95\gamma$, the largest part of the incoming light is reflected at the first subsystem and thus the cavity modes and the excited state of the atom next to cavity two are hardly populated. The low transmittivity and reflectivity are achieved because the respective detunings correspond to the eigenvalues of the Hamiltonian for a single subsystem. In contrast, for other detunings, pronounced resonances in the "superness" ΔT can be observed at certain distances. These resonances exceed $\Delta T = 0.4$ for

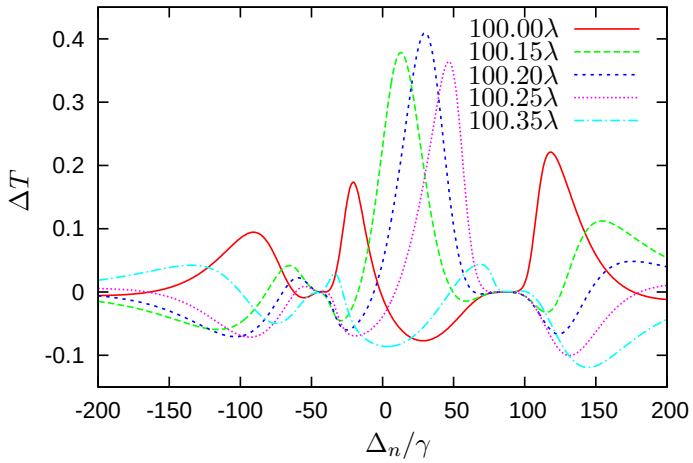

Figure III.10.: Formation of supermodes indicated by large modification ΔT of transmission compared to a chain of independent atom-cavity systems. Parameters are $N = 2$, $h_n = 50\gamma$, $g_{\mathcal{B}_n} = 70\gamma$, and intercavity distances $L_1 = 100.0\lambda$, $L_1 = 100.15\lambda$, $L_1 = 100.2\lambda$, $L_1 = 100.25\lambda$, and $L_1 = 100.35\lambda$.

optimum parameters, demonstrating clearly the relevance of the backscattering between the cavities. For these detunings $|t_n| \approx |r_n|$ and thus the energy exchange in both directions is enhanced. Interestingly, for the detunings with high ΔT, the modes $\mathcal{B}_n$ which couple to the atoms are hardly populated in both the cavities, whereas the non-coupling modes $\mathcal{A}_n$ are highly populated, demonstrating the significance of the non-coupling normal mode.

Next, we study the importance of supermodes in longer chains of atom-cavity systems. Since in case of $N = 2$ for $L_n = 100.2\lambda$ the supermode leads to maximum transmission enhancement, we consider this intercavity distance when investigating the dependence on the chain length from $N = 2$ up to $N = 20$ subsystems. This dependency of the supermode on the chain length identified in Fig. III.9.(b) and III.10. is shown in the left subfigure of Fig. III.11. For the highest peak in ΔT at $\Delta_n \approx 30\gamma$ we found that in absolute terms, the superness ΔT decreases with increasing N until it almost vanishes for $N = 20$. This reduction can be traced back to the overall reduction in transmission T for increasing N, since each resonator leads to a certain amount of loss and reflection. By contrast, the "relative superness" $\Delta T/T$ increases with N, as shown in the right panel of Fig. III.11. The reason is that the reduction in transmission becomes stronger with increasing N for independent resonators, such that eventually all relevant residual transmission must originate from an enhancement via constructive interference through the formation of a supermode.

III.4.2. Asymmetric chains

We present our results for different arrangements of asymmetric chains. We begin in Sec. III.4.2.1. with the consideration of a chain of $N = 3$ subsystems, however, we now allow different intercavity distances L_n. A detailed analysis of an occurring supermode is provided in terms of pathway interference. In Sec. III.4.2.2., $N = 2$ chains with different atomic coupling parameters $g_{\mathcal{B}_n}$ are studied. We find, that the reflection signal can be

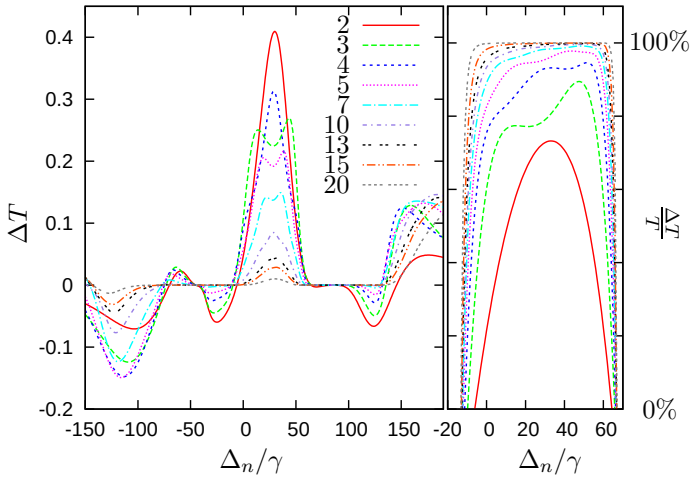

Figure III.11.: Dependence of the supermode contribution ΔT on the chain length N. The left panel shows the absolute "superness" ΔT, the right panel the relative value $\Delta T/T$. The parameters are as in Fig. III.6., with $L_n = 100.2\lambda$.

used to determine, which of the cavities couple to a nearby atom. This is important information in experiments where it can be difficult to achieve simultaneous coupling of atoms to all cavities of the chain. In Sec. III.4.2.3., we present our results for two cavity constellations where the intracavity scattering rates h_n are different for each resonator. This is of relevance in experiments, since it can be difficult to fabricate exactly identical resonators, especially for the optical wavelength regime, where the dimensions of such WGM resonators are in the order of μm. Rather, material imperfections and surface roughness differ at least slightly.

III.4.2.1. Supermode analysis for $N = 3$ with different intercavity distances L_n

We consider a chain of $N = 3$ subsystems and analyze the formation of a supermode in terms of pathway interference. This chain consists of three coupled subsystems where the distance between subsystem 1 and 3 is fixed ($L_{tot} = L_1 + L_2$) and the central cavity 2 is moved, which means the distances L_1 and $L_2 = L_{tot} - L_1$ are varied. We show, that only by moving this cavity-atom subsystem on a sub-wavelength scale, the transmission properties of the complete coupled chain change considerably.

In Fig. III.12., we show our results for the transmission T (a), the superness ΔT (b), the transmission of a single subsystem T_{sc} (c), and the reflection R (d) for the parameters $h_n = 50\gamma$ and $g_{\mathcal{B}_n} = 70\gamma$ for different positions of cavity 2, i.e., in dependence on L_1. Here, the total distance $L_{tot} = L_1 + L_2 = 200.3\lambda$. Additionally, the transmission for a single cavity-atom system is shown (c). Clear maxima in the superness can be observed in Fig. III.12.(b) around $\Delta_n = 25\gamma$ for certain distances L_1. For a better analysis of the supermode, in Fig. III.13. we show some curves for ΔT depending on the detuning Δ_n for $L_1 = 100.00\lambda$, $L_1 = 100.05\lambda$, $L_1 = 100.10\lambda$, and $L_1 = 100.15\lambda$. These curves are cuts at certain values of L_1 of Fig. III.12.(b). In this figure we observe that for some detunings the transmission difference ΔT depends strongly on the distance L_1, whereas for other detunings the superness of the coupled chain is almost independent of

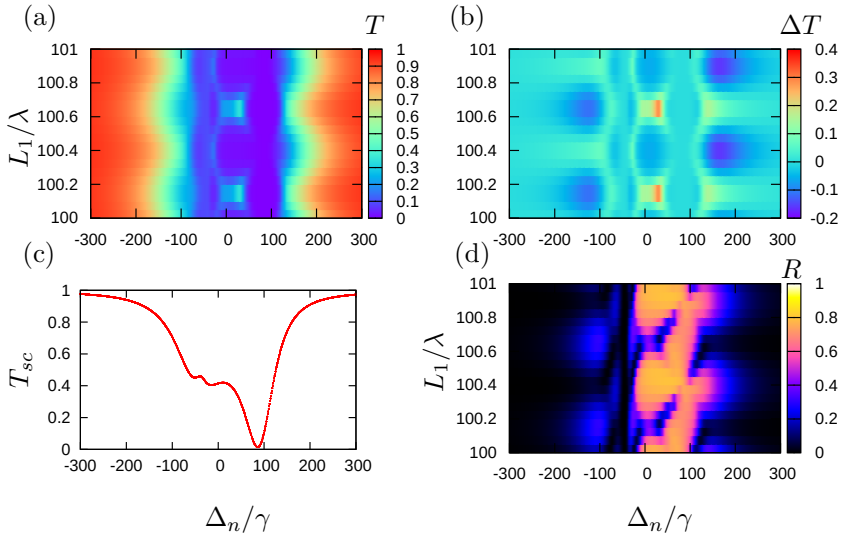

Figure III.12.: Observables for a $N = 3$ chain with $h_n = 50\gamma$, $g_{\mathcal{B}_n} = 70\gamma$ and $L_{tot} = L_1 + L_2 = 200.3\lambda$. These are the same parameters as for the supermode analysis for an $N = 2$ chain depicted in Fig. III.10. Curve (a) shows the transmission T, (b) the superness ΔT, (c) the transmission of a single subsystem T_{sc}, and (d) the reflection R.

the position of the middle cavity. For example, the peak structure around $\Delta_n = -80\gamma$ is only weakly influenced by a change of L_1. The impact of L_1 in the spectral region around $\Delta_n = -50\gamma$ and $\Delta_n = 80\gamma$ on ΔT is negligible. By contrast, the peak around $\Delta_n = 25\gamma$ is influenced crucially by a movement of cavity 2. While $\Delta T \approx 0$ for $L_1 = 100.0\lambda$ it approaches values up to almost 0.4 for $L_1 = 100.15\lambda$.

In the following, we analyze this high peak in ΔT around $\Delta_n = 25\gamma$ in terms of interference effects. The highest superness is reached for equal intercavity distances $L_1 = L_2 = 100.15\lambda$. For the explanation we use the transmittivity and reflectivity plotted in Fig. III.2.(a) and the pathways which were described in Sec. III.3.4. and depicted in Fig. III.4. We found in Sec. III.3.4. that loop pathways of PW2 kind interfere constructively with the simplest transmission pathway PW1 if the condition $\phi_r + \phi_L = m \cdot \pi$ (see Eq. (III.4.29)) is fulfilled. In order to interpret the high peak in ΔT by interference, in Fig. III.14. we plotted $\phi_r + \phi_L$ and the normalized absolute values of output field amplitudes in transmission direction originating from PW1 and PW2 $\frac{|a_{3,PW1}|}{|a_{in,1}|}$ and $\frac{|a_{3,PW2}|}{|a_{in,1}|}$, respectively, for $L_1 = 100.15\lambda$. In our chain consisting of three coupled subsystems two different loop pathways of PW2 kind are possible. Firstly, this loop can take place between cavity 1 and 2. Secondly, light can move back and forth between cavity 2 and 3. For $L_1 = L_2 = \frac{L_{tot}}{2} = 100.15\lambda$, the contributing fluxes arising from both these loop pathways are identical and denoted by $\frac{|a_{3,PW2}|}{|a_{in,1}|}$. In Fig. III.14. we see, that the condition for the phase angles given in Eq. (III.4.29) is fulfilled at $\Delta_n = -60\gamma$, $\Delta_n = -45\gamma$, and $\Delta_n = 15\gamma$ where $\phi_r + \phi_L = 0$ and $\Delta_n \approx 200\gamma$ where $\phi_r + \phi_L = \pi$. In the region around $\Delta_n = -45\gamma$ the output flux of PW2 is minimum. This means, that the light intensity which could interfere constructively with $a_{N,PW1}$ almost vanishes. For this reason the system here behaves similarly to a chain of independent atom-cavity systems and $\Delta T = 0$ for these detunings, see Fig. III.13. For the far detuned case of $\Delta_n = 200\gamma$, almost no

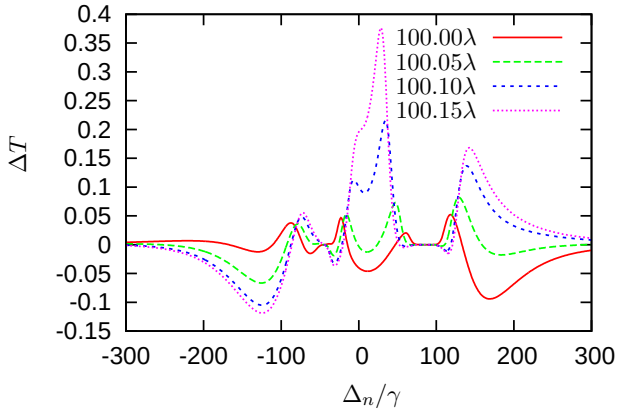

Figure III.13.: Formation of supermodes in a chain of $N = 3$ subsystems. The parameters are $h_n = 50\gamma$ and $g_{\mathcal{B}_n} = 70\gamma$ (as in Fig. III.12.), $L_{tot} = 200.3\lambda$ and $L_1 = 100.00\lambda$, 100.05λ, 100.10λ, and 100.15λ.

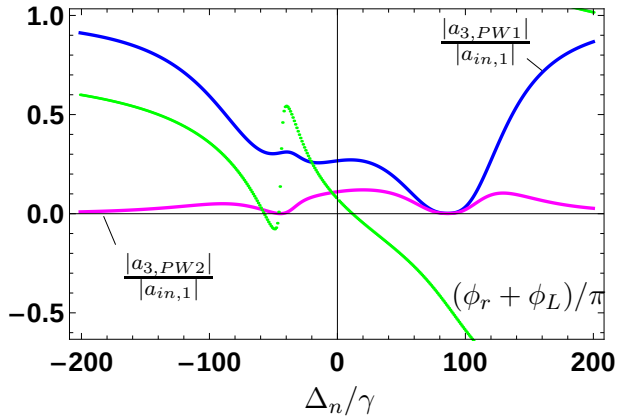

Figure III.14.: Contributions to the transmission T arising from the different pathways to explain interference effects $\phi_r + \phi_L$, $|a_{3,PW1}|$, and $|a_{3,PW2}|$ plotted for parameters as in Fig. III.13. and $L_1 = 100.15\lambda$.

light enters the system due to the large detuning and thus, as expected, the chain geometry has no crucial impact on the system's dynamics. For $\Delta_n = -60\gamma$ the contributing intensity of PW2 has small values but is different from zero. Thus constructive interference influences the superness and a minor peak in ΔT visible for this detuning and certain distances L_1. In case of $\Delta_n = 15\gamma$ the formation of a supermodes more dominantly governs the dynamics of the system. Here, the absolute values of both contributing output mode field amplitudes $a_{3,PW1}$ and $a_{3,PW2}$ have relatively high values.

Since light can also take higher order pathways such as shown in Fig. III.4. PW3 or multi-loops of PW2 kind, i.e. light moves back and forth more than once between two cavities, this interference description does not describe the whole system, although it explains the main structures of the transmission and the superness ΔT. For example, the contribution to the output flux in transmission direction arising from a double-loop pathways would read $a_{3,out} = a_{in,1} \cdot t_1 \cdot r_2 \cdot r_1 \cdot r_2 \cdot r_1 \cdot t_2 \cdot t_3 \cdot e^{6i\phi_L}$. In Fig. III.15. we show some curves for the superness when taking only these multi-loop pathways into account. We denote the respective transmission difference between the case of taking

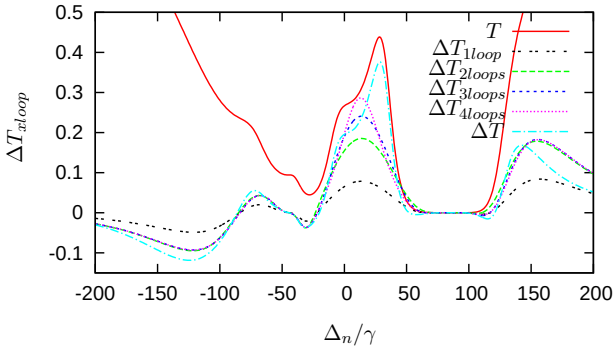

Figure III.15.: Superness for a reduced system ΔT_{xloops}, where certain pathways are artificially suppressed, for $L_{tot} = 200.3\lambda$, $N = 3$ and $L_1 = 100.15\lambda$. The further parameters are chosen as in Fig. III.13. and pathways with x loops between two cavities (PW2 kind) are taken into account.

x loops into account and the transmission of the independent chain by ΔT_{xloops}. Here, the x determines how many loops of PW2 kind within a pathway are taken into account. All these pathways interfere constructively if the condition of Eq. (III.4.29) is fulfilled for the phase angles. However, pathways as shown in Fig. III.4. as PW3 are omitted in the calculation of ΔT_{xloops}. For this reduced system, where certain pathways are artificially suppressed, we find that a symmetric peak in ΔT_{xloop} occurs at $\Delta_n = 15\gamma$. This is at the detuning, where constructive interference of the considered pathways occurs. For the complete system, however, we found that destructive interference with other pathways, e.g., PW3, leads to the shift of the main peak in ΔT and T to $\Delta_n = 25\gamma$ also shown in Fig. III.15.

In Fig. III.16. we show the populations of the atomic states for each of our three coupling atoms. We find that for distances L_1, where the superness ΔT is high at $\Delta_n = 25\gamma$, also the upper state population of the atom coupling to cavity 3 is maximum. This also shows that the atom plays a key role for the transmission properties and the formation of supermodes in our coupled chain system.

III.4.2.2. Chains of subsystems with different atomic couplings $g_{\mathcal{B}_n}$

We start studying chains with different atomic coupling strengths $g_{\mathcal{B}_n}$ by looking at systems where not all cavities within the chain are coupled to a nearby atom, i.e., $g_n = 0$ for certain subsystems n. We focus on $N = 2$ chains and assume two cavities with $h_n = 50\gamma$ as in the last section. In Fig. III.17. we show our results for the reflection R for (a) none of the two cavities has a nearby atom ($g_{\mathcal{B}_1} = g_{\mathcal{B}_2} = 0$), (b) the atom is close to the left cavity ($g_{\mathcal{B}_1} = 70\gamma$ and $g_{\mathcal{B}_2} = 0$), (c) $g_{\mathcal{B}_1} = 0$ and $g_{\mathcal{B}_2} = 70\gamma$, and (d) both the cavities have a nearby atom, i.e, $g_{\mathcal{B}_1} = g_{\mathcal{B}_2} = 70\gamma$. Here, we focus on the reflection since we found that the transmission is not dependent on whether the atom couples to cavity 1 or cavity 2. This is because light contributing to T has to pass both subsystems and thus parameters of both cavity-atom systems contribute no matter which cavity the atoms couple to, see also the mirror description in Sec. III.3.4. By contrast, the reflection is influenced crucially by the position of the atom. For example, if $\Delta_n = 0$ and the atom is located close to cavity 2, almost no light is transmitted from

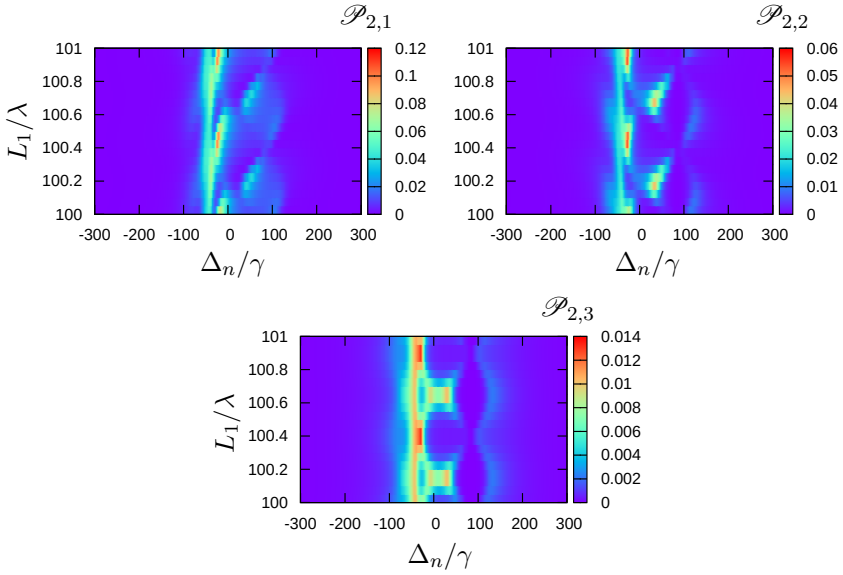

Figure III.16.: Atomic populations of the upper level $\mathscr{P}_{2,n}$ for the subsystems 1, 2 and 3. The parameters are chosen as in Fig. III.13. and $L_1 = 100.15\lambda$. Note that the color scale is chosen differently for the subfigures and appropriate to the respective values of the populations.

the first cavity, since $|t| \approx 0$, see Fig. III.2. Then almost no light enters cavity 2 and thus the dynamics of the coupled chain is nearly totally governed by subsystem 1. However, if the atom is located close to cavity 1, light can be transmitted for $\Delta_n = 0$ only at cavity 1 but not at cavity 2. This means for the reflection that pathways affected by the parameters describing subsystem 2 contribute as well. In an experiment, this feature could be used to determine whether a nearby atom couples to cavity 1 or cavity 2. This is of relevance for experiments where it is difficult to achieve simultaneous coupling of single atoms to all cavities of a chain, i.e., if falling clouds of atoms are used to achieve atom-cavity coupling [99, 100, 105]. As shown in Fig. III.17.(b), if the atom couples to cavity 1, a root in R can be observed at $\Delta_n \approx 37\gamma$. However, if the atom couples to cavity 2 (c), there is only a slight local minimum at this detuning. Furthermore, the cases with no nearby atom (a) or both cavities with atom (d) can be well distinguished from each other and from the two asymmetric cases by measuring the reflection intensity. For example, the root at $\Delta_n \approx -42\gamma$ is only visible if both cavities have a coupling atom (d). If none of the cavities has a nearby atom, even the slight dip in the reflection at $\Delta_n = 40\gamma$ vanishes (a). Concerning the transmission, if at least one subsystem has no nearby atom, the transmission is suppressed over a wide range of detunings around the resonance frequency. This is because $|t|$ in case of no nearby atom is very small in this spectral range, see Fig. III.2.(b). This leads to very small superness and therefore, chains with missing atoms at distinct subsystems are not favorable for the formation of supermodes.

In Fig. III.18. we show some results for different values of g_{B_n}, where the atomic coupling within one subsystem is much stronger than in the other subsystem. This situation can occur in an experiment, if the atom-cavity distances are not equal for the subsystems of the chain, e.g., if falling clouds of cold atoms are used to achieve atom-cavity coupling. In

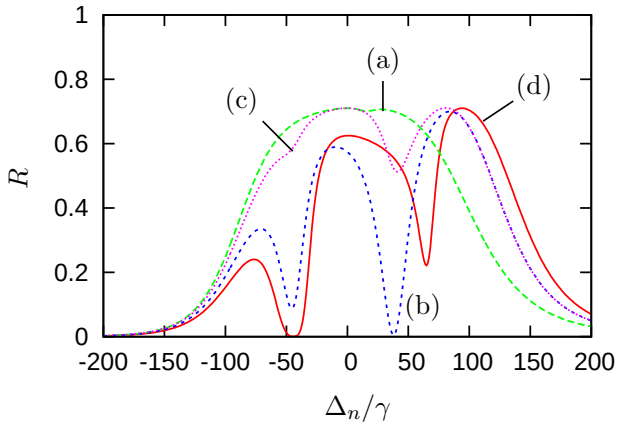

Figure III.17.: Reflection R for asymmetric constellations for $N = 2$ with $h_n = 50\gamma$. $L_1 = 100.3\lambda$. In curve (a) none of the two cavities has a nearby atom, i.e., $g_{\mathcal{B}_1} = g_{\mathcal{B}_2} = 0$, in (b) the atom is close to the left cavity, i.e., $g_{\mathcal{B}_1} = 70\gamma$ and $g_{\mathcal{B}_2} = 0$, in (c) $g_{\mathcal{B}_1} = 0$ and $g_{\mathcal{B}_2} = 70\gamma$ and in (d) both the cavities have a nearby atom, i.e., $g_{\mathcal{B}_1} = g_{\mathcal{B}_2} = 70\gamma$.

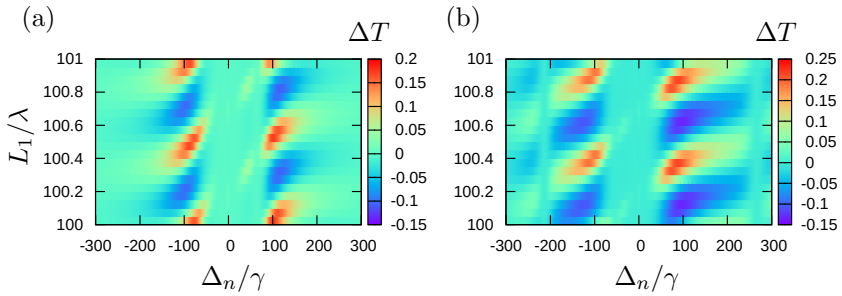

Figure III.18.: ΔT for a chain of two subsystems with different g_{B_n} for $h_n = 50\gamma$. In (a) $g_{B_1} = 5\gamma$ and $g_{B_2} = 50\gamma$ and in (b) $g_{B_1} = 5\gamma$ and $g_{B_2} = 250\gamma$.

Fig. III.18.(a) we choose $g_{B_1} = 5\gamma$ and $g_{B_2} = 50\gamma$ and in (b) $g_{B_1} = 5\gamma$ and $g_{B_2} = 250\gamma$. Interestingly, in both figures, periodic minima and maxima occur for $\Delta_n \approx 100\gamma$. This means, continuously varying the distance L_1 between the two cavities leads to periodic maxima and minima in ΔT.

III.4.2.3. Chains of subsystems with different scattering rates h_n

For an experiment, it can be difficult to fabricate microcavities of exactly identical surface roughness and imperfection rates. Since all these material properties enter the internal scattering rate h_n, here, we consider asymmetric chains of 2 cavities, whose intracavity scattering rates h_n are not equal. We found that the dependence on the value of h_n is not very sensitive. Quantitatively spoken this means the results for the transmission as well as for the reflection or ΔT for h_n and $h_n \pm 2\gamma$ are hardly distinguishable. We checked this for various values between $h_n = 5$ and $h_n = 250\gamma$. As our results do not sensitively depend on small changes in the scattering rate h_n, an experimental setup with slightly different resonators would lead to the same formation of supermodes in the system.

In Fig. III.19. we show our results for a larger difference of the two h_n values. In subfigure

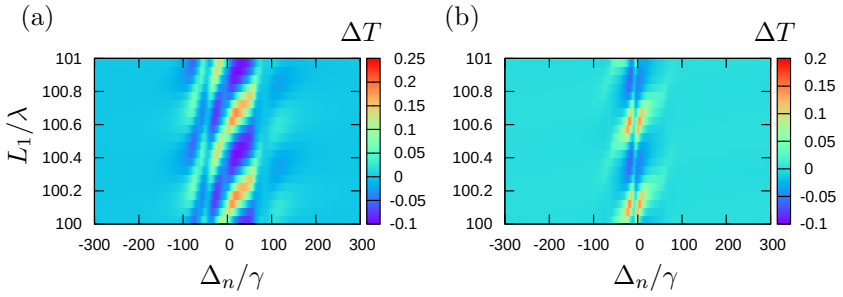

Figure III.19.: ΔT for asymmetric constellations for $N = 2$ with $g_n = 70\gamma$ and different h_n. In (a) $h_1 = 5\gamma$ and $h_2 = 50\gamma$ and in (b) $h_1 = 5\gamma$ and $h_2 = 250\gamma$.

(a) $h_1 = 5\gamma$ and $h_2 = 50\gamma$ whereas in (b) $h_1 = 5\gamma$ and $h_2 = 250\gamma$. Note that the order of the subsystems in the chain has no influence on our results, since we only consider the transmission and ΔT here. Since the transmittivity t and the reflectivity r vastly differ for these two values of h_n, the spectral range, where the superness is not negligible, is confined to a region where both the transmittivities and reflectivities are considerably different from zero. Comparing Fig. III.2.(a) and III.5., we observe that $|t|$ has high values for both the h_n between $\Delta_n = 40\gamma$ and $\Delta_n = 60\gamma$. Together with the reflectivities, this leads to the high values in ΔT for these detunings. Similarly, in Fig. III.19.(b) we see, that the superness is only considerably different from zero in a sharp region between $\Delta_n = \pm 20\gamma$. Here, the atom-cavity system with $h_n = 5\gamma$ is in the strong coupling regime whereas the subsystem with $h_n = 250\gamma$ is in the bad cavity regime. The confinement of the supermode occurrence to this small detuning range is caused by the transmission spectrum in the strong coupling regime. Here, the transmission has only one peak close to zero and almost vanishes in the environment until the far detuned case, where the transmission reaches 1 independent of the presence of the atom.

III.5. Possible applications

On the one hand our coupled chain of N atom-cavity systems could be used for detecting to which cavity a nearby atom couples. For example, as shown in Sec. III.4.2. the reflection intensity depends strongly on whether an atom couples to cavity 1 or 2, none of the two cavities is coupled to a nearby atom or both cavities couple to an atom. For resonant input light and an intercavity distance of $L_1 = 100.3\lambda$ the reflection vanishes in case of the atom coupling to cavity 2 but is maximum when coupling to cavity 1. This could be used, e.g., in an experiment where it is difficult to simultaneously couple single atoms to the cavities of a cavity chain, for detecting to which resonator an atom couples. This could be of relevance for experiments in which atom-cavity coupling is achieved with a falling cloud of cold atoms [99, 100, 105].

On the other hand our setup could be used to precisely determine the position of a cavity, even on a sub-wavelength scale. As shown in Sec. III.4.2.1. for a chain of $N = 3$ cavity-atom systems, the formation of supermodes depends crucially on the position of the middle cavity. Shifting cavity 2 leads to a very high peak in ΔT which vanishes for other positions of cavity 2. Already shifts of one twentieth of the light wavelength lead to a clearly visible difference in ΔT.

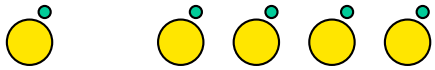

III.6. Discussion and summary

We investigated a chain of N subsystems each of which consists of a toroidal microcavity coupled to a nearby two-level atom. These subsystems are connected by a waveguide, which is used to probe the system by a weak input laser field. We studied the transmission and reflection behavior of this coupled system. Especially the impact of the backward fluxes between neighboring cavity-atom subsystems was studied in detail. As observables we considered the transmission, the reflection and the so-called "superness" which denotes the difference between the transmissions for a chain with and without backward fluxes. A chain in which backward fluxes are suppressed corresponds to a chain of independent cavities. We described two different calculation methods for solving the equations of motion in detail and discussed their advantages and drawbacks. The first method requests a numerical solution of the differential equation system. The second method is based on a coupling matrix description in the limit of weak input fields.
We found that interference of different light pathways influences crucially our system's dynamics. This can be controlled via the distance between the cavities and the length of the chain. For different parameter sets we found supermodes leading to strongly enhanced transmissions. We analyzed these supermodes in terms of light pathway interference. The relative transmission difference, which is denoted by "relative superness", increases with the number of subsystems for long chains. Furthermore, we identified spectral ranges in which the geometry has strong influence on the formation of supermodes whereas for other input detunings the transmission is insensitive to the geometry. While the transmission signal contains information on the formation of supermodes, the reflection signal could be used to detect which of the subsystems in the chain is coupled to a nearby atom. This information is not contained in the transmission, since the transmission is independent of the order of the subsystems in the chain. However, in an experiment, in which simultaneous coupling of single atoms to cavities of a chain can be difficult to obtain, this information is important. This is the case, e.g., in setups, in which atom-cavity coupling is achieved by a falling cloud of cold atoms or an atomic fountain.

Our two calculation methods allow to determine transmission and reflection intensities and the atomic populations. However, in an experiment second order correlations could also be of interest. Since the system is very complex and the number of degrees of freedom is very high, calculating second order correlations is computationally challenging. In order to calculate second order correlations, fluctuations have to be taken into account and thus a Fock state analysis would require all states with up to at least two photons per mode in each subsystem. A total excitation of each subsystem of two photons would not be sufficient. We checked this by calculating second order correlations for a single two-level atom coupled to a whispering gallery mode pair, where the number of states is sufficiently small. For a coupled chain, however, this expands our equation system to such a large number of equations of motion that a solution is almost impracticable. A more promising way to obtain higher order correlations could be the method of Monte Carlo simulations, see [148–150].

PART IV

Pathway interference in a loop array of three coupled microresonators

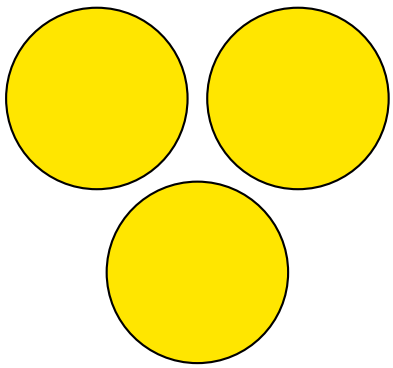

IV Pathway interference in a loop array of three coupled microresonators

In this part, a system of three coupled toroidal microresonators arranged in a loop configuration is studied. This setup allows light entering the resonator array from a tapered fiber to evolve along a variety of different pathways before leaving again through the fiber. In particular, the loop configuration of the resonators allows for an evolution which we term roundtrip process, in which the light evolves from one resonator sequentially through all others back to the initial one. This process renders the optical properties of the system sensitive to the phases of all coupling and scattering constants in the system. We analyze the transmission and reflection spectra, and interpret them in terms of interference between the various possible evolution pathways through the resonator system. In particular, we focus on the phase dependence of the optical properties. Finally, we discuss possible applications for this phase sensitivity induced by the roundtrip process, such as the measurement of the position of a nanoparticle close to one of the resonators, and the measurement of changes in the refractive index between two resonators.

IV.1. Introduction

In recent years, optical microresonators have received considerable attention, since they offer a wide range of applications such as strong-coupling cavity quantum electrodynamics, the modification of spontaneous emission, optical communication, or as sources of light [20, 21]. A particular promising example combining several of these ideas is the goal of establishing quantum networks [108, 145]. By now, a large variety of implementations has been achieved [17, 21, 99, 101, 151–154]. Naturally, also the extension to more than one cavity has been suggested, for example, as chains of coupled ring or disc resonators [155, 156], of defects in photonic crystal hosts [157, 158], of coupled resonator spheres [67, 69, 159], or of coupled square resonators on a grid [160].

A particular variant of coupled cavities involves two-dimensional arrays of microcavities, which can be used, e.g., to form photonic molecules [90, 91], or optical filters [55, 67, 68, 70, 161]. Light entering such an array can take a number of different pathways inside the cavities before leaving the coupled system, and the interference between these different pathways determines the optical properties of the resonator system. This in a certain sense can be seen in analogy to an atom with multiple energy levels connected

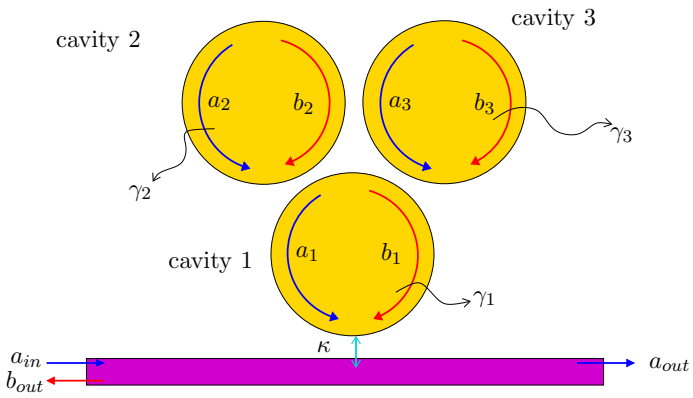

Figure IV.1.: The considered setup of three coupled resonators in loop configuration. The resonators are probed by a fiber coupled to one of the resonators. Due to the arrangement of the resonators, light can evolve in a roundtrip process, e.g., from cavity 1 via cavities 2 and 3 back to cavity 1 without leaving the resonator array, which leads to rich interference effects.

by several driving laser fields. Also the atom can evolve via different pathways. But a particularly interesting case arises if the laser fields are applied to the atom in a so-called closed-loop configuration [162–175]. This means that the laser fields are applied such that the atom can evolve in a non-trivial loop pathway from one initial state through the level scheme back to the initial state, e.g., $|1\rangle \rightarrow |2\rangle \rightarrow |3\rangle \rightarrow |1\rangle$ with atomic states $|i\rangle$ ($i \in \{1,2,3\}$). The loop structure induces rich possibilities for interference between the different pathways, and at the same time renders the optical properties of the atoms sensitive to the phase of the applied driving fields. This prompts the question whether similar interference effects and phase-sensitivity could also arise in arrays of microresonators. The couplings between the resonators are mediated via their evanescent fields, and the corresponding coupling constants are in general complex. Similarly, the scattering inside a given cavity is characterized by a complex scattering constant. Thus it is not surprising that even for simple systems such as two coupled cavities the phase of the couplings can strongly influence the output fluxes. However, there are also cases in which the phases do not influence the final transmission or reflection observed from a resonator, and therefore the coupling constants often are treated as real numbers, neglecting the phase information [68, 69].

Motivated by these previous works, we here study an array of microresonators in situations in which the phase of the coupling constants are crucial. In particular, we focus on situations in which processes analogous to the closed-loop pathways in atoms occur. To that end, we analyze an array of three coupled microresonators probed by a tapered fiber, see Fig. IV.1. This setup is the simplest arrangement which allows for a closed-loop roundtrip pathway in analogy to the closed-loop atomic level systems. Due to the arrangement of the resonators, light can evolve in a roundtrip process, e.g., from cavity 1 via cavities 2 and 3 back to cavity 1 without leaving the resonator array. We identify the evolution pathways for the photons entering the resonator array contributing to the transmission and reflection, and determine conditions for the dependence of these optical properties on the phases of the coupling and scattering constants. Based on these results, we analyze the phase dependence for several configurations in detail. Furthermore, we discuss possible applications for the phase-sensitivity of our system. Our analytical results

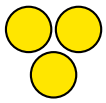

and interpretations are based on coupled mode theory.

This part of the thesis is organized as follows. In Sec. IV.2., we describe our model and the observables. In Sec. IV.3., we present our results. We start by analyzing the different pathways light can take through the resonator array, and how phase-sensitivity can arise from these pathways. We then move on to a discussion of transmission and reflection spectra for phase-dependent systems, and of the most important roundtrip process enabled by the loop structure of the resonators. Finally, possible applications are discussed in Sec. IV.4. Here, we suggest how to use our setup in order to measure the refractive index of a medium or to determine the position of a nanoparticle.

IV.2. Theoretical considerations

IV.2.1. Description of the model system

The considered system consists of three equal nearby whispering gallery mode microresonators coupled to a tapered glass fiber, arranged as shown in Fig. IV.1. This is a reduction of the general system introduced in part I where $N = 1$, $D = 3$, $X = 1$ and all $g_{x,n} = 0$. In a toroidal microresonator a photon can be many times totally reflected at the edges of the cavity and thus move on a polygonal path very similar to a circle. The originally undisturbed resonances of the cavity occur in pairs of clock- and anticlockwise propagating modes. Photons belonging to such a pair $\{a_m, b_m\}$ ($m \in \{1, 2, 3\}$) differ only by their propagation direction but have the same frequency. Due to scattering processes, e.g., caused by material imperfections, the modes of such pairs can be scattered into each other. This scattering affects the eigenmodes of the system and thus also changes its eigenenergies.

As input field we consider a weak probe field of mode $a_{1,in}$, which is coupled into cavity 1. The scattering inside cavity number n we describe by the parameter h_n with $n \in \{1, 2, 3\}$. The coupling between resonators n and m is described by the coupling constant ξ_{mn} with $m, n \in \{1, 2, 3\}$. κ denotes the coupling strength between the fiber and cavity 1. Using these definitions, in a suitable interaction picture the Hamiltonian of our system reads [120]

$$\mathcal{H} = \mathcal{H}_0 + \mathcal{H}_L + \mathcal{H}_{CS}\,, \tag{IV.2.1}$$

with

$$\mathcal{H}_0 = \hbar \sum_{l=1}^{3} \Delta_l (a_l^\dagger a_l + b_l^\dagger b_l)\,, \tag{IV.2.2a}$$

$$\mathcal{H}_L = i\hbar\sqrt{2\kappa}[a_{1,in} a_1^\dagger - a_{1,in}^* a_1]\,, \tag{IV.2.2b}$$

$$\mathcal{H}_{CS} = \hbar \sum_{m,n=1}^{3} (\xi_{nm} a_n^\dagger b_m + \xi_{nm}^* b_m^\dagger a_n)\,. \tag{IV.2.2c}$$

Here for notational simplicity we defined $h_n = \xi_{nn}$, and used $\xi_{nm} = \xi_{mn}$. The detunings are defined as $\Delta_l = \omega_l - \omega_{in}$, where ω_l is the resonance frequency of resonator l and ω_{in} is the frequency of the probing light. In the following, we assume equal resonance frequencies of the resonators $\Delta_1 = \Delta_2 = \Delta_3 = \Delta$ in our calculations. We write the complex couplings constants as $\xi_{mn} = |\xi_{mn}| e^{i\phi_{mn}}$. For our calculations we assume the

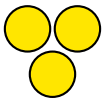

critical coupling condition $\kappa = \sqrt{\xi_{11}^2 + (\gamma_1/2)^2}$ for the coupling between the fiber and cavity 1 to be fulfilled [105]. Since the modes $\{a_m, b_m\}$ are assumed to have the same frequency it is reasonable to assume equal internal loss rates $\gamma_1 = \gamma_2 = \gamma_3 = \gamma$ for all modes $\{a_m, b_m\}$. Then the total decay of mode a_1 $[b_1]$ can be calculated according to $\gamma_{a_1} = 2\kappa + \gamma_1$ $[\gamma_{b_1} = 2\kappa + \gamma_1]$, whereas $\gamma_{a_2} = \gamma_{b_2} = \gamma_{a_3} = \gamma_{b_3} = \gamma$.

From the Heisenberg equation, the time evolutions of the six mode operators a_m and b_m can be obtained as

$$\dot{a}_m = -\left(i\Delta_m + \frac{1}{2}\gamma_{a_m}\right) a_m - i\sum_{n=1}^{3} \xi_{mn} b_n + \delta_{m1}\sqrt{2\kappa}\, a_{m,in}\,, \tag{IV.2.3a}$$

$$\dot{b}_m = -\left(i\Delta_m + \frac{1}{2}\gamma_{b_m}\right) b_m - i\sum_{n=1}^{3} \xi_{nm}^{*} a_n\,, \tag{IV.2.3b}$$

where δ_{ij} is the Kronecker Delta function. Since only cavity one couples to the fiber, in the following we write $a_{1,in} = a_{in}$, $a_{1,out} = a_{out}$ and $b_{1,out} = b_{out}$.

IV.2.2. Observables

In our numerical calculations we investigate the transmission and reflection of light sent into the system via the coupled fiber. In particular, we are interested in the steady state mean values of the output mode operators. We neglect fluctuations of the photon mode operators and calculate the steady state by setting $\dot{a}_m = \dot{b}_m = 0$ in Eq. (IV.2.3). For the calculation of the output operators, we use the input-output relation [141]

$$\langle a_{out}\rangle = -\,a_{in} + \sqrt{2\kappa}\langle a_m\rangle\,, \tag{IV.2.4a}$$

$$\langle b_{out}\rangle = \sqrt{2\kappa}\langle b_m\rangle\,. \tag{IV.2.4b}$$

Then the transmission and reflection become

$$T = \frac{|\langle a_{out}^{\dagger} a_{out}\rangle|^2}{|a_{in}|^2} \approx \frac{|\langle a_{out}\rangle|^2}{|a_{in}|^2}\,, \tag{IV.2.5a}$$

$$R = \frac{|\langle b_{out}^{\dagger} b_{out}\rangle|^2}{|a_{in}|^2} \approx \frac{|\langle b_{out}\rangle|^2}{|a_{in}|^2}\,. \tag{IV.2.5b}$$

It should be noted that neglecting the quantum fluctuations in Eqs. (IV.2.4) and restricting the analysis to the transmission and reflection essentially renders the analysis classical. Nevertheless, in the following, we will continue our discussion based on mode operators, individual photons, and scattering processes, since this allows to conveniently interpret the underlying physics.

IV.3. Results

IV.3.1. Light pathway analysis

Light entering our three coupled resonator system can travel along a variety of different pathways before leaving cavity 1 as a transmitted or reflected photon. The different

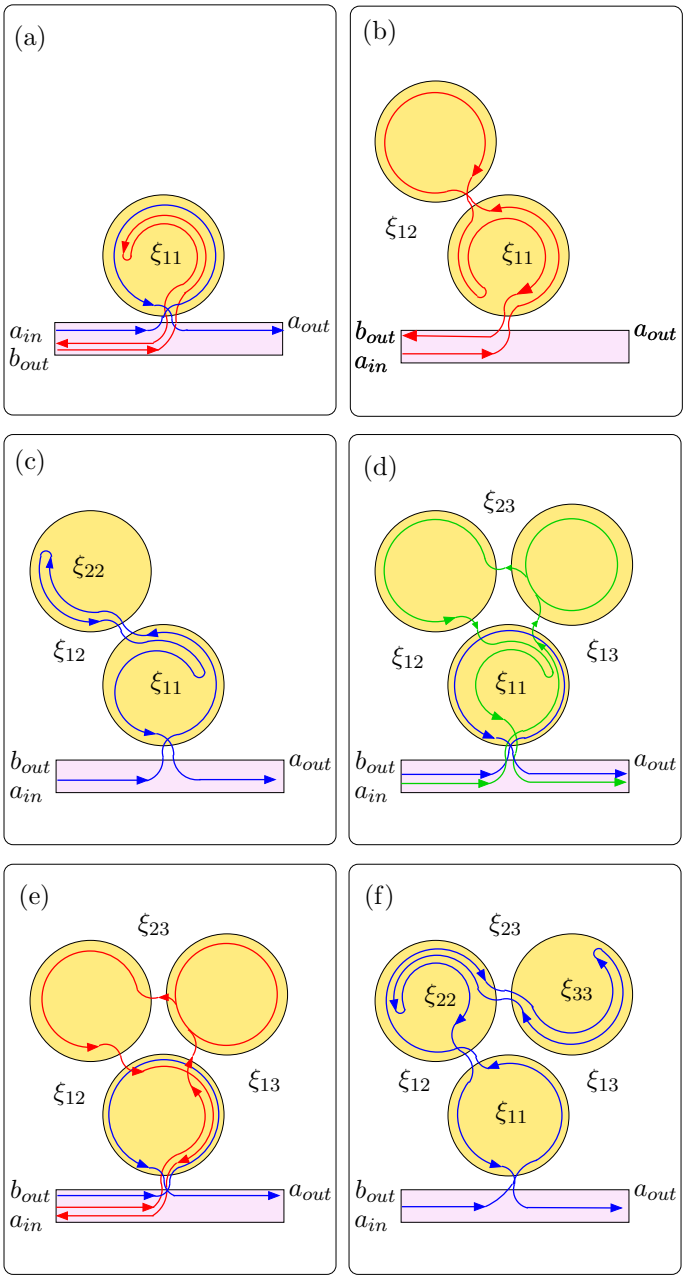

Figure IV.2.: Example pathways of photons passing through the resonator array. In (a), the photon enters only the first cavity, scatters inside cavity 1, and then leaves the cavity back into the fiber. In (b), the photon traverses two cavities, but scatters only in cavity 1. (c) shows a pathway through two cavities with scattering in both the cavities, (d) a path through all cavities with scattering in cavity 1 only, (e) a path through all cavities without scattering, and (f) an evolution through three cavities with scattering in cavities 2 and 3.

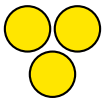

pathways have relative phases, since every time a photon is scattered inside one cavity or moves between two cavities the pathway amplitude is multiplied by the respective complex coupling constant or scattering parameter with phase angle ϕ_{ij}. The total reflected and transmitted light then arises as the interference of all possible pathways amplitudes. Therefore the phase angles ϕ_{ij} can be expected to have a great impact on the resulting output fluxes. In the following, we analyze conditions of the system parameters for obtaining phase-dependent or phase-independent reflections and transmissions.

We start with a reduced system in which only phase independent pathways are possible and afterwards explain how a phase dependence can arise. For this we set some of the couplings and scattering rates to zero. If we decouple cavities 2 and 3 from cavity 1 by setting $\xi_{12} = \xi_{13} = 0$ as shown in Fig. IV.2.(a), no coupling process can take place but only scattering $a_1 \xrightarrow{\xi_{11}^*} b_1$ and vice versa is possible. Although the scattering parameter ξ_{11} has an impact on the light's phase, the overall transmission or reflection are not phase dependent. The reason for this is that all pathways contributing to the transmission include no or an even number of scattering processes, e.g. from a_1 to b_1 and back. Since the respective scattering parameters are complex conjugates, they have no net influence on the phase of the outcoming flux of each pathways. Similarly, the reflected light constitutes of contributions from pathways with an uneven number of scattering processes. This also means that all interfering contributions have the same phase when leaving the system and thus their interference is constructive independent of the phase of the scattering parameter.

In the next step, we consider two coupled microcavities by setting $\xi_{12} \neq 0$ whereas the scattering rate ξ_{22} in cavity 2 is assumed to be zero, see Fig. IV.2.(b). Taking into account only small numbers of scattering or coupling processes, the following three different pathways are possible:

$$a_1 \xrightarrow{\xi_{11}^*} b_1 \,, \tag{IV.3.6a}$$

$$a_1 \xrightarrow{\xi_{12}^*} b_2 \xrightarrow{\xi_{12}} a_1 \,, \tag{IV.3.6b}$$

$$a_1 \xrightarrow{\xi_{12}^*} b_2 \xrightarrow{\xi_{12}} a_1 \xrightarrow{\xi_{11}^*} b_1 \,. \tag{IV.3.6c}$$

Note that we have omitted here pathways differing from the ones in Eqs. (IV.3.6) by a double scattering within cavity 1. In this reduced system, light evolving into cavity 2 always returns to cavity 1 on the same way, and these processes are described by ξ_{12} and ξ_{12}^*, such that the phase of the coupling constant ξ_{12} does not affect the output intensities. Similar to the case in Fig. IV.2.(a), also the phase of ξ_{11} does not affect the transmission or reflection.

Next, in addition we set ξ_{22} non-zero, see Fig. IV.2.(c). In this case, the phases ϕ_{ij} do affect the transmission and reflection, since now in addition to the pathways in Eqs. (IV.3.6), two additional leading order pathways are possible:

$$a_1 \xrightarrow{\xi_{12}^*} b_2 \xrightarrow{\xi_{22}} a_2 \xrightarrow{\xi_{12}^*} b_1 \,, \tag{IV.3.7a}$$

$$a_1 \xrightarrow{\xi_{11}^*} b_1 \xrightarrow{\xi_{12}} a_2 \xrightarrow{\xi_{22}^*} b_2 \xrightarrow{\xi_{12}} a_1 \,. \tag{IV.3.7b}$$

Thus incoming light can propagate through cavity 1, enter cavity 2, scatter there, and then leave the system in reflection direction. Also, it can pass through cavities 1 and 2

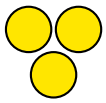

and be scattered in both cavities, leaving the system in transmission direction. These pathways depend on the phase of ξ_{22}, ξ_{11} and ξ_{12}, and thus the transmission and reflection become dependent on these phases.

Adding the third cavity, a qualitatively different evolution through the cavity system becomes possible. We first only chose the scattering rate ξ_{11} as nonzero, see Fig. IV.2.(d). Now incoming light can evolve on a roundtrip through all three cavities, be scattered in cavity 1 from mode b_1 to a_1 and afterwards leave the coupled resonator system in transmission direction. Processes like this in which light moves along pathways which describe a loop through all three cavities will play a special role in our further investigations, as they depend on the phases of all coupling constants between the coupled cavities. In the following we will refer to them as *roundtrip processes*. Beside these roundtrip pathways, also non-roundtrip processes are possible, and the transmission and reflection in leading order are superpositions of the pathways mentioned in Eqs. (IV.3.6) and the following pathways:

$$a_1 \xrightarrow{\xi_{13}^*} b_3 \xrightarrow{\xi_{23}} a_2 \xrightarrow{\xi_{12}^*} b_1 \ , \tag{IV.3.8a}$$

$$a_1 \xrightarrow{\xi_{12}^*} b_2 \xrightarrow{\xi_{23}} a_3 \xrightarrow{\xi_{13}^*} b_1 \ , \tag{IV.3.8b}$$

$$a_1 \xrightarrow{\xi_{13}^*} b_3 \xrightarrow{\xi_{23}} a_2 \xrightarrow{\xi_{12}^*} b_1 \xrightarrow{\xi_{11}} a_1 \ , \tag{IV.3.8c}$$

$$a_1 \xrightarrow{\xi_{12}^*} b_2 \xrightarrow{\xi_{23}} a_3 \xrightarrow{\xi_{13}^*} b_1 \xrightarrow{\xi_{11}} a_1 \ , \tag{IV.3.8d}$$

$$a_1 \xrightarrow{\xi_{13}^*} b_3 \xrightarrow{\xi_{23}} a_2 \xrightarrow{\xi_{23}^*} b_3 \xrightarrow{\xi_{13}} a_1 \ , \tag{IV.3.8e}$$

$$a_1 \xrightarrow{\xi_{12}^*} b_2 \xrightarrow{\xi_{23}} a_3 \xrightarrow{\xi_{23}^*} b_2 \xrightarrow{\xi_{12}} a_1 \ , \tag{IV.3.8f}$$

plus the pathway in which light enters cavity 1 and leaves the system without any further scattering. The resulting superposition of these amplitudes renders the transmission and reflection dependent on both the phases of the couplings constants ϕ_{ij} and the phases of the scattering rate ϕ_{11}.

It should be noted, however, that without scattering $\xi_{ii} = 0$ as in Fig. IV.2.(e), also the dependence of the output intensities on the phases of the coupling constants ϕ_{ij} disappears. All leading order pathways contributing to the reflection lead the light on a roundtrip pathway [see Eq. (IV.3.8a) and (IV.3.8b)] such that they have the same final phase and thus interfere constructively for all choices of the phase angles ϕ_{ij}. Similarly, the phase dependence in transmission direction vanishes.

In the most general case with all coupling constants and scattering rates different from zero as indicated in Fig. IV.2.(f), many interfering phase dependent pathways become possible, such that a dependence on all phases can be expected. In the following, we will analyze this phase dependence in detail.

IV.3.2. Transmission and reflection without roundtrip process

We now turn to numerical results for the transmission and reflection in the loop system. In Fig. IV.3. the transmission and reflection are shown for different values of the phase angles ϕ_{ij} in dependence of the detuning Δ of the modes in cavity 1 to the incident light. We choose the scattering rates $\xi_{11} = 30\gamma$, $\xi_{22} = 20e^{i\phi_{22}}\gamma$ and $\xi_{33} = 20\gamma$. The couplings between the two cavities are $\xi_{12} = 30e^{i\phi_{12}}\gamma$, $\xi_{13} = 30e^{i\phi_{13}}\gamma$ and $\xi_{23} = 0$. Since

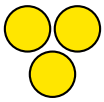

$\xi_{23} = 0$, no roundtrip process is possible. For this choice of parameters, the pathways in Eq. (IV.3.6) and (IV.3.7) are possible as shown in Fig. IV.2.(c), and additionally the analogous ones for cavity 3 instead of cavity 2.

While studying the phase dependence, our variables are the angles ϕ_{12}, ϕ_{13} and ϕ_{22}. In the solid lines in Fig. IV.3.(a) all $\phi_{ij} = 0$, i.e. all coupling and scattering constants are taken as real numbers. In order to explain this result we consider the occupancy and the phase of each light mode inside cavity 1.

Since coupling light out of the cavity into the glass fiber leads to a phase shift of π, the outcoupled light of mode a_1 interferes constructively with a_{in} when its phase $\phi_{a_1} = \pi$ whereas we obtain destructive interference for $\phi_{a_1} = 0$, see also the input-output relations Eq. (IV.2.4). As we choose $a_{in} \in \mathbb{R}$ only the absolute value of ϕ_{a_1} is of relevance for analyzing the interference. Therefore we define $\phi_a = |\phi_{a_1}|$. According to the input-output relations Eq. (IV.2.4) we can expect zero transmission $T = 0$ if both the phase has a value leading to destructive interference in forward direction, and the amplitude satisfies $2\kappa|a_1|^2 = |a_{in}|^2$. If only one of the two conditions is fulfilled, only partial transmission can be expected. In contrast, for mode b, there is no input field which can interfere with the field leaking out of cavity 1 into reflection direction. Therefore the reflected intensity is proportional to the intensity of b_1 inside cavity 1.

To verify this interpretation quantitatively, in the upper two subfigures of Fig. IV.4. we show (a) the scaled photon mode occupancies $\mathcal{O}_{a_1}$ and $\mathcal{O}_{b_1}$ inside cavity 1 proportional to $|a_1|^2$ and $|b_1|^2$, respectively, and (b) the angle ϕ_a. Note that the amplitude condition for maximum transmission corresponds to the horizontal line at scaled occupancies equal to one in Fig. IV.4.(a). As one can see from Fig IV.4.(a), the occupancies of both the modes a_1 and b_1 have maxima around $\Delta = \pm 20\gamma$. By contrast, the transmission in Fig. IV.3.(a) shows minima for these detunings. The reason for this is that $\phi_a(\Delta = \pm 20\gamma) = 0$. Thus, the field leaking from a_1 into the fiber interferes destructively with the input field a_{in}. Almost perfect suppression in forward direction $T \approx 0$ is achieved since for this detuning $2\kappa|a_1|^2 \approx |a_{in}|^2$. A similar interpretation holds for $\Delta = \pm 60\gamma$. For resonant light, i.e. $\Delta = 0$, a maximum in T can be observed in Fig. IV.3.(a). This can be traced back to the low occupancy of mode a_1 in Fig IV.4.(a), such that the transmission mainly consists of a_{in}. Note that for the parameters chosen in Fig. IV.3.(a), both the occupancies and the phases shown in Fig. IV.4. are symmetric with respect to the detuning. Consequently, also T and R are symmetric functions of Δ.

In the next example in Fig. IV.3.(b), we in contrast to (a) set $\phi_{12} = 0.2\pi$, but keep all other $\phi_{ij} = 0$. Compared to the reflection and transmission in (a), we can observe two additional peaks in the transmission and two additional zeros in the reflection signal around $\Delta = \pm 20\gamma$. In order to explain these results, we consider Fig. IV.4.(c) and (d). The minima in T at positions $\Delta = \pm 10\gamma$, $\Delta = \pm 30\gamma$ and $\Delta = \pm 60\gamma$ again arise from destructive interference with $\phi_a = 0$ and nearly fulfilled amplitude condition. At $\Delta = \pm 20\gamma$ the modes of cavity 1 are nearly unpopulated. Thus $R \approx 0$ and the transmission is governed by the input flux a_{in}. Interestingly, cavities 2 and 3 nevertheless contain much higher light intensities, which leads to decoherence via γ. From $T(\Delta = \pm 20) = 0.82 \neq 1$ we find that even though cavity 1 is almost empty, about 20% of the input light is coupled into the system. For larger detunings Δ all results in Fig. IV.4.(c) and (d) are similar to the graphs in (a) and (b). From this we conclude that in the off-resonant case, as expected the phase angles ϕ_{ij} of the coupling and scattering parameters have only weak

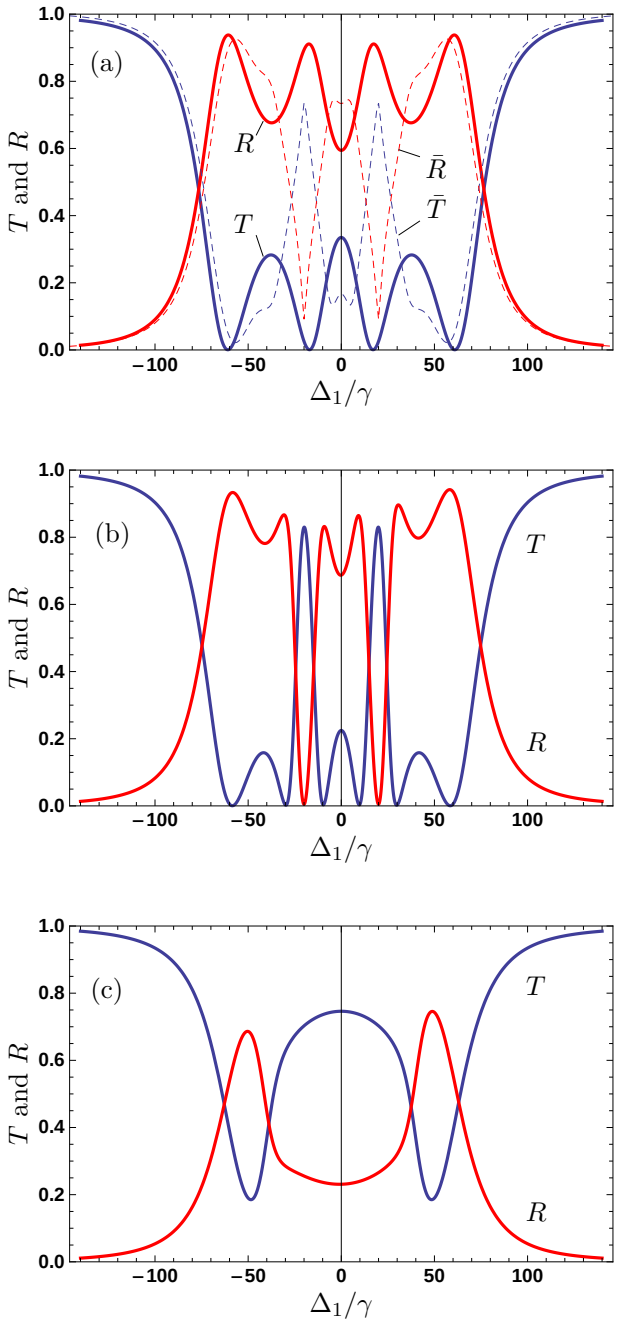

Figure IV.3.: Transmission T and reflection R in the loop system. The parameters are $\xi_{12} = \xi_{13} = 30\gamma$ and $\xi_{23} = 0$, such that scattering between cavities $1 \leftrightarrow 2$ and $1 \leftrightarrow 3$ is possible, but not between 2 and 3. Scattering occurs in all cavities with rates $\xi_{11} = 30\gamma$ and $\xi_{22} = \xi_{33} = 20\gamma$. In (a) all phases are chosen zero, $\phi_{ij} = 0$. The dashed lines show corresponding results for transmission ($\bar{T}$) and reflection ($\bar{R}$) averaged over the phase angles ϕ_{12} (or over ϕ_{22} which leads to the same curves). In (b), the phases are chosen as $\phi_{12} = 0.2\pi$, and all other $\phi_{ij} = 0$. In (c), $\phi_{12} = -0.6\pi$ and $\phi_{13} = 0.4\pi$, and all other $\phi_{ij} = 0$.

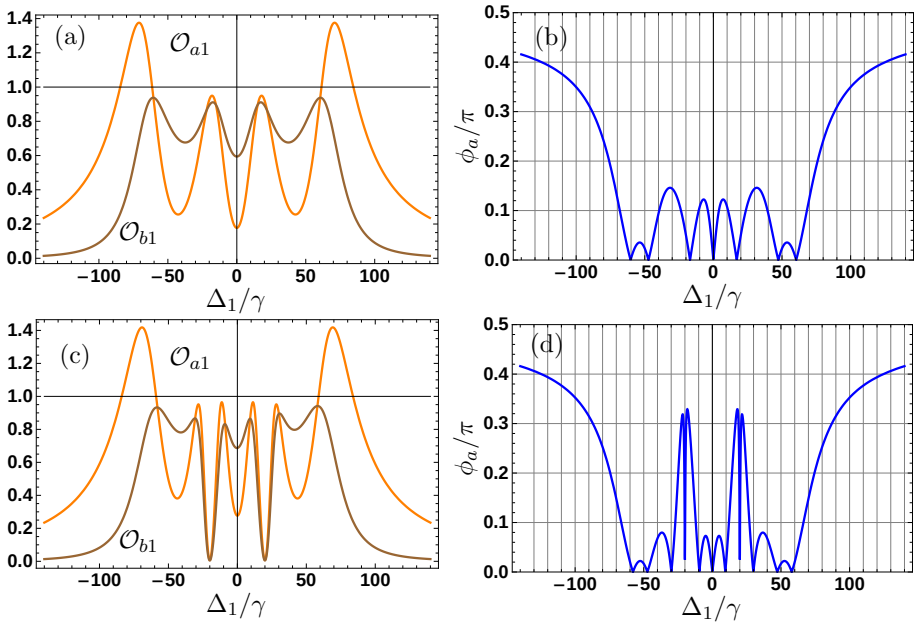

Figure IV.4.: Field configuration in resonator 1. (a) and (c): Scaled occupancies $\mathcal{O}_{a_1} = 2\kappa|a_1|^2/|a_{in}|^2$ and $\mathcal{O}_{b_1} = 2\kappa|b_1|^2/|a_{in}|^2$ of the two counter-propagating modes a_1 and b_1 inside cavity 1. (b) and (d): Phase $\phi_a = |\phi_{a_1}|$ of the counter-clockwise propagating mode inside cavity 1 which is coupled out into the fiber in transmission direction. In (a) and (b), the parameters are chosen as in Fig. IV.3.(a), whereas in (c) and (d) they are as in Fig. IV.3.(b).

influence on the systems dynamics. Additionally, the reflection in Fig. IV.3.(b) is not a symmetric function of the detuning, while the transmission still is symmetric. This difference can arise since different pathways contribute to T and R.

For the third example in Fig. IV.3.(c) we choose $\phi_{12} = -0.6\pi$ and $\phi_{13} = 0.4\pi$, but keep all other phases zero. Thus transitions between resonators $1 \leftrightarrow 3$ and $1 \leftrightarrow 2$ are possible, but not between 2 and 3. It can be seen that this change in the phase of the coupling parameters leads to considerable modifications of the transmission and reflection properties. Both transmission and reflection have a simple structure, but are not symmetric with respect to Δ. The interpretation of the peak structure is similar to the two previous cases.

Analyzing the phase-dependence, we found that the transmission and reflection are π-periodic in ϕ_{12} and ϕ_{13} but 2π-periodic in the phases of the scattering parameters ϕ_{ii}. In the following section, we study and interpret this periodicity of our results in more detail using an eigenvalue analysis.

IV.3.3. Eigenvalue analysis

In this section, we analyze the phase-dependence of the transmission and reflection spectra in a more general way. For this, we consider the eigenvalues of the matrix governing our system's dynamics. The equations of motion for the six mode operators $\{a_i, b_i\}$ can

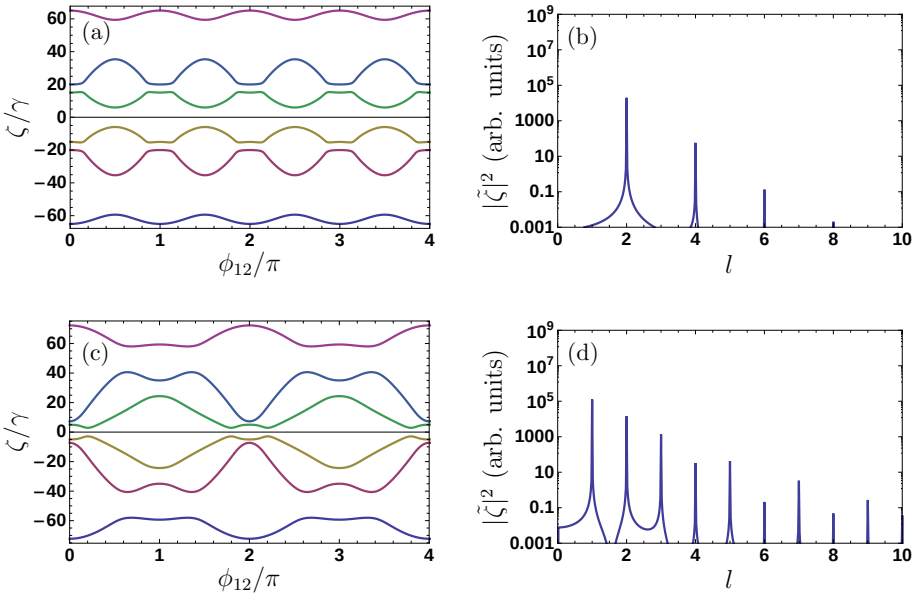

Figure IV.5.: Eigenvalue analysis to interpret the phase dependence. The left subfigures (a) and (c) show the imaginary part of the eigenvalues (ζ) of the matrix $\mathcal{M}$ describing the system dynamics, which correspond to the energy of the system's dressed states. They are plotted against the phase angle ϕ_{12}. The right subfigures (b) and (d) show the power spectrum $|\tilde{\zeta}|^2$ of one eigenvalue as example, revealing the periodicity of the eigenenergies in ϕ_{12}. The parameters in (a) and (b) are $\xi_{11} = \xi_{13} = 30\gamma$, $\xi_{22} = \xi_{33} = 20\gamma$, $\xi_{12} = 30\gamma e^{i\phi_{12}}$ and $\xi_{23} = 0$, thus no roundtrip process is possible. In (c) and (d) $\xi_{23} = 15\gamma$, thus the roundtrip process is possible.

be written as

$$\frac{\partial}{\partial t}\vec{C} = \mathcal{M} \cdot \vec{C}\,, \tag{IV.3.9a}$$

$$\vec{C} = (a_1, b_1, a_2, b_2, a_3, b_3)^T\,. \tag{IV.3.9b}$$

By diagonalizing $\mathcal{M}$, the dressed states of the system can be evaluated. The complex eigenvalues correspond to the complex eigenenergies of these dressed states. The real part of the eigenvalues of $\mathcal{M}$ can be interpreted as the decay rates whereas the imaginary parts correspond to the eigenenergies. Coupling constants as well as scattering parameters included in $\mathcal{M}$ shift the original eigenfrequencies of the resonators. Thus the imaginary parts ζ of the eigenvalues of matrix $\mathcal{M}$ are possible positions for peaks or dips in the reflection and transmission. These eigenvalues thus allow for a study of the dependence of the transmission and reflection spectra on the phase angles ϕ_{ij}. For example, to study the dependence on ϕ_{12}, a Fourier transformation of one of the eigenvalues ζ gives

$$\zeta(\phi_{12}) = \frac{1}{\sqrt{2\pi}} \int_l \tilde{\zeta}(l) e^{il\phi_{12}}\, \mathrm{d}l\,. \tag{IV.3.10}$$

The Fourier coefficients $\tilde{\zeta}(l)$ then determine the periodicity of the eigenvalues in the phase ϕ_{12}. First, we consider the case where no roundtrip process is possible, i.e. $\xi_{23} = 0$. In Fig. IV.5. we show the six eigenvalues (a) and their power spectrum (b) for the

parameters $\xi_{11} = \xi_{13} = 30\gamma$, $\xi_{22} = \xi_{33} = 20\gamma$, $\xi_{12} = 30\gamma \exp[i\phi_{12}]$ and $\xi_{23} = 0$. In this case, we observe that $\tilde{\zeta}(l)$ is different from zero only for even numbers of l. This means that the eigenvalues are π periodic in ϕ_{12}. If no roundtrip process can take place, light evolving from cavity 1 into cavity 2 or 3 has to move the same way back in order to leave the system and to be detected as output light. Thus it interacts two times with the same coupling constant. This is the reason why the Fourier coefficient belonging to ϕ_{12} vanishes for uneven numbers of l. In Fig. IV.5.(c) and (d) we show the eigenvalues for $\xi_{23} = 15\gamma$. All further parameters are the same as before. This setup corresponds to Fig. IV.2.(f). In this case, a roundtrip process is possible, and the Fourier coefficients $\tilde{\zeta}(l)$ are different from zero both for even or uneven numbers of l. The reason is that light can evolve, e.g., from cavity 1 via cavities 2 and 3 back to 1 such that the phase ϕ_{12} influences the path amplitude only once. Thus in this case, the eigenenergies are 2π periodic in ϕ_{12}. Similar analysis allows to also reveal the phase dependence of the other coupling constants.

IV.3.4. The roundtrip process

In this section, we study the roundtrip process and the resulting effects in detail. For this, we make use of the fact that by turning the coupling ξ_{23} on and off it can be controlled whether or not a roundtrip pathway can be taken by entering light. Therefore, in the first step we expand the transmission T in this coupling constant around $\xi_{23} = 0$. This expansion will reveal the leading order effects of the roundtrip process for small ξ_{23}. Afterwards we present numerical results for T and R for more general parameter sets which allow the roundtrip processes to take place.

IV.3.4.1. Expansion in orders of the roundtrip process

To elucidate the impact of the roundtrip process on the transmission spectrum, we perform a Taylor expansion of the transmission amplitude to the second order in $|\xi_{23}|/\gamma$ around $\xi_{23} = 0$. This refers to the case where the coupling between cavity 2 and 3 is much weaker than the other couplings ξ_{ij}. The expanded transmission reads:

$$\frac{|\langle a_{out}\rangle|^2}{|\langle a_{in}\rangle|^2} \approx \left| c_0 + c_1 \frac{|\xi_{23}|}{\gamma} + c_2 \frac{|\xi_{23}|^2}{\gamma^2} \right|^2 . \qquad \text{(IV.3.11)}$$

Here, c_n are the Taylor expansion coefficients. The 0th order corresponds to the case where no roundtrip process is possible, i.e. $\xi_{23} = 0$. The respective result is shown in Fig. IV.6.(a). The parameters are chosen as $\xi_{11} = 50\gamma$, $\xi_{22} = 20e^{i\phi_{22}}\gamma$, $\xi_{33} = 20\gamma$, $\xi_{12} = 10\gamma$, $\xi_{13} = 30e^{i\phi_{13}}\gamma$ and all $\phi_{ij} = 0$. In Fig. IV.6.(b) and (c) we show the first and second order Taylor coefficients c_1 and c_2 which provide the respective correction terms for the transmission. The first order corresponds to a pathway in which light interacts once with the coupling constant ξ_{23}. The most probable process of this kind that ends in a_1 is a single roundtrip through all three cavities, see e.g. Eq. (IV.3.8c) and (IV.3.8d). The second order contributions correspond to pathways where light moves twice between cavity 2 and 3, including a double roundtrip process. Examples for such pathways are given in Eq. (IV.3.8e) and (IV.3.8f).

We can see from these figures that the first order correction leads to a small dip that overlaps with the broad resonance round $\Delta = 0$. By contrast, the second order correction

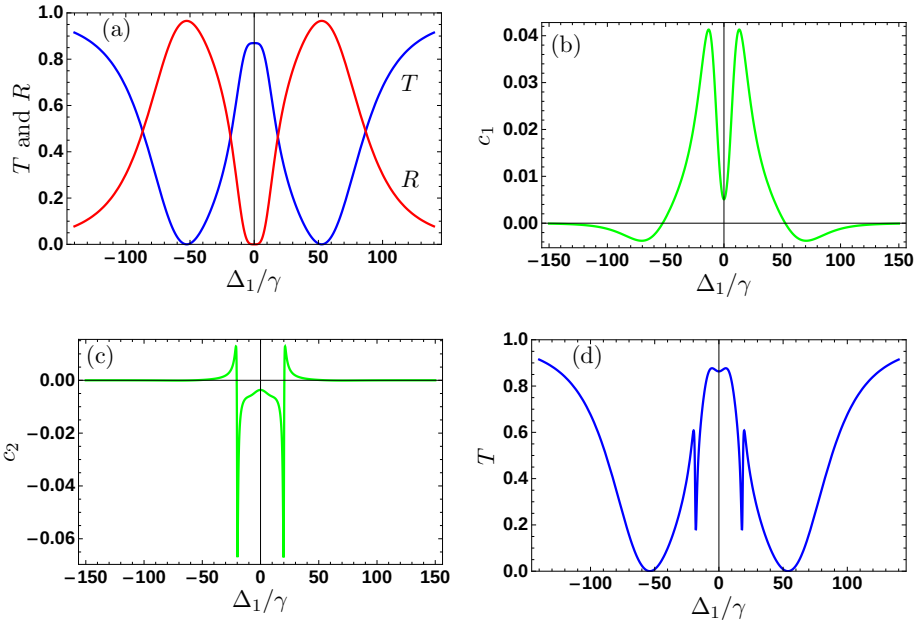

Figure IV.6.: Expansion of the transmission in orders of the roundtrip process. For this, the transmission is expanded around 0 in $|\xi_{23}|/\gamma$. The parameters are $\xi_{11} = 50\gamma$, $\xi_{22} = 20e^{i\phi_{22}}\gamma$, $\xi_{33} = 20\gamma$, $\xi_{23} = 10\gamma$, $\xi_{13} = 30e^{i\phi_{13}}\gamma$ and all $\phi_{ij} = 0$. (a) zero order contribution ($\xi_{23} = 0$), (b) first order contribution c_1, (c) second order contribution c_2, (d) complete transmission for $\xi_{23} = 3\gamma$.

consists of two sharp resonances round $\Delta = 20\gamma = \xi_{22} = \xi_{33}$. Comparing the sum of the curves of Fig. IV.6.(b) and (c) to the full output for $\xi_{23} = 3\gamma$ (d), we find that for the small value of ξ_{23} taken in our example the first two orders in the expansion are sufficient to almost perfectly approximate the full result in (d).

The structure of T can be explained using the same interpretation techniques as applied for Fig. IV.3. based on the occupancy and phase of the fields inside cavity 1.

IV.3.4.2. Transmission and reflection with roundtrip process

Next, we study the phase dependence of the transmission T and reflection R for a choice of parameters for which a roundtrip process is possible. For this, we choose all coupling constants and all scattering parameters non-zero, as shown in Fig. IV.2.(f). All parameters are as in Fig. IV.6. except for $\xi_{23} = 5\gamma$. We start by considering the transmission and reflection if all phase angles $\phi_{ij} = 0$. The respective results are shown in Fig. IV.7.(a) and (b). We can see clearly the two side band dips around $|\Delta| = 20\gamma = |\xi_{22}| = |\xi_{33}|$ arising from the second order Taylor correction of Eq. (IV.3.11).

Figs. IV.7.(c) and (d) show corresponding results with phase angles changed to $\phi_{22} = 1.6\pi$ and $\phi_{13} = 0.4\pi$. We observe that the reflection becomes asymmetric and only one sharp dip around $\Delta = 20\gamma$ remains. The transmission also changes, but remains symmetric. Upon changing the sign of phase ϕ_{13}, the sharp dip moves to the opposite side of the spectrum, i.e., to $\Delta \approx -20\gamma$, see subfigures (e) and (f). The transmission

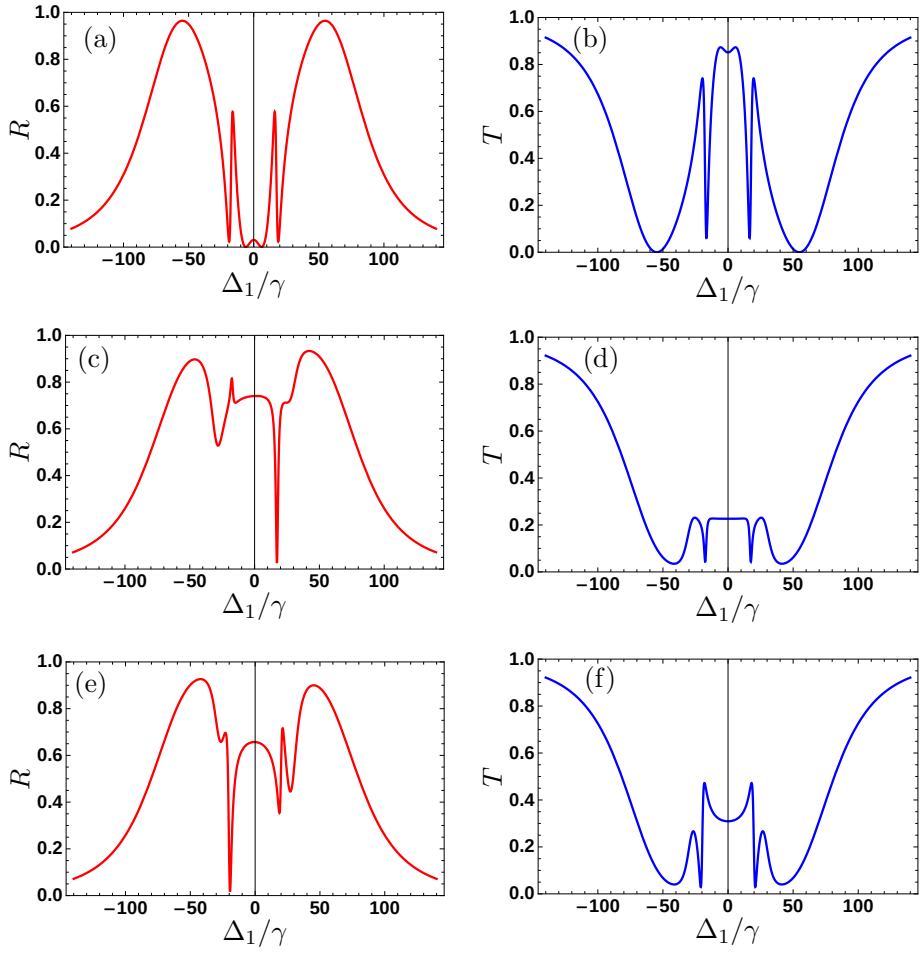

Figure IV.7.: Transmission (blue) and reflection (red) spectra for parameters which allow for the roundtrip process. The parameters are the same as in Fig. IV.6. except for $\xi_{23} = 5\gamma$. In (a) and (b), all phases are zero ($\phi_{ij} = 0$). In (c) and (d), $\phi_{22} = 1.6\pi$ and $\phi_{13} = 0.4\pi$ and all other phases are chosen zero. In (e) and (f), $\phi_{22} = 1.6\pi$ and $\phi_{13} = -0.4\pi$ and all other $\phi_{ij} = 0$.

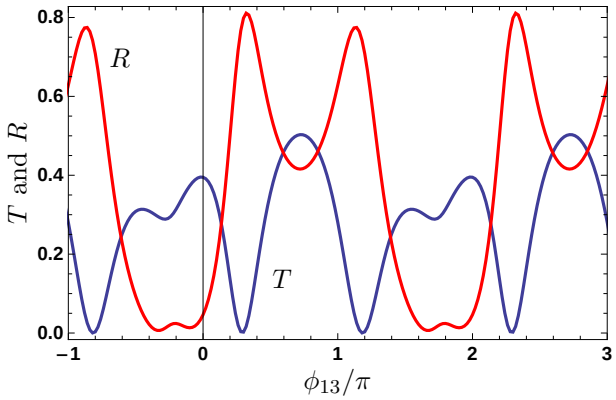

Figure IV.8.: Transmission (blue) and reflection (red) spectra for parameters which allow for the roundtrip process. The spectra are plotted against the phase ϕ_{13}. The other parameters are chosen as in Fig. IV.7. with $\Delta = -19.5\gamma$.

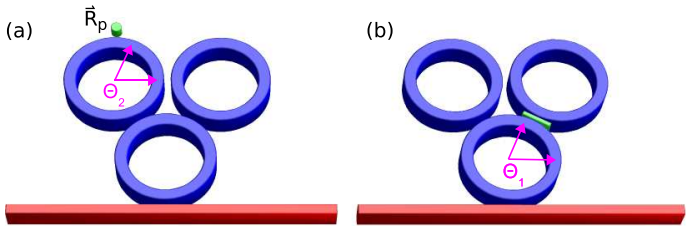

Figure IV.9.: Setups for the two example applications. (a) shows the measurement of the position of a particle at position $\vec{R}_p$ close to resonator 2. (b) shows the measurement of changes in the index of refraction between resonators 2 and 3 induced, e.g., by slabs of different refractive indices.

still remains symmetric, but is also affected by the phase change of ϕ_{13}. In Fig. IV.8. we show T and R in dependence on the phase angle ϕ_{13} for $\Delta = -19.5\gamma$ which is the position of one of the narrow structures. We find that even for small changes of the angle ϕ_{13}, the transmission and reflection changes considerably.

We thus conclude that the possibility of taking a roundtrip pathway in the loop system is the origin of narrow structures in both the transmission and the reflection, and these narrow structures are sensitive to the phases of the coupling constants. This invites applications based on the dependence of these coupling constants on an observable. In the following section we discuss two possible applications based on the sensitivity of the transmission spectrum on the phase angles ϕ_{ij}.

IV.4. Applications[1]

In this section, we discuss two possible applications of our setup. They rely on the dependency of the transmission and reflection on the scattering and coupling parameters. First, we analyze the possibility to detect the position of a small particle such as an atom or a nano object close to one of the resonators as shown in Fig. IV.9.(a). Second, we aim at measuring small changes in the refractive index between two cavities. These changes could be induced by an object placed in the free space, or by embedding the interface area in a liquid. The corresponding setup is sketched in Fig. IV.9.(b).

In the following, we first provide a theoretical background to our calculations, and then discuss numerical results based on the coupled mode theory. Moreover, in the next part in Sec. V.3. we additionally discuss our results for numerical integration of Maxwell's equations on a grid using the FDTD (finite-difference time-domain) method. There, a quantitative analysis for the sensitivity of the suggested precision measurement device for detecting the position of a particle or the refractive index of a thin slab by measuring the transmission intensity is provided.

IV.4.1. Monitoring the position of a nano particle

A sub-wavelength refractive object located very close to one of our cavities as shown in Fig. IV.9.(a) gives rise to a scattering of the fields propagating inside the cavities.

[1] Keyu Xia contributed to this application part with useful ideas and discussions.

This results in damping and in a coupling between counterpropagating WGM pairs $\{a_n, b_n\}$ [35, 176]. The scattering resulting from a nano particle has been studied in [35, 102], where it was demonstrated that the size of a nano particle can be determined using high-Q WGM. This raises the question, whether also the particle position can be determined. To address this question, we note that in the coupled mode theory, the complex electric fields of the modes a_n and b_n in the n-th cavity are related and can be written in cylindrical coordinates $\mathbf{R} = (\rho, \theta, z)^T$ as [102]

$$\mathbf{E}_b^0(\mathbf{R}) = \left(E_\rho^0(\rho,z), iE_\theta^0(\rho,z), E_z^0(\rho,z)\right)^T e^{im\theta} \tag{IV.4.12a}$$

$$\mathbf{E}_a^0(\mathbf{R}) = \left(E_\rho^0(\rho,z), -iE_\theta^0(\rho,z), E_z^0(\rho,z)\right)^T e^{-im\theta}\,. \tag{IV.4.12b}$$

The origin of the used coordinate system is at the center of the WGM cavity. For high-Q WGMs with small loss rates, a_n and b_n are to a good approximation complex conjugates of each other, such that the three components $E_\rho^0, E_\theta^0, E_z^0$ are real functions [102]. We assume that a scattering particle at position $\mathbf{R_p}$ giving rise to a point-like dielectric fluctuation with size much smaller than the wavelength. We denote the dielectric constant of the resonators as ε_c, that of the homogeneous medium surrounding the resonators as ε_s, and that of the medium with added particle as $\varepsilon_p(\mathbf{R})$. The scattering parameter ξ_{nn} is the proportional to the difference $\delta\varepsilon(\mathbf{R}) = \varepsilon_p(\mathbf{R}) - \varepsilon_s$ as well as to the intensity of the electric field at the position of the particle, and can be written as [102, 177]

$$\xi_{nn} = \frac{\omega_m}{2}\frac{\int_{V_p}(\varepsilon_p(\mathbf{R})-\varepsilon_s)\mathbf{E}_a^{0*}(\mathbf{R})\mathbf{E}_b^0(\mathbf{R})d\mathbf{R}}{\int_{V_p}\varepsilon_s|\mathbf{E}_n^0(\mathbf{R})|^2 d\mathbf{R}} \tag{IV.4.13a}$$

$$\propto \delta\varepsilon(\mathbf{R_p})e^{2im\theta_n(\mathbf{R_p})}|\mathbf{E}_n^0(\mathbf{R_p})|^2\,. \tag{IV.4.13b}$$

Here, m is the azimuthal mode number, and in Eq. (IV.4.13b), for simplicity, we set $\mathbf{E}^0(\mathbf{R}) = \mathbf{E}_b^0(\mathbf{R}) = \mathbf{E}_a^{0*}(\mathbf{R})$. It can be seen that the scattering resulting from the particle is a complex number. Its phase depends on the position $\theta_n(\mathbf{R_p})$ of the particle, see Fig. IV.9.(a). According to Eq. (IV.4.13b), this angle enters the phase of the coupling constants via $2m\theta_n(\mathbf{R_p})$, such that an increase of the azimuthal mode number leads to higher position sensitivity, but at the cost of a smaller range of uniquely determined positions, since the phase is only determined modulo 2π. Since we found in the previous sections that the transmission and the reflection in our loop setup is sensitive to the phase of the coupling constants, in principle, a position determination becomes possible.

IV.4.2. Monitoring the dielectric constant of a nano slab

Next, we turn to the measurement of the dielectric constant of a thin object located in the space between two of the cavities and thus influences the coupling between the respective resonators. Alternatively, this slight change of the refractive index could also be induced by the concentration of a fluid between the two resonators, or by varying the temperature [36]. In general, modifying the dielectric constant in between the two cavities gives rise to a change of the coupling of two cavities and to scattering. However, for a larger sample exceeding the wavelength scale, the scattering can be small such that the change in the coupling constant is dominant. In the following, we assume this condition to be fulfilled and neglect the scattering induced by the slab, and consider

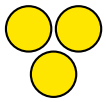

a slab in the region V_{slab}. The total coupling can then be separated into three parts: The coupling without slab $\xi_{nm}^{(0)}$, the contribution $\xi_{nm}^{(slab)}$ from the slab with a reference constant ε_{slab}^{0} inserted in the gap of two cavities, and a change $\delta\xi_{nm}^{(slab)}$ as the dielectric constant of the slab varies according to $\delta\varepsilon_{slab} = \varepsilon_{slab} - \varepsilon_{slab}^{0}$. Thus the total coupling is given by

$$\xi_{nm}^{(0)} = \mathcal{N} \int_{V_{cavity}} (\varepsilon_c - \varepsilon_s)\mathbf{E}_n^{0*}(\mathbf{R})\mathbf{E}_m^{0}(\mathbf{R})d\mathbf{R} \tag{IV.4.14a}$$

$$\xi_{nm}^{(slab)} = \mathcal{N} \int_{V_{slab}} (\varepsilon_{slab}^{0} - \varepsilon_s)\mathbf{E}_n^{0*}(\mathbf{R})\mathbf{E}_m^{0}(\mathbf{R})\, d\mathbf{R} \tag{IV.4.14b}$$

$$\delta\xi_{nm}^{(slab)} = \mathcal{N} \int_{V_{slab}} (\varepsilon_{slab} - \varepsilon_{slab}^{0})\mathbf{E}_n^{0*}(\mathbf{R})\mathbf{E}_m^{0}(\mathbf{R})d\mathbf{R} \tag{IV.4.14c}$$

$$\xi_{nm} = \xi_{nm}^{(0)} + \xi_{nm}^{(slab)} + \delta\xi_{nm}^{(slab)}\,, \tag{IV.4.14d}$$

where

$$\mathcal{N} = \frac{\omega_m}{2}\left(\int \varepsilon_s|\mathbf{E}_n^{0}(\mathbf{R})|^2 d\mathbf{R} \int \varepsilon_s|\mathbf{E}_m^{0}(\mathbf{R})|^2 d\mathbf{R}\right)^{-1/2}. \tag{IV.4.15}$$

Using a similar approximation as in case of the nano particle, the change $\delta\xi_{nm}^{(slab)}$ induced is proportional to $\delta\varepsilon_{slab}$ and given by [102, 177]

$$\delta\xi_{nm}^{(slab)} = \frac{\delta\varepsilon_{slab}}{\varepsilon_{slab}^{0} - \varepsilon_s}\xi_{nm}^{(slab)}\,. \tag{IV.4.16}$$

Thus a large static coupling $\xi_{nm}^{(slab)}$ is favorable. Again, since the transmission and reflection in our setup depend on the coupling constants, such a variation of the coupling constants can be detected.

IV.4.3. Reflection and transmission averaged over coupling and scattering phases

In this section we study the impact of averaging over certain phase angles ϕ_{ij} on the transmission and reflection spectra. In all cases, we average over the full range of 2π. The averaging over the coupling constant phase ϕ_{12} could be visualized as an experimental setting in which the refractive index of the medium between cavity 1 and 2 changes between several measurements, e.g., due to changes in the concentration of a fluid filling this region. The averaging over a scattering constant ϕ_{22} can be visualized as arising from different particle positions throughout the measurements [117].

In general, we find that the averaged curves differ considerably from the curves obtained for fixed phases such as $\phi_{ij} = 0$. Fig. IV.3.(a) shows that averaging over ϕ_{12} or ϕ_{22} lead to the same results, as long as resonators 2 and 3 are uncoupled, i.e., $\xi_{23} = 0$. This can be understood by noting that in case of $\xi_{23} = 0$, all pathways in which ϕ_{12} or ϕ_{22} lead to a final phase shift of the corresponding amplitude include both an interaction with the coupling ξ_{12} and an interaction with the scattering rate ξ_{22}, see Eq. (IV.3.7a). Therefore both averaging possibilities have the same effect.

In contrast, if $\xi_{23} \neq 0$, the spectra averaged over the scattering phase ϕ_{22} or over the coupling phase ϕ_{12} differ, see Fig. IV.10. The reason is that now ϕ_{12} and ϕ_{22} affect

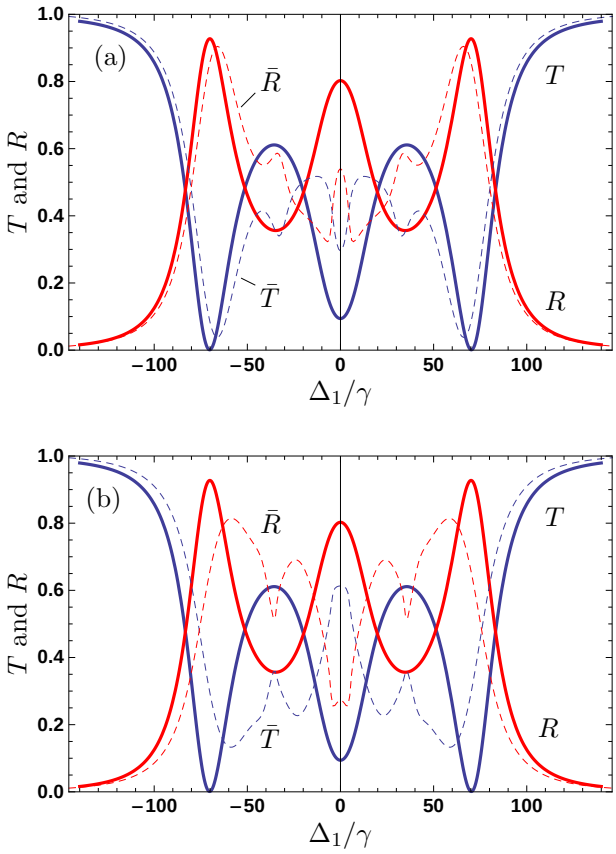

Figure IV.10.: Transmission $T, \bar{T}$ and reflection $R, \bar{R}$ for parameters as in Fig. IV.5. In (a), the solid lines T, R show the case with phases $\phi_{ij} = 0$, the dashed lines $\bar{T}, \bar{R}$ show results averaged over ϕ_{22}. In (b), the solid lines T, R show the case with phases $\phi_{ij} = 0$, the dashed lines $\bar{T}, \bar{R}$ show results averaged over ϕ_{12}.

different pathways. For example, the pathways in Eqs. (IV.3.8a)-(IV.3.8d) include a phase contribution of ϕ_{12}, but not of ϕ_{22}. Thus in contrast to the case without roundtrip process, the averaging over the two phases leads to different results.

IV.5. Summary

In this part, we analyzed interference effects in a system consisting of three coupled microcavities arranged in a loop. In this loop array, light can evolve through the resonators in a non-trivial closed-loop roundtrip. The system is probed by a fiber coupled to one of the resonators. The interplay of the different pathways light can take while passing through the resonator array leads to rich structures in the transmission and reflection spectra of the system. In particular, we have focused on a sensitivity of the spectra on the phases of the different complex scattering and coupling constants. We found, that the roundtrip process in which light moves on a circle through all three cavities, enabled by the special loop arrangement of the resonators, leads to additional pathways which considerably increase the sensitivity of the spectra on the phases. Finally, we

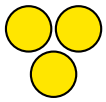

discussed two applications for the studied phase-sensitivity. First, we investigated the determination of the position of a particle placed in the evanescent field of one of the resonators. Second, we analyzed the measurement of the index of refraction of a slab placed between two cavities. Our results are based on coupled mode theory, which allows to interpret the spectra in terms of the underlying physical mechanisms. In order to provide a quantitative analysis of the suggested precision sensing devices, in the next part (in Sec. V.3.) we verify the sensitivity of the transmission spectra by numerical finite-difference time-domain (FDTD) simulations of Maxwell's equations on a grid.

PART V

FDTD simulations

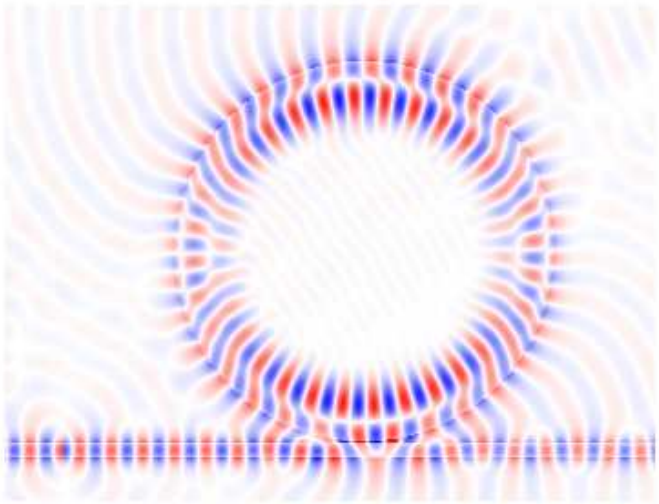

FDTD simulations

In this part, we investigate the light propagation through different coupled systems of whispering gallery mode cavities and fibers by applying FDTD (finite-difference time-domain) simulations to the structures of interest. The method of FDTD with its theoretical background is introduced. Results for the transmission spectra and the mode configuration of the electromagnetic field are presented. We quantitatively study the sensitivity of the setups of the loop array suggested in the preceding part IV as precision measurement devices for the refractive index of a thin slab or the position of a nearby particle. Moreover, we study the transmission spectrum and the radiation characteristics of a disk resonator in the terahertz regime with a hole as finite scatterer. We compare our results to experimental data measured at the Max Planck Institute for the Science of Light in Erlangen and observe a very good agreement. Eventually, we explain how to exploit this system for sensing or microlaser applications.

V.1. Introduction

In this part, numerical FDTD (finite-difference time-domain) simulations are applied on coupled systems of microcavities. FDTD is a very powerful tool to simulate electromagnetic (EM) fields propagating through an arbitrary material structure. This simulation method is used in various fields and for different wavelength regimes. FDTD is for example applied for modeling of room acoustics [178, 179] or underwater acoustic waves [180], low frequency waves around the earth [181, 182] or cancer detection [183]. We use this calculation method in the optical and in the terahertz regime and apply it to our photonic structures. This numerical modeling method, also known as the Yee algorithm was introduced already some decades ago by K. Yee in 1966 [184]. After the pioneering work of A. Taflove and S. Hagness since 1980 [185, 186], applying it to photonic nanostructures has drawn tremendous interest in recent years. With the help of FDTD, the time evolution of an EM field propagating through a defined material structure can be simulated. The dynamics of EM waves can be obtained as long as the refractive indices of the structure's media are known.

The photonic systems of interest often consist of microcavities or photonic crystal structures. Moreover, couplings between nearby particles and microresonators are studied via FDTD [118]. In this case, the atom is simulated as an almost point-like structure of the size of a few nanometers of different refractive index compared to the surroundings.

In our work, on the one hand, we simulate EM wave propagation through the loop

array of three microcavities introduced in the preceding part IV. On the other hand, we investigate a disk resonator in the terahertz regime with a hole which functions as a finite scatterer.

This part is organized as follows. In Sec. V.2., we provide the necessary theoretical background for our numerical FDTD simulations. Firstly, we explain how to implement our systems of material structures on a numerical grid. Adequate boundary conditions for our finite simulation grid are described. Furthermore, we introduce different possible input sources of the electromagnetic field. After these technical comments, we then present our simulation results for different structures. In Sec. V.3., we investigate the loop array system already considered in part IV by applying the FDTD method. We perform a quantitative analysis of the suggested sensing devices for measuring the refractive index of a thin slab or the position of a small nearby particle on a sub-wavelength scale. In Sec. V.4., a disk resonator with a hole as finite scatterer is considered. Here, the observables are the transmission spectrum as well we as the radiation characteristics around the resonator. Finally, we compare our results to experimental data measured by Sascha Preu et al. [187, 188] at the Max Planck Institute for the Science of Light in Erlangen and find a very good agreement between our theoretical simulations and the experimental data.

V.2. Theoretical background of the FDTD simulation technique

In this section, we provide the theoretical background of the FDTD method used for our simulations. We introduce the equations for the EM field which we numerically solve on a grid. Then we show different kinds of sources for the input field and finally describe appropriate boundaries surrounding our finite simulation grid.

V.2.1. Our simulation model

For the electric field $\vec{E}$, the magnetic field $\vec{H}$, the electric flux density $\vec{D}$ and the magnetic flux density $\vec{B}$ Maxwell's equations read [186, 189]

$$\begin{aligned} \frac{\partial \vec{H}}{\partial t} &= -\frac{1}{\mu_{tot}} \nabla \times \vec{E} - \frac{1}{\mu_{tot}} \left(\vec{M}_{source} + \sigma_m \vec{H} \right) , \\ \frac{\partial \vec{E}}{\partial t} &= \frac{1}{\varepsilon_{tot}} \nabla \times \vec{H} - \frac{1}{\varepsilon_{tot}} \left(\vec{J}_{source} + \sigma_e \vec{E} \right) \end{aligned} \tag{V.2.1}$$

Here, $\vec{J}$ is the electric current density, $\vec{M}$ the magnetic current density, $\varepsilon_{tot} = \varepsilon_0 \varepsilon$ the electric permittivity, and $\mu_{tot} = \mu_0 \mu$ denotes the magnetic permeability. ε_0 and μ_0 are the free-space electric permittivity and magnetic permeability, respectively, and ε and μ the relative permittivity and permeability. For our calculations, we set $\mu = 1$. σ_e is the electric conductivity and σ_m the magnetic loss. The energy sources of the electric and magnetic field are described by $\vec{J}_{source}$ and $\vec{M}_{source}$, respectively.

Now, we introduce the general model for our simulations of photonic structures. We assume a 2D system which is located in the x-y plane and in the z direction extended to infinity in the shape of its x-y cross section. We discretize our system on a Yee grid

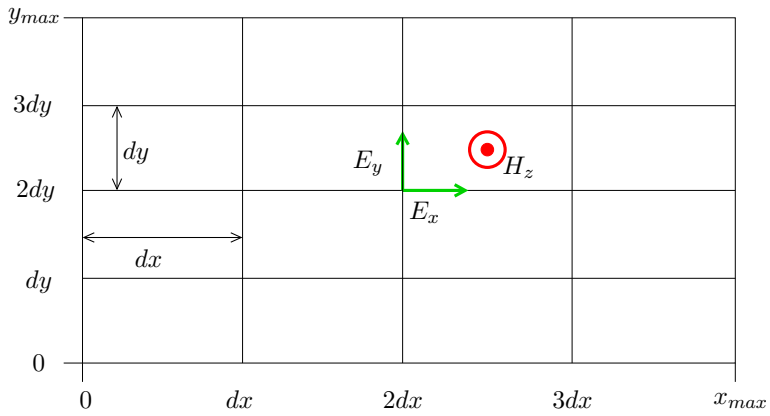

Figure V.1.: Sketch of our Yee grid for TE_z polarized EM field.

in the x-y plane as shown in Fig. V.1. The size of the simulated region is defined by the lengths of the rectangle x_{max} and y_{max}. The grid constant which defines the distance between the discrete points on the grid is dx and is assumed to be equal in the x and y direction, i.e., $dy = dx$. The coordinates x and y are discrete points on the simulation grid, i.e., $x \in \{0, dx, 2dx, .., x_{max}\}$ and $y \in \{0, dy, 2dy, .., y_{max}\}$.

In our work, the structures of interest consist of ring or disk cavities coupled to a fiber, such as, e.g., the loop array depicted in Fig. IV.1. In case of a round shaped photonic structure such as a disk or ring shaped resonator, we have to approximate the shape using our grid points on the rectangular Yee grid. Therefore, the simulated structure is no longer round but approximated via rectangular steps. However, although this is a numerical challenge, this renders our simulated system even closer to the real physical system. In fact, the steps at the resonator's circumference act as "surface roughness" of the resonator's material [190]. This does not only decrease the Q factor of the cavity but also leads to scattering into the counterpropagating WGM [29] which also occurs in experimental setups.

Our physical model consists of a photonic structure surrounded by the vacuum without material boundaries which confine our system. Thus we have no natural boundaries of the system. However, since our computer memory is finite, we can simulate only a finite domain. For this reason, in order to avoid unwanted artifacts such as reflections at the boundaries of the grid, we have to choose appropriate boundary conditions for our simulated rectangle. An extension to infinity is simulated by using absorbing boundaries of the grid. This corresponds to an anechoic chamber for acoustic waves. Different approaches of modeling absorbing boundaries in order to simulate an unbounded area can be found in [186]. The difficulty in creating such boundaries is, that waves have to be perfectly absorbed independent of their angle of incidence without any back reflection to the system. In 1994, Berenger suggested a particularly effective model, the so-called perfectly matched layers (PML) [191]. Since the PML promise very low reflections, in our calculations, we also use these kind of boundaries. In order to simulate a free grid, here, a boundary material composed of an artificial absorbing medium is employed. This medium is a few grid cells thick and surrounds the area of the grid including the structure of interest such as, e.g., resonators and waveguides.

V.2.2. Input source of the EM field

In this paragraph, we introduce the sources of the EM field used for our numerical simulations. There are two main types of sources for the EM field, namely soft and hard sources. A soft source impresses an input current, whereas a hard source impresses an electric field at the position of the source [192]. In order to avoid reflections at the source, we use a soft source for our simulations. On the one hand, we execute simulations with a distributed pulsed source. On the other hand, we perform continuous wave (cw) calculations using a specific resonance frequency of our system as cw input wavelength especially for studying resonance phenomena. We calculate the propagation of the EM field in TE$_z$ polarization, i.e., non-vanishing components of H_z, E_x and E_y, using a field source polarized in the H_z direction placed at the left edge of the waveguide which couples to the resonator structure. For this polarization in 2D, Maxwell's equations Eq. (V.2.1) reduce to

$$\begin{aligned}
\frac{\partial E_x}{\partial t} &= \frac{1}{\varepsilon_{tot}}\left[\frac{\partial H_z}{\partial y} - \left(J_{source_x} + \sigma_e E_x\right)\right] , \\
\frac{\partial E_y}{\partial t} &= \frac{1}{\varepsilon_{tot}}\left[-\frac{\partial H_z}{\partial x} - \left(J_{source_y} + \sigma_e E_y\right)\right] , \\
\frac{\partial H_z}{\partial t} &= \frac{1}{\mu_{tot}}\left[\frac{\partial E_x}{\partial y} - \frac{\partial E_y}{\partial x} - \left(M_{source_z} + \sigma_m H_z\right)\right] .
\end{aligned} \tag{V.2.2}$$

In the following, we calculate the appropriate mode profile for a distributed pulsed input source. Since we assume the material parameters to be independent of frequency and time in the frequency regime of interest, Maxwell's equations reduce to the Helmholtz equation for the electric field

$$\Delta\vec{E} = \frac{n^2}{c^2}\frac{\partial^2\vec{E}}{\partial t^2} , \tag{V.2.3}$$

where n is the refractive index of the medium the EM field is propagating through. Analogously, this also holds for the magnetic $\vec{H}$ field. In principle $n \in \mathbb{C}$, where the imaginary part is the material's specific absorption. However, in our calculations we assume a real index of refraction, i.e., the internal absorption of the material is assumed to be negligibly low. If we know the refractive index on the line parallel to the y axis where the input source is located, we can solve the discrete Helmholtz equation

$$0 = \frac{U(y+dy) + U(y-dy) - 2U(y)}{dy^2} + (n_y^2 - \beta^2)\left(\frac{2\pi}{\lambda}\right)^2 U(y) \tag{V.2.4}$$

Here, $y \in \{y_w - r_s, .., y_w + r_s\}$ and n_y is the refractive index at position (x_s, y). x_s is the x coordinate of the source and r_s the source's radius, i.e., its extension in y direction. y_w is the y value of the waveguide's center and β the propagation constant. We calculate the eigenvalues and eigenvectors of the coefficient matrix with respect to the $U(y)$ variables. Then the input mode profile is given by the normalized eigenvector belonging to the eigenvalue with the lowest absolute value, i.e., the fiber's eigenmode of minimum energy.

V.2.3. Observables

In our investigations, we are interested in three main observables: The field configuration in our system, the transmission spectrum and the radiation characteristics. The field

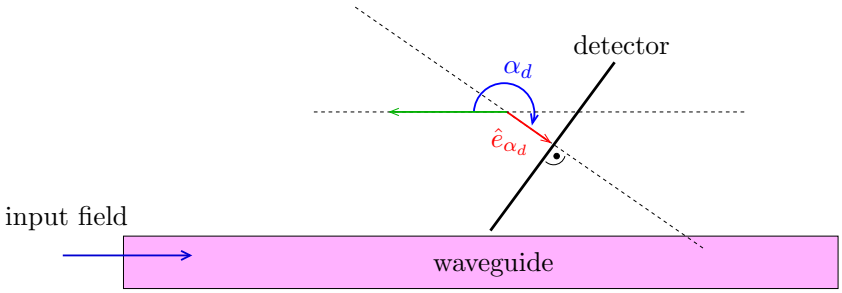

Figure V.2.: Orientation of the detector for the calculation of the Poynting vector.

configuration is calculated at different times during our simulations. From the values of the $\vec{E}$ and $\vec{H}$ components we can see how light propagates through our system and where resonant modes are excited.

In order to calculate the spectrum normally incident on a certain region within the x-y plane, we place a one dimensional detector into our simulation grid. This detector is a line of length l_d in our simulated rectangle which detects the orthogonally incident power, i.e., the absolute value of the Poynting vector component in the respective direction summed over all grid points on the respective detector line. Afterwards, this sum is normalized by the input power. The orientation of the detector is defined by the angle α_d. As shown in Fig. V.2., α_d is the angle between the vector pointing into negative propagation direction of the input flux in the waveguide and the unit vector $\hat{e}_{\alpha_d}$ normally incident on the detector plane. Note that choosing the same detector plane with the inclination angle $\alpha_d - \pi$ is possible and means considering the component of the Poynting vector at the same position, however, in opposite direction.

The Poynting vector, which is a measure for the field energy flux density is defined as

$$\vec{S}(\vec{x},t) = \vec{E}(\vec{x},t) \times \vec{H}(\vec{x},t)\,. \tag{V.2.5}$$

Its absolute value $|\vec{S}(\vec{x},t)|$ has the units $\frac{[\text{energy}]}{[\text{time}]\cdot[\text{area}]}$. For our definition of the orientation of the detector as shown in Fig. V.2., the component of the $\vec{E}$ field normally incident on the detector is calculated using the inclination angle α_d as

$$E_\perp(\vec{x},t,\alpha_d) = -E_x(\vec{x},t)\sin\alpha_d - E_y(\vec{x},t)\cos\alpha_d\,. \tag{V.2.6}$$

Hence, the component of the Poynting vector normally incident on a detector whose inclination angle is α_d can be calculated as

$$\vec{S}(\vec{x},t,\alpha_d) = E_\perp(\vec{x},t,\alpha_d)\cdot H_z(\vec{x},t)\hat{e}_{\alpha_d}\,, \tag{V.2.7}$$

where $\hat{e}_{\alpha_d}$ is the unit vector normally incident on the detector plane, see Fig. V.2. Note that in our 2D model, $\vec{H}$ is always oriented into the z direction and thus independent of α_d. However, since we are interested in the incident power spectrum, i.e., the incident power as function of the frequency ω, we have to Fourier transform the respective fields before calculating the Poynting vector.

For this reason, we calculate the Fourier transform of the time signal for each detector point $\vec{x}$ and obtain $E_\perp(\vec{x},\omega,\alpha_d)$ and $H_z(\vec{x},\omega)$. Therewith we calculate the incident energy flux density for the respective frequency ω as

$$S(\vec{x},\omega,\alpha_d) = E_\perp(\vec{x},\omega,\alpha_d)\cdot H_z(\vec{x},\omega)\,. \tag{V.2.8}$$

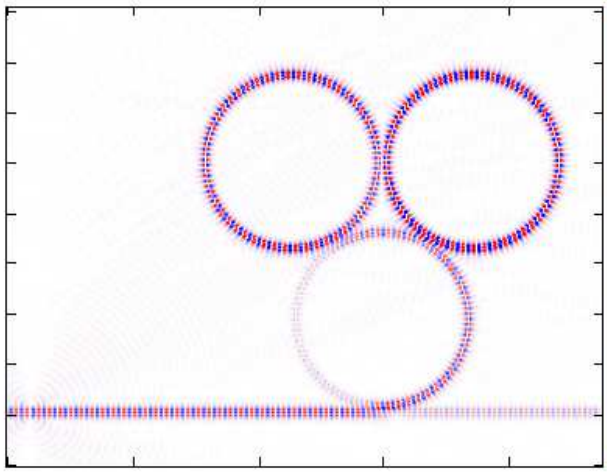

Figure V.3.: Configuration of the field component H_z obtained from the FDTD-simulation for three resonators in loop configuration without particle or slab, see also part IV. The image shows one snapshot in time. The excitation wavelength is $\lambda = 577.21$ nm.

This component of the Poynting vector in frequency space has the unit $\frac{[\text{energy}]\cdot[\text{time}]}{[\text{area}]}$. Since we are interested in the normally incident energy onto the whole detector, we sum up these Poynting vector values over all points $\vec{x}$ belonging to the detector line and thus obtain $S(\omega)$. In general, $S(\omega)$ can be negative. This is to be interpreted as a resulting energy flux in $-\hat{e}_{\alpha_d}$ direction. However, in our calculations, we choose a detector plane, where the Poynting vector always points into the same direction and therefore the angle α_d is chosen in such a way that $\vec{S}(\vec{x}, t, \alpha_d) \cdot \hat{e}_{\alpha_d}$ and $\vec{S}(\vec{x}, \omega, \alpha_d) \cdot \hat{e}_{\alpha_d}$ and thus also $S(\omega)$ have only positive values.

In order to determine the output transmission intensity or spectrum through the coupling waveguide, we place a detector at the right end of the fiber. This detector is orientated orthogonal to the fiber ($\alpha_d = \pi$), i.e. we calculate the component of the Poynting vector in propagation direction in the fiber. The normalized transmission spectrum is defined as

$$T(\omega) = \frac{|S(\omega)|}{|S(\omega)|_{fiber}}\,, \tag{V.2.9}$$

where the index $fiber$ refers to the case where no material structure except the waveguide is present. Since for the calculation of $|S(\omega)|$ and $|S(\omega)|_{fiber}$ the fields are detected over the same period of time which also defines the integration time of the Fourier transform, the transmission $T(\omega)$ can also be understood as the normalized time averaged power spectrum.

When studying the radiation characteristics as a function of the radiation direction, we place several detectors around our structure, e.g., a disk resonator, and calculate the incident power for the respective frequency ω of the cw input field radiated into the different directions.

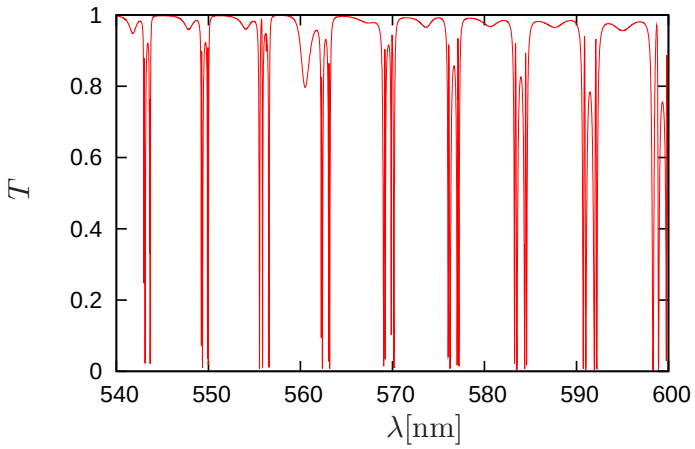

Figure V.4.: Transmission spectrum obtained from FDTD simulations for three resonators in loop configuration with neither particle nor slab.

V.3. Loop array of three microcavities[1]

In this section, we numerically verify the suggested applications for the loop array introduced in part IV using a FDTD solution of Maxwell's equations on a 2D grid (see Eq. (V.2.2)) [185, 186]. A quantitative analysis of the proposed applications of this setup as precision sensing devices for the refractive index of a thin slab or the position of a nearby particle is presented.

The simulations consider two dimensions for TE_z modes propagating in the x direction (field components E_x, E_y, H_z) on a Yee-grid with a grid size of 10 nm. Note that the grid size not only determines the accuracy of the finite-difference approximation, but also introduces a surface roughness for the resonators due to the staircase approximation applied to implement the curved surfaces [29, 190]. The grid boundaries are modeled using Berenger-type perfectly absorbing boundary conditions, and we use a pulsed soft source in H_z with a mode profile obtained from numerically solving the transversal Helmholtz equation, see Sec. V.2. We consider a background with relative permittivity $\varepsilon_s = 1$, and resonators and a waveguide with relative permittivity $\varepsilon_c = 4$. The waveguide resonators have an outer radius of 3500 nm and an inner radius of 3350 nm. The distance between waveguide and resonator is 120 nm, the distances between the resonators are chosen equal as 200 nm. The waveguide has a width of 150 nm.

To illustrate the effect of the loop configuration, we have additionally calculated the field configuration for monochromatic continuous wave driving close to a resonance of the system. A typical result is shown in Fig. V.3. The figure shows the field component H_z after the time evolution has reached a stationary state. The source is in the lower left corner, and is placed in the center of the waveguide which runs along the lower edge of the figure. Since the source does not exclusively excite waveguide modes, circularly spreading background waves of relatively low intensity originating from the source can be seen as well. The excitation then runs along the waveguide to the three resonators seen as the circular field arrangements. In this particular example, the two upper cavities

[1] Helpful discussions with Keyu Xia as well as his contribution to the FDTD simulation code which was used and further developed for this project are appreciated.

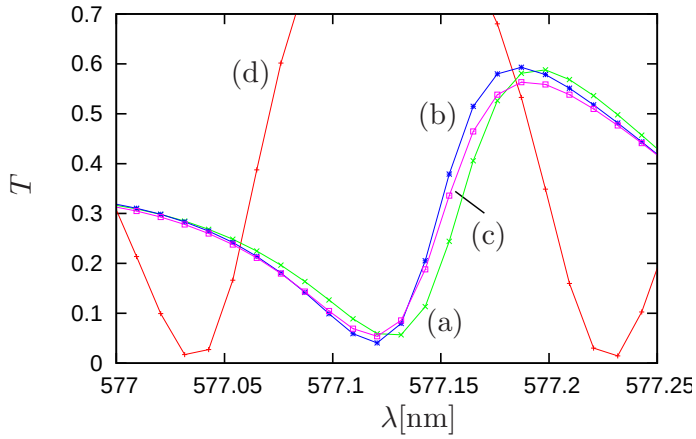

Figure V.5.: Transmission spectrum obtained from FDTD simulations for three resonators in loop configuration with a particle placed close to the top left resonator. The different curves show spectra for the particle positions (a) $\theta = 90°$, (b) $\theta = 95°$, and (c) $\theta = 180°$, whereas (d) shows the result for the case without nearby particle.

contain standing wave excitations, which manifest themselves as modulated total intensity ("blinking") in the time-dependent dynamics of the field configuration. The right half of the lower cavity exhibits a less pronounced standing wave, whereas the left half is mostly filled by a running wave in clockwise direction. This "blinking" can be seen by comparing the figure to a corresponding snapshot slightly later in time. If the time is chosen appropriately, the time evolution of the standing waves is close to a minimum, such that the bright field regions in Fig. V.3. are almost invisible. In contrast, the running wave parts remain similar. In total, the setup in Fig. V.3. leads to a weak forward transmission $(T \ll 1)$, which can be seen from the low field excitation downstream of the resonators. Instead, the energy is mostly reflected, which again is evidenced by standing wave field components in the waveguide between source and resonators. In contrast, the other waveguide parts only carry running wave excitations, as expected.

To evaluate the transmission, we sum over the Poynting vector components in frequency space obtained by the Fourier transformed fields for all points in the plane transversal to the waveguide to the right of the resonators, see Sec. V.2. According to Eq. (V.2.9), the obtained energy flux for each ω is normalized with respect to the case without resonators. A typical example for a transmission spectrum of this loop system is shown in Fig. V.4.

For the applications, we add a particle or a slab to the cavities as indicated in Fig. IV.9. In our simulations, the particle has a radius of 90 nm, and it is placed at different azimuthal positions with a radial distance of 90 nm to the top left cavity. The transmission spectrum around one spectral dip is shown for different particle positions in Fig V.5. Other than the azimuthal position, no parameters are changed between the three curves (a), (b) and (c) in this figure whereas curve (d) shows the transmission for the case without nearby particle. It can be seen that changing the position leads to a shift of the resonance line in the transmission spectrum. This shift can be observed over a large range of position values, as indicated by the lines with $\theta = 90°$ and $\theta = 180°$. On the other hand, a shift can already be observed for a change of position by $\Delta\theta = 5°$. This has to be compared to the angular range of about $7°$ for one wavelength in the azimuthal mode number 52

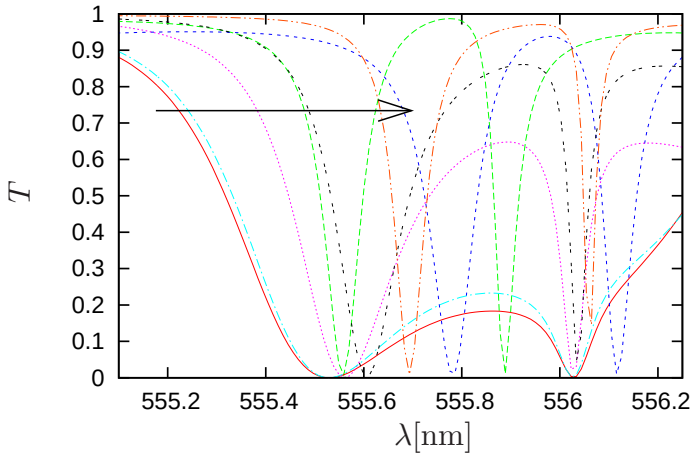

Figure V.6.: Transmission spectrum obtained from FDTD simulations for three resonators in loop configuration with a slab placed between the two rightmost cavities, see Fig. IV.9.(b). The curves show two spectral lines at different wavelengths. In direction of the arrow the graphs correspond to the case with a slab with relative permittivity $\varepsilon = 4.0$, $\varepsilon = 4.001$, $\varepsilon = 4.01$, $\varepsilon = 1$ (without slab), $\varepsilon = 4.02$, $\varepsilon = 4.05$, $\varepsilon = 4.1$.

realized in this numerical example, see the mode configuration in Fig. V.3. The shift is periodic with a particle movement of one wavelength.

Fig. V.6. shows corresponding results for a slab. The slab has a width of 60 nm, a length 1500 nm and is placed symmetrically between the two rightmost resonators as shown in Fig. IV.9.(b). We consider slabs with relative permittivity $\varepsilon = 4.0$, $\varepsilon = 4.001$, $\varepsilon = 4.01$, $\varepsilon = 4.02$, $\varepsilon = 4.05$, and $\varepsilon = 4.1$. Fig. V.6. shows a few resonances in the transmission spectrum. It can be seen that the change in the relative permittivity from 4.0 to 4.1 shifts the position of a resonance line considerably. It is interesting to note that not the whole spectrum is shifted, but some parts of the spectral lines are shifted more than other parts.

We thus conclude that the FDTD simulations of the considered loop systems with additional particle or slab serve as a proof of principle for the applications discussed in Sec. IV.4. While a direct connection to the coupled-mode calculations presented in part IV is not possible since the individual coupling constants and resonator properties realized in the numerical simulations are unknown, both the variation of the particle position and the index of refraction of the slab led to a considerable shift of resonance lines in the transmission spectrum. According to our results, the position of an atom on a sub-wavelength scale as well as a change in the relative permittivity of a thin slab of 0.01 should be detectable with our setup.

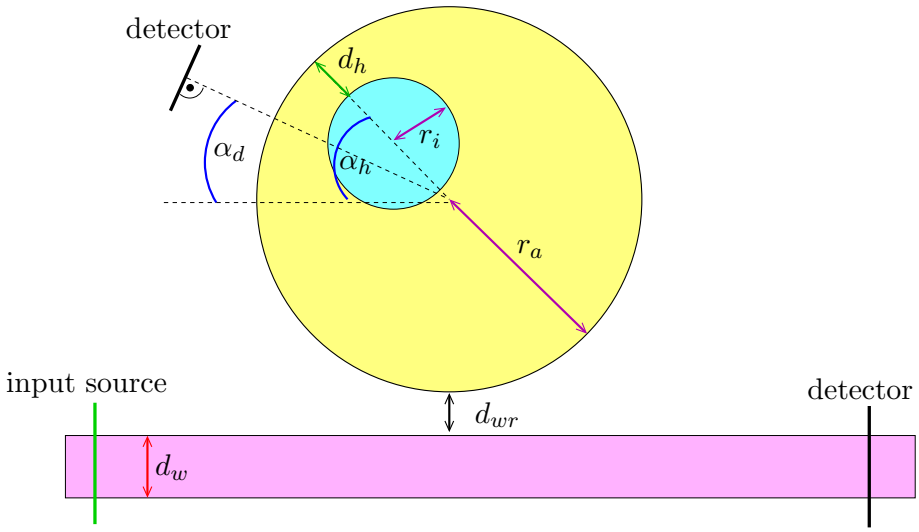

Figure V.7.: Setup for our simulations of a disk cavity with hole.

V.4. Disk resonator with a hole as finite scatterer[1]

V.4.1. The model system

In this section, we consider a structure consisting of a disk cavity with a hole coupled to a fiber as shown in Fig. V.7. The disk resonator has a radius r_a and a hole of radius r_i. The distance between the resonator's boundary and the hole is d_h. The hole in the disk resonator functions as a finite scatterer. Due to the different refractive index inside the hole as well as the surface roughness of the hole boundary, scattering of WGMs into the counterpropagating part of the WGM pair occurs. Moreover, via this scattering process, the presence of the hole leads to an energy shift of the system's resonances.

V.4.2. Results for the transmission spectrum

We start by calculating the transmission spectrum for a disk resonator with radius $r_a = 12.5$ mm of a material with relative permittivity $\varepsilon_{cav} = 2.56$. The center wavelength of the input pulse is $\lambda_c = 3$ mm which corresponds to a frequency of 100 GHz. Our results are shown in Fig. V.8. In the upper subfigure V.8.(a), we present the spectra for a disk without hole (red) and for two different holes, one of radius $r_i = 0.75$ mm (green) and one of $r_i = 1.5$ mm (blue). The holes' centers are located at a distance of 9.75 mm from the disk's center which results in distance $d_h = 2$ mm and $d_h = 1.25$ mm, respectively, from the cavity's boundary. We choose $\alpha_h = 90°$, yet, we found for the transmission spectrum, that the influence of the angle α_h on the dip positions is negligible. In the result for the disk without hole, clear resonances, most of them with transmission $T < 0.2$, are visible. Between these clear resonance dips, further less prominent dips can be observed.

[1] This project is part of a cooperation with Harald Schwefel of the University of Erlangen-Nuremberg and his experimental group in the division of Gerd Leuchs at the Max Planck Institute for the Science of Light in Erlangen. The main part of the experiments referred to have been performed by Sascha Preu. Helpful discussions with Harald Schwefel, Sascha Preu, and Florian Sedlmeir as well as the permission to show the experimental data here are very much appreciated.

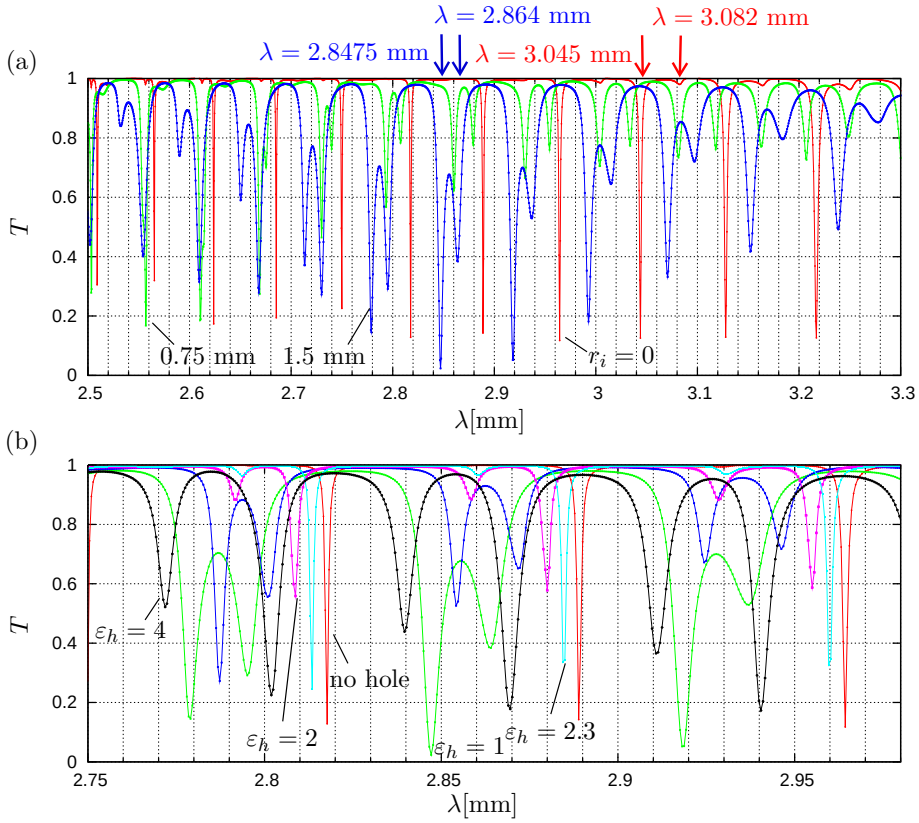

Figure V.8.: Transmission spectra for a disk resonator with $r_a = 12.5$ mm without hole and with holes of different sizes at $\alpha_h = 90°$. (a) Spectra for disk without hole ($r_i = 0$), for a hole with $r_i = 0.75$ mm and a hole with $r_i = 1.5$ mm. (b) Spectra for disk without hole, $r_i = 1.5$ mm and different relative electric permittivities inside the hole of $\varepsilon_h = 1$, $\varepsilon_h = 1.5$, $\varepsilon_h = 2$, $\varepsilon_h = 2.3$, and $\varepsilon_h = 4$.

In case of $r_i = 0.75$ mm and $r_i = 1.5$ mm, both these dips are clearly visible and their relative separation $\Delta\lambda$ depends on the hole's radius. Additionally, all resonances are shifted due to scattering processes occurring at the hole and the surface roughness of the hole's boundaries. We found that the dip splitting occurs due to scattering by the hole into another resonant radial mode as can be seen in Fig. V.9. In this figure, we show the field configuration of the component H_z for the four resonance wavelengths marked in the spectra of Fig. V.8.: without hole ($\lambda = 3.045$ mm and $\lambda = 3.082$ mm) and with hole ($\lambda = 2.8475$ mm and 2.864 mm), respectively.

In the lower subfigure V.8.(b), we show the transmission spectra for the larger hole with $r_i = 1.5$ mm for different refractive indices inside the hole. In an experiment, this could be realized, e.g., by guiding a fluid via a thin tube through the hole and changing the concentration of a dissolved substance. For our calculations, the relative permittivity inside the hole is chosen as $\varepsilon_h = 1$, $\varepsilon_h = 1.5$, $\varepsilon_h = 2$, $\varepsilon_h = 2.3$, and $\varepsilon_h = 4$, respectively. In case of ε_h similar to ε_{cav} of the disk, e.g., $\varepsilon_h = 2.3$, we see pairs of dips where one part is very weak, similar to the result for the disk without hole. Increasing the permittivity difference increases the splitting. We observe that both the wavelengths and the splitting of the resonance dips strongly depend on ε_h. This effect could be used to measure the

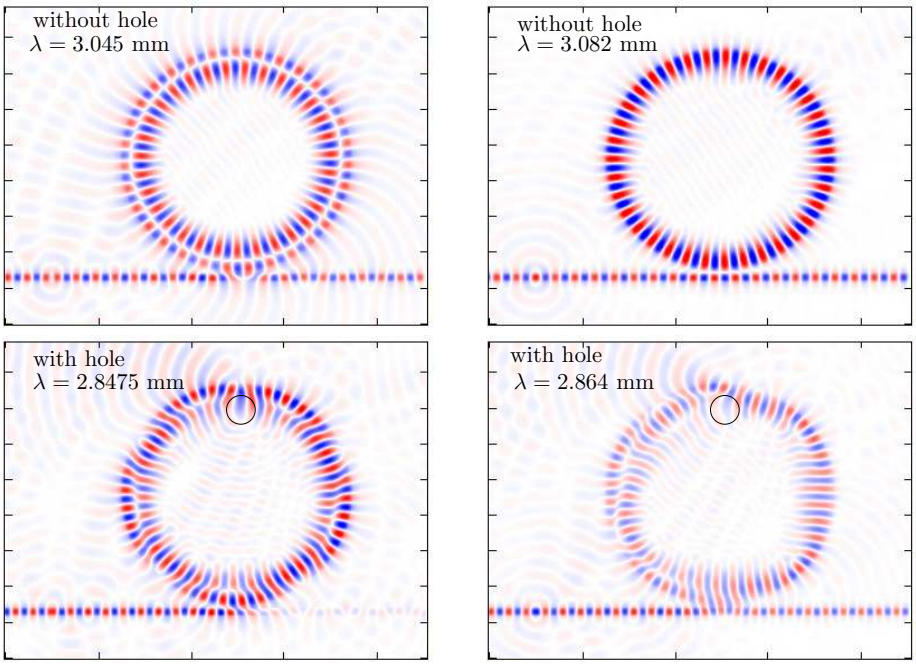

Figure V.9.: Field component H_z to demonstrate the mode structure inside the cavity for split modes obtained for the resonator with $r_a = 12.5$ mm without and with hole of $r_i = 1.5$ mm and at $d_h = 1.25$ mm for the respective resonance wavelength marked in Fig. V.8.(a). The position of the hole is marked by a black circle.

refractive index of the substance inside the hole. Concerning the sensitivity of such a measurement device, we found that for a change in the relative permittivity of 0.1 from $\varepsilon_h = 2.3$ to $\varepsilon_h = 2.4$ the main transmission dips in the wavelength region plotted in Fig. V.8.(b) are shifted by 0.001 mm.

We proceed with simulations performed for parameters corresponding to an experimental setup at the Max Planck Institute for the Science of Light in Erlangen. Here, the dimensions are $r_a = 5.2$ mm, $r_i = 0.51$ mm and PE with $\varepsilon_{cav} = 2.25$ in the terahertz regime is used as cavity material. In the experiment, the hole is located at $d_h = 0.41$ mm from the resonator's boundary. The resonator couples to a 1 mm thick teflon waveguide with $\varepsilon_{wg} = 2.07$. Fig. V.10. shows our result for the transmission spectrum of this disk resonator with and without hole. For the wavelength regime of interest, within the experimental measurement inaccuracy of the resonator dimensions of 0.1 mm, these two curves are in very good agreement with the experimental data measured by Sascha Preu et al., see [187, 188]. The small difference can be explained by slightly differing radii, originating from the rectangular approximation of the round structure on the simulation grid as well as the experimental measurement inaccuracy. We found that increasing the radius of the disk by 0.1 mm already leads to larger shifts in the spectrum than the here observed difference between the experimental and the simulation results. Additionally, the finite thickness of the disk in the experiment (in the order of a few mm) leads to a 3D effect we do not take into account in our 2D simulations. The extension into the z direction causes an effective value ε_{eff} with $\varepsilon_{eff} \in [1, \varepsilon_{cav}]$. The larger discrepancy for $\lambda < 1.5$ mm should be explainable in terms of dispersion effects and the frequency depen-

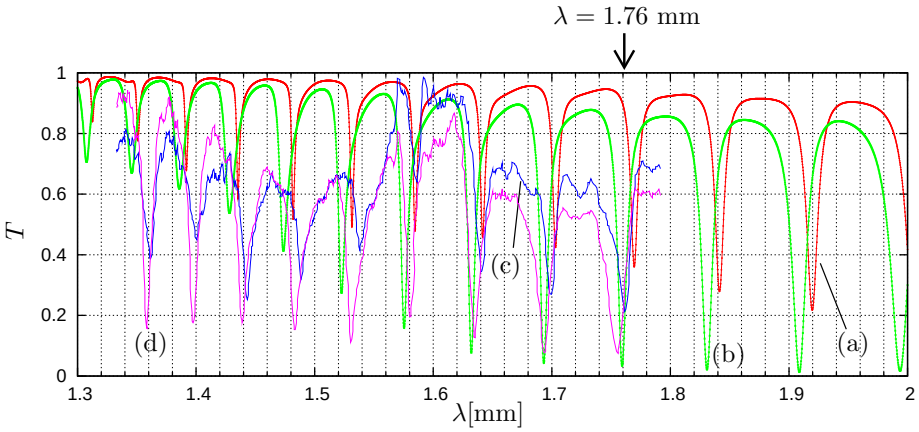

Figure V.10.: Transmission spectrum for a disk resonator of radius $r_a = 5.2$ mm without hole and with hole of $r_i = 0.51$ mm at $d_h = 0.41$ mm. (a) simulation results without hole and (b) simulations results with hole, (c) experimental data for disk without hole, (d) experimental data for disk with hole. For the simulation $\alpha_h = 90°$ whereas in the experiment α_d was not measured, since this angle has negligible impact on the transmission spectrum.

dence of the 3D effects. This means, especially for shorter wavelengths, we would have to calculate with another effective value of ε_{cav} in order to obtain a better agreement with the experimental data.

In Fig. V.11., we show results for the transmission for different refractive indices inside the hole. In the direction of the black arrow in this figure $\varepsilon_h = 3$, $\varepsilon_h = 15$, $\varepsilon_h = 1$, $\varepsilon_h = 10$, and $\varepsilon_h = 6$. In this plot, a clear dependence of the resonances on the permittivity in the hole can be observed. The positions of the dips in the transmission for $\varepsilon_h = 1$ and $\varepsilon_h = 3$ differ by around 0.015 mm. Although the curves for $\varepsilon_h = 3$ and $\varepsilon_h = 15$ seem to have minima at similar positions, we found that these minima do not belong to the same resonances but the change of the refractive index is high enough to shift the spectrum by more than one free spectral range. For even higher ε_h such as $\varepsilon_h > 20$, the system's resonances are shifted out of the plot region of Fig. V.11.

Next, we study the dependence of the spectrum on the position of the hole. Since the light intensity is not homogeneously distributed over the disk but concentrated to a circle of an effective radius smaller than the disk radius r_a, the scattering is modified depending on the hole position. In Fig. V.12., we show our results for different positions of the hole. We present the results for two different relative permittivities inside the hole, namely (a) $\varepsilon_h = 1$ (vacuum) and (b) $\varepsilon_h = 6$. The distance of the hole (in the direction of the black arrows in the figures) is chosen as $d_h = 0.2$ mm, $d_h = 0.41$ mm, $d_h = 0.6$ mm, $d_h = 0.8$ mm, and $d_h = 1$ mm. In both cases (a) and (b), a shift of the resonance dips is observable when changing the hole position. We found, that the direction of the shift depends on whether the refractive index inside the hole is smaller or larger as compared to the refractive index of the resonator's material. For $\varepsilon_h < \varepsilon_{cav}$ as in Fig. V.12.(a) the dips are shifted to shorter wavelengths with increasing d_h. By contrast, for $\varepsilon_h > \varepsilon_{cav}$ as in Fig. V.12.(b) the dips are shifted to longer wavelengths with increasing d_h. We checked this for a number of values between $\varepsilon_h = 1$ and $\varepsilon_h = 20$. The shift increases with increasing permittivity difference $|\varepsilon_h - \varepsilon_{cav}|$. For the parameter regime shown in

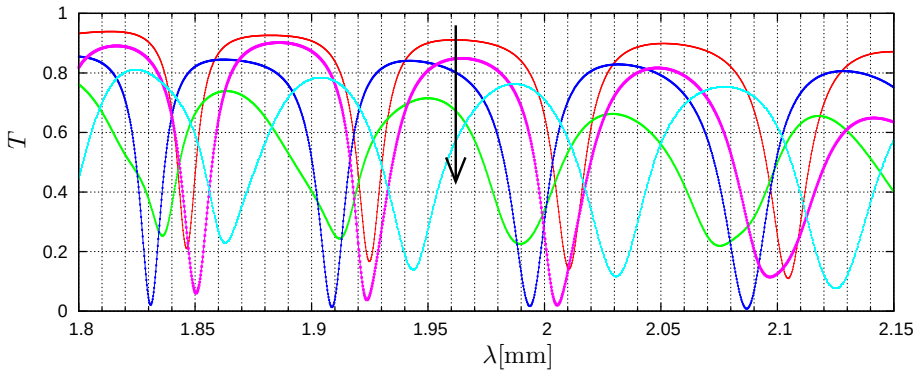

Figure V.11.: Transmission spectra for disk resonator with radius $r_a = 5.2$ mm without hole and with hole for different relative permittivities inside the hole ε_h. In the direction of the arrow $\varepsilon_h = 3$, $\varepsilon_h = 15$, $\varepsilon_h = 1$, $\varepsilon_h = 10$, and $\varepsilon_h = 6$. All further parameters are chosen as in Fig. V.10.

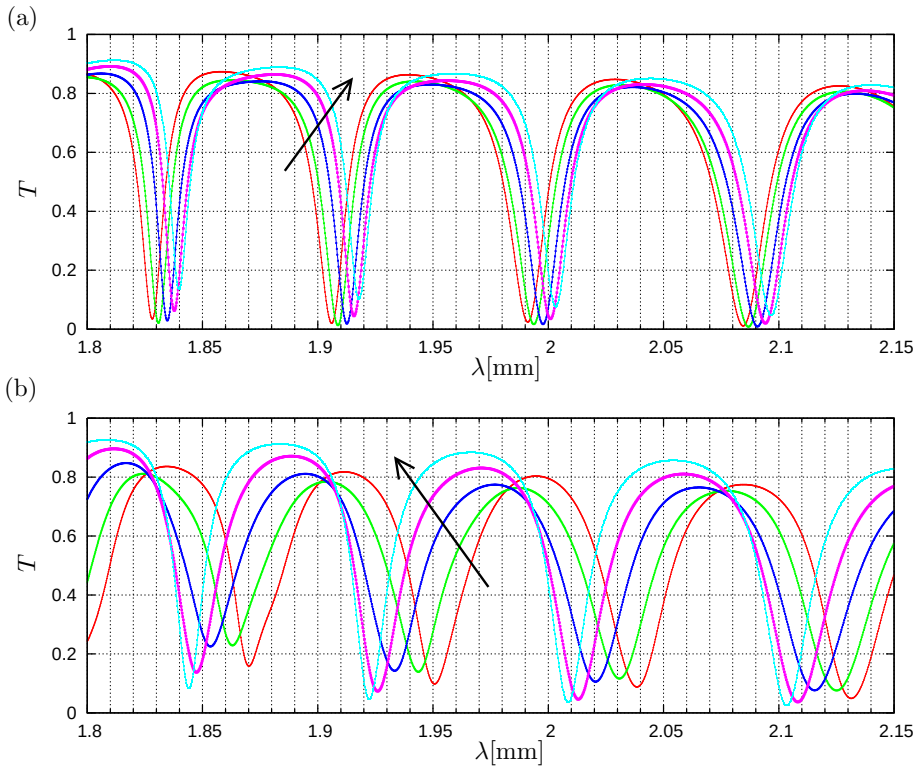

Figure V.12.: Transmission spectra for different hole positions for a disk with radius $r_a = 5.2$ mm. In the direction of the arrows in the figures the hole is located at a distance from the resonator's boundary of $d_h = 0.2$ mm, $d_h = 0.41$ mm, $d_h = 0.6$ mm, $d_h = 0.8$ mm, and $d_h = 1$ mm. In (a) the relative permittivity inside the hole is $\varepsilon_h = 1$ and in (b) $\varepsilon_h = 6$. All further parameters are chosen as in Fig. V.10.

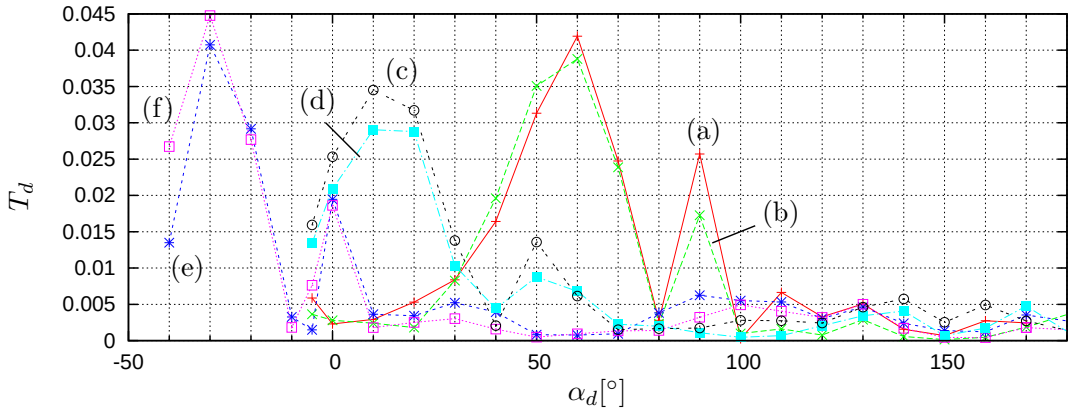

Figure V.13.: Radiation characteristics as a function of the detector position α_d for the disk resonator with $r_a = 5.2$ mm and with hole of $r_i = 0.51$ mm for two different resonance wavelengths and three different hole positions calculated at a distance of $r_d = r_a + 2$ mm from the center of the disk. (a) $\alpha_h = 90°$ and $\lambda = 1.76$ mm, (b) $\alpha_h = 90°$ and $\lambda = 1.692$ mm, (c) $\alpha_h = 45°$ and $\lambda = 1.76$ mm, (d) $\alpha_h = 45°$ and $\lambda = 1.692$ mm, (e) $\alpha_h = 0°$ and $\lambda = 1.76$ mm, and (f) $\alpha_h = 0°$ and $\lambda = 1.692$ mm.

Fig. V.12.(a), at $\varepsilon_h = 1$ a movement of the hole of $\Delta d_h = 0.2$ mm leads to a shift of $\Delta\lambda \approx 0.004$ mm whereas for $\varepsilon_h = 6$ this shift already amounts to $\Delta\lambda \approx 0.01$ mm. If d_h is too large, the shift decreases since the overlap between the hole and the radial region, where the intensity is high, becomes smaller.

V.4.3. Results for the radiation characteristics

In this section, we investigate the radiation behavior of the disk resonator with hole. In [193], unidirectional light emission from high-Q modes of a free disk cavity which is not coupled to a waveguide was found for TM_z polarized light. Motivated by an experiment performed at the Max Planck Institute for the Science of Light in Erlangen [187, 188], in which the far field radiation of a disk with hole coupled to an external fiber for a TE_z polarized terahertz source was measured, we perform a FDTD simulation for this system and calculate the radiated intensity in the near field around the disk resonator with $r_a = 5.2$ mm already considered in the last section V.4.2. Here, the term near field denotes the field in a region around the resonator with a distance not larger than the cavity dimensions from the resonator's boundary. This definition is chosen since we observe typical near field effects with non-radial scattering in this area, even though the distance from the scattering object, i.e., the resonator, is not small as compared to the wavelength. We explain the major structures in the far field radiation in terms of near field effects.

For the simulation, we place small detectors of size $l_d = 0.4$ mm at a distance of $r_d = r_a + 2$ mm$= 7.2$ mm from the center of the resonator at different angles α_d around the disk cavity. For the angle definitions see Fig. V.7. We calculate the component of the Poynting vector normally incident on the respective detector plane for a period of time when the system has reached a steady state. T_d denotes the radiation normally incident on the respective detector normalized by the transmission through the waveguide without

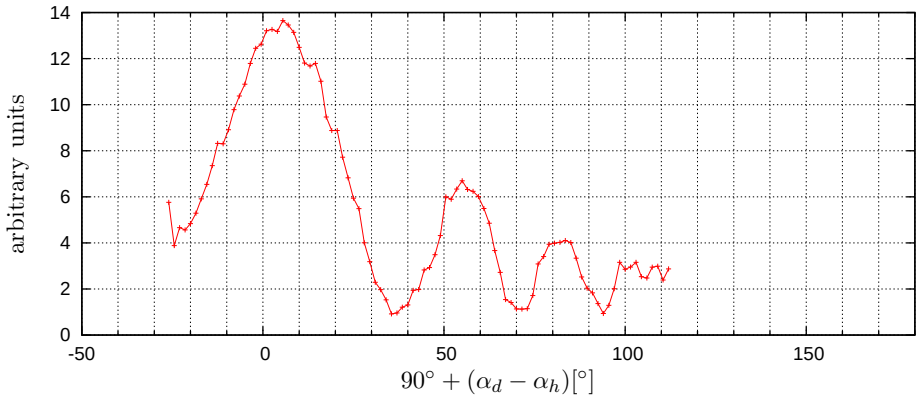

Figure V.14.: Experimental data for the far field radiation characteristics for the disk resonator with $r_a = 5.2$ mm and with hole of $r_i = 0.51$ mm for the resonance wavelength $\lambda = 1.754$ mm measures with a detector of $15°$ aperture at a distance of $r_d \approx 10$ cm from the center of the disk. In the experiment, the relative angle $\alpha_h - \alpha_d$ was measured and the hole position is not exactly clear.

resonator. We perform calculations for three different hole positions with respect to the coupling point of the fiber to the resonator $\alpha_h = 0$, $\alpha_h = 45°$ and $\alpha_h = 90°$ and for two different resonance wavelengths $\lambda = 1.76$ mm and 1.692 mm (this corresponds to the frequencies of 170.5 GHz and 177.3 GHz). Our results are shown in Fig. V.13. From this figure we can see, that a clear maximum occurs at an angle around $\alpha_h - 30°$ and a weaker maximum is visible at around α_h itself. Relative to the hole's position α_h, the structure of the curves is similar for the different hole positions. Note that the detectors with $\alpha_d < -40°$ are very close to the waveguide and thus effects occurring due to light leaking out of the waveguide would modify the result for the radiation for smaller α_d.

For a quantitative estimate, we compare the detected T_d to the results obtained for a completely isotropic and radial radiation of the input light. If the reflection for $\lambda = 1.76$ mm was zero, all input light would be radiated by the cavity since $T \approx 0$ (see Fig. V.10.). Additionally assuming all light is radiated isotropically and radially by the cavity, each detector would detect $\frac{0.4 \text{ mm}}{2\pi \cdot 7.2 \text{ mm}} \approx 0.88\ \%$ of the input light. Comparing this to the portions shown in Fig. V.13., we find that the radiation intensity into specific directions is enhanced by a factor 3-5 for the two highest maxima. Note that this estimate is very conservative since we considered the case without reflection as reference. In reality, the reflection is generally by far not negligible and the radiation is neither completely isotropic nor completely radial.

In order to get a better understanding of the radiation behavior of the system, we additionally calculate the radiated intensity for a larger distance of the detectors from the resonator, namely $r_d = r_a + 5$ mm$= 10.2$ mm. We found, that the large maximum is then located at around $\alpha_h - 60°$ whereas the lower maximum at α_h vanished. Instead, two new maxima occur at around $\alpha_h - 10°$ and $\alpha_h + 10°$.

In the following, we explain the peaks of our simulation results as well as the experimentally measured far field radiation plotted in Fig. V.14. in terms of the mode configuration shown in Fig. V.15. The peaks of the curves in Fig. V.13 can be explained as follows. If we look at the mode structure for $\alpha_h = 90°$ shown in Fig. V.15., we observe that light

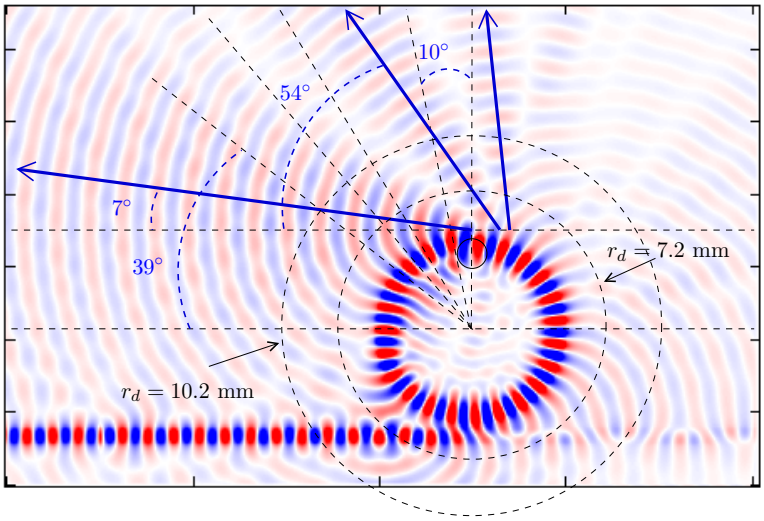

Figure V.15.: H_z component to depict the mode configuration inside a disk resonator with hole at $\alpha_h = 90°$ obtained from a cw simulation for the resonance wavelength $\lambda = 1.76$ mm. The position of the hole is marked by a black circle. Since this figure is to show the radiated field, the color scale is chosen in such a way that the field outside the cavity is well visible. Thus intensities above a certain value are depicted in the same color and therefore the field in the surrounding vacuum from the figure appears to be higher as compared to the field inside the cavity as it is in reality.

is mainly radiated along three straight lines, see the blue arrows in the figure. The line on which the light contributing to the major maximum is radiated crosses the circle with radius $r_d = 7.2$ mm between $\alpha_d = 50°$ and $\alpha_d = 60°$. However, the intersection point of this line with the circle of $r_d = 10.2$ mm is at around $39°$. If we extend this line to the far field region and calculate the intersection point with a circle of radius $r_d = 10$ cm, we arrive at an angle $\alpha_{d,far} \approx 9°$. This is in very good agreement with the experimental results for the far field radiation behavior measured with a detector of $15°$ aperture at a distance of around 10 cm from the resonator's center as plotted in Fig. V.14., see also [187, 188].

Next, we focus on the second largest maximum in the radiation at the angle $\alpha_d = \alpha_h$ for $r_d = r_a + 2$ mm. From the mode configuration in Fig. V.15. we can see, that light contributing to this maximum leaves the resonator at a different point than light leading to the highest maximum discussed above. In our simulations we find this maximum at $\alpha_d = \alpha_h$ for $r_d = 7.2$ mm and at $\alpha_d = 80°$ for $r_d = 10.2$ mm. In a movie made out of the mode configuration H_z at different time steps, we found that light is emitted straight along this line crossing these two points. Extending this line to the far field region leads to a detection angle of $\alpha_{d,far} = 56°$ for $\alpha_d = 10$ cm. This also agrees very well with the experimental results of [187, 188] shown in Fig. V.14., where the second largest maximum in the far field is observed for this angle. Light emitted along the third straight radiation line reaches a far field detector at $\alpha_d = 85°$ which is also in very good agreement with the experimental data of Fig. V.14. In our near field simulation we detect the contribution originating from this line only for $r_d = 10.2$ mm at $\alpha_h + 10°$ but not for $r_d = 7.2$ mm, since in this region typical near field effects occur. This means that the

straight radiation line is not developed at a distance of 2 mm from the cavity's boundary yet, but can be observed by detectors at $r_d = 10.2$ mm.

For the angle region of $\alpha_{d,far} > 100°$ the situation seems to be more complicated. In the mode configurations which we plotted for different times we cannot observe clear straight lines along which the light is radiated. In the experimental data of the far field presented in [187, 188], a very weak maximum of much less intensity than the three main maxima described above is observed around the angle $\alpha_{d,far} \approx 100°$. However, the far field radiation structure for these large angles $\alpha_{d,far} > 100°$ seems to be more complicated also in the experimental results. From our calculations we conclude, that the position of these minor maxima cannot be explained in terms of the near field behavior of the system, but far field effects such as interference effects have to be considered.

V.4.4. Applications

Possible applications of the here investigated setups are label-free biosensing devices or a further step in the development of microlasers. The transmission spectrum of a disk resonator with hole is strongly dependent on the refractive index inside the hole. Hence, the setup can be used as measurement device for precisely measuring ε_h. If, e.g., a fluid via a thin tube is guided through the hole, the refractive index of the fluid can be determined. Such sensing devices are needed in the field of biology or medical sciences, where low concentrations or even few biomolecules, bacteria or viruses are to be detected. If we compare the wavelength shifts $\Delta\lambda$ for the two resonators studied in Sec. V.4.2., the large resonator seems to be more sensitive for changes in ε_h. For a change of $\varepsilon_h = 1$ to $\varepsilon_h = 2$ the resonances are shifted by around $\Delta\lambda = 0.015$ mm. This value of $\Delta\lambda$ is achieved for the smaller resonator for a change of $\varepsilon_h = 1$ to $\varepsilon_h = 3$. However, we have to consider that for the large resonator the area covered by the hole is larger. Especially for tiny objects the sensitivity would decrease. Therefore, the resonator setup for which a higher sensitivity is obtained depends on the size of the objects to be detected.

Furthermore, we found that the radiation of the disk with hole is very anisotropic. The radiation characteristics with clear radiation directions could be exploited for lasing purposes. Additionally, since the radiation direction strongly depends on the hole position, another possible application would be sensing. Here, the position of a particle or another object with refractive index different from the resonator material could be detected by measuring the radiation characteristics.

V.5. Outlook

In this outlook we discuss some results for a further resonator with hole which was also experimentally studied at the Max Planck Institute for the Science of Light in Erlangen. This is particularly for demonstrating, that in principle the radiation of a disk cavity with a hole can be guided into fundamentally different directions by the hole. For the resonator with $r_a = 5.2$ mm considered in the preceding Sec. V.4.3., radiation occurs mainly in forward direction (relative to the light's propagation direction inside the resonator). Considering ray optics, due to refraction at the hole, this intuitively seems to be the most probable radiation direction. By contrast, we now show results for a system, which radiates in backward direction. This resonator has a radius of $r_a = 12.5$ mm, a hole

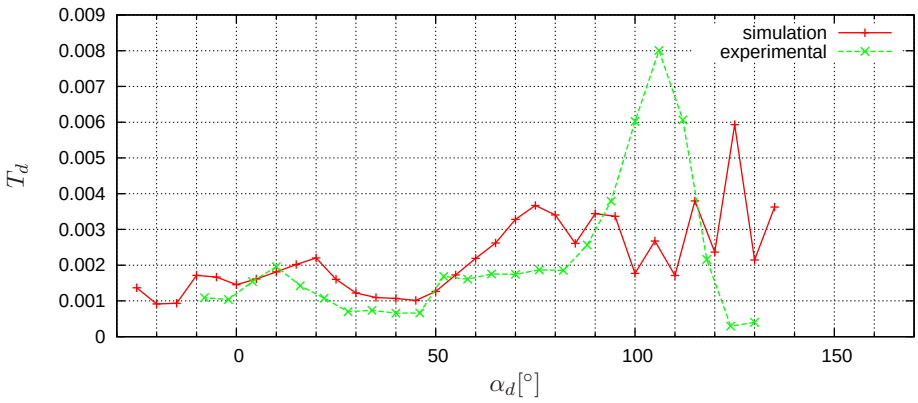

Figure V.16.: Simulated near field and experimentally measured far field radiation of a resonator with $r_a = 12.5$ mm, $r_i = 1.25$ mm and $\alpha_h = -43°$. For the simulation $\lambda = 2.3024$ mm, $r_d = r_a + 2$ mm, and $l_d = 0.4$ mm. In the experiment $r_d \approx 10$ cm and $\lambda = 2.317$ mm. The experimental curve is plotted in arbitrary units whereas the simulation curve shows the transmission T_d through the detector which is normalized by the input flux.

radius of $r_i = 1.25$ mm, $d_h = 1$ mm and $\alpha_h = -43°$. Our simulation results for the near field radiation T_d of this resonator and the experimental data for the far field radiation are presented in Fig. V.16. In our simulation data for the near field at $r_d = r_a + 2$ mm, we observe a peak at an angle of $\alpha_d = 125°$. This is almost in opposite direction from the hole position. If light is scattered at the hole, it has to travel through the whole disk in order to be radiated into this direction. We can observe such a behavior in a movie made out of the figures for the mode configurations of H_z at different times. One of these snapshots in time is shown in Fig. V.17. However, here, we cannot distinguish clear lines along which light is radiated from the disk. This makes it difficult to propose positions, where light observed in the near field is expected to be measured in the far field. In the experiment, the highest peak of the far field radiation is observed at around $\alpha_d = 105°$ and for slightly larger angles, the measured radiation almost vanishes, see Fig. V.16. On the one hand, since the radiation direction is found to be very sensitive on the geometry, even within the experimental error range, this difference could be caused, e.g., by the fuzzy borders of the hole or the measurement inaccuracy of the resonator dimensions of 0.1 mm in the experiment. On the other hand, the resonator is mounted by a rod of ≈ 3.1 mm radius penetrating the center of the PE disk in the experimental setup. Since the rod's material is absorbing in the terahertz regime, this setup does not allow light to travel through the resonator to the side opposite of the hole as depicted by the blue arrow in Fig. V.17. We found that the angle of $\alpha_d = 105°$ is the largest angle, where light can pass the rod. Most probably this absorbing rod is the reason why in the experimental data the radiation peak is observed at a smaller angle and additionally, exceeding this angle the measured radiation intensity almost vanishes.

From our simulations we have seen that the complicated structure of the mode configuration (H_z component) in the near field around our resonator as depicted in Fig. V.17. makes it very difficult to predict features of the far field radiation. A more promising method for calculating the far field radiation would be a near-to-far-field transformation.

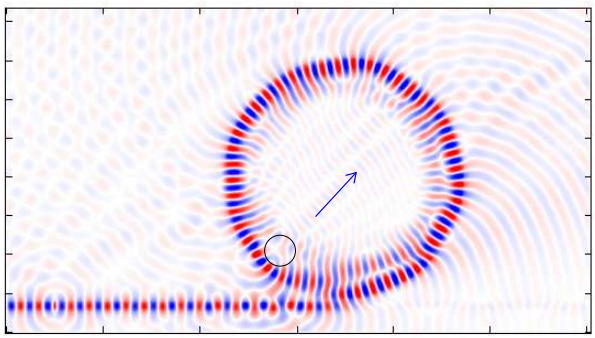

Figure V.17.: Configuration of the field component H_z for a disk resonator with hole, where reflections at the hole lead to backward radiation. The parameters are chosen as in Fig. V.16. The position of the hole is marked by a black circle.

This method is used to simulate the far field of radiating structures, e.g., antennas surrounded by vacuum [186, 194–198]. In these cases, Green's theorem [199] is exploited and an integration over the near field on a surface encompassing the scattering structure, e.g., a particle or antenna, is necessary. Unfortunately, since our disk structure is coupled to a waveguide, which is assumed to extend to infinity, we cannot find an appropriate surface encompassing our whole structure, and thus this method is not straightforward applicable for our system. Still, for some special cases of more complicated structures, near-to-far-zone transformations have already been developed. For example, in [200] a transformation method for a multi-layered medium on a lossy dielectric half space was found. In [201, 202] near-to-far-field transformations for nanostructures or antennas, respectively, radiating above an infinite, grounded dielectric slab are presented. Both these models are based on the special properties of the surroundings of the considered structure and they are not applicable in the presence of a coupling waveguide.

Another option to obtain further information of the far field radiation would be a Husimi transformation [203]. As long as the electromagnetic fields and their spacial derivatives in radial direction are known on the surface of the resonator, the Husimi function along this dielectric interface can be calculated [204, 205]. This formalism allows the determination of field contributions originating from the surface points of the resonator and their respective directions. Whereas simple ray optics, including Snell's and Fresnel's law, is only valid in the limit of short wavelengths as compared to the system's size, the Husimi representation also takes into account interference effects. It was found in [206–208], that this method allows predictions of the far field of WGM resonator structures which are in very good agreement with experimental measurement results.

V.6. Summary

In this part, we studied light propagation through different photonic structures using numerical FDTD (finite-difference time-domain) simulations of Maxwell's equations on

a grid. After providing the necessary theoretical background about the simulation technique, we first analyzed an array of three coupled microcavities arranged in a loop configuration, which was already introduced in the preceding part IV. We showed how to exploit this setup as precision sensing devices for determining the index of refraction of a thin slab placed between two cavities or the position of a nano particle close to one of the cavities by measuring the resulting transmission intensity. Moreover, we verified the sensitivity of these suggested precision measurement devices for the position of a nearby particle on a sub-wavelength scale or the refractive index of a thin slab.

Second, we investigated a disk resonator with a hole which acts as a finite scatterer. We studied the transmission properties as well as the radiation characteristics and compared our results to experimental data measured at the Max Planck Institute for the Science of Light in Erlangen [187, 188]. For the transmission spectra, we found that our simulations results are in very good agreement with these measurement results. For the radiation behavior, we studied the near field radiation whereas in the experiment the far field was measured. We explained the main structures in the measured spectra by near field effects. We found that the radiation into specific directions is strongly enhanced by the hole. This directed radiation could be exploited, e.g., for lasing or sensing purposes. The sensitivity of both the transmission spectra and the radiation characteristics on the position of the hole as well as the refractive index inside the hole could be used for label-free sensing applications which are, e.g., needed in life sciences. For theoretically studying the far field radiation in more detail, a near-to-far-field transformation or a Husimi projection as described in the outlook are promising tools.

Summary and outlook

In this Ph.D. thesis, different coupled systems consisting of whispering gallery resonators, atoms and fibers were investigated. The dynamics of such a system is governed by many different coupling mechanisms. Since standard literature does not provide a theoretical description including all these coupling mechanisms yet, a general mathematical model to treat such a complex system was presented in part I. We assumed a chain of subsystems connected by a common waveguide. Each subsystem consists of an array of an arbitrary number of microcavities, which is additionally coupled to a nearby atom. The different coupling mechanisms and their contributions to the Hamiltonian were discussed and a master equation for this general system as well as the equations of motion for the system's operators were derived. Most of the setups which were investigated in the later parts of this thesis are reductions of this general system, for which the mathematical model was presented.

In part II, a cavity coupled to a nearby three-level atom in the Λ configuration was investigated. In previous experimental work [105], it was shown, that a toroidal whispering gallery cavity coupled to a nearby two-level atom can be exploited as a photon turnstile device. Motivated by this experiment, we showed that in case of a nearby three-level atom in the Λ configuration, such a setup allows more flexible control schemes than achievable using a coupling two-level atom. The transmission and reflection properties as well as higher order photon correlations and cross correlations between the different output modes were considered as observables. We presented results for the strong coupling regime, where the atomic coupling dominates the dynamics, and the so-called bad cavity regime, where the atomic coupling is weak as compared to further coupling and scattering mechanisms. We described adequate calculation methods for both these parameter regimes and interpreted the results in terms of appropriate eigenstate analyses. On the one hand, we solved the equations of motion by a truncated Fock state analysis. On the other hand, an adiabatical elimination of the cavity modes was explained for the bad cavity regime. It was shown how to exploit the properties of the output photon statistics in order to build a controllable photon turnstile for the different photon modes. This suggests a further development of the previous experimental realization of a photon turnstile presented in [105] where a two-level atom coupling to a single mode pair was used. Moreover, photonic switches and precision measurements of the position of a nearby particle on a sub-wavelength scale were discussed as possible applications.

In part III, we considered a chain of coupled cavity-atom systems connected by a common fiber and probed by a weak input field. Each of the subsystems consists of a whispering gallery cavity coupled to a nearby two-level atom. The formation of so-called supermodes, which are special collective modes with strongly enhanced transmission, was studied in detail. We found that these supermodes are resonances originating from backcoupling fluxes between the subsystems which are possible in both directions. To quantify these supermodes, we defined a "superness" measure, which is the difference between the transmission with and without backcoupling fluxes. For long chains, the relative transmission difference which is denoted by "relative superness" was found to increase with the chain length. Since the number of degrees of freedom for this system is very high especially for long chains, numerically solving the equations of motion is challenging. Therefore, in the limit of weak input fields, we presented a method to calculate our observables via a coupling matrix which allows for a more efficient calculation of the output fluxes. We discussed the advantages and drawbacks of both these calculation methods as well as their respective validity ranges in detail. We analyzed certain supermodes in terms of constructive interference of different contributing light pathways. Spectral ranges were defined, in which the formation of supermodes depends considerably on the geometry whereas for other input detunings the chain is insensitive to the geometry. For example, in a chain consisting of three subsystems, this feature could be used to measure precisely the position of a single cavity within the chain with a precision smaller than one twentieth of the wavelength. We found that the transmission behavior of the coupled chain is independent of the sequence of the respective subsystems in the chain. By contrast, the reflection signal is strongly dependent on the order of the different subsystems. This property could be used for detecting, e.g., which of the subsystems couples to a nearby atom. Furthermore, the coupling strengths of each single atom to the respective microcavity could be detected via the reflected intensity. This information is important for experiments in which it is difficult to achieve simultaneous coupling of all atoms, e.g., if a falling cloud of atoms or an atomic fountain is used to realize atom-cavity coupling. Whether really all subsystems have a coupling atom can be measured via the reflection intensity.

In part IV, a coupled array of three whispering gallery resonators arranged in a loop configuration was investigated. One of the cavities is additionally coupled to a waveguide, which allows to probe the system with an input laser field. Complex parameters described the coupling between the ring or disk resonators. We provided a detailed analysis of the various light pathways through the coupled system and found that interference effects of these pathways influence vastly the output fluxes in both transmission and reflection direction. In previous works, the coupling parameters were often treated as real numbers, since there are cases, where the phases do not influence the final transmission or reflection signal. However, in our setup, the phase angles of the complex coupling constants were found to play an important role in our system's dynamics. In our special arrangement of resonators, a closed-loop process, where light travels on a pathway through all three cavities can take place and leads to sharp resonance lines. Via suppressing single pathways by artificially turning off certain couplings, we demonstrated, that the mentioned roundtrip pathway is the source of these sharp resonances. These narrow resonance lines in the transmission and reflection could be exploited for label-free precision sensing devices for determining the refractive index of a thin slab or the position of a nearby particle on a sub-wavelength scale. The coupled mode analysis of this loop array was

followed by a quantitative analysis of the sensitivity of these measurement devices via FDTD (finite-difference time-domain) simulations in the following part.

In part V, light propagation through different photonic structures was studied via numerical FDTD simulations of Maxwell's equations on a two-dimensional grid. The sensitivity of the measurement devices suggested for the loop array in the preceding part IV were quantitatively analyzed. We found, that changes in the relative electric permittivity of 0.01 already lead to a resonance shift of $\Delta\lambda \approx 0.05$ nm in the considered parameter region. An azimuthal movement of a nearby particle with 60 nm radius of around 0.7λ results in $\Delta\lambda \approx 0.01$ nm for the considered optical wavelength regime. Thus both these effects should be detectable.
Besides resonator arrays in the optical regime, the propagation of electromagnetic waves in the terahertz regime through disk resonators with holes of different sizes in the order of millimeters was simulated. These simulations were motivated by an experiment performed by the group of Harald Schwefel in the division of Gerd Leuchs at the Max Planck Institute for the Science of Light in Erlangen [187, 188]. Here, the transmission as well as the far field radiation was measured for disk resonators with holes of different dimensions. These holes function as light scatterer. The dependence of the transmission behavior on the hole's position and size as well as the refractive index inside the hole was analyzed. For different disk radii we found fundamentally different mode structures excited in the respective resonator, which in some cases lead to mode splitting in the transmission spectra. Our results for different parameters were compared with the experimental measurement data and found to be in very good agreement with the experimental findings. Such a setup could, e.g., serve as a sensing device for measuring the refractive index of a substance inside the hole. For biosensing applications, a liquid could be guided through the hole via a thin tube and the concentration of a solute could be detected.
Furthermore, the near field radiation characteristics was simulated for different disk resonators with hole. We found, that the hole influences strongly the radiation pattern of the cavity and causes an anisotropic, directional radiation characteristics. We identified straight lines along which light is radiated. We explained the main features of the experimentally measured far field radiation pattern by effects observed in our simulation results for the near field. This strongly anisotropic radiative behavior can be exploited, e.g., for the design of microlasers or sensing devices.

In the following, we provide an outlook for future research. First, we discuss approaches which could optimize our suggested setups for lasing purposes and sensing applications. Second, we discuss further potentially interesting and useful features such as non-Markovian behavior, non-classical light sources, time dependent phenomena and entanglement in similar coupled systems.

Towards efficient microlasing

For a further investigation of the disk resonator with hole and its radiation characteristics, it would be interesting to simulate the experimentally better accessible far field rather than the near field radiation. Therefore, a near-to-far-field transform or a Husimi projection could provide a means to calculate the far field which is usually measured in experiments such as the setup at the Max Planck Institute for the Science of Light in Erlangen. For the considered system, we found that the radiation is rather directional than isotropic. This behavior can be exploited for sensing or lasing applications. In order to use our

setup as microlaser, a non-circular hole could be advantageous. For example, based on the mode configuration in the disk without hole, one could calculate a hole border line, which is encountered by propagating whispering gallery modes in the disk in such a way, that - in the language of ray optics - all rays are reflected into one direction. This would lead to a concave line as front border of the hole. With such an optimized hole form, higher directionalities and more narrow beam divergences could possibly be achieved. However, every change in the resonator structure also changes the whole system's resonance mode formation and usually reduces the Q factor of the resonator. Therefore, although this is a promising approach in the direction of even more directional radiation characteristics, we cannot a priori be sure, that light would really be reflected in the calculated direction by the borderline of this optimized hole shape. Another concept for the design of highly directionally emitting microlasers are deformed disk resonators. Deformations of microdisks often lead to decreased finesse. However, some works on asymmetric high-Q resonators [209] have shown strongly directed radiation patterns even in the far field. For example, limaçon shaped deformed microdisks were studied in [210, 211] and a highly directional light output as well as ultralow loss was found. A peanut shaped whispering gallery resonator with highly directional far field characteristics and a beam divergence as narrow as 2.5° has just been presented in [212]. In [213], elliptic whispering gallery cavities with a notch in the size of the wavelength have been investigated in theory and experiment.
A combination of these peanut, ellipse or limaçon resonators with a suitably shaped hole could potentially lead to a more narrow collimation of light and thus offer a promising advanced setup for microlasing with strong directionality and narrow beams in the far field.
Another approach to improve the lasing properties is to couple several cavities. To that end, a coupled pair of a disk resonator and a circular-elliptic microcavity was studied in [214]. In this setup, the disk resonator is used to provide the high quality factor whereas the deformed microdisk plays the role of a light collimator and thus leads to the directionality necessary for microlasing. In part IV, we found that pathway interference effects play a key role in the dynamics of the studied loop array consisting of three coupled whispering gallery cavities. A roundtrip process, where light propagates through all three resonators before leaving the system leads to very sharp high-Q resonances in the coupled array. For further investigations, the influence of deforming one of the resonators on the system's finesse could be interesting. If it was possible to deform one of the resonators or use a resonator with a notch or hole instead of a disk or ring cavity while the Q factor of the observed sharp resonance lines does not decrease considerably, this coupled array could form an advanced microlaser setup. Specifically, the sharp resonance lines caused by pathway interference due to a closed-loop pathway could provide a high Q factor, whereas a deformation of one of the upper two cavities and a hole in the other upper resonator could provide directional light emission and thus make the system particularly suited for microlasing purposes.

Optimizing sensing applications

When studying interference effects in the loop array in part IV, we focused on three cavity systems, where the number of leading order pathways governing the system's dynamics is limited, which allows to perform an analytic pathway analysis. In more complex arrays

which consist of more than three resonators, more and more pathways become significant. Similar to the closed-loop roundtrip pathway which we identified to lead to very sharp resonance lines of the three cavity loop, further pathways, e.g., more complicated closed-loop pathways, could lead to further and possibly even sharper resonances. This could increase the sensitivity of the suggested sensing devices for precision measurements of the position of a particle such as a nearby molecule or virus or for determining the refractive index of a thin slab or a fluid.
For the disk resonator with a hole, we found that the azimuthal position of the hole has negligible impact on the transmission spectrum whereas the radial position influences considerably the transmission behavior. Here, the radial direction is defined with respect to the disk's center and not the hole's center. This difference to the loop array can be explained by the field configuration inside the system. Whereas the mode configuration in the upper two cavities of the loop array is governed by standing waves, mainly traveling waves propagate in the disk resonator with hole. Therefore, the sensitivity on azimuthal changes almost vanishes for a single disk resonator with hole. In an experiment, the position and the radial motion of particles in a fluid guided through the hole via a thin tube could be measured via the transmission intensity. For label-free real-time detection of, e.g., molecular motion in both radial and azimuthal direction, an asymmetrically deformed disk resonator, in which the field configuration in the absence of a scatterer is not as symmetric as in a disk resonator, such as a limaçon or an ellipse, could be a promising setup. Besides, we found for the coupled loop arrangement consisting of three ring cavities, that azimuthal position of a particle close to one of the upper two resonators can be detected on a sub-wavelength scale. In our setup, the particle is located close to the outer border of the ring. However, similar scattering mechanisms would occur for a particle located close to the inner border of the ring. Due to the standing wave pattern inside the two upper ring cavities, also the azimuthal position could be measured. Additionally, particle motion, both radial and azimuthal, within a fluid, guided through one of the upper rings via a thin tube, could be detected. For this application also coupled arrays of more than three cavities could offer even sharper resonance lines which correspond to even higher sensibilities.

Control of supermodes

During our investigations of a chain of coupled atom-cavity systems in part III, we focused on the formation of supermodes which are detectable by measuring the transmission and reflection signal. Here, the atoms were modeled with two internal energy levels. In future, considering a chain of coupled atom-cavity systems in which the coupling atoms are modeled by more than two internal energy levels could be interesting as well. This promises advanced control schemes for tuning the formation of supermodes. It would be interesting to know, if similar control schemes as presented for the tunable photon turnstile in part II were applicable on the formation of supermodes and thus on the transmission enhancement caused by backward fluxes between the subsystems found in part III. For example, using an appropriate internal atomic structure, it could be possible to switch the formation of supermodes on and off only by slightly varying the input fields.

Non-Markovian effects

Furthermore, the investigation of non-Markovian effects in coupled atom-cavity systems could lead to fascinating system dynamics. For example, a strong non-Markovian memory effect for certain coupling strengths between a microcavity coupling to a waveguide in a photonic crystal was observed in [215]. It was shown in that study, that the dissipative behavior of the cavity dynamics can be controlled via the parameter which describes the coupling strength between the microcavity and the waveguide. A parameter regime was found, in which the cavity field becomes dissipationless and the cavity can maintain a coherent state with an arbitrary small number of photons. It would be interesting to investigate the influence of a nearby atom or quantum dot coupling to this cavity on the parameter regimes, where Markovian and non-Markovian behavior, respectively, can be observed. A setup in which the cavity additionally couples to an atom or quantum dot with an appropriate internal structure could potentially offer more advanced dissipation control of the microresonator.

Non-classical light sources and quantum information applications

Apart from the transmission and reflection signal, in experiment and theory higher order photon correlations are of interest. Depending on the resulting photon statistics, coupled atom-cavity systems could be exploited as non-classical light sources such as single-photon sources. In part II, we calculated second order correlations and cross correlations between different photon output modes in a parameter regime, in which the cavity modes can be adiabatically eliminated. We showed via the photon statistics that our setup can be exploited as a controllable single photon source or turnstile device in the bad cavity limit. In order to obtain higher order correlation functions in the strong coupling regime or in more complex systems such as the coupled chain considered in part III, the method of Monte Carlo simulations is a possible ansatz [148–150].
Furthermore, coupled atom-cavity systems are interesting for studying the formation of entanglement which is essential for transmitting information within quantum networks. Thus, sources of entangled photons are crucial tools for quantum information processing systems. In [216], entanglement between pairs of atom-cavity systems in an array of coupled resonators was studied. It was found how this steady state entanglement can coherently be controlled via the driving laser fields. In a very recent publication [217], entanglement of two distant cavities connected by a coupled resonator optical waveguide in a photonic crystal was demonstrated. Motivated by these works, one could study the occurrence of entanglement in a chain of coupled atom-microcavity systems and possibly develop advanced control mechanisms of steady state entanglement. The generation of polarization entangled photons from a V type quantum system or a four-level quantum dot embedded in Fabry-Pérot microcavities was theoretically proposed in [134] and [218], respectively. Similarly, entangled photons could be generated by systems consisting of whispering gallery microcavities with two counterpropagating modes coupling to nearby atoms. Potentially, the degree of entanglement could be enhanced for optimized internal atomic structures. Such control schemes and sources of non-classical light are necessary for many applications in quantum information sciences and quantum networks.

Time-dependent phenomena and stability of supermodes

In our investigations, we studied the steady state of resonator arrays and coupled atom-cavity systems. However, time dependent phenomena can also occur in such coupled systems. For example, the formation of supermodes in a chain of oscillating atom-cavity subsystems could exhibit interesting features. In such a system, the distance between the cavities and the common waveguide could be modulated in time. This would result in a time modulated coupling strength of the resonators to the waveguide and thus, this motion would probably influence crucially the system's dynamics. On the one hand, such oscillations could be experimentally realized by using cavities in a crystal coupled to a nearby quantum dot where phonons propagate through the crystal structure and thus excite mechanical cavity oscillations. On the other hand, the thermal motion of, e.g., microtoroids causes a time-dependent coupling to the fiber. In addition to the transmission enhancement found for our chain of atom-cavity systems in part III, coupling effects of the occurring supermodes with mechanical oscillation modes and resonances could potentially lead to new system dynamics.
The thermal motion of microtoroids can lead to a fluctuation of the cavity radius which also affects the resonance frequencies [63]. Additionally, phonon propagation can modulate the photonic resonances of a cavity embedded, e.g., in a photonic crystal in time. In [219], coupling effects of mechanical and photonic resonances in an optomechanical crystal were studied in detail. Such a crystal is a combination of a photonic crystal, in which the periodicity of the material structure is used to manipulate the properties of light, and a phononic crystal, in which mechanical vibrations are manipulated. It has been shown for these optomechanical crystals, that enhanced interactions between light and matter lead to high sensitivity for optical measurements of, e.g., mechanical vibrations. Very recently, it was experimentally shown [220], how to periodically modulate the resonance frequency of photonic crystal cavities using acoustic phonons. During this dynamic tuning the high quality factor of the optical modes is preserved.
Similar to the coherent acoustic control of optomechanical crystals, one could develop control methods for the supermodes occurring in a coupled cavity-atom chain where phonons modulate the cavity mode frequencies periodically. This would also modulate the coupling strength to the nearby quantum structure such as an atom or quantum dot. Here, also a coupling atom or quantum dot with more than two internal states could allow for more advanced control schemes. It would be particularly interesting, to similarly couple the photonic supermodes which we found when studying the atom-cavity chain in part III with mechanical oscillation modes. This could be realized by a chain of photonic crystal cavities, each of which is coupled to a nearby quantum dot, connected, e.g., by a coupled resonator optical waveguide. Maybe it would be possible to find a constellation where not only the relative but even the absolute transmission is considerably enhanced for a long chain as compared to a chain of independent cavity-quantum-dot systems.
Moreover, it would be interesting to study the influence of mechanical motion of a chain of cavity-atom systems driven by an external force which leads to nonlinear effects. Depending on the force and the chain length, this can even give rise to chaotic motion behavior [221, 222]. In this case, the stability of photonic modes, such as the observed supermodes in our coupled chain system, could be of particular interest.

Bibliography

[1] *The Echoes of the Statuary Hall – The Curious Properties of the old Representatives' Chamber*, The New York Times (August 28, 1892).

[2] J. Verne, *Voyage au Centre de la Terre* (1864).

[3] Y. Satô, Nature, **189**, 475 (1961).

[4] Lord Rayleigh, Scientific Papers, **5**, 617 (1912).

[5] C. V. Raman and G. A. Sutherland, Nature, **108**, 193 (1921).

[6] G. N. Watson, Proc. of the Royal Society of London, **95**, 546 (1919).

[7] W. O. Schumann, Zeitschrift für Naturforschung, **7a**, 149 (1952).

[8] W. O. Schumann, Zeitschrift für Naturforschung, **7a**, 250 (1952).

[9] W. O. Schumann and H. König, Die Naturwissenschaften, **41**, 183 (1954).

[10] K. G. Budden and H. G. Martin, Proc. of the Royal Society of London, **256**, 554 (1962).

[11] J. R. Wait and K. Spies, J. of Geophys. Research, **65**, 2325 (1960).

[12] J. R. Wait, Electronics Lett., **4**, 377 (1968).

[13] V. B. Braginsky, M. L. Gorodetsky, and V. S. Ilchenko, Phys. Lett. A, **137**, 393 (1989).

[14] D. K. Armani, T. J. Kippenberg, S. M. Spillane, and K. J. Vahala, Nature, **421**, 925 (2003).

[15] M. L. Gorodetsky, A. A. Savchenkov, and V. S. Ilchenko, Opt. Lett., **21**, 453 (1996).

[16] Y. Louyer, D. Meschede, and A. Rauschenbeutel, Phys. Rev. A, **72**, 031801(R) (2005).

[17] M. Pöllinger, D. O'Shea, F. Warken, and A. Rauschenbeutel, Phys. Rev. Lett., **103**, 053901 (2009).

[18] V. S. Ilchenko, A. A. Savchenkov, A. B. Matsko, and L. Maleki, Phys. Rev. Lett., **92**, 043903 (2004).

[19] T. Beckmann, H. Linnebank, H. Steigerwald, B. Sturmann, D. Haertle, K. Buse, and I. Breunig, Phys. Rev. Lett., **106**, 143903 (2011).

[20] A. B. Matsko, A. A. Savchenkov, D. Strekalov, V. S. Ilchenko, and L. Maleki, "Review of application of whispering-gallery mode resonators in photonics and nonlinear optics," IPN Progress Report 42-162 (2005), http://tmo.jpl.nasa.gov/progresslowbarreport/42-162/162D.pdf.

[21] K. Vahala, Nature, **424**, 839 (2003).

[22] S. L. McCall, A. F. J. Levi, R. E. Slusher, S. J. Pearton, and R. A. Logan, Appl. Phys. Lett., **60**, 289 (1992).

[23] V. Sandoghdar, F. Treussart, J. Hare, V. Lefèvre-Seguin, J. M. Raimond, and S. Haroche, Phys. Rev. A, **54**, R1777 (1996).

[24] O. Painter, R. K. Lee, A. Scherer, A. Yariv, J. D. O'Brien, P. D. Dapkus, and I. Kim, Science, **284**, 1819 (1999).

[25] S. M. Spillane, T. J. Kippenberg, and K. J. Vahala, Nature, **415**, 621 (2002).

[26] M. Cai, O. Painter, K. J. Vahala, and P. C. Sercel, Opt. Lett., **25**, 1430 (2000).

[27] O. Schwelb, J. of Lightwave Technol., **22**, 1380 (2004).

[28] K. Djordjev, S.-J. Choi, S.-J. Choi, and R. Dapkus, IEEE Photon. Technol. Lett., **14**, 828 (2002).

[29] B. E. Little, J.-P. Laine, and S. T. Chu, Opt. Lett., **22**, 4 (1997).

[30] X. Fan, I. M. White, S. I. Shopova, H. Zhu, J. D. Suter, and Y. Sun, Anal. Chim. Acta, **620**, 8 (2008).

[31] H. K. Hunt, C. Soteropulos, and A. M. Armani, Sensors, **10**, 9317 (2010).

[32] A. M. Armani and K. J. Vahala, Proc. of SPIE, **6376**, 637606 (2006).

[33] S. Arnold, S. I. Shopova, and S. Holler, Opt. Express, **18**, 281 (2010).

[34] R. W. Boyd and J. E. Heebner, Appl. Opt., **40**, 5742 (2001).

[35] J. Zhu, S. K. Ozdemir, Y.-F. Xiao, L. Li, L. He, D.-R. Chen, and L. Yang, Nature Photon., **4**, 46 (2010).

[36] A. M. Armani, R. P. Kulkarni, S. E. Fraser, R. C. Flagan, and K. J. Vahala, Science, **317**, 783 (2007).

[37] F. Vollmer and S. Arnold, Nature Methods, **5**, 591 (2008).

[38] F. Vollmer, S. Arnold, and D. Keng, Proc. Natl. Acad. Sci. USA, **105**, 20701 (2008).

[39] L. He, S. K. Ozdemir, J. Zhu, W. Kim, and L. Yang, Nature Technol., **6**, 428 (2011).

[40] F. Vollmer, D. Braun, A. Libchaber, M. Khoshsima, I. Teraoka, and S. Arnold, Appl. Phys. Lett., **80**, 4057 (2003).

[41] S. Arnold, M. Khoshsima, I. Teraoka, S. Holler, and F. Vollmer, Opt. Lett., **28**, 272 (2003).

[42] M. A. Santiago-Cordoba, S. V. Boriskina, F. Vollmer, and M. C. Demirel, Appl. Phys. Lett., **99**, 073701 (2011).

[43] T. Udem, R. Holzwarth, and T. W. Hänsch, Nature, **416**, 233 (2002).

[44] T. J. Kippenberg, S. M. Spillane, and K. J. Vahala, Phys. Rev. Lett., **83**, 083294 (2004).

[45] A. A. Savchenkov, A. B. Matsko, D. Strekalov, M. Mohageg, V. S. Ilchenko, and L. Maleki, Phys. Rev. Lett., **93**, 243905 (2004).

[46] P. Del'Haye, A. Schliesser, O. Arcizet, T. Wilken, R. Holzwarth, and T. J. Kippenberg, Nature, **450**, 1214 (2007).

[47] T. J. Kippenberg, R. Holzwarth, and S. A. Diddams, Science, **332**, 555 (2011).

[48] A. A. Savchenkov, A. B. Matsko, W. Liang, V. S. Ilchenko, D. Seidel, and L. Maleki, Nature Photon., **5**, 293 (2011).

[49] P. Del'Haye, O. Arcizet, A. Schliesser, R. Holzwarth, and T. J. Kippenberg, Phys. Rev. Lett., **101**, 053903 (2008).

[50] P. Del'Haye, O. Arcizet, M. L. Gorodetsky, R. Holzwarth, and T. J. Kippenberg, Nature Photon., **3**, 530 (2009).

[51] T. J. Kippenberg and K. Vahala, Optics Express, **15**, 17172 (2007).

[52] T. J. Kippenberg and K. J. Vahala, Science, **321**, 1172 (2008).

[53] P. T. Rakich, M. A. Popovic, M. Soljacic, and E. P. Ippen, Nature Photon., **1**, 658 (2007).

[54] G. Anetsberger, O. Arcizet, Q. P. Unterreithmeier, R. Rivière, A. Schliesser, E. M. Weig, J. P. Kotthaus, and T. J. Kippenberg, Nature, **5**, 909 (2009).

[55] M. Eichenfeld, C. P. Michael, R. Perahia, and O. Painter, Nature Photon., **1**, 416 (2007).

[56] J. M. Dobrindt, I. Wilson-Rae, and T. J. Kippenberg, Phys. Rev. Lett., **101**, 263602 (2008).

[57] R. Ma, A. Schliesser, P. Del'Haye, A. Dabirian, G. Anetsberger, and T. J. Kippenberg, Opt. Lett., **32**, 2200 (2007).

[58] T. J. Kippenberg, H. Rokhsari, T. Carmon, A. Scherer, and K. J. Vahala, Phys. Rev. Lett., **95**, 033901 (2005).

[59] V. B. Braginsky, *Measurement of Weak Forces in Physics Experiments* (University of Chicago Press, 1977).

[60] G. Anetsberger, R. Rivière, A. Schliesser, O. Arcizet, and T. J. Kippenberg, Nature Photon., **2**, 627 (2008).

[61] J. Lin, J. Rosenberg, D. Chang, R. Camacho, M. Eichenfield, K. J. Vahala, and O. Painter, Nature Photon., **4**, 236 (2010).

[62] X. Jiang, Q. Lin, J. Rosenberg, K. Vahala, and O. Painter, Opt. Express, **17**, 20911 (2009).

[63] A. Schliesser, P. Del'Haye, N. Nooshi, K. J. Vahala, and T. J. Kippenberg, Phys. Rev. Lett., **97**, 243905 (2006).

[64] F. Marquardt, J. P. Chen, A. A. Clerk, and S. M. Girvin, Phys. Rev. Lett., **99**, 093902 (2007).

[65] A. Schliesser, O. A. R. Rivière, G. Anetsberger, and T. J. Kippenberg, Nature, **5**, 509 (2009).

[66] S. Weis, R. Rivière, S. Deleglise, E. Gavartin, O. Arcizet, A. Schliesser, and T. J. Kippenberg, Science, **330**, 1520 (2010).

[67] M. A. Popovic, T. Barwicz, P. T. Rakich, M. S. Dahlem, C. W. Holzwarth, F. Gan, L. Socci, M. R. Watts, H. I. Smith, F. X. Kärtner, and E. P. Ippen, "Experimental demonstration of loop-coupled microring resonators for optimally sharp optical filters," in Conference on Lasers and Electro-Optics/Quantum Electronics and Laser Science Conference and Photonic Applications Systems Technologies, OSA Technical Digest (CD) (Optical Society of America, 2008), paper CTuNN3.

[68] M. A. Popovic, C. Manolatou, and M. R. Watts, Opt. Express, **14**, 3 (2006).

[69] V. Van and M. A. Prabhu, "Multiple coupled microresonator devices for advanced spectral shaping applications," in SPIE Photonics West, 2008, paper 6872-29.

[70] J. K. S. Poon, J. Scheuer, and A. Yariv, IEEE Photon. Technol. Lett., **16**, 1331 (2004).

[71] S. T. Chu, B. E. Little, W. Pan, T. Kaneko, S. Sato, and Y. Kokuburn, IEEE Technol. Lett., **11**, 691 (1999).

[72] B. E. Little, S. T. Chu, H. A. Haus, J. Foresi, and J.-P. Laine, J. of Lightwave Technol., **15**, 998 (1997).

[73] B. E. Little, S. T. Chu, and H. A. Haus, Opt. Lett., **23**, 1570 (1998).

[74] B. E. Little, S. T. Chu, J. V. Hryniewicz, and P. P. Absil, Opt. Lett., **25**, 344 (2000).

[75] B. E. Little, S. T. Chu, W. Pan, and Y. Kokubun, IEEE Photon. Technol. Lett., **12**, 323 (2000).

[76] Y.-F. Xiao, X.-B. Zou, W. Jiang, Y.-L. Chen, and G.-C. Guo, Phys. Rev. A, **75**, 063833 (2007).

[77] T. Barwicz, M. A. Popovic, P. T. Rakich, M. R. Watts, H. A. Haus, E. P. Ippen, and H. I. Smith, Opt. Express, **12**, 1437 (2004).

[78] A. Poon, X. Luo, F. Xu, and H. Chen, Proc. of the IEEE, **97**, 1216 (2009).

[79] H. L. R. Lira, S. Manipatruni, and M. Lipson, Opt. Express, **17**, 22271 (2009).

[80] B. E. Little, H. A. Haus, J. S. Foresi, L. C. Kimerling, E. P. Ippen, and D. L. Ripin, IEEE Photon. Technol. Lett., **10**, 816 (1998).

[81] Z. Qiang, W. Zhou, and R. A. Soref, Opt. Express, **15**, 1823 (2007).

[82] S. Fan, P. R. Villeneuve, J. D. Joannopoulus, and H. A. Haus, Opt. Express, **3**, 4 (1998).

[83] K. Yamaguchi, M. Fujii, M. Haraguchi, T. Okamoto, and M. Fukui, in *Nonlinear Photonics* (Opt. Soc. of Am., 2010) p. NMB7.

[84] K. Nozaki, T. Tanabe, A. Shinya, S. Matsuo, T. Sato, H. Taniyama, and M. Notomi, Nature Photon., **4**, 477 (2010).

[85] T. Tanabe, M. Notomi, S. Mitsugo, A. Shinya, and E. Kuramochi, Appl. Phys. Lett., **87**, 151112 (2005).

[86] M. A. Mansouri-Birjandi, M. K. Moravvej-Farshi, and A. Rostami, Appl. Opt., **47**, 5041 (2008).

[87] K. Yamaguchi, M. Fujii, M. Haraguchi, T. Okamoto, and M. Fukui, Opt. Express, **17**, 23205 (2009).

[88] M. Notomi, E. Kuramochi, and T. Tanabe, Nature Photon., **2**, 741 (2008).

[89] M. Bayer, T. Gutbrod, J. P. Reithmaier, A. Forchel, T. L. Reinecke, and P. A. Knipp, Phys. Rev. Lett., **81**, 2582 (1998).

[90] S. V. Boriskina, Opt. Lett., **31**, 338 (2006).

[91] S. V. Boriskina, T. M. Benson, and P. Sewell, Proc. of SPIE, **6452**, 64520X (2007).

[92] S. V. Boriskina, Opt. Lett., **32**, 1557 (2007).

[93] Y. Hara, K. Takeda, and M. Kuwata-Gonokami, *Conference on Lasers and Electro-Optics/Quantum Electronics and Laser Science Conference*, Conference on Lasers and Electro-Optics/Quantum Electronics and Laser Science Conference, QThA6 (2003).

[94] Y. Hara, T. Mukaiyama, K. Takeda, and M. Kuwata-Gonokami, Opt. Lett., **28**, 2437 (2003).

[95] E. I. Smotrova, A. I. Nosich, T. M. Benson, and P. Sewell, Opt. Lett., **31**, 921 (2006).

[96] E. I. Smotrova, A. I. Nosich, T. M. Benson, and P. Sewell, IEEE Selected Topics in Quant. Electron., **12**, 78 (2006).

[97] S. V. Boriskina, J. Opt. Soc. Am. B, **23**, 1565 (2006).

[98] S. V. Boriskina and L. D. Negro, Opt. Lett., **35**, 2496 (2010).

[99] T. Aoki, B. Dayan, E. Wilcut, W. P. Bowen, A. S. Parkins, T. J. Kippenberg, K. J. Vahala, and H. J. Kimble, Nature, **443**, 671 (2006).

[100] D. J. Alton, N. P. Stern, T. Aoki, H. Lee, E. Ostby, K. J. Vahala, and H. J. Kimble, Nature, **7**, 159 (2011).

[101] K. Srinivasan and O. Painter, Nature, **450**, 862 (2007).

[102] K. Srinivasan and O. Painter, Phys. Rev. A, **75**, 023814 (2007).

[103] F.-Y. Hong and S.-J. Xiong, Nanoscale Res. Lett, **3**, 361 (2008).

[104] F.-Y. Hong and S.-J. Xiong, Phys. Rev. A, **78**, 013812 (2008).

[105] B. Dayan, A. S. Parkins, T. Aoki, H. J. Kimble, E. P. Ostby, and K. J. Vahala, Science, **319**, 1062 (2008).

[106] W. Yao, R.-B. Liu, and L. N. Sham, Phys. Rev. Lett., **95**, 030504 (2005).

[107] J. L. O'Brien, A. Furusawa, and J. Vuckovic, Nature Photon., **3**, 687 (2009).

[108] H. J. Kimble, Nature, **453**, 1023 (2008).

[109] W. J. Munro, K. A. Harrison, A. M. Stephens, S. J. Devitt, and K. Nemoto, Nature Photon., **4**, 792 (2010).

[110] F.-Y. Hong and S.-J. Xiong, Phys. Rev. A, **76**, 052302 (2007).

[111] L.-M. Duan, A. Kuzmich, and H. J. Kimble, Phys. Rev. A, **67**, 032305 (2003).

[112] A.-C. Ji, X. C. Xie, and W. M. Liu, Phys. Rev. Lett., **99**, 183602 (2007).

[113] D. O'Shea, C. Junge, A. Rauschenbeutel, M. Pöllinger, and A. Vogler, "All-optical switching and strong coupling using tunable whispering gallery mode microresonators," ArXiv:1105.0330[physics.optics].

[114] E. Vetsch, D. Reitz, G. Sagué, R. Schmidt, S. T. Dawkins, and A. Rauschenbeutel, Phys. Rev. Lett., **104**, 203603 (2010).

[115] F. Le Kien, V. I. Balykin, and K. Hakuta, Phys. Rev. A, **70**, 063403 (2004).

[116] M. A. Popovic, T. Barwicz, P. T. Rakich, M. S. Dahlem, C. W. Holzwarth, F. Gan, L. Socci, M. R. Watts, H. I. Smith, F. X. Kärtner, and E. P. Ippen, Conference on Laser and Electronics (2008).

[117] D. J. Alton, N. P. Stern, T. Aoki, H. Lee, E. Ostby, K. J. Vahala, and H. J. Kimble, "Strong interactions of single atoms and photons near a dielectric boundary," Nature Phys. Advance online publication, doi:10.1038/nphys1837. (2010).

[118] M. Rosenblit, P. Horak, S. Helsby, and R. Folman, Phys. Rev. A, **70**, 053808 (2004).

[119] M. O. Scully and M. S. Zubairy, *Quantum Optics* (Cambridge University Press, 1997).

[120] H. Miao, C. Zhao, L. Ju, and D. G. Blair, Phys. Rev. A, **79**, 063801 (2009).

[121] X.-W. Wu, C.-L. Zou, J.-M. Cui, Y. Yang, Z.-F. Han, and G.-C. Guo, J. of Physics B: Atomic, Molecular and Optical Physics, **42**, 085401 (2009).

[122] F. Schwabl, *Quantenmechanik* (Springer, 2002).

[123] G. Lindblad, Communications in Mathematical Physics, **48**, 119 (1976).

[124] M. Born, W. Heisenberg, and P. Jordan, Zeitschrift für Physik, **35**, 557 (1926).

[125] W. Rao, Y. Song, M. Liu, and C. Jin, Optik - International Journal for Light and Electron Optics, **121**, 1934 (2010).

[126] H. Ajiki and H. Ishihara, Phys. Status Solidi, **3**, 2440 (2006).

[127] A. H. Safavi-Naeini, T. P. M. Alegre, J. Chan, M. Eichenfield, M. Winger, Q. Lin, J. T. Hill, D. E. Chang, and O. Painter, Nature, **472**, 69 (2011).

[128] S. Groeblacher, K. Hammerer, M. R. Vanner, and M. Aspelmeyer, Nature, **460**, 724 (2009).

[129] A. D. O'Connell, M. Hofheinz, M. Ansmann, R. C. Bialczak, M. Lenander, E. Lucero, M. Neeley, D. Sank, H. Wang, M. Weides, J. Wenner, J. M. Martinis, and A. N. Cleland, Nature, **464**, 697 (2010).

[130] T. Rocheleau, T. Ndukum, C. Macklin, J. B. Hertzberg, A. A. Clerk, and K. C. Schwab, Nature, **463**, 72 (2010).

[131] T. Aoki, A. S. Parkins, D. J. Alton, C. A. Regal, B. Dayan, E. Ostby, K. J. Vahala, and H. J. Kimble, Phys. Rev. Lett., **102**, 083601 (2009).

[132] H. Ajiki and H. Ishihara, J. of Appl. Phys., **104**, 123105 (2008).

[133] J. Dowling and J. Gea-Banacloche, Adv. At. Mol. Opt. Phys., **37**, 1 (1996).

[134] H. Ajiki and H. Ishihara, Phys. Status Solidi, **6**, 395 (2009).

[135] X. Mi, J. X. Bai, D. Li, and H. Zhao, Opt. Commun., **284**, 2937 (2011).

[136] M. T. Cheng, Y. Q. Luo, Y. Y. Song, and G. X. Zhao, Opt. Commun., **283**, 3721 (2010).

[137] D. Witthaut and A. S. Sorensen, New Journal of Physics, **12**, 043052 (2010).

[138] P. Meystre and M. Sargent III, *Elements of Quantum Optics* (Springer Verlag, Heidelberg, 1998).

[139] H. M. Wiseman and G. J. Milburn, Phys. Rev. A, **47**, 642 (1993).

[140] C. W. Gardiner and M. J. Collett, Phys. Rev. A, **31**, 3761 (1985).

[141] D. F. Walls and G. J. Milburn, *Quantum Optics* (Springer Verlag, Heidelberg, 1994).

[142] R. J. Glauber, Phys. Rev., **130**, 2529 (1963).

[143] J. C. Cuevas and E. Scheer, *Molecular Electronics: An Introduction to Theory and Experiment* (World Scientific, Singapore, 2010).

[144] A. Mazzei, S. Götzinger, L. de S. Menezes, G. Zumofen, O. Benson, and V. Sandoghdar, Phys. Rev. Lett., **99**, 173603 (2007).

[145] J. I. Cirac, P. Zoller, H. J. Kimble, and H. Mabuchi, Phys. Rev. Lett., **78**, 3221 (1997).

[146] X. Zang and C. Jiang, J. of Physics B: Atomic, Molecular and Optical Physics, **43**, 065505 (2010).

[147] Y.-F. Xiao, B. Min, X. Jiang, C.-H. Dong, and L. Yang, IEEE J. of Quantum Electronics, **44**, 1065 (2008).

[148] D. Meiser and M. J. Holland, Phys. Rev. A, **81**, 063827 (2010).

[149] K. Mølmer, Y. Castin, and J. Dalibard, J. Opt. Soc. Am. B, **10**, 524 (1993).

[150] K. Mølmer and Y. Castin, Quantum and Semiclassical Optics: Journal of the European Optical Society Part B, **8**, 49 (1996).

[151] E. Peter, P. Senellart, D. Martrou, A. Lemaître, J. Hours, J. M. Gérard, and J. Bloch, Phys. Rev. Lett., **95**, 067401 (2005).

[152] T. Kippenberg, S. Spillane, and K. Vahala, Appl. Phys. Lett., **85**, 6113 (2004).

[153] N. L. Thomas, U. Woggon, O. Schöps, M. V. Artemyev, M. Kazes, and U. Banin, Nano Lett., **6**, 557 (2006).

[154] Y.-S. Park, A. K. Cook, and H. Wang, Nano Lett., **6**, 2075 (2006).

[155] A. Yariv, Y. Xu, R. Lee, and A. Scherer, Opt. Lett., **24**, 711 (1999).

[156] B. Little, S. Chu, P. Absil, J. Hryniewicz, F. Johnson, F. Seiferth, D. Gill, V. Van, O. King, and M. Trakalo, IEEE Photon. Technol. Lett., **16**, 2263 (2004).

[157] M. Bayindir, B. Temelkuran, and E. Ozbay, Phys. Rev. B, **61**, R11855 (2000).

[158] A. Reynolds, U. Peschel, F. Lederer, P. Roberts, T. Krauss, and P. de Maagt, IEEE Trans. Microwav. Theo. Tech., **49**, 1860 (2001).

[159] S. Trebaol, Y. Dumeige, and P. Feron, Phys. Rev. A, **81**, 043828 (2010).

[160] M. Hammer, Opt. Quant. Electron., **40**, 821 (2008).

[161] B. Sprenger, H. G. L. Schwefel, Z. H. Lu, S. Svitlov, and L. J. Wang, Opt. Lett., **35**, 2870 (2010).

[162] S. J. Buckle, S. M. Barnett, P. L. Knight, M. A. Lauder, and D. T. Pegg, Opt. Acta, **33**, 2473 (1986).

[163] E. A. Korsunsky, N. Leinfellner, A. Huss, S. Baluschev, and L. Windholz, Phys. Rev. A, **59**, 2302 (1999).

[164] E. A. Korsunsky and D. V. Kosachiov, Phys. Rev. A, **60**, 4996 (1999).

[165] A. J. Merriam, S. J. Sharpe, M. Shverdin, D. Manuszak, G. Y. Yin, and S. E. Harris, Phys. Rev. Lett., **84**, 5308 (2000).

[166] S. Kajari-Schröder, G. Morigi, S. Franke-Arnold, and G.-L. Oppo, Phys. Rev. A, **75**, 013816 (2007).

[167] A. F. Huss, R. Lammegger, C. Neureiter, E. A. Korsunsky, and L. Windholz, Phys. Rev. Lett., **93**, 223601 (2004).

[168] V. S. Malinovsky and I. R. Sola, Phys. Rev. Lett., **93**, 190502 (2004).

[169] H. Shpaisman, A. D. Wilson-Gordon, and H. Friedmann, Phys. Rev. A, **71**, 043812 (2005).

[170] M. Mahmoudi and J. Evers, Phys. Rev. A, **74**, 063827 (2006).

[171] O. Kocharovskaya and P. Mandel, Phys. Rev. A, **42**, 523 (1990).

[172] C. H. Keitel, O. A. Kocharovskaya, L. M. Narducci, M. O. Scully, S.-Y. Zhu, and H. M. Doss, Phys. Rev. A, **48**, 3196 (1993).

[173] G. Morigi, S. Franke-Arnold, and G.-L. Oppo, Phys. Rev. A, **66**, 053409 (2002).

[174] R. Fleischhaker and J. Evers, Phys. Rev. A, **80**, 063816 (2009).

[175] R. Fleischhaker and J. Evers, Phys. Rev. A, **78**, 051802 (2008).

[176] A. Mazzei and S. Götzinger and L. de S. Menezes and G. Zumofen and O. Benson and V. Sandoghdar, Phys. Rev. Lett., **99**, 173603 (2007).

[177] M. Borselli, T. J. Johnson, and O. Painter, Opt. Express, **13**, 1515 (2005).

[178] K. Kowalczyk and M. van Walstijn, IEEE Transactions on Audio, Speech, and Language Processing, **18**, 78 (2010).

[179] K. Kowalczyk and M. van Walstijn, IEEE Transactions on Audio, Speech, and Language Processing, **19**, 34 (2011).

[180] S. Wang, J. Acoust. Soc. Am., **99**, 1924 (1996).

[181] M. Hayakawa and T. Otsuyama, ACES Journal, **17**, 239 (2002).

[182] J. Simpson and A. Taflove, IEEE Antennas and Wireless Propagation Letters, **1**, 53 (2002).

[183] S. Hagness, A. Taflove, and J. Bridges, IEEE Transactions on Biomedical Engineering, **45**, 1470 (1998).

[184] K. Yee, IEEE Transactions on Antennas and Propagation, **14**, 302 (1966).

[185] A. Taflove, IEEE Transactions on Electromagnetic Compatibility, **22**, 191 (1980).

[186] A. Taflove and S. C. Hagness, *Computational electrodynamics: the finite-difference time-domain method, 3rd* (Artech House Boston, 2005).

[187] S. Preu, *Continuous-Wave, Tunable THz I-N-PN-I-P Superlattice Photomixers and Applications*, Ph.D. thesis, University of Erlangen-Nuremberg (2009).

[188] S. Preu, G. H. Döhler, S. Malzer, L. J. Wang, and A. C. Gossard, Journal of Applied Physics, **109**, 061301 (2011).

[189] J. C. Maxwell, Philosophical Transactions of the Royal Society of London, **155**, 459 (1865).

[190] B. E. Little and S. T. Chu, Opt. Lett., **21**, 1390 (1996).

[191] J.-P. Berenger, J. of Computational Physics, **114**, 185 (1994).

[192] F. Costen, J.-P. Berenger, and A. Brown, IEEE Transactions on Antennas and Propagation, **57**, 2014 (2009).

[193] J. Wiersig and M. Hentschel, Phys. Rev. A, **73**, 031802 (2006).

[194] T. K. Sarkar and A. Taaghol, IEEE Transactions on Antennas and Propagation, **47**, 566 (1999).

[195] P.-W. Zhai, Y.-K. Lee, G. W. Kattawar, and P. Yang, Appl. Opt., **18**, 3738 (2004).

[196] T. Martin, IEEE Transactions on Antennas and Propagation, **46**, 1263 (1998).

[197] P. Török, P. R. T. Munro, and E. E. Kriezis, J. Opt. Soc. Am., **23**, 713 (2006).

[198] K. Umashankar and A. Taflove, IEEE Transactions on Electromagnetic Compatibility, **24**, 397 (1982).

[199] J. D. Jackson, *Classical Electrodynamics* (Wiley, New York, 1998).

[200] T. Martin and L. Pettersson, ACES Journal, **16**, 45 (2001).

[201] I. R. Capoglu and G. S. Smith, IEEE Transactions on Antennas and Propagation, **54**, 3805 (2006).

[202] C. H. Schmidt and T. F. Eibert, IEEE Transactions on Antennas and Propagation, **57**, 1382 (2009).

[203] K. Husimi, Proc. Phys. Math. Soc. Jpn., **22**, 246 (1940).

[204] M. Hentschel, H. Schomerus, and R. Schubert, Europhys. Lett., **62**, 636 (2003).

[205] H. Schomerus and M. Hentschel, Phys. Rev. Lett., **96**, 243903 (2006).

[206] H. G. L. Schwefel, N. B. Rex, H. E. Tureci, R. K. Chang, A. D. Stone, T. Ben-Messaoud, and J. Zyss, J. Opt. Soc. Am. B, **21**, 923 (2004).

[207] H. E. Tureci, H. G. L. Schwefel, A. D. Stone, and P. Jacquod, Progress in Optics, **47**, 75 (2005).

[208] H. G. L. Schwefel, *Directionality and Vector Resonances of Regular and Chaotic Dielectric Microcavities*, Ph.D. thesis, Yale University (2004).

[209] Y. Baryshnikov, P. Heider, W. Parz, and V. Zharnitsky, Phys. Rev. Lett., **93**, 133902 (2004).

[210] J. Wiersig and M. Hentschel, Phys. Rev. Lett., **100**, 033901 (2008).

[211] M. Hentschel, Physik Journal, **9**, 39 (2011).

[212] F.-J. Shu, C.-L. Zou, F.-W. Sun, and Y.-F. Xiao, Phys. Rev. A, **83**, 053835 (2011).

[213] Q.-J. Wang, C. Yan, N. Yu, J. Unterhinninghofen, J. W. C. Pflügl, L. Diehl, T. Edamura, M. Yamanishi, H. Kan, and F. Capasso, Proc. Natl. Acad. Sci. USA, **107**, 22407 (2010).

[214] J.-W. Ryu and M. Hentschel, Opt. Lett., **36**, 2011 (2011).

[215] W.-M. Zhang, M.-H. Wu, C. U. Lei, and H.-N. Xiong, Opt. Express, **18**, 18407 (2010).

[216] D. G. Angelakis, L. Dai, and L. C. Kwek, EPL, **91**, 10003 (2010).

[217] H.-T. Tan, W.-M. Zhang, and G.-x. Li, Phys. Rev. A, **83**, 062310 (2011).

[218] H. Ajiki and H. Ishihara, Phys. Status Solidi, **5**, 2469 (2008).

[219] M. Eichenfeld, J. Chan, R. M. Camacho, K. J. Vahala, and O. Painter, Nature, **462**, 78 (2009).

[220] D. A. Fuhrmann, S. M. Thon, H. Kim, D. Bouwmeester, P. M. Petroff, A. Wixforth, and H. J. Krenner, "Dynamic modulation of photonic crystal nanocavities using gigahertz acoustic phonons," Nature Photon. Advance Online Publication, doi:10.1038/nphoton.2011.208 (2011).

[221] D. K. Umberger, C. Grebogi, E. Ott, and B. Afeyan, Phys. Rev. A, **39**, 4835 (1989).

[222] J. Sieber and T. Kalmár-Nagy, Phys. Rev. E, **84**, 016227 (2011).

Thanks

Last but not least, I would like to thank everyone who supported me during my Ph.D. time.

In particular, I want to thank

- Prof. Christoph H. Keitel for accepting me as a Ph.D. student in his theoretical quantum dynamics division at the Max Planck Institute for Nuclear Physics and thus giving me the possibility to carry out the exciting research presented in this thesis.
- my supervisor PD Dr. Jörg Evers, for the excellent supervision, the enjoyable collaboration, and especially the freedom to follow my own ideas.
- Prof. Thomas Gasenzer for reading my thesis and writing the second reference report.
- the further members of my examination committee Prof. Selim Jochim and Prof. Kurt Roth for their interest in my research topic.
- the experimentalists of the division of Gerd Leuchs at the Max Planck Institute for the Science of Light in Erlangen Harald Schwefel and Florian Sedlmeir as well as Sascha Preu from the University of California in Santa Barbara for the fruitful collaboration and the interesting discussions on theoretical as well as experimental challenges.
- our secretaries Vera Beyer and Sibel Babacan for their help in bureaucracy aspects.
- Peter Brunner and Dominik Hertel for their constant help whenever computer problems occurred.
- Ben King for his good English language proficiency.
- my colleagues, who joined me in the office for shorter or longer periods of time during the last years Martin Gärttner, Dominic Wörner, Kilian Heeg, Shuai Yang, Roman Hennig, and Robert Fleischhaker for the pleasant atmosphere in our office.
- the proof readers Benjamin Galow, Martin Gärttner, Qurrat-ul-Ain Gulfam, Kilian Heeg, Marcel Hellmann, Manuel Jütte, Michael Klaiber, Patrick Klenk, Wen-Te Liao, Sebastian Meuren, and Norman Neitz for their hints and comments.
- my colleagues from mainland China and Taiwan, Huayu Hu, Ni Cui, Feng He, Keyu Xia, Shuai Yang, Tian-Min Yan, and Wen-Te Liao for patiently teaching me Chinese and correcting my homework.
- my beloved Patrick for the personal support, the wonderful time together, and his patience during the last years.